III-V/Silicon Photonic Integrated Circuits
for Spectroscopic Sensing in the 2-2.5 µm Wavelength Range

Fotonische geïntegreerde circuits op basis van III-V-op-silicium
voor spectroscopische sensoren in het golflengtebereik van 2 µm tot 2.5 µm

Ruijun Wang

Promotor: prof. dr. ir. G. Roelkens
Proefschrift ingediend tot het behalen van de graad van
Doctor in de ingenieurswetenschappen: fotonica

UNIVERSITEIT
GENT

Vakgroep Informatietechnologie
Voorzitter: prof. dr. ir. B. Dhoedt
Faculteit Ingenieurswetenschappen en Architectuur
Academiejaar 2017 - 2018

ISBN 978-94-6355-064-2
NUR 950
Wettelijk depot: D/2017/10.500/99

UNIVERSITEIT
GENT

Universiteit Gent
Faculteit Ingenieurswetenschappen en
Architectuur
Vakgroep Informatietechnologie

Promotor:
Prof. dr. ir. Gunther Roelkens

Examencommissie:

Prof. dr. ir. D. De Zutter (voorzitter)	Universiteit Gent
Prof. dr. ir. G. Roelkens (Promotor)	Universiteit Gent
Prof. dr. ir. R. Baets	Universiteit Gent
Prof. dr. ir. G. Morthier	Universiteit Gent
Prof. dr. ir. J. Missinne	Universiteit Gent
Prof. dr. ir. M.-C. Amann	Technical University of Munich
Prof. dr. ir. W. Chen	University of the Littoral Opal Coast
Prof. dr. ir. Y. Jiao	Eindhoven University of Technology

Universiteit Gent
Faculteit Ingenieurswetenschappen en Architectuur

Vakgroep Informatietechnologie
Technologiepark-Zwijnaarde 15, B-9052 Gent, België

Tel.: +32-9-264.48.45
Fax.: +32-9-331.35.93

Proefschrift tot het bekomen van de graad van
Doctor in de ingenieurswetenschappen: fotonica
Academiejaar 2017-2018

Acknowledgment

Looking back to the whole journey toward this PhD degree, I can't recall when I started to think about studing abroad, but I still remember how I knew there is a photonics research group in Belgium and how I came here. Everything starts from the first year of my master study. During that period, part of my work is investigating how to improve efficiency of optoelectronic devices by photonic crystals. One of the most famous scientists in this field is John Joannopoulos, who is a professor of Physics at Massachusetts Institute of Technology (MIT). At that time, I knew it is quite hard for me to get a PhD position from MIT. So I checked where his PhD students and postdoctors were working, which can be easily found from his group website. I found most of people were working in different universities, but two of his postdoctors were working in the same place: Photonics Research Group (PRG) of Ghent University. So I put the website link of PRG as a favorite of my Firefox and occasionally checked it in the next two years, even the research topics of PRG are quite different from what I was working. In one evening of late February 2012, I clicked the PRG link again and excitedly seen several PhD vacancies. I applied one position about $\chi(2)$ nonlinear optics on a III-V/silicon platform. Actually, at that time, I was waiting for some PhD application results from some European universities. After a Skype interview, Prof. Gunther Roelkens offered me a PhD position about III-V/silicon VCSELs, which is different from that one I applied and more closely match my background. Almost at the same time, I got a PhD scholarship from a long-desired German university. After one week of comparison and hesitation, I chose Ghent. After more than five years of working here, I know I made a right choice. So wonderful! I got so much from these five years of PhD work. Coming to Ghent not only changed my academic career, but also my life. In the first flight to Belgium, I got to know a beautiful Chinese girl, Ning Liu, who was going to join Ghent University as a visiting PhD student. Now she is my wife. Thanks, Ghent.

Working towards a PhD is always not an easy journey, especially when you need to spend a long time to find the right direction. During this PhD period, I tried to work on high contrast grating VCSELs and heterogeneously integrated GaSb-based edge emitters in the first two years. Because we didn't have available epitaxial materials and repeatable fabrication processes, there were so many frustrated days and nights in those two years. Fortunately, we switched the direction to heterogeneously integrated InP-based type-II devices in the third

year. Then a door to a happy PhD life was opened. I still remember the exciting moments when I saw the first photodetector and laser was working. Thankfully, there are people can share the disappointing and happy moments. I really appreciate the help from so many people.

For the last five years of PhD work, I would like to firstly thank my supervisor, Prof. Gunther Roelkens. Gunther is the best supervisor I can expect. I really appreciate his help during my PhD journey. In the beginning of my PhD, he patiently led me to the PhD road and taught some practical skills. When I got feeling of this PhD work, he also gave me enough freedom in research. In the meanwhile, his office door is always open when I got problems. He always can give valuable suggestions on design, fabrication and measurements. Working with you is a so pleasant experience, Gunther. Thank you.

Secondly, thank all professors of Photonics Research Group. They make PRG so international and successful, especially thanks to our group leader Prof. Roel Baets. Roel also gave me a lot of support in research funding. Discussions with Roel, Geert and Bart are always quite helpful.

Special thanks to all members of my PhD Jury: prof. Daniël De Zutter, prof. Roel Baets, prof. Geert Morthier, prof. Jeroen Missinne, prof. Markus-Christian Amann, prof. Weidong Chen and prof. Yuqing Jiao. Thank you for your time and very valuable suggestions.

When working on III-V/silicon devices, we always need to pray that we can get good III-V epitaxial materials. It is a great opportunity to cooperate with prof. Amann's research group of Technical University of Munich from the third year of my PhD. Stephan Sprengel and Gerhard Boehm provides me one and a half 2-inch InP-based type-II epitaxial wafers, which are one of the most important parts of my PhD story. I also need to thank Brolis Semiconductors for their very good GaSb-based gain chips.

Processing in clean room is always not an easy job, especially when your devices require around ten lithography steps. Thanks to help from Steven, Liesbet and Muhammad, I can finish most processes as I want in the clean room of Ghent University. They really do a great job. In measurement rooms, Michael helped me a lot in coding. He also translated the English summary of this thesis into Dutch.

I am grateful to the help from several previous mid-infrared team members: Dorian, Nannicha, Aditya, Muhammad and Chen. They taught me a lot of processing and measurement skills, which are very useful for my PhD work. I also would like thank other mid-infrared team members: Anton, Utsav, Fabio, Sanja and Bahawal. My colleagues working on III-V-on-silicon devices shared a lot of processes secrets and measurement equipments with me. Thank you, Lianyan, Jing, Sulakshna, Amin, Soren, Mahmoud, Sarah and Andreas. I also would like to thank Daan, Eva and Kasper, Ilse, Mike and Kristien for their kind help.

Thank all of my Chinese colleagues, Yanlu, Chen, Yunpeng, Ang, Haolan, Jing, Yufei, Yuting, Xiaomin, Xiaoning, Yuxin, Lianyan, Haifeng, Xin, Bin, Zhechao, Weiqiang, Hui, Qiangsheng, Ye and Yingtao. Because of you, working in Ghent is full of fun and pleasure. Thank you very much for your help in the last five years.

I will switch to Chinese for the final part.

念了这么多年书，心里最感激的还是我的家人。我知道不管我做得怎么样，爸妈对我的关心永远都不会变化，谢谢你们的支持，辛苦了，让你们感觉骄傲一直是我前进的动力。谢谢我的岳父母和我弟，因为你们的支持，所以我能坚持做得更好。老婆，与你相遇是我在根特最大的收获，谢谢你这几年的付出与等待，遇到一个支持我懂我的你是我的幸运，因为你的陪伴，根特充满了美好。

Ghent, November 2017
Ruijun Wang

Table of Contents

ACKNOWLEDGMENT .... **I**

TABLE OF CONTENTS .... **V**

LIST OF FIGURES .... **IX**

LIST OF TABLES .... **XVII**

LIST OF ACRONYMS .... **XIX**

NEDERLANDSE SAMENVATTING .... **XXIII**

ENGLISH SUMMARY .... **XXXI**

1 INTRODUCTION **1**

1.1 SILICON PHOTONIC INTEGRATED CIRCUITS 2
1.2 ON-CHIP INFRARED SPECTROSCOPIC SENSING 5
1.2.1 Semiconductor laser sources and photodetectors 6
1.2.2 Waveguide circuits for the mid-infrared wavelength range 9
1.2.3 Evanescent sensing 11
1.3 III-V/SILICON PHOTONIC INTEGRATED CIRCUITS FOR SPECTROSCOPIC SENSING 12
1.4 APPLICATIONS OF 2 μM RANGE III-V/SILICON PHOTONIC COMPONENTS AND INTEGRATED CIRCUITS 14
1.4.1 Optical communication 14
1.4.2 Gas sensing 15
1.4.3 On-chip bio-sensing 17
1.5 OUTLINE OF THIS THESIS 18
1.6 PUBLICATIONS 19
REFERENCES 23

2 III-V-ON-SILICON PLATFORM FOR THE 2 μM WAVELENGTH RANGE **31**

2.1 INTRODUCTION 32
2.2 HETEROGENEOUS III-V-ON-SILICON PLATFORM 32
2.2.1 Direct and adhesive bonding 32
2.2.2 Optical coupling between the III-V layers and silicon waveguides 35

2.2.3 III-V-on-silicon photonic devices 37
2.3 III-V MATERIALS FOR THE 2 μM WAVELENGTH RANGE 39
2.3.1 InP-based type-I heterostructure 40
2.3.2 GaSb-based type-I heterostructure 40
2.3.3 InP-based type-II heterostructure 41
2.4 DESIGN OF INP-BASED TYPE-II EPITAXIAL LAYER STACK 44
2.5 FABRICATION OF 2 μM RANGE III-V-ON-SILICON PHOTONIC DEVICES 47
2.5.1 A general overview of the process flow 47
2.5.2 Fabrication of silicon waveguide circuits 49
2.5.3 Sample preparation for DVS-BCB adhesive bonding 50
2.5.4 Adhesive DVS-BCB bonding and substrate removal 51
2.5.5 Mesa definition 52
2.5.6 Etching of the active region 54
2.5.7 N-type contact metallization 56
2.5.8 Device isolation 57
2.5.9 Passivation 57
2.5.10 P-type contact metallization 58
2.5.11 Final metallization 59
2.5.12 Wire bonding 60
2.6 CONCLUSION 61
REFERENCES 63

3 III-V-ON-SILICON 2-μM-RANGE PHOTODETECTORS AND SPECTROMETERS 69

3.1 INTRODUCTION 70
3.2 III-V PHOTODETECTORS IN THE 2 μM WAVELENGTH RANGE 70
3.3 ADIABATICALLY-COUPLED PHOTODETECTORS 73
3.3.1 Device design 73
3.3.2 Device Fabrication 76
3.3.3 Characterization 77
3.4 GRATING-ASSISTED PHOTODETECTORS 80
3.4.1 Design and fabrication 80
3.4.2 Characterization 81
3.5 2.3 μM AWG SPECTROMETERS 81
3.6 AWGS INTEGRATED WITH PHOTODETECTORS 84
3.6.1 AWGs integrated with adiabatically-coupled photodetectors 84
3.6.2 AWGs integrated with grating-assisted photodetectors 87
3.7 AWG INTEGRATED WITH SLED 87
3.8 CONCLUSION 88
REFERENCES 90

4 III-V-ON-SILICON 2.3 μM RANGE LASER SOURCES 93

4.1 INTRODUCTION......94
4.2 TYPE-II QUANTUM WELL LASER DIODES ON INP......94
4.3 OPTICAL COUPLING DESIGN......96
4.4 III-V-ON-SILICON 2.3 μM FABRY-PEROT LASER......98
4.4.1 Design and fabrication......98
4.4.2 Characterization......100
4.4.3 Towards a widely tunable single mode laser......103
4.5 III-V-ON-SILICON 2.3 μM DFB LASER......104
4.5.1 Distributed feedback laser for the 2 μm range......104
4.5.2 Design and fabrication......105
4.5.3 Measurements......108
4.5.4 Tunable diode laser absorption spectroscopy......110
4.6 BROAD WAVELENGTH COVERAGE 2.3 μM RANGE III-V-ON-SILICON DFB LASER ARRAY......111
4.6.1 Design and Fabrication......111
4.6.2 Measurement results......112
4.6.3 Pulsed characterization and thermal resistance......117
4.7 CONCLUSION......118
REFERENCES......119

5 WIDELY TUNABLE GASB/SILICON HYBRID EXTERNAL CAVITY LASER......123

5.1 INTRODUCTION......124
5.2 EXTERNAL CAVITY LASER......124
5.3 DESIGN OF GASB/SILICON HYBRID EXTERNAL CAVITY LASER......127
5.3.1 A general overview of the device design......127
5.3.2 GaSb-based gain chip......128
5.3.3 Chip-to-chip coupling......128
5.3.4 Distributed grating reflector......130
5.3.5 Vernier filter......131
5.4 FABRICATION......133
5.5 CHARACTERIZATION OF THE VERNIER FILTER......134
5.6 MEASUREMENT SETUP......136
5.7 LASER PERFORMANCE......137
5.7.1 L-I-V properties......137
5.7.2 Tuning by one MRR......139
5.7.3 Tuning by two MRRs......140
5.7.4 Tuning by phase section......141
5.8 CONCLUSION......142
REFERENCES......143

6 CONCLUSIONS AND PERSPECTIVES......145

6.1 CONCLUSIONS 146
6.2 PERSPECTIVES 148
REFERENCES 150

List of Figures

Figuur 1. (a) Schema en (b) SEM-beeld van de doorsnede van een heterogeen geïntegreerde III-V-op-silicium type II actieve component......................xxiv

Figuur 2. (a) Schema van een adiabatisch gekoppelde fotodetector geïntegreerd op een silicium golfgeleider; (B) I-V-curve van de fotodetector onder verschillende golfgeleider-gekoppelde ingangsvermogens bij een golflengte van 2.35 μm. xxv

Figuur 3. (a) Microscoopbeeld van een 2.3 μm AWG spectrometer geïntegreerd met een InP-gebaseerde type-II kwantumput fotodetector array; (c) foto-respons van de 2.3 μm III-V-op-silicium AWG spectrometer. xxv

Figuur 4. (a) Schema van een III-V-op-silicium Fabry-Perot laser; (b) vezelgekoppeld emissiespectrum van een heterogeen geïntegreerde InP-gebaseerde type II Fabry-Perot laser. xxvi

Figuur 5. (a) Schema van een heterogeen geïntegreerde InP-gebaseerde type II DFB laser op silicium; Emissiespectrum van een DFB laser array voor verschillende siliciumrasterperiodes (b) en verschillende III-V golfgeleiderbreedten (c); (D) directe TDLAS meting van CO met behulp van een III-V-on-silicium DFB laser en het bijbehorende HITRAN spectrum. xxvii

Figuur 6. (a) Schema van een GaSb/silicium hybride externe caviteit laser; Spectra van de laser thermisch geregeld door één MRR (b), twee MRRs (c) en faseverschuiver (d), wanneer de koppelingkloof van de MRRs 500 nm is...xxix

Figure 7. Schematic drawing (a) and SEM image (b) of the cross section of a heterogeneously integrated III-V-on-silicon type-II active device. xxxii

Figure 8. (a) Schematic of an adiabatically-coupled photodetector integrated on a silicon waveguide; (b) I-V curve of the photodetector under different waveguide-coupled input powers at a wavelength of 2.35 μm. xxxiii

Figure 9. (a) Microscope image of a 2.3 μm AWG spectrometer integrated with a InP-based type-II quantum well photodetector array; (c) photo-response of the 2.3 μm III-V-on-silicon AWG spectrometer. xxxiii

Figure 10. (a) Schematic of a III-V-on-silicon Fabry-Perot laser; (b) fiber coupled emission spectrum of a heterogeneously integrated InP-based type-II Fabry-Perot laser...xxxiv

Figure 11. (a) Schematic of a heterogeneously integrated InP-based type-II DFB laser on silicon; emission spectrum of a DFB laser array with varied silicon grating

periods (b) and varied III-V waveguide widths (c); (d) direct TDLAS measurement of CO using a III-V-on-silicon DFB laser and the corresponding HITRAN spectrum. xxxv

Figure 12. (a) Schematic of a GaSb/silicon hybrid external cavity laser; superimposed spectra of the laser by thermally tuning one MRR (b), two MRRs (c) and phase shifter (d) when the coupling gap of MRRs is 500 nm. xxxvi

Figure 1.1. (a) Bird-view SEM image of a silicon waveguide bend [18]; (b) TE-polarized fundamental mode intensity distribution in the silicon waveguide. 3

Figure 1.2. (a) Microscope image of a silicon photonic integrated circuit. This silicon chip contains plenty of 2 μm-wavelength-range passive photonic components such as silicon waveguides, filters, spectrometers and active opto-electronic components such photodiodes, light emitting diodes and semiconductor optical amplifiers; (b) microscope image of a silicon photonic chip wire bonded to a printed circuit board. 4

Figure 1.3. The electromagnetic spectrum split up in different regions. 5

Figure 1.4. Schematic of band profiles and active region processes in type-I (a) and type-II (b) quantum well diode lasers, QCLs (c) and ICLs (d). 6

Figure 1.5. Emission wavelength coverage of semiconductor lasers based on different III-V active regions. 8

Figure 1.6. Comparison of the specific detectivity of various commercially available infrared detectors [49]. 9

Figure 1.7. Material systems for low-loss waveguides in the SWIR and MIR wavelength range. The white areas represent windows with a good optical transparency while the red areas indicate high loss [52]. 10

Figure 1.8. Illustration of a waveguide-based evanescent sensor [57]. 11

Figure 1.9. Schematic picture of a waveguide-based evanescent gas sensing system [58], non-integrated light sources and detectors are used in the sensing system. 12

Figure 1.10. Schematic of two silicon photonic configurations to realize an integrated on-chip absorption spectroscopy sensor. Broadband source and spectrometer, best suited for liquid and solid analytes (a). Tunable single mode laser source for trace gas detection (b). 13

Figure 1.11. (a) SEM image of the hollow core photonic bandgap fiber (HC-PBGF); (b) Transmission loss of the HC-PBGF and the output from the thulium doped fiber amplifiers (the location of the signal channel is at 2008 nm) [62]. 14

Figure 1.12. Absorption spectra for CO, CO_2 overlaid with water in the 1-6 μm wavelength range, taken from the HITRAN database. 16

Figure 1.13. Absorption spectra of HF, CH_4, CO and NH_3 in the 2.2-2.5 μm wavelength range. 17

Figure 1.14. Theoretical change in transmission because the absorption of glucose solution in the first overtone band (a) and the combination band for different glucose concentrations (b) [56]. 18

Figure 2.1. Schematic process flow for O_2 plasma-assisted SiO_2 covalent direct wafer bonding [3]. 33

Figure 2.2. Absorption of DVS-BCB versus wavelength [4]. 34

Figure 2.3. A two inch III-V membrane bonded on a Pyrex glass wafer (a), a silicon wafer (b), and a patterned SOI wafer (c) after substrate removal;(d) four III-V

dies bonded to a patterned SOI wafer before substrate removal (d) and after substrate removal (e)[7]. 35
Figure 2.4. (a) Schematic drawing of the III-V-on-silicon evanescent laser (a) [8], and adiabatically-coupled laser (b) [11]. 36
Figure 2.5. Photo of a 8 × 8 × 40 Gbps III-V-on-silicon transceiver chip [31]. 38
Figure 2.6. (a) Schematic of the cross-section of a QCL integrated on a SONOI waveguide; (b) the dependence of pulsed single-sided output power and voltage on drive current for the heterogeneously integrated QCL [34]. 39
Figure 2.7. (a) Emission spectra of GaSb-based DFB lasers covering the 1.8–3.0 μm wavelength range; (b) threshold current and slope efficiency versus lasing wavelength. All of these results are acquired at room-temperature in CW operation [42]. 41
Figure 2.8. (a) Band structure of a InGaAs/GaAsSb superlattice structure, the wavefunctions of electrons and heavy holes are plotted. Recombination processes mainly take place between electrons and heavy holes, because the ground state of heavy holes is the lowest state due to its low quantization energy. (b) 'W-shaped' InGaAs/GaAsSb active region [49]. 42
Figure 2.9. Photoluminescence (PL) spectra of a InGaAs/GaAsSb superlattice (SL) and a "W"-shaped active region [50]. 43
Figure 2.10. (a) Room-temperature photoluminescence spectra of "W"-shaped InGaAs/GaAsSb quantum wells; (b) emission spectra of InP-based type-II quantum well diode lasers [52]. 43
Figure 2.11. Schematic of the layer stack of passive and active photonic devices for the 2 μm wavelength range: (a) a silicon rib waveguide, (b) a III-V opto-electronic device bonded to a silicon waveguide. 44
Figure 2.12. Biased band structure of the InP-based type-II epitaxial layer stack bonded on the silicon waveguide circuit. 45
Figure 2.13. Biased band structure of one "W"-shaped period of the active region. 45
Figure 2.14. (a)-(q) Fabrication process flow of the 2 μm range III-V-on-silicon devices; (r) SEM image of the device cross section. 48
Figure 2.15. (a) Microscope image of a fabricated silicon waveguide circuit. SEM image of the cross-section of a fabricated SOI waveguide (b) and grating (c). 49
Figure 2.16. Microscope image of the top surface of the III-V wafer in different positions: center (a) and edge (b). Some defects are markerd. 50
Figure 2.17. Schematic process flow for adhesive bonding using DVS-BCB as the bonding agent [7]. 51
Figure 2.18. Microscope image of a InP-based type-II epitaxial layer stack bonded to a SOI die after substrate removal. 52
Figure 2.19. Bonding interface between the III-V layer and the silicon device layer with different BCB thickness. 52
Figure 2.20. SEM image of the inverted trapezoidal p-InP layer after HCl wet etching. 54
Figure 2.21. SEM image of (a) tapered III-V waveguides with suspended InGaAs and SiN_x tip, (b) an overetched III-V waveguide structure. (c-e) Microscope image of the sample surface after HCl wet etching. 54

Figure 2.22. Etch depth of a 300 nm thick GaAsSb layer and a 280 nm thick AlGaAsSb layer grown on a InP substrate. Etching is performed in a H_3PO_4: Citric Acid: H_2O_2:H_2O 1:1:20:70 solution. 55
Figure 2.23. (a) SEM image of the cross-section of a III-V waveguide after etching; (b) Microscope image of the III-V taper after active region etching.................... 56
Figure 2.24. (a) Microscope image of the sample after n-contact metallization; (b) I-V curve of the n-contact before and after annealing... 57
Figure 2.25. Microscope image of the sample after device isolation. 57
Figure 2.26. Microscope image of the sample after passivation.................................... 58
Figure 2.27. (a) Microscope image of the sample after p-contact metallization; (b) I-V curve of the p-contact before and after annealing... 59
Figure 2.28. Windows of DVS-BCB covered n-contacts are opened before the final metallization process. 60
Figure 2.29. Microscope image of the final III-V-on-silicon photonic IC....................... 60
Figure 2.30. Half of the sample shown in Figure.2.29 is wire bonded to a PCB. 61
Figure 3.1. Room temperature detectivity of InP-based InGaAs photodetectors with different cutoff wavelengths [1]. 71
Figure 3.2. I-V curve of the evanescently coupled InGaAsSb photodetectors under different input power at 2.29 μm. (■)Photocurrent measured at -0.1 V [8]..... 72
Figure 3.3. (a) I-V curve of a normal-incidence InP-based type-II photodetector in dark. (b) Responsivity of the device under different reverse voltage [14].............. 73
Figure 3.4. Schematic drawing of the top view (a) and cross section (b) of the adiabatically-coupled type-II quantum well photodetector heterogeneously integrated on a SOI waveguide circuit. 74
Figure 3.5. Schematic of the simulated structure with mode profiles of two cross-sections. 75
Figure 3.6. Mode-to-mode coupling efficiency as a function of taper tip width. 75
Figure 3.7. (a) Intensity distribution in a longitudinal cross section of the designed taper structure, without considering the active region absorption; (b) Intensity distribution in the designed taper structure taking the active region absorption into account ($1000cm^{-1}$ quantum well absorption coefficient). 76
Figure 3.8. (a) Microscope image of the heterogeneously integrated type-II quantum well photodetector; (a) SEM image of the cross section of the fabricated devices. 77
Figure 3.9. (a) I-V curve of the photodetector without light input; (b) I-V curve of the photodetector for different fiber-coupled input powers at a wavelength of 2.3 μm. 78
Figure 3.10. (a) Dependence of the fiber-coupled responsivity (R) on the input laser wavelength under reverse bias of 0 V and 0.5 V, the inset figure shows the grating coupler efficiency; (b) responsivity as a function of the reverse bias at a wavelength of 2.3 μm and 2.4 μm.. 79
Figure 3.11. (a) Schematic cross-section of the grating-assisted photodetector; (b) SEM image of the device cross-section.. 80
Figure 3.12. (a) I-V characteristic of the photodetector in the dark, the inset picture shows the device dark current as a function of reverse bias; (b) I-V curve of the device under different waveguide-coupled input power levels. 81

Figure 3.13. Microscope image of (a) the low-resolution AWG; (b) magnification of the input section of the low-resolution AWG; (c) the high-resolution AWG........ 82
Figure 3.14. The measured spectral responses of all the channels in four different AWGs. 84
Figure 3.15. (a) I-V curve of the adiabatically-coupled photodetectors without light input, the inset figure shows the dark current of the devices; (b) photoresponse of the devices under different input power levels; (c) linearity analysis of the adiabatically-coupled III-V-on-silicon photodetectors. 85
Figure 3.16. (a) Microscope image of an AWG integrated with adiabatically-coupled photodetectors; (b) and (c) response of two AWG spectrometers with integrated photodetectors. 86
Figure 3.17. (a) Microscope image of the hig- resolution AWG integrated with grating-assisted photodetectors; (b) and (c) measurement results of AWG-2 and AWG-4 integrated with grating-assisted photodetectors... 87
Figure 3.18. (a) Microscope image of an AWG integrated with an InP-based type-II LED; (b) fiber-coupled emission spectrum of the heterogeneously integrated LED; (c) filtered spectrum of the light coupled from LED to the different channels of the AWG. 88
Figure 4.1. Lasing performance of the firstly demonstrated 2.3 μm InP-based type-II quantum well laser diode [1]. (a) CW L-I-V curve; (b) Pulsed threshold current as a function of temperature. 95
Figure 4.2. Performance of improved type-II quantum well laser diodes on InP. (a) CW L-I-V curve of a λ=2.5 μm edge emitting laser; (b) emission spectrum of a λ=2.49 μm InP-based type-II VCSEL, driven at 15 mA and -20 ℃. 95
Figure 4.3. (a) Schematic drawing of the top view of the InP-based type-II SOA heterogeneously integrated on a SOI waveguide circuit, showing the III-V mesa and SOI waveguide structure. The electrical contacts were omitted for clarity; (b) detailed cross-section of the III-V/silicon waveguide; (c) and (d) TE- polarized mode intensity distribution in different parts of the device, the position of which is marked in (a) 96
Figure 4.4. (a) Simulated coupling efficiency of a 180 μm long adiabatic taper as a function of the taper tip width. (b) coupling efficiency of the adiabatic tapers with different tip widths as a function of the taper length. 97
Figure 4.5. Fundamental mode intensity evolution in a 180 μm long adiabatic taper with 0.5 μm wide III-V taper tip. 98
Figure 4.6. Fiber coupled emission spectrum from a heterogeneously integrated InP-based type-II SOA with 150 mA driven current... 98
Figure 4.7. Schematic drawing of the top view of the InP-based type-II Fabry-Perot laser heterogeneously integrated on a SOI waveguide circuit................................. 99
Figure 4.8. Simulated reflectivity of the two DBRs. 99
Figure 4.9. (a) Microscope image of the heterogeneously integrated lasers; (b) SEM image of the cross-section of the device.. 100
Figure 4.10. I-V curve of the laser and CW output power as a function of drive current at 5 ℃. 101
Figure 4.11. (a) Two typical emission spectra from the heterogeneously integrated Fabry-Perot lasers with different DBR period (420 nm and 435 nm),

characterized under CW operation at 5 ℃ and 160 mA injected current; (b) zoom of the emission spectrum from the Fabry-Perot laser with DBR period of 435 nm. 102

Figure 4.12. Peak laser output power as a function of pulsed driving current at temperatures from 15 ℃ to 40 ℃, for a pulse length of 0.5 μs and a repetition rate of 20 kHz. The inset picture shows the dependence of the pulsed threshold current density on temperature. 102

Figure 4.13. Schematic of a tunable single mode III-V-on-silicon laser by integrating two cascaded MRRs in the Fabry-Perot cavity. 103

Figure 4.14. Fiber coupled emission spectrum from the tunable single mode III-V-on-silicon laser with 150 mA driven current. 103

Figure 4.15. A commonly used DFB laser structure for the 2 μm wavelength range GaSb-based device, employing a laterally coupled metal grating as the feedback structure [15]. 105

Figure 4.16. (a) Top view and (b) three-dimensional schematic of a heterogeneously integrated InP-based type-II DFB laser on a silicon waveguide. 106

Figure 4.17. Calculated coupling strength of the DFB grating as a function of the DVS-BCB thickness for three different etch depths (150, 180, 210 nm) in the 400 nm silicon device layer. 107

Figure 4.18. SEM image of the longitudinal cross section of the III–V-on-silicon DFB laser. 107

Figure 4.19. CW L-I-V curve of the DFB laser with a 5 μm×1000 μm gain section and with a grating period of 348 nm. 108

Figure 4.20. Normalized emission spectra of the DFB laser with a grating period of 348 nm, measured at 10 ℃ with 190 mA bias current. 109

Figure 4.21. (a) Evolution of the lasing spectra as a function of the heat-sink temperature for the laser with grating period of 348 nm, the device is biased at 190 mA. The inset pictures show the dependence of the lasing wavelength on temperature. (b) Emission wavelength as a function of bias current for the laser operated at a heat-sink temperature of 10 °C. The inset pictures show the laser wavelength as a function of injected current at a temperature of 5 °C, 10 °C and 15 °C. 110

Figure 4.22. TDLAS spectrum of CO and the corresponding HITRAN spectrum. 111

Figure 4.23. (a) Schematic of the III-V-on-silicon DFB laser array; (b) SEM image of the longitudinal cross-section of the gain section. 112

Figure 4.24. (a) CW L-I-V characteristics of a heterogeneously integrated DFB laser with grating pitch of 353 nm at different heat-sink temperatures. The solid portions of the L-I curve indicate a single-mode emission with a SMSR of at least 20 dB, while the dashed portions correspond to dual-mode operation. (b) Spectral map of the laser device as a function of the bias current at a heat-sink temperature of 5°C. 113

Figure 4.25. Emission spectra and single mode peak output power of six DFB lasers with different silicon grating pitch in an array. The width of Laser1-Laser5 and Laser6 is 3.8 μm and 3.2 μm, respectively. 114

Figure 4.26. (a) CW L-I-V plot of a heterogeneous InP-based type-II DFB laser with a 5 μm wide and 700 μm long gain section and grating pitch of 353 nm; (b) The

inset shows the evolution of the laser emission spectrum with increasing bias current at 5˚C. 115
Figure 4.27. Normalized lasing spectra of four 700 μm long DFB lasers with a grating pitch ranging from 343 nm to 357 nm. 115
Figure 4.28. Evolution of the lasing spectra as a function of the bias current (20 mA step) for four DFB lasers with different gain section widths and the same silicon grating pitch of 353 nm (a) and 357 nm (b). (c) and (d): the dependence of optical output power on lasing wavelength. 116
Figure 4.29: (a) Peak laser output power as a function of pulsed drive current at temperatures from 5 ˚C to 25 ˚C; (b) Dependence of the pulsed threshold current on temperature. 117
Figure 5.1. Two principal designs of semiconductor external cavity lasers with bulk diffraction gratings: (a) Littrow configuration and (b) Littman configuration [1]. 125
Figure 5.2. Tuning curve of three GaSb-based external cavity lasers based on the Littrow configuration [3]. 125
Figure 5.3. A picture of an external cavity laser from Thorlabs [3]. 126
Figure 5.4. Schematic of a tunable GaSb/silicon external cavity laser using a silicon photonic IC as the feedback circuit. 127
Figure 5.5. Schematic of the silicon spot size converter. 129
Figure 5.6. (a) Microscope image of the silicon SSC; (b) TE-polarized fundamental mode intensity distribution at the facet of the SSC at a wavelength of 2 μm; (c) simulated mode conversion loss for SSCs with different taper tip width, a SEM image of the 180 nm wide taper tip is shown in the inset. 130
Figure 5.7. (a) Simulated reflectivity of the DBR outcoupling mirror; (b) SEM image of the fabricated DBR. 131
Figure 5.8. (a) Simulated transmission spectra of two different MRRs with coupling coefficient κ=0.3; (b) transmission spectrum of the Vernier filter. 132
Figure 5.9. Modal transmission difference between the dominant lasing mode and the nearest side-mode as a function of the coupling coefficient of the MRRs. 133
Figure 5.10. Microscope image of the fabricated silicon waveguide circuit. 133
Figure 5.11. Microscope image of the metal heater on the silicon MRRs. 134
Figure 5.12. (a) Transmission spectrum of a SOI MRR with coupling gap of 350 nm, measured from the drop port; (b) Comparison of the quality factor of three MRRs with different coupling gaps. 135
Figure 5.13. Measured transmission spectrum of the Vernier filter consisting of MRRs with coupling coefficient κ = 0.3. 135
Figure 5.14. (a) Schematic of the experimental setup; (b) top view of the butt-coupling between the GaSb-based gain chip and silicon photonic IC. 136
Figure 5.15. Measured amplified spontaneous emission coupled to a silicon waveguide when the gain chip is driven with 100 mA injection current. 137
Figure 5.16. Light-current-voltage curves of the GaSb/silicon external cavity lasers. Three devices with different coupling gap are shown. 138
Figure 5.17. A typical output spectrum from the laser with coupling gap of 500 nm, measured at an injection current of 300 mA. 138

Figure 5.18. Superimposed spectra of three lasers with coupling gap of 200 nm (a), 350 nm (b) and 500 nm (c), tuned by varying the heater power of Ring1; (d) wavelength tuning as a function of Heater1 power, for the case of MRRs with a coupling gap of 500 nm. 139
Figure 5.19. Dependence of on-chip output power (a) and SMSR (b) on the lasing wavelength for the lasers with different coupling gap. 140
Figure 5.20. Superimposed spectra of the laser with 500 nm coupling gap showing 0.7 nm (a) and 0.2 nm (b) resolution tuning over 25 nm and 2 nm, respectively; (c) dependence of the lasing wavelength on the power of Heater2 for the 0.2 nm resolution tuning shown in (b). 141
Figure 5.21. Contour map of the fiber-coupled laser spectra as a function of the dissipated power in the heater of the phase shifter of the laser with 500 nm coupling gap. 142

List of Tables

Table 2.1. Properties of DVS-BCB [3]..34
Table 2.2. Parameters of the III-V epitaxial layer stack used for 2.35 μm range III-V-on-silicon photonic devices. 46
Table 3.1 Design and layout parameters summary for AWGs 83

List of Acronyms

A

ASE	Amplified Spontaneous Emission
AWG	Arrayed Waveguide Grating

C

CMOS	Complementary Metal-Oxide-Semiconductor
CMP	Chemical Mechanical Polishing
CW	Continuous-Wave

D

DBR	Distributed Bragg Reflector
DFB	Distributed Feedback
DI	Deionized
DVS-BCB	Divinylsiloxane-Benzocyclobutene

E

EAM	Electroabsorption Modulators
EC	External Cavity
EDFA	Erbium Doped Fiber Amplifiers
EL	Electroluminescence

F

FPR	Free Propagation Region
FSR	Free Spectral Range

H

HC-PBGF	Hollow Core Photonic Bandgap Fiber

I

IC	Integrated Circuit
ICL	Interband Cascade Laser
ICP	Inductively-Coupled Plasma

L

LED	Light Emitting Diode
L-I-V	Light-Current-Voltage
LPCVD	Low-Pressure Chemical Vapor Deposition

M

MBE	Molecular Beam Epitaxy
Mid-IR	Mid-Infrared
MIR	Mid-Infrared
MMI	Multimode Interference
MPW	Multi-Project Wafer
MRR	Micro-Ring Resonator

N

NEP	Noise-Equivalent Power

O

OSA	Optical Spectrum Analyzer

P

PCB	Printed Circuit Board
PECVD	Plasma-Enhanced Chemical Vapor Deposition
PRBS	Pseudo-Random Bit Sequence

Q

QCL	Quantum Cascade Laser
QW	Quantum Well

R

RIE	Reactive Ion Etching

S

SC-1	Standard Clean 1
SCH	Separate Confinement Heterostrcture
SEM	Scanning Electron Microscope
SLD	Superluminescent Diode
SMF	Single Mode Fiber
SMSR	Side-Mode Suppression Ratio
SOA	Semiconductor Optical Amplifiers
SOI	Silicon-On-Insulator
SON	Silicon-On-Nitride
SONOI	Silicon-On-Nitride-On-Insulator
SSC	Spot Size Converter
SWIR	Short-Wavelength Infrared

T

TDFA	Thulium ($Tm3^{+}$) Doped Fiber Amplifier
TDLAS	Tunable Diode Laser Absorption Spectroscopy
THz	Terahertz
Ti	Titanium
TIA	Trans-Impedance Amplifiers
TUM	Technical University of Munich

V

VCSEL	Vertical-Cavity Surface-Emitting Laser

W

WDM	Wavelength Division Multiplexing

Nederlandse Samenvatting

Silicium fotonica krijgt veel belangstelling als een veelbelovend geïntegreerd optisch platform voor diverse toepassingen bij optische communicatiegolflengtes. Dit platform kan gebruik maken van de silicium processen gebruikt voor de realizatie van elektronische geïntegreerde circuits om fotonische componenten te produceren met hoog rendement en in hoog volume. Bovendien laat het hoge indexcontrast van silicium-op-isolator (SOI) golfgeleiders toe om ultra-compacte fotonische componenten en systemen te realizeren. Met deze voordelen zijn de mogelijke toepassingen van geïntegreerde siliciumfotonische schakelingen (ICs) in de afgelopen jaren uitgebreid naar sensoren, die niet noodzakelijk bij telecommunicatiegolflengtes werken, zeker in het geval van spectroscopische sensoren.

Het 2 µm golflengtebereik bijvoorbeeld is van belang voor biomedische toepassingen, milieu-monitoring en procescontrole, aangezien veel belangrijke gassen sterke absorptielijnen hebben in dit golflengtebereik. De beschikbaarheid van silicium fotonische ICs in het 2 µm golflengtebereik zou toelaten om geminiaturizeerde optische sensoren te realizeren, in staat om gassen in lage concentraties te detecteren. Ze zijn ook waardevol voor biosensortoepassingen, zoals voor de meting van bloedglucose. Bij deze toepassingen moet de spectroscopische sensor beschikken over een lichtbron, een probe en een spectrometer/fotodetector. Silicium is een indirecte bandkloof halfgeleider met extreem lage efficiëntie voor lichtemissie, transparant boven 1.1 µm golflengte. Om volledig geïntegreerde fotonische systemen voor het 2 µm golflengtebereik te realiseren, moet daarom een heterogeen III-V-op-silicium platform worden ontwikkeld om performante III-V laserbronnen en fotodetectoren op deze golfgeleidercircuits te integreren.

III-V-op-silicium platform voor het 2 µm golflengte bereik

In dit proefschrift presenteren wij de ontwikkeling van een 2 µm golflengtebereik III-V-op-silicium platform, gebaseerd op een InP-gebaseerde type-II heterostructuur. Heterogeen geïntegreerde III-V-op-silicium lasers en fotodetectoren worden gerealiseerd met hetzelfde epitaxiale lagenpakket. Figuur 1(a) toont schematisch de doorsnede van de heterogene InP-gebaseerde type II-component op een SOI-golfgeleider. Het III-V epitaxiale lagenpakket wordt verlijmd op een SOI-golfgeleidercircuit met behulp van een ultra-dunne divinylsiloxaan-benzocyclobuteen (DVS-BCB) laag van een paar tientallen nanometer dik. Na binding wordt het InP-substraat verwijderd door nat etsen met HCl. Vervolgens worden de lasers en fotodetectoren samen gerealizeerd op het III-V membraan. Eerst wordt een anisotrope HCl natte ets van de *p*-InP mantellaag gebruikt om een "V"-vormige mesa te creëren. Dan wordt het actieve gebied geëtst met behulp van een 1:1:20:70 H_3PO_4:H_2O_2:citroenzuur:H_20 oplossing. Vervolgens worden de componenten geïsoleerd door nat etsen van de *n*-InP laag met behulp van HCl. Een combinatie van SiN_x en DVS-BCB wordt gebruikt om de mesa van de component te passiveren. Een afbeelding onder de elektronenmicroscoop (SEM) van de doorsnede van de vervaardigde III-V-op-silicium componenten is te zien in Figuur 1(b).

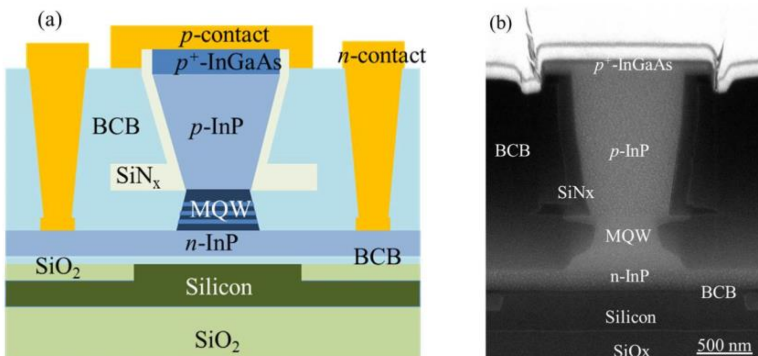

Figuur 1. *(a) Schema en (b) SEM-beeld van de doorsnede van een heterogeen geïntegreerde III-V-op-silicium type II actieve component.*

III-V-op-silicium fotodetectoren en spectrometers

Voor een golfgeleidergebaseerde optische sensor dienen de fotodetectoren geïntegreerd te worden met de golfgeleidercircuits om de optische signalen om

te zetten in een elektrische respons. In dit proefschrift bestuderen we III-V-op-silicium fotodetectoren op basis van twee verschillende koppelingsmethoden tussen het III-V actieve gebied en de siliciumgeleider: adiabatische koppeling en roosterkoppeling. In de eerste structuur wordt licht efficiënt gekoppeld van de silicium golfgeleider naar de III-V-golfgeleider door een vernauwende tip en vervolgens geabsorbeerd door het actieve gebied, zoals schematisch weergegeven in Figuur 2(a). Figuur 2(b) toont de I-V-curve van de adiabatisch gekoppelde fotodetector onder verschillende ingangsvermogens bij een golflengte van 2.35 μm. Een responsiviteit van 1.6 A/W bij 2.35 μm golflengte kan uit de grafiek worden afgeleid. De donkerstroom is 10 nA bij -0.5 V. In de rooster-geassisteerde fotodetector wordt het licht in de silicium golfgeleider naar het III-V actieve gebied gekoppeld door middel van een siliciumrooster. Dit type fotodetector toont een responsiviteit van 0.1 A/W en een donkerstroom van 5 nA bij -0.5 V.

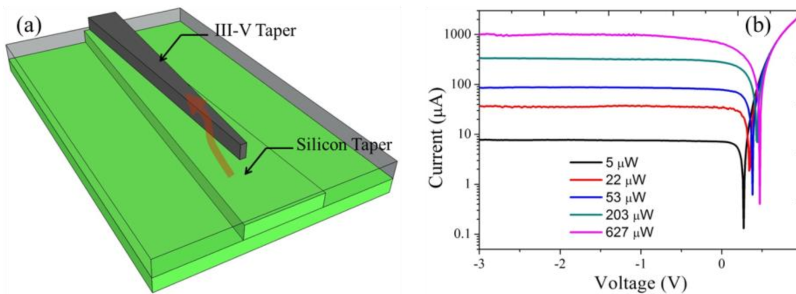

Figuur 2. *(a) Schema van een adiabatisch gekoppelde fotodetector geïntegreerd op een silicium golfgeleider; (b) I-V-curve van de fotodetector onder verschillende golfgeleidergekoppelde ingangsvermogens bij een golflengte van 2.35 μm.*

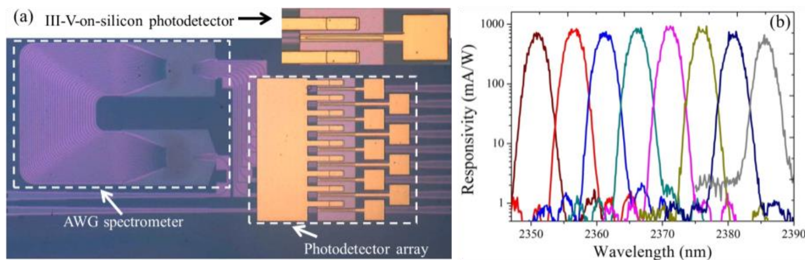

Figuur 3. *(a) Microscoopbeeld van een 2.3 μm AWG spectrometer geïntegreerd met een InP-gebaseerde type-II fotodetector array; (b) foto-respons van de 2.3 μm III-V-op-silicium AWG spectrometer.*

Een AWG (arrayed waveguide grating) wordt veel gebruikt als (de)multiplexer in golflengtemultiplexingsystemen en kan ook worden gebruikt als spectrometer in spectroscopische sensoren. Figuur 3(a) toont het microscoopbeeld van een 2.3 µm AWG spectrometer geïntegreerd met een adiabatisch gekoppelde InP-gebaseerde type II fotodetector array. Vóór heterogene integratie met III-V fotodetectoren heeft de passieve AWG spectrometer een insertieverlies van 2.5 dB en een overspraak van -30 dB. Figuur 3(b) toont de fotorespons van de 2.3 µm III-V-op-silicium spectrometer. Een insertieverlies van 3 dB en overspraak van -27 dB wordt verkregen door de responsiviteit te normaliseren ten opzichte van een referentie geïntegreerde fotodetector. Dit resultaat geeft aan dat de integratie van III-V materiaal op silicium en de daaropvolgende processen de prestaties van de AWG spectrometer niet verminderen.

III-V-op-silicium 2.3 µm-golflengtebereik lasers

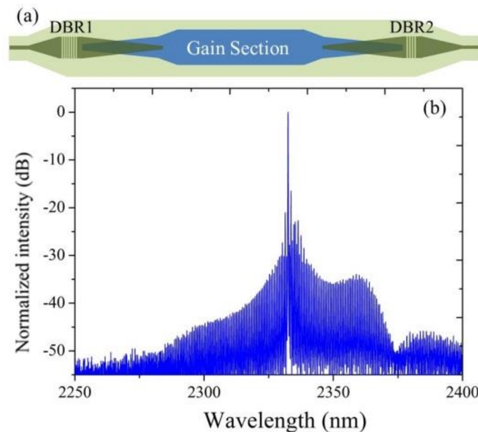

Figuur 4*. (a) Schema van een III-V-op-silicium Fabry-Perot laser; (b) vezelgekoppeld emissiespectrum van een heterogeen geïntegreerde InP-gebaseerde type II Fabry-Perot laser.*

Met hetzelfde epitaxiale lagenpakket als bij de heterogeen geïntegreerde InP-gebaseerde type II fotodetectoren werden 2 µm golflengtebereik III-V-op-silicium Fabry-Perot lasers en gedistribueerde feedback (DFB) lasers gerealiseerd. Figuur 4(a) toont schematisch de III-V-op-silicium Fabry-Perot laser. De component bestaat uit een versterkersectie, een III-V/silicium spot size converter (SSC) aan beide zijden, en twee silicium Bragg-roosterreflectoren (DBRs) om de lasercaviteit te vormen. Een efficiënte lichtkoppeling van de III-V-golfgeleider naar de siliciumgeleider wordt gerealiseerd met behulp van de

III-V/silicium SSCs. Bij werking in continu bedrijf wordt een drempelstroomdichtheid van 2.7 kA/cm^2 en uitgangsvermogen van 1.3 mW bij 5 ℃ bereikt voor de Fabry-Perot laser. De laser produceert meer dan 3.7 mW piekvermogen met een drempelstroomdichtheid van 1.6 kA/cm^2 in gepulste sturing bij kamertemperatuur. Een hoge resolutie emissiespectrum van de Fabry-Perot laser is weergegeven in Figuur 4(b).

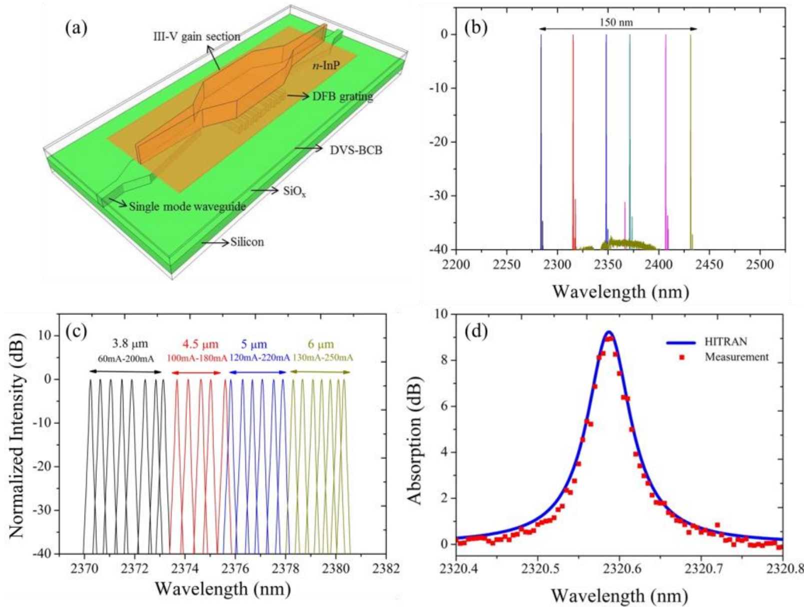

Figuur 5. *(a) Schema van een heterogeen geïntegreerde InP-gebaseerde type II DFB laser op silicium; Emissiespectrum van een DFB laser array voor verschillende silicium roosterperiodes (b) en verschillende III-V golfgeleiderbreedtes (c); (d) directe TDLAS meting van CO met behulp van een III-V-on-silicium DFB laser en het bijbehorende HITRAN spectrum.*

DFB lasers zijn goed geschikte lichtbronnen voor afstembare diode laser spectroscopie (TDLAS) van gassen. Figuur 5(a) toont schematisch een InP-gebaseerde type II DFB laser die heterogeen geïntegreerd is op een siliciumgeleider. Een kwartgolf verschoven eerste-orde DFB rooster met een etsdiepte van 180 nm in een 400 nm siliciumlaag wordt onder de versterkersectie geïmplementeerd. De evanescente staart van de optische mode interageert met het rooster, wat de lasergolflengte van de DFB-laser selecteert. In continu bedrijf kan de heterogeen geïntegreerde InP-gebaseerde type II DFB-laser werken bij een maximale temperatuur van 25 ℃ en meer dan 3 mW uitgangsvermogen opwekken, in een enkele longitudinale mode en met een drempelstroomdichtheid van 1.8 kA/cm^2 bij 5 ℃. De lasergolflengte van de III-

V-op-silicium DFB lasers wordt bepaald door de periode van het siliciumrooster. Figuur 5(b) toont de emissiespectra van zes 1000 μm lange heterogeen geïntegreerde DFB lasers. Naarmate de periode van het siliciumrooster toeneemt van 343 nm naar 368 nm, verschuift de lasergolflengte van 2280 nm naar 2430 nm. Dit brede golflengtebereik overspant absorptiepieken van verschillende belangrijke gassen, zoals NH_3, CO, CH_4, C_2H_2 en HF. Een andere methode om de lasergolflengte te regelen is de versterkersectie van de DFB-lasers aan te passen. Figuur 5(c) toont de CW-laserspectra van vier 700 μm lange DFB lasers voor verschillende breedtes van de III-V golfgeleider, als functie van de stroom doorheen de diode. Een continue bereik van meer dan 10 nm, regelbaar door de stroom, wordt op die manier verkregen. We hebben een TDLAS CO meting uitgevoerd met behulp van een dergelijke III-V-on-silicium DFB laserbron. Uit Figuur 5(d) blijkt dat het meetresultaat goed overeenstemt met gegevens uit de HITRAN-database.

GaSb/silicium hybride externe caviteit laser

We realiseerden ook een GaSb/silicium hybride externe caviteit laser met wijd afstembereik door koppeling van een GaSb-gebaseerde versterkerchip en een silicium fotonisch IC. Het IC bevat een Vernier filter bestaande uit twee thermisch ingestelde micro-ring resonatoren (MRR's), een fasesectie voor het mogelijk maken van quasi-continue golflengteregeling en een DBR zoals getoond in Figuur 6(a). Figuur 6(b) toont de laserspectra van de GaSb/silicium hybride laser door één MRR af te stemmen. Een afstembereik van 58 nm wordt bereikt met een SMSR beter dan 52 dB over het volledige bereik en meer dan 60 dB bij de optimale golflengte. Wanneer slechts één MRR wordt afgestemd, wordt de afstemresolutie bepaald door het vrij spectraal bereik van de andere MRR. Fijne quasi-continue golflengteregeling kan worden bereikt door gelijktijdige afstemming van beide MRR's. Figuur 6(c) toont de spectra met 0,7 nm resolutie tuning over 25 nm bereik, gerealiseerd op deze manier. Maar zelfs bij het afstemmen van beide MRR's is de afstemresolutie nog steeds beperkt door het vrij spectraal bereik van de longitudinale modi van de Fabry-Perot caviteit. Doorlopende regeling kan worden bereikt door de fasesectie thermisch af te stemmen, zoals getoond in Figuur 6(d). Wanner de afstand tussen de MRRs en de busgolfgeleider van 200 nm tot 500 nm toeneemt, vermidert het maximale uitgangsvermogen van de GaSb/siliciumhybride laser van 7.5 mW tot 3.8 mW, maar de SMSR en precisie van de afstemming worden beter.

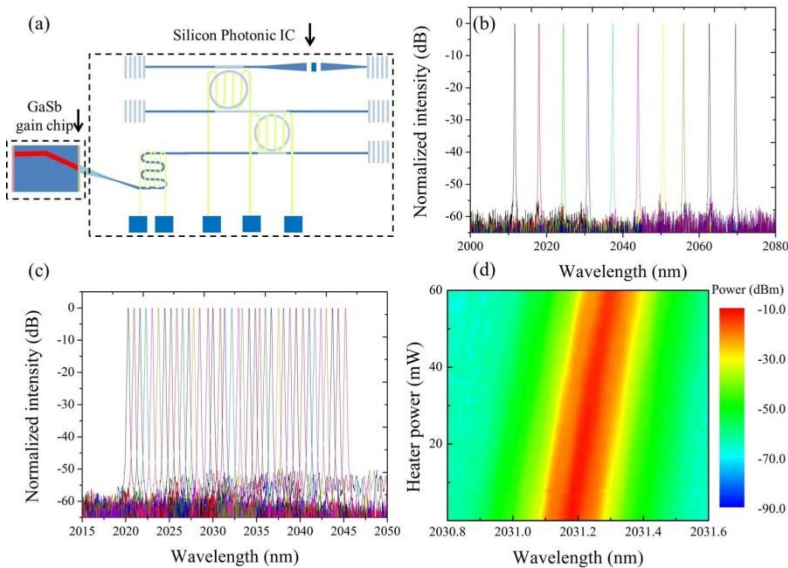

Figuur 6. *(a) Schema van een GaSb/silicium hybride externe caviteit laser; Spectra van de laser thermisch geregeld door één MRR (b), twee MRRs (c) en faseverschuiver (d), voor een afstand tussen MRR en busgolfgeleider van 500 nm.*

Conclusie

In dit proefschrift rapporteren we volledig geïntegreerde 2 µm-golflengtegebied III-V-op-silicium fotonische circuits, bestaande uit silicium golfgeleiders, laserbronnen, fotodetectoren en AWG spectrometers. De actieve opto-elektronische fotonische componenten worden gerealiseerd door heterogene integratie van een InP-gebaseerde type II epitaxiaal lagenpakket op silicium golfgeleiders. Daarnaast rapporteren we een breed afstembare GaSb/silicium hybride externe caviteit laser door een GaSb-gebaseerde versterkerchip en een silicium fotonisch IC te combineren.

English Summary

Silicon photonics has received great interest as a promising integrated-optics platform for various applications in the telecommunication wavelength range, such as optical interconnects. This platform can take advantage of the silicon electronics processes to fabricate photonic devices in high yield and high volume. In addition, the high refractive index contrast of silicon-on-insulator (SOI) waveguides enables a tight bending radius, and consequently ultra-compact photonic devices and systems. With these advantages, in recent years the potential applications of silicon photonic integrated circuits (ICs) are extended to spectroscopic sensing. However, the silicon photonic devices used at telecommunication wavelengths are typically retained for most of these new applications due to the lack of components at other wavelengths, which limits the performance of these silicon photonics sensing systems.

The 2 μm wavelength range is of interest for security, environmental and process control applications since many important gases have strong absorption lines in this wavelength range. The availability of silicon photonic ICs in the 2 μm wavelength range enables miniature optical sensors for trace gas. Besides, it is also valuable for bio-sensing applications, such as blood glucose measurements. In these applications, the silicon photonic spectroscopic sensor should have a light source, a probe component and a spectrometer or single pixel detector. Silicon is an indirect bandgap semiconductor with extremely low light emission efficiency, transparent beyond 1.1 μm wavelength. In order to realize fully integrated silicon photonic systems for the 2 μm wavelength range, a heterogeneous III-V-on-silicon platform is developed to integrate high-performance III-V laser sources and photodetectors on silicon waveguide circuits.

III-V-on-silicon platform for the 2 μm wavelength range

In this thesis, we present the development of a 2 μm wavelength range III-V-on-silicon platform based on a InP-based type-II heterostructure. Heterogeneously

integrated III-V-on-silicon lasers and photodetectors are realized using the same epitaxial layer stack. Figure 7(a) shows the schematic cross-section of the heterogeneous InP-based type-II device on a SOI waveguide. The III-V epitaxial layer stack is adhesively bonded to a SOI waveguide using an ultra-thin divinylsiloxane-benzocyclobutene (DVS-BCB) layer of a few tens of nanometers. After bonding, the InP-substrate is removed by HCl wet etching. Then the lasers and photodetectors are co-processed on the III-V membrane. First, an anisotropic HCl wet etch of the *p*-InP cladding layer is employed to create a "V"-shaped mesa. Then the active region is etched by using a 1:1:20:70 H_3PO_4:H_2O_2:citric acid:H_2O solution. Subsequently, the devices are isolated by wet etching of the *n*-InP layer using HCl. A combination of SiNx and DVS-BCB is used to passivate the device mesa. A scanning electron microscope (SEM) image of the cross-section of the fabricated III-V-on-silicon devices is shown in Figure 7(b).

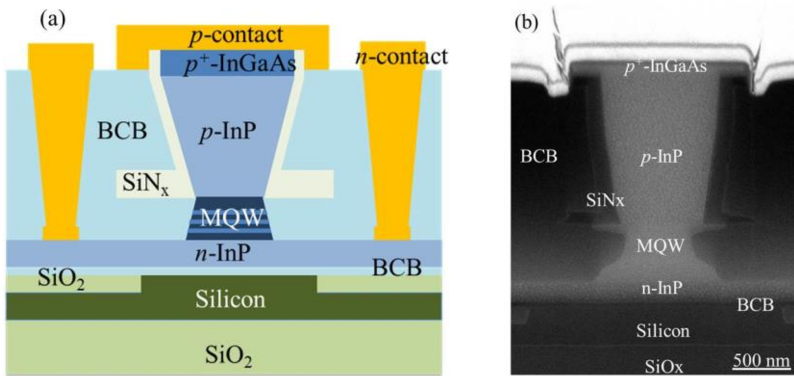

Figure 7. *Schematic drawing (a) and SEM image (b) of the cross section of a heterogeneously integrated III-V-on-silicon type-II active device.*

III-V-on-silicon photodetectors and spectrometers

For a waveguide-based optical sensor, photodetectors should be integrated with the waveguide circuits to convert the optical signals to an electrical response. In this thesis, we study III-V-on-silicon photodetectors based on two different coupling methods between the III-V active region and the silicon waveguide: adiabatically-coupled and grating-assisted photodetectors. In the first structure, light is efficiently coupled from the silicon waveguide into the III-V waveguide by a narrow taper tip, and subsequently absorbed by the active region, as schematically shown in Figure 8(a). Figure 8(b) shows the I-V curve of the adiabatically-coupled photodetector under different waveguide-referred input power levels at 2.35 µm wavelength. A responsivity of 1.6 A/W at 2.35 µm

wavelength and dark current of 10 nA at −0.5 V can be extracted from the curve. In the grating-assisted photodetector, light in the silicon waveguide is diffracted to the III-V active region by using a silicon grating. This type of photodetector shows a responsivity of 0.1 A/W and dark current of 5 nA at −0.5 V.

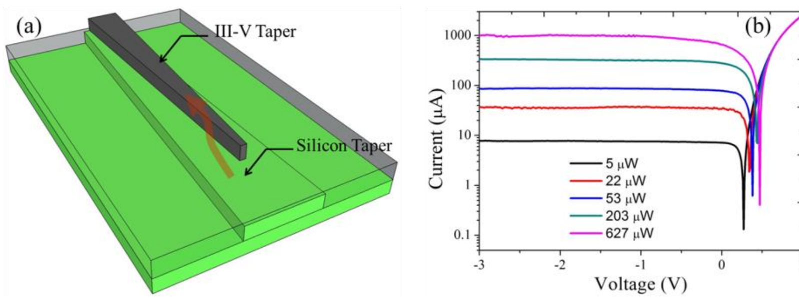

Figure 8. *(a) Schematic of an adiabatically-coupled photodetector integrated on a silicon waveguide; (b) I-V curve of the photodetector under different waveguide-coupled input powers at a wavelength of 2.35 μm.*

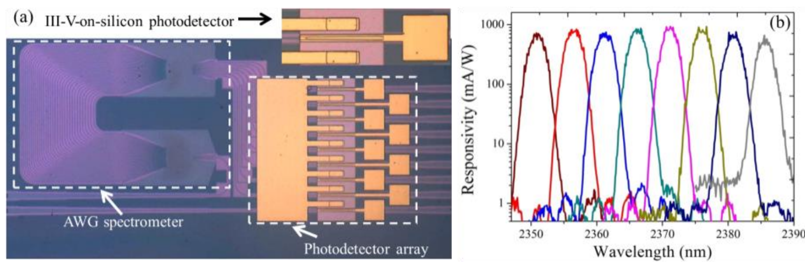

Figure 9. *(a) Microscope image of a 2.3 μm AWG spectrometer integrated with a InP-based type-II quantum well photodetector array; (b) photo-response of the 2.3 μm III-V-on-silicon AWG spectrometer.*

Arrayed waveguide gratings (AWGs) are widely used as (de)multiplexers in wavelength division multiplexing systems and can also be used as spectrometers in spectroscopic sensors. Figure 9(a) displays a microscope image of a 2.3 μm AWG spectrometer integrated with an adiabatically-coupled InP-based type-II quantum well photodetector array. Before heterogeneous integration with III-V photodetectors, the passive AWG spectrometer has an insertion loss of 2.5 dB and the crosstalk level of −30 dB. Figure 9(b) shows the photo-response of the 2.3 μm III-V-on-silicon spectrometer. An insertion loss of 3 dB and crosstalk level of -27 dB is obtained by normalizing the responsivity to the reference photodetector. This result indicates that the bonding of III-V material on silicon and related post-processes do not degrade the performance of the AWG spectrometer.

III-V-on-silicon 2.3 μm-wavelength-range lasers

Using the same epitaxial layer stack as the heterogeneously integrated InP-based type-II photodetectors, 2 μm wavelength range III-V-on-silicon Fabry-Perot lasers and distributed feedback (DFB) lasers are realized. Figure 10(a) shows the schematic of a III-V-on-silicon Fabry-Perot laser. The device consists of a gain section, a III-V/silicon spot size converter (SSC) on both sides and two silicon distributed Bragg reflectors (DBRs) to form the laser cavity. An efficient light coupling from the III-V waveguide to the silicon waveguide is realized using the III-V/silicon SSCs. In continuous-wave (CW) operation, a threshold current density of 2.7 kA/cm^2 and output power of 1.3 mW at 5 ℃ is achieved for the Fabry-Perot laser. The laser emits over 3.7 mW of peak power with a threshold current density of 1.6 kA/cm^2 in pulsed regime at room temperature. A high-resolution emission spectrum of the Fabry-Perot laser is shown in Figure 10(b).

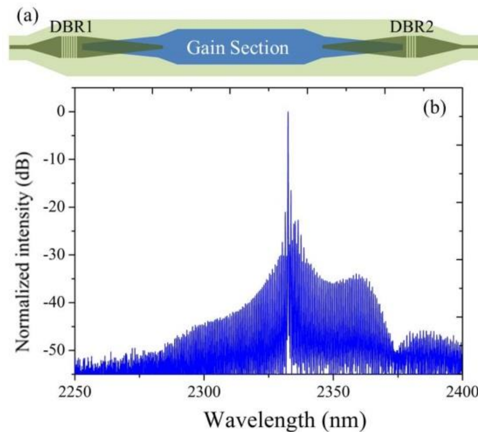

Figure 10. *(a) Schematic of a III-V-on-silicon Fabry-Perot laser; (b) fiber coupled emission spectrum of a heterogeneously integrated InP-based type-II Fabry-Perot laser.*

DFB lasers are well-suited light sources for the tunable diode laser absorption spectroscopy (TDLAS) measurement of gases. Figure 11(a) shows the schematic of an InP-based type-II DFB laser heterogeneously integrated on a silicon waveguide. A quarter-wave shifted first-order DFB grating with an etch depth of 180 nm in a 400 nm silicon device layer are implemented beneath the gain section. The evanescent tail of the optical mode interacts with this grating, which selects the lasing wavelength of the DFB laser. In CW regime, the heterogeneously integrated InP-based type-II DFB laser can operate up to 25 ℃ and emits more than 3 mW output power in a single mode with a threshold current density of 1.8 kA/cm^2 at 5 ℃. The lasing wavelength of the III-V-on-

silicon DFB lasers is determined by the silicon grating pitch. Figure 11(b) shows the emission spectra of six 1000 μm-long heterogeneously integrated DFB lasers in an array. As the silicon grating pitch increases from 343 nm to 368 nm, the lasing wavelength shifts from 2280 nm to 2430 nm. This broad wavelength span overlaps with absorption features of several important gases, such as NH_3, CO, CH_4, C_2H_2 and HF. Besides adjusting the grating pitch, another method to control the lasing wavelength is to adjust the gain section width of the DFB lasers. Figure 11(c) shows the CW lasing spectra of four 700 μm-long DFB lasers with different III-V waveguide widths as a function of bias current. More than 10 nm continuous current-tuning range is achieved this way. We carried out a gas sensing measurement using a III-V-on-silicon DFB laser source. It can be seen from Figure 11(d) that the measurement result fits very well to data from the HITRAN database.

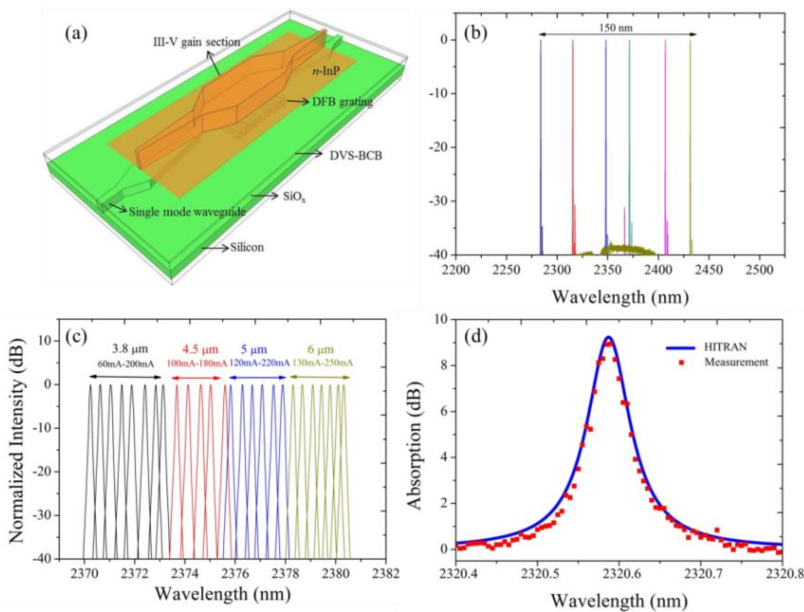

Figure 11. *(a) Schematic of a heterogeneously integrated InP-based type-II DFB laser on silicon; emission spectrum of a DFB laser array with varied silicon grating periods (b) and varied III-V waveguide widths (c); (d) direct TDLAS measurement of CO using a III-V-on-silicon DFB laser and the corresponding HITRAN spectrum.*

GaSb/silicon hybrid external cavity laser

We also realized a GaSb/silicon hybrid external cavity laser by butt coupling a GaSb-based gain chip and a silicon photonic IC. The silicon photonic IC contains a Vernier filter consisting of two thermally tuned micro-ring resonators (MRRs), a phase section to allow for quasi-continuous wavelength tuning and a DBR as shown in Figure 12(a) . Figure 12(b) shows the superimposed lasing spectra of the GaSb/silicon hybrid laser by tuning one MRR. A tuning range of 58 nm is achieved with a side mode suppression ratio (SMSR) better than 52 dB over the full tuning range and more than 60 dB at the optimal wavelength. When only one MRR is tuned, the tuning resolution is determined by the FSR of the other MRR. Fine quasi-continuous wavelength tuning can be achieved by simultaneously tuning both MRRs. Figure 12(c) shows the superimposed spectra with 0.7 nm resolution tuning over 25 nm range realized in this way. But even when tuning both MRRs, the tuning resolution is still limited by the free spectral range (FSR) of the longitudinal modes of the Fabry-Perot cavity. Continuous tuning can be achieved by thermally tuning the phase section as shown in Figure 12 (d). As the coupling gap of the MRRs increases from 200 nm to 500 nm, the maximum output power of the GaSb/silicon hybrid laser reduces from 7.5 mW to 3.8 mW. But the SMSR and tuning smoothness are lowered as the coupling gap is reduced.

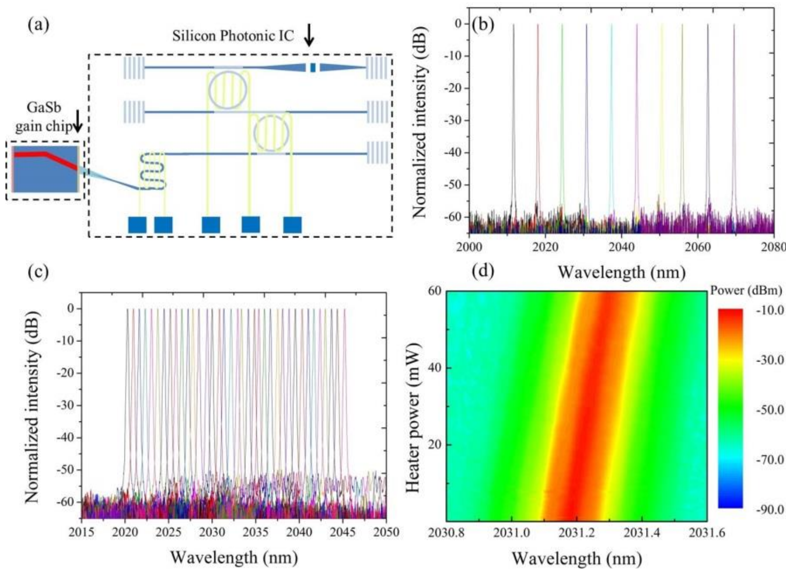

Figure 12. *(a) Schematic of a GaSb/silicon hybrid external cavity laser; superimposed spectra of the laser by thermally tuning one MRR (b), two MRRs (c) and phase shifter (d) when the coupling gap of MRRs is 500 nm.*

Conclusion

In this thesis, we report fully integrated 2 μm-wavelength-range III-V-on-silicon photonic circuits consisting of silicon waveguides, laser sources, photodetectors and AWG spectrometers. The active opto-electronic photonic devices are realized by heterogeneously integrating a InP-based type-II epitaxial layer stack on silicon waveguides. In addition, a widely tunable GaSb/silicon hybrid external cavity laser by combing a GaSb-based gain chip and a silicon photonics IC is reported.

1

Introduction

1.1 Silicon photonic integrated circuits

Silicon has become the key material in practically all modern electronics since 1954, when the first commercial silicon transistor was produced by Texas Instruments [1]. The integration of large numbers of silicon transistors into a small chip led to electronic circuits that are orders of magnitude smaller, cheaper, and faster than those constructed of discrete components. With the explosive growth of the electronic integrated circuits (ICs) industry in the last decades, the feature size of transistors has decreased from tens of μm in the early 1970s to 5 nm in 2017 [2]. Now a silicon IC has up to 25 million transistors per mm^2. Following such great successes in electronics, the photonics society is trying to integrate optical functionalities as much as possible into a chip and produce smaller, cheaper and faster photonic integrated circuits. One of the most promising integrated photonics platforms is based on silicon, which takes advantage of the well-established silicon electronics processes, and is referred to as "silicon photonics".

The story of silicon photonics started with R. Soref *el al.* and their pioneering study of silicon waveguides and its electro-optic effect in the late 1980s [3,4]. A few years later, silicon microelectronics manufacturing technologies were used to fabricate a set of silicon waveguide structures [5,6]. At that time, however, the losses of single mode silicon waveguides were too high for practical applications. High-volume manufacturing of low-loss silicon waveguide circuits was enabled by processing the circuits in silicon electronics foundries. In 2004, single mode silicon-on-insulator (SOI) waveguides with propagation losses as low as 2.4 ±1.6 dB/cm were demonstrated by P. Dumon *et al.* from Ghent University-IMEC [7]. In the same year, Y. A. Vlasov *et al.* from IBM also reported low propagation losses of 3.6 ± 0.1 dB/cm for SOI waveguides fabricated in a standard 200mm complementary metal-oxide-semiconductor (CMOS) pilot line [8]. Besides compatibility with silicon electronic processes, another large asset of the silicon photonics platform is the high refractive index contrast ($\Delta n \approx 2$) available in an SOI waveguide structure, leading to sub-micrometer waveguide dimensions and ultra-tight waveguide bend radii. A scanning electron microscope (SEM) image of a fabricated SOI waveguide bend is shown Figure 1.1(a). Figure 1.1(b) shows the intensity distribution of fundamental TE-mode at a wavelength of 1550 nm in the waveguide. It can be found that most of the light is confined in the waveguide core. Based on these ultra-compact waveguide structures, plenty of basic passive photonic components with small footprint can be fabricated, such as beam splitters/combiners, arrayed-waveguide grating (AWG) spectrometers and micro-ring resonators.

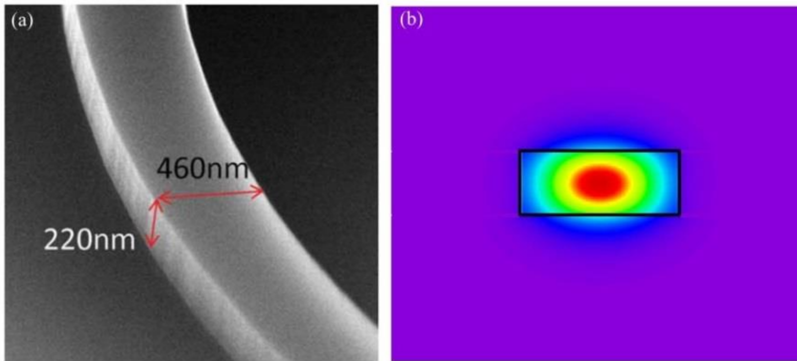

Figure 1.1. *(a) Bird-view SEM image of a silicon waveguide bend [18]; (b) TE-polarized fundamental mode intensity distribution in the silicon waveguide.*

In 2005, the demonstration of high-speed modulators indicated that silicon was capable of 10 Gb/s and higher modulation speeds [9,10]. Concurrently, a lot of efforts resulted in high-performance germanium photodetectors on silicon waveguides that can be realized in a CMOS pilot line [11, 12]. As silicon is an indirect-band-gap material, the realization of compact light sources on silicon is one of the most challenging works in the whole journey to a fully integrated silicon photonic IC [13]. In 2006, A. W. Fang *et al.* report an electrically pumped III-V evanescent Fabry-Perot laser heterogeneously integrated on a silicon waveguide [14]. Since then, the heterogeneous integration of III-V light sources on silicon photonic ICs is believed to be one of the most promising solutions to realize silicon photonic integrated light sources.

After more than one decade of rapid development, silicon photonic ICs integrated with silicon electronics are lighting up high-speed optical interconnects in datacenters and I/O in high-performance processors. In 2016, Intel announced volume production and shipping of 100 Gb/s silicon photonic transceivers [15]. Recently, P. De Heyn *et al.* from IMEC reported a 896 Gb/s silicon photonics transceiver combining 16×56 Gb/s germanium-silicon (GeSi) electroabsorption modulators and GeSi waveguide photodetectors with a multicore fiber interface [16]. In addition, C. Sun *et al.* report an electronic-photonic processor chip integrating over 70 million transistors and 850 photonic components that work together to provide logic, memory, and interconnect functions [17].

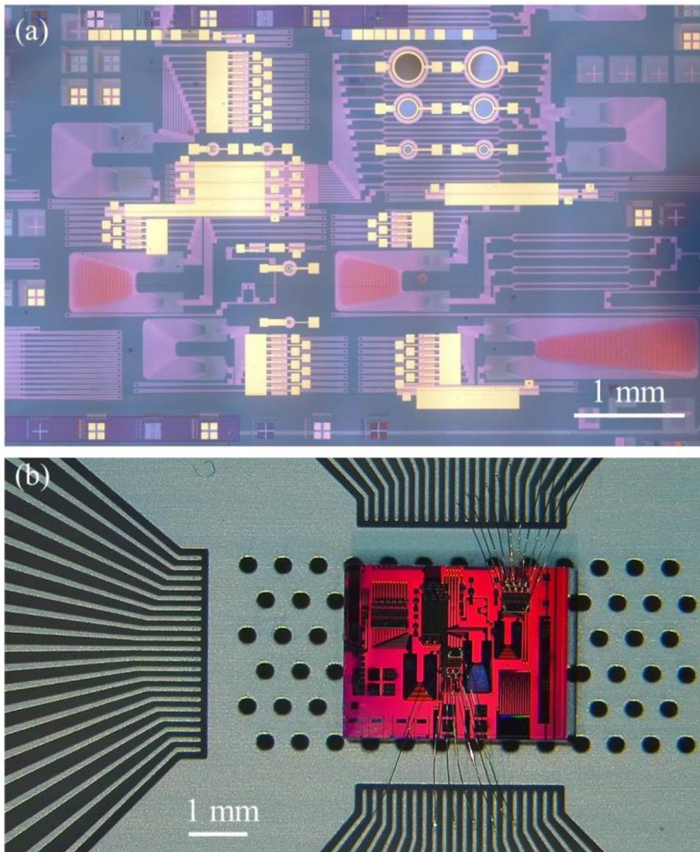

Figure 1.2. *(a) Microscope image of a silicon photonic integrated circuit. This silicon chip contains plenty of 2 μm-wavelength-range passive photonic components such as silicon waveguides, filters, spectrometers and active opto-electronic components such photodiodes, light emitting diodes and semiconductor optical amplifiers; (b) microscope image of a silicon photonic chip wire bonded to a printed circuit board.*

In recent years, silicon photonics also has attracted great interest in the field of spectroscopic sensing since the well-established fabrication technologies and compact SOI waveguide platform provide a promising solution to realize low-cost and miniature optical sensors [19-23]. In most of the demonstrated silicon photonic sensors, the photonic components used at telecommunication wavelengths are typically retained due to the lack of components at other wavelengths, which limits the performance of these optical sensors. In this thesis, I will focus on studying 2-2.5 μm fully integrated silicon photonic ICs for spectroscopic sensing applications. To give the first impression of our work, Figure 1.2(a) shows a microscopy image of a silicon photonic IC operating in

the 2 μm wavelength range, which consists of various passive and active photonic components. In order to interact with electronic circuits, the tiny silicon photonic chip is wire bonded to a printed circuit board (PCB) as shown in Figure 1.2 (b), and then connected with electronic components.

1.2 On-chip infrared spectroscopic sensing

Infrared spectroscopy is the study of the interaction between matter and infrared waves. It covers a lot of technologies, mostly based on absorption spectroscopy. This technology provides highly discriminatory information of molecules as the excitation of vibrational and rotational transitions are specific to these species in the gas, liquid and solid phases [24]. The infrared range of the electromagnetic spectrum is usually divided into three regions: short-wavelength infrared (SWIR, 0.7-2 μm), mid-infrared (Mid-IR, 2-30 μm) and terahertz (THz, 30-1000 μm), as shown in Figure 1.3. In general, the molecular absorption signals are stronger and richer in the infrared range, especially in MIR and THz range, than in the ultraviolet (UV) and visible wavelength range [25]. However, most of infrared spectroscopic sensing applications remain confined to a laboratory environment. Considering the achievements in miniaturization of silicon electronic and photonic system for telecommunication applications, the application opportunities for on-chip infrared spectroscopic sensing systems are evident. For an on-chip spectroscopic sensor, three parts should be taken into account in the design: (i) infrared light sources and detectors, (ii) appropriate waveguide structures serving as optical probes, and (iii) the method of spectroscopic sensing. In this section, I will give a brief review on recent research progress on these three parts, for wavelengths ranging from the SWIR to the mid-IR.

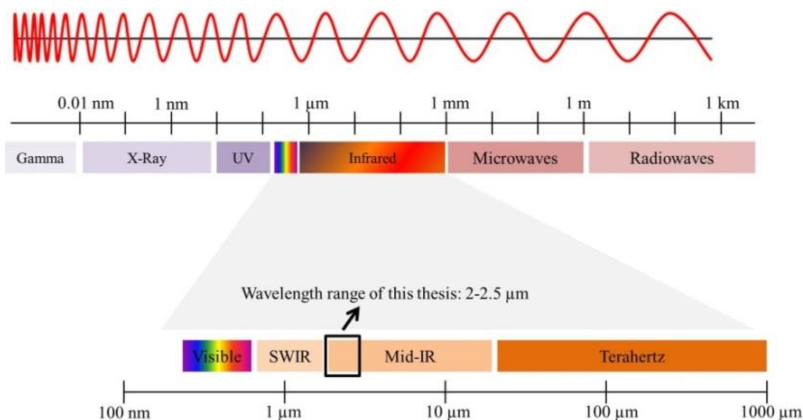

Figure 1.3. *The electromagnetic spectrum split up in different regions.*

1.2.1 Semiconductor laser sources and photodetectors

In the mid-infrared wavelength range, quantum cascade structures and interband cascade structures can be used as the active region for high-performance lasers above 3 μm wavelength [26,27], while InP-based type-I, type-II and GaSb-based type-I heterostructures can provide the gain for diode lasers in the 2-3 μm wavelength range [28]. A schematic picture of the active regions of type-I and type-II quantum well laser, quantum cascade laser (QCL) and interband cascade laser (ICL) are shown in Figure 1.4.

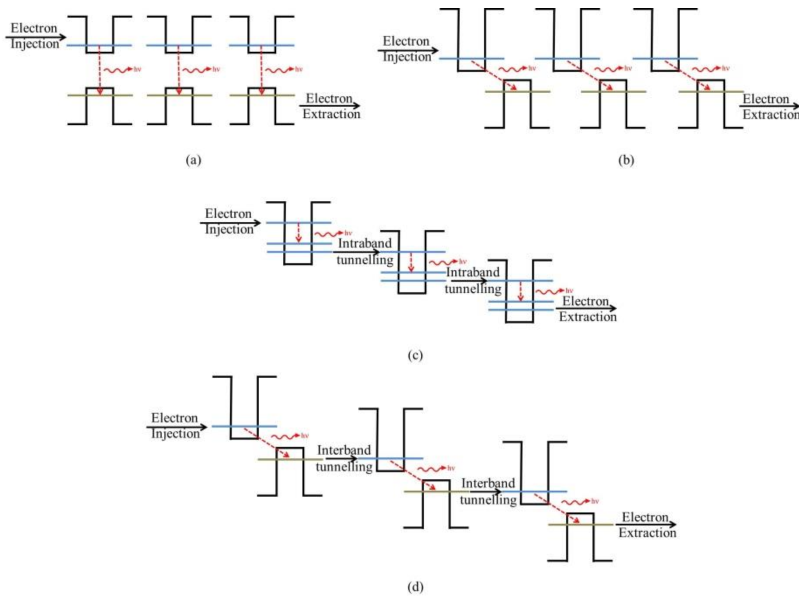

Figure 1.4. *Schematic of band profiles and active region processes in type-I (a) and type-II (b) quantum well diode lasers, QCLs (c) and ICLs (d).*

In type-I quantum well structures, electrons and holes are confined in the same material. Therefore, their wave functions can overlap substantially. The emission wavelength of type-I diode lasers is determined by the bandgap of the quantum well material. The longest wavelength that can be obtained from lattice-matched InP-based type-I quantum well diode lasers is limited to 1.75 μm. Applying highly strained InGaAs quantum well active regions, the laser wavelength can reach around 2.3 μm [29]. GaSb-based type-I quantum well lasers can cover wavelengths ranging from 1.9 to 3.7 μm and have already demonstrated excellent performance at room-temperature in the wavelength range from 1.9 to 3 μm [30,31].

The basic idea of type-II quantum well lasers is the separation of electrons and holes into two materials with a type-II band alignment. In this way, the

emission wavelength is not limited by the bandgap of the quantum well materials. Instead, it can be tuned by adjusting the band alignment. Using InGaAs/GaAsSb type-II quantum wells as the active region, S. Sprengel *et al.* demonstrated InP-based type-II lasers operating up to 2.7 μm [32]. An electrically pumped $\lambda = 4$ μm vertical-cavity surface-emitting lasers (VCSELs) using a GaSb-based active region with eight type-II quantum wells as the active region was recently reported [33].

In these two types of diode lasers, all quantum wells are pumped in parallel. Therefore, low bias voltages only slightly above the theoretical limit given by the photon energy are required for laser operation. However, the efficiency of type-I diode lasers is significantly reduced as the wavelength goes above 3 μm since non-radiative losses (i.e. Auger recombination) and free-carrier absorption become much stronger. Cascade pumping schemes can significantly increase the laser efficiency and are commonly used in lasers operating at a wavelength beyond 3 μm, which are named quantum cascade lasers (QCLs) and interband cascade lasers (ICLs) [26,27].

The QCL is a unipolar device that exploits optical transitions between electronic states in multiple quantum wells. It was invented by J. Faist, F. Capasso and co-workers in 1994 [34]. After more than two decades of tremendous development, QCLs emission can cover the mid-infrared and THz regions [35]. Recently, single mode QCLs based on a distributed feedback (DFB) configuration have demonstrated optical output power up to 2.4 W in continuous-wave (CW) operation at room temperature [36]. The physics of quantum cascade structures is beneficial for their operation as broadband gain medium [26]. The most common approaches to achieve broadly tunable single mode emission are assembling the QCLs in DFB arrays or realizing external cavity (EC) configurations. B. G. Lee *et al.* reported an array of 24 DFB lasers on a single chip covering about 220 cm^{-1} (8.0-9.8 μm) operating in pulsed mode [37]. Using a grating as a tuning element, EC QCLs have achieved 400 cm^{-1} (7.6-11.4 μm) broadband single-mode tuning [38].

ICLs are based on band-to-band transitions in heterostructures with a type-II band alignment. Its basic concept was first introduced by R. Yang in 1994 [39], the same year that the QCL was first demonstrated. Within 2-3 years, some critical improvements were added to the concept, including a hole injector and replacement of the single type-II interface with a “W”-shaped active region configuration [40,41]. The first experimental demonstration of an ICL ($\lambda = 3.8$ μm) was reported in 1997 [42]. In 2008, an ICL emitting at 3.75 μm became the first to operate CW at room temperature [43]. A carrier rebalancing concept was introduced in 2011, which drastically accelerated the research and application progress of ICLs [44]. Recently, GaSb-based ICLs that are operating in CW mode at room temperature have been realized covering a wavelength range from 2.8 to 5.6 μm [45,46]. Using InAs-based plasmon waveguides, the

lasing wavelength of ICLs can reach up to 10 μm [47]. Compared with QCLs, attractive advantages of ICLs are that their efficiency and low drive current potentially make them suitable for battery-operated applications [48].

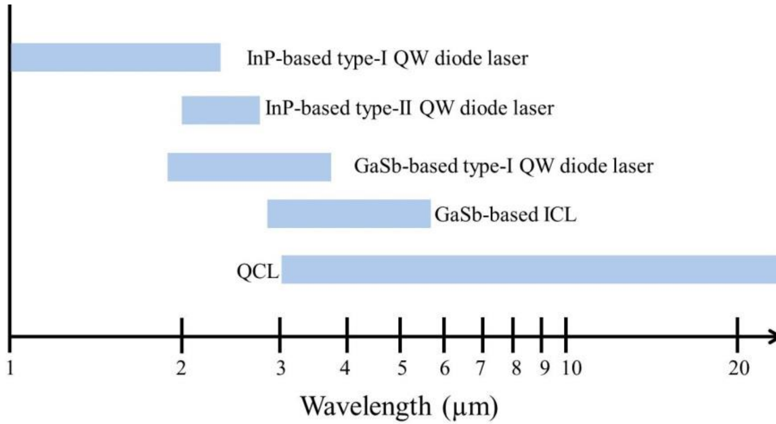

Figure 1.5. *Emission wavelength coverage of semiconductor lasers based on different III-V active regions.*

The emission wavelength coverage of InP-based type-I, type-II and GaSb-based type-I quantum well (QW) diode lasers, GaSb-based ICLs, and QCLs are shown in Figure 1.5.

Photodetectors perform the opposite function of light sources. They absorb the light and convert the optical signals to electrical current. The bandgap of the material that is used to make a photodetector is critical to defining its operating wavelength, because only photons with sufficient energy to excite electrons across the bandgap will produce significant absorption. Silicon and Germanium (Ge) are commonly used material for visible and near-infrared wavelengths. The cutoff wavelength of photodectors based on these two group-IV material are around 1.1 μm and 1.7 μm, respectively. In order to realize photodetectors in mid-infrared range, many material systems have been explored. For example, by adding Sn to the Ge matrix the cut-off wavelength can be extended to beyond 2 μm [49].

Specific detectivity (D^*) is a figure of merit used to characterize the performance of photodetectors. It is equal to the reciprocal of noise-equivalent power (NEP), normalized per square root of the detector's area and frequency bandwidth. Figure 1.6 shows the spectral specific detectivity curves for commercially available IR detectors based on a number of material systems [50]. Among these materials, HgCdTe is the only material that can detect infrared radiation from 2 μm to 10 μm. However, detectors based on HgCdTe suffer from instability of the material surface and interfaces and of inferior material

uniformity. Strained InGaAs, InGaAsSb and InP-based type-II heterostructures can be used to fabricate high-performance photodetector operating in the 2-3 μm wavelength range, which will be discussed in the third chapter in detail.

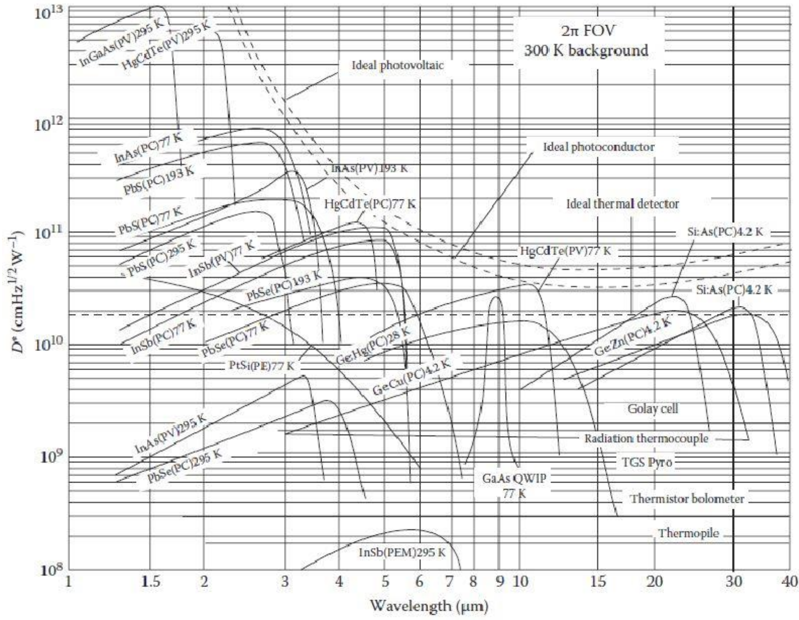

Figure 1.6. Comparison of the specific detectivity of various commercially available infrared detectors [50].

1.2.2 Waveguide circuits for the mid-infrared wavelength range

The attraction of using mid-infrared photonic ICs is that it provides a compact platform to integrate a variety of passive and active opto-electronic devices at chip level. There are many applications for mid-infrared photonic ICs. For example, lab-on-a-chip sensors based on mid-infrared photonic ICs can be used for trace-gas detection, bio-sensing, and environmental monitoring. In addition, the mid-infrared photonics platform can be employed to fabricate compact photonic components to miniaturize optical systems, e.g., feedback circuits for mid-infrared external cavity lasers and power combiners for DFB laser arrays.

A low-loss waveguide is the basic building block for a photonic IC. Waveguide platforms based on different material systems have been developed for operation in the mid-infrared [51]. Figure 1.7 shows the transparency windows of materials used to develop low-loss mid-infrared waveguides [52]. SOI is the most prevalent one for photonic ICs operating in the telecommunication wavelength range since its CMOS compatible processes enable low-cost fabrication. In recent years, this platform has been explored for

longer wavelengths as well. Propagation losses of ~0.5 dB/cm were achieved for SOI waveguides operating in the 2-2.5 μm wavelength range [53]. As the wavelength increases to 3.8 μm, a low propagation loss of ~1.5 dB/cm for 400 nm SOI rib waveguides with 220 nm etch depth was reported by M. Nedeljkovic *et al* [54]. The accessible spectral window of monocrystalline silicon goes up to 8 μm, while the transparency of silicon dioxide rapidly reduces when λ>4 μm as shown in Figure 1.7. Therefore, SOI is a suitable material platform for 2-4 μm wavelength range waveguide circuits. New waveguide platforms need to be developed for operating beyond 4 μm wavelength.

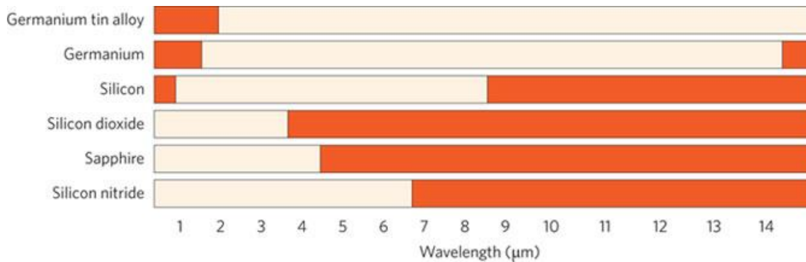

Figure 1.7. *Material systems for low-loss waveguides in the SWIR and MIR wavelength range. The white areas represent windows with a good optical transparency while the red areas indicate high loss [52].*

An alternative silicon-based waveguide platform for the mid-infrared wavelength range is the use of silicon-on-sapphire. Sapphire starts absorbing beyond 5 μm, which limits the operation wavelength of this waveguide platform. Another suitable approach is a silicon-on-nitride (SON) waveguide, as SiN has a wide optical transparency window from the visible up to 6.7 μm. This SON waveguide platform has been used for the integration of QCLs on silicon substrates by A. Spott *et al.* [55]. Besides these silicon-based materials, Germanium-based waveguide platforms (e.g. germanium-on-silicon and germanium-on-SOI) are proposed for longer wavelengths. For example, A. Malik *et al*. demonstrated a germanium-on-silicon waveguide with a propagation loss of 3 dB/cm in the 5-5.5 μm wavelength range [56]. Based on this waveguide platform, a 5×200 GHz AWG was realized with an insertion loss of 2.5 dB and crosstalk of -20 dB. The choice of material platform for mid-infrared photonic ICs is determined by the application wavelength range and fabrication capacity. Considering the CMOS compatible processes, high index contrast and transparency window, the SOI waveguide platform is a well-suited platform for 2-4 μm wavelength range photonic ICs.

1.2.3 Evanescent sensing

Compared with traditional optical sensors, waveguide-based sensors offer lower costs, higher reliability, and smaller size, weight and power. To probe the analyte through the waveguide, the optical field leaking into the environment, i.e., the evanescent field, can be utilized. The intensity of the evanescent field decays exponentially away from the waveguide, leaving it concentrated in a region (depth = d_e) very close to the interface. If analyte molecules are present within d_e, they will interact with the evanescent field, which results in light absorption when the propagating light is in resonance with corresponding molecular vibrations and/or rotations. A schematic of the waveguide-based evanescent sensing is shown in Figure 1.8 [57]. The absorption process follows a modified Beer−Lambert relationship:

$$T = e^{-\alpha_v \Gamma L} e^{-\alpha_{wg} L} \tag{1.1}$$

where T is the light transmission, L is the waveguide length, Γ is the confinement factor of the optical field in the environment, α_v and α_{wg} is the loss coefficient in the environment and waveguide. Increasing the intensity of the evanescent field and waveguide length can enhance the sensitivity of the waveguide-based sensor. Consequently, slot waveguides [58], spiral waveguides [59], and microring resonators [60] have been employed as the probe components for on-chip sensors.

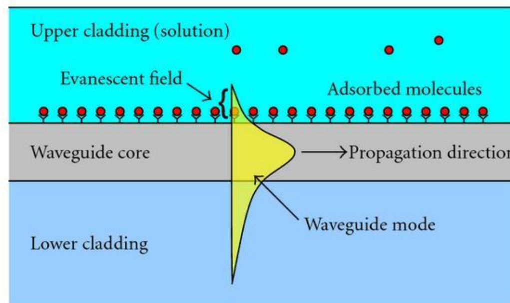

Figure 1.8. *Illustration of a waveguide-based evanescent sensor [57].*

In recent years, a lot of silicon photonic sensors have been developed for industrial, medical and environmental applications. For example, a silicon photonic on-chip sensor for evanescent field absorption spectroscopy of methane near 1.65 μm was recently demonstrated [59], which is expected to enable a next generation of economical wide area sensor networks for continuous fugitive emissions monitoring. A sensitivity of 756 ppmv·Hz$^{-1/2}$ is obtained by using a 10 cm long silicon spiral waveguide as the probe component.

Similar to other previously demonstrated waveguide-based sensors, in this methane sensor, the light from an external laser source is coupled to the photonic IC and then detected by an external detector, as schematically shown in Figure 1.9. Extending the operation wavelength of the silicon photonic on-chip sensor to around 2.35 μm or 3.25 μm would enable a more compact on-chip sensor with higher sensitivity since the absorption coefficient of CH_4 at these longer wavelengths is much higher than that at 1.65 μm [25].

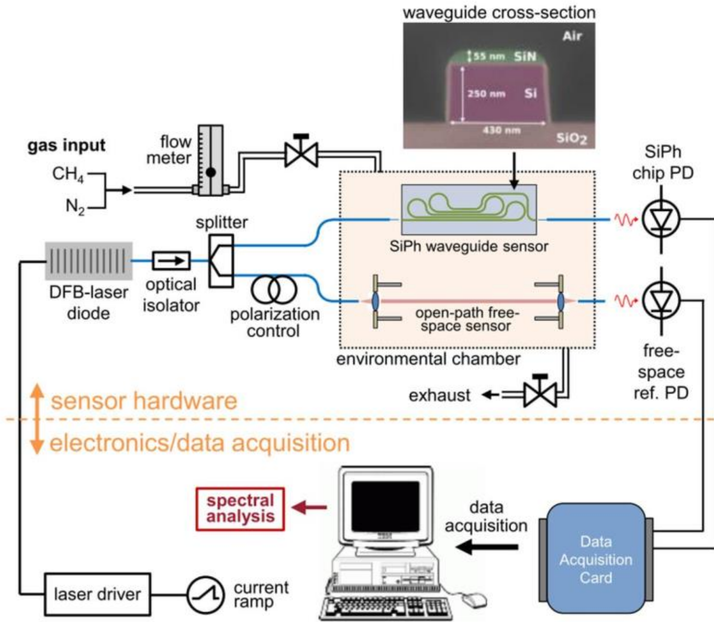

Figure 1.9. *Schematic picture of a waveguide-based evanescent gas sensing system [59], non-integrated light sources and detectors are used in the sensing system.*

1.3 III-V/silicon photonic integrated circuits for spectroscopic sensing

In most applications, a spectroscopic sensing system should have a light source, a probe component and a spectrometer or single pixel detector. In previously demonstrated on-chip optical sensors, light from an external light source is coupled to the probe component (waveguide circuit), which interacts with the environment, and afterwards is read by an external detector. For a genuinely compact on-chip sensor, both the light source and detector should be integrated together with the waveguide circuit. Silicon is an indirect bandgap

semiconductor with extreme low light emission efficiency, transparent beyond 1.1 μm wavelength. Transferring III-V material on Si enables integrated lasers and photodetectors on silicon photonic ICs, which will be introduced in detail in the second chapter.

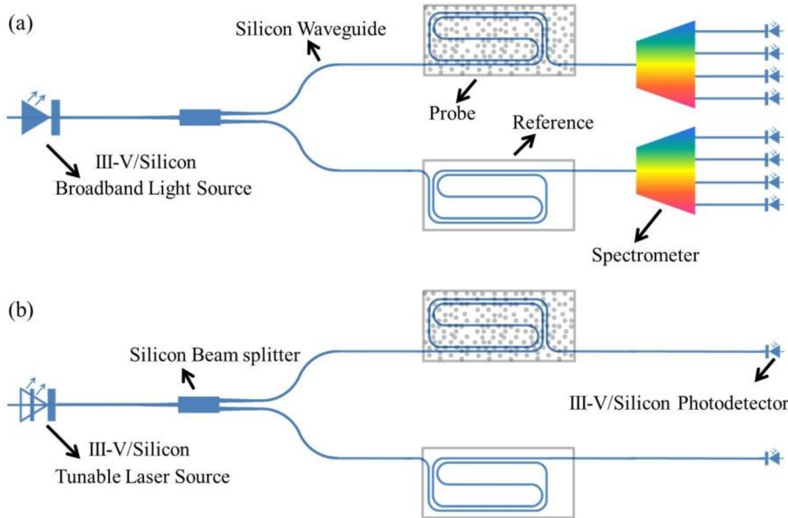

Figure 1.10. *Schematic of two silicon photonic configurations to realize an integrated on-chip absorption spectroscopy sensor. Broadband source and spectrometer, best suited for liquid and solid analytes (a). Tunable single mode laser source for trace gas detection (b).*

Figure 1.10 shows two typical configurations for fully integrated mid-infrared on-chip spectroscopic sensors. In both configurations, light is coupled from the integrated light source to the waveguide and then split to two arms. The probe component in one arm interacts with environment while the other one provides the reference information. In the case of liquid sensing, a low-cost broadband light source such as a light emitting diode (LED) can be used since liquid samples typically have broad absorption features. In this configuration, a spectrometer with integrated photodetectors should be implemented to analyze the absorption spectra. For gas sensing, typically a tunable single mode laser is required to probe the absorption lines of gases, as used in the popular tunable diode laser absorption spectroscopy (TDLAS) technique. Integrating a widely tunable laser or a broadband wavelength coverage laser array on the waveguide circuit enables to simultaneously detect several gases or even broad absorption features of liquids using the configuration shown in Figure 1.10(b).

For the III-V/silicon photonic ICs, low-loss passive waveguides, beam splitters and filters (spectrometers) can be fabricated in silicon foundries , which is an asset of silicon photonic sensors.

1.4 Applications of 2 μm range III-V/silicon photonic components and integrated circuits

As a wavelength region overlapping with the telecommunication wavelength window and molecular fingerprinting region, the 2 μm wavelength range offers various potential applications from optical communication to spectroscopic sensing.

1.4.1 Optical communication

Single mode glass fibers are commonly used in datacenter, metro and long-haul links as they have extremely low loss in 1310 nm and 1550 nm wavelength windows. With the help of erbium doped fiber amplifiers (EDFA), long-haul telecommunication is realized in the 1.55 μm wavelength range. In recent years, researchers are however looking for new optical transmission systems to meet the increasing demand for high volume data transmission over optical networks. One of the proposed supplement solutions is to use a hollow core photonic bandgap fiber (HC-PBGF) as the high-rate data transmission medium in the 2 μm wavelength region. As the light propagates through the air core, such fibers offer low latency and low non-linearity. A scanning electron microscopy (SEM) image of the cross-section of a HC-PBGF is shown in Figure 1.11(a). Theory indicates that the transmission loss of HC-PBGFs can be as low as low as 0.1 dB/km [61]. A low transmission loss of 4.5 dB/km at 1980 nm wavelength and a wide surface-mode-free transmission window (>150 nm) are obtained in one recent study [62]. Meanwhile, the thulium (Tm^{3+}) doped fiber amplifier (TDFA) offers a high gain (>35 dB) and a broadband (>100nm) amplification around 2 μm wavelength [63]. Therefore, optical communication in the 2 μm range has attracted strong interest in recent years.

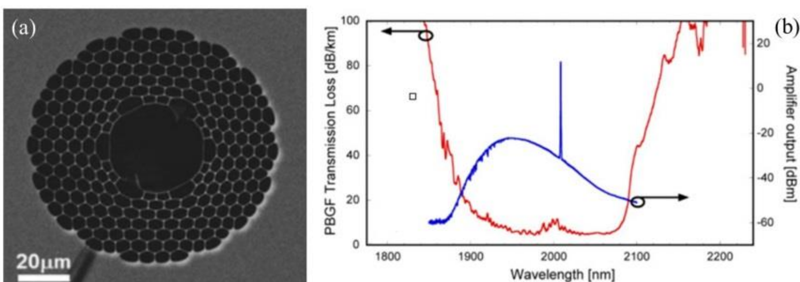

Figure 1.11. *(a) SEM image of the hollow core photonic bandgap fiber (HC-PBGF); (b) Transmission loss of the HC-PBGF and the output from the thulium doped fiber amplifiers (the location of the signal channel is at 2008 nm) [62].*

Shifting the optical communication window to the 2 μm wavelength range requires the development of a set of photonic components operating in such wavelength region, including single mode lasers, photodetectors, modulators, arrayed waveguide grating (AWG), etc. Different integrated-optics platforms have been used to develop the photonic devices and systems in the 2 μm wavelength region. Here are three recent examples:

(1) A monolithic silicon detector operating near 2 μm was demonstrated, which exhibits a responsivity of 0.3 A/W at 2.02 μm and enables high-speed operation [64].

(2) An InP-based Mach–Zehnder modulator operating around 2 μm was reported. An electro-optic bandwidth of at least 9 GHz and back-to-back communication with a 10 Gb/s pseudo-random bit sequence (PRBS) of length 2^7 -1 was achieved [65].

(3) A monolithically integrated InP-based extended cavity ring laser with 31 nm wide wavelength tuning range centered at 2027 nm was reported in [66].

1.4.2 Gas sensing

The 2 μm spectral range is also of interest for biomedical, environmental and process control applications since many important gases have strong absorption lines in this wavelength range. Figure 1.12 shows the absorption spectra of CO, CO_2 and H_2O in the 1-6 μm wavelength range [25]. For CO, the fundamental band near 4.6 μm offers the strongest absorption signal. Therefore, 4.6 μm range QCLs or ICLs can be used as the light source to detect CO at very low concentration [67]. However, QCLs are quite expensive and power hungry. In addition, a bulky cooling system is required for photodetectors operating at this wavelength. These two issues result in the fact that the 4.6 μm range CO detection system cannot easily be made portable. The second overtone band of CO near 1.55 μm has been used for TDLAS measurement in many situations, by using inexpensive telecommunication diode lasers and photodiodes [68]. But weak absorption cross-section in this band requires use of large path lengths. Besides, the interference between CO and H_2O also limits the detection sensitivity. The first overtone band around 2.3 μm offers the first water absorption free spectral window for CO detection as shown in Figure 1.12(a). Relative cheap laser sources, room-temperature operated photodetectors and strong absorption cross-section make it possible to realize portable CO sensors operating near 2.3 μm wavelength.

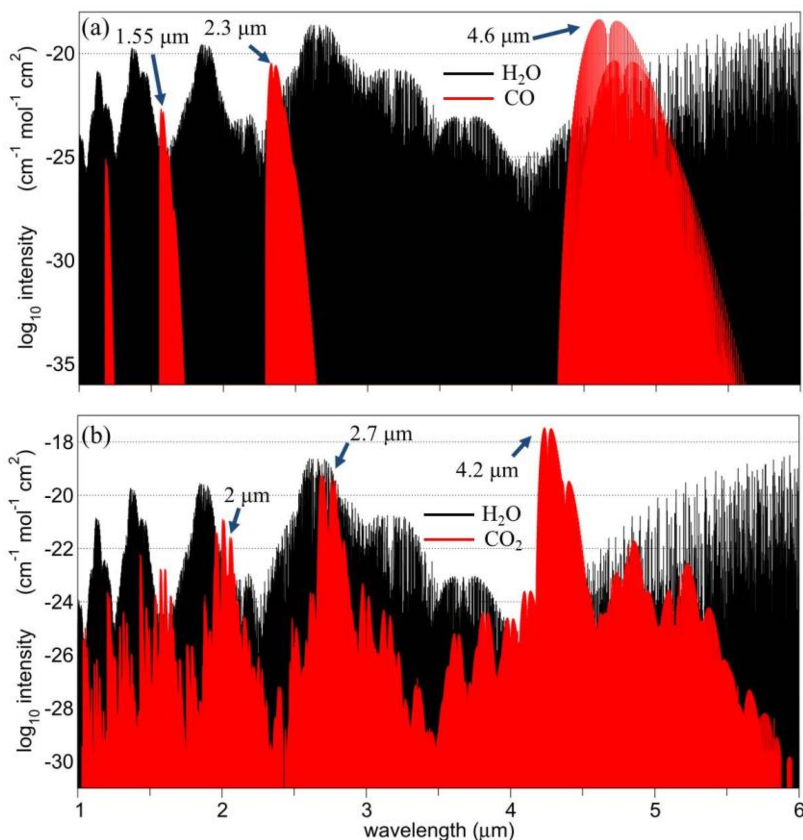

Figure 1.12. *Absorption spectra for CO, CO_2 overlaid with water in the 1-6 µm wavelength range, taken from the HITRAN database.*

TDLAS measurements of CO_2 at different wavelengths has the same features as the measurement of CO. 2.05 µm has been considered as the optimal wavelength for both strong CO_2 absorption and minimal sensitivity to variations in temperature and water vapor concentration [69]. Diode lasers operating at such wavelength have been used to seed lasers in space-borne lidar systems for continuous global-scale measurement of CO_2 and other greenhouse gases [70].

Besides CO_2 and CO, some other important industrial gases (e.g., CH_4, NH_3 and HF) also have strong and dense absorption lines in the 2 µm wavelength region as shown in Figure 1.13. High resolution measurements of these gases in the 2 µm range have been demonstrated based on different optical detection techniques [71]. For example, CO gas with a concentration < 11 pm was detected by employing wavelength modulation TDLAS technique with a 2.36 µm VCSEL and a 40 cm long pathlength [72].

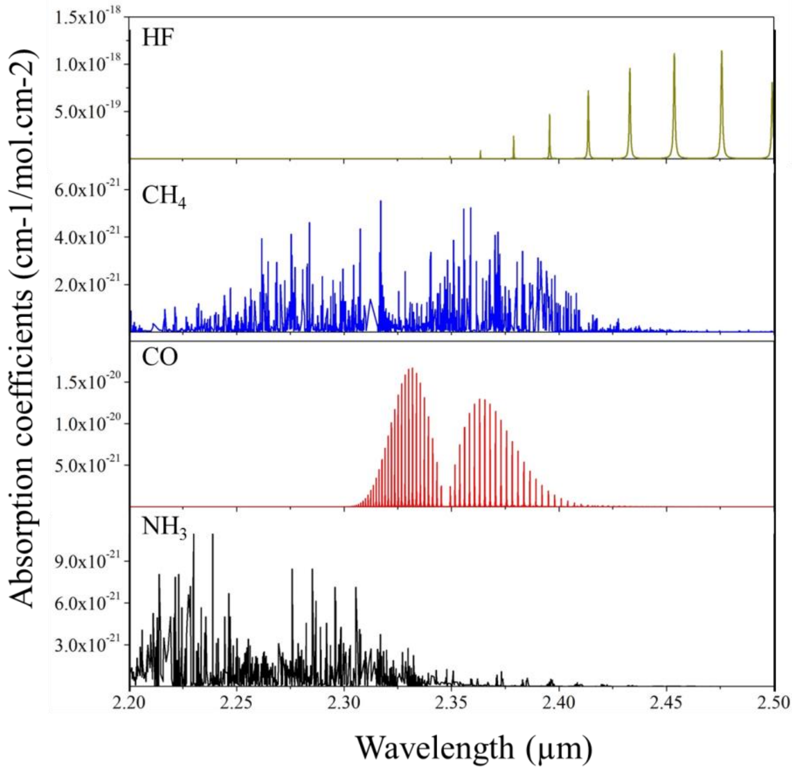

Figure 1.13. *Absorption spectra of HF, CH_4, CO and NH_3 in the 2.2-2.5 μm wavelength range.*

1.4.3 On-chip bio-sensing

Another major application field of the 2 μm-wavelength-range III-V/silicon photonic sensors is the analysis of bio-fluids. Similar to other waveguide-based bio-sensors [51], silicon photonic bio-sensors also use waveguides for propagating photons from a light source to a measurement location, and after interaction with the analyte to an optical detector. The advantages of such bio-sensors implemented in silicon are the ultra-compact structure, low-cost fabrication and low-loss waveguides. The silicon waveguide structures can use the evanescent field to detect the attenuation due to the presence of an analyte. A broadband light source such as a LED or a widely tunable laser is required in such spectroscopic bio-sensors since liquid samples have broad absorption features. Compared with gas sensing, liquid sensing can also be more effected by the strong interference from water.

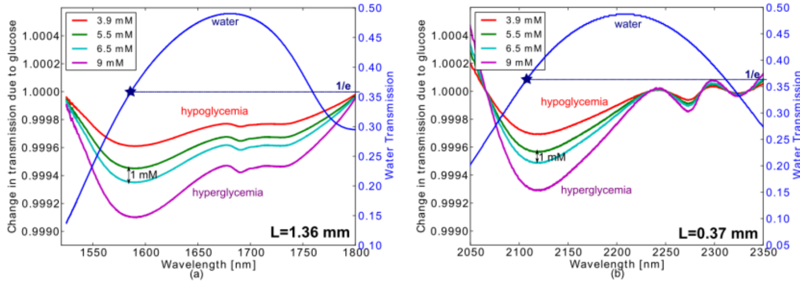

Figure 1.14. *Theoretical change in transmission because the absorption of glucose solution in the first overtone band (a) and the combination band for different glucose concentrations (b) [73].*

Recently, our group reported an on-chip silicon photonic sensor for evanescent sensing of glucose in the telecommunication wavelength range [73]. A small error-of-fitting of 1.14 mM concentration is achieved in the sensor. Extending the operation wavelength of the glucose sensors to the 2 µm wavelength range enables a more reliable detection. Figure 1.14 shows the comparison of the absorption of glucose solution in the first overtone and the combination band. We can see that glucose absorbs 4 to 5 times stronger in the 2 µm range than the telecommunication wavelength range. However, also the water absorption is stronger in this wavelength range.

1.5 Outline of this thesis

In this thesis, we focus on III-V/silicon photonic integrated circuits for spectroscopic sensing in the 2 µm wavelength range. In the introductory chapter, the recent research progress on silicon photonic integrated circuits and infrared spectroscopic sensing is briefly reviewed. Then we introduce fully integrated photonic circuits for spectroscopic sensing applications. The second chapter focuses on the development of a heterogeneous III-V-on-silicon platform for the 2 µm wavelength range. InP-based type-II heterostructures are chosen as the active material to realize heterogeneously integrated laser sources and photodetectors on silicon waveguide circuits. Our efforts on the processes development are summarized in this chapter. The third chapter firstly presents InP-based type-II quantum well photodetectors heterogeneously integrated on silicon waveguides. Then our work on high-performance SOI AWG spectrometers operating in the 2 µm wavelength range is discussed. Afterwards, the integration of photodetectors on the AWGs is also introduced in the third chapter. In the fourth chapter, the heterogeneously integrated 2.3 µm range InP-based type-II Fabry-Perot laser, DFB lasers and laser arrays are presented,

together with the TDLAS measurements of CO gas using the DFB laser. The fifth chapter introduces a compact 2 μm-wavelength-range widely tunable external cavity laser using a silicon photonic IC for the wavelength selective feedback. Finally, we conclude the thesis in the sixth chapter.

1.6 Publications

Publications in international journals

[1] **R. Wang**, A. Vasiliev, M. Muneeb, A. Malik, S. Sprengel, G. Boehm, M.-C. Amann, I. Šimonytė, A. Vizbaras, K. Vizbaras, R. Baets and G. Roelkens, "III-V-on-Silicon Photonic Integrated Circuits for Spectroscopic Sensing in the 2-4 μm Wavelength Range," Sensors **17**(8), 1788 (2017).

[2] **R. Wang**, S. Sprengel, G. Boehm, R. Baets, M.-C. Amann and G. Roelkens, "Broad wavelength coverage 2.3 μm III-V-on-silicon DFB laser array," Optica **4**(8), 972-975 (2017).

[3] Z. Wang, A. Abbasi, U.D. Dave, A. De Groote, S. Kumari, B. Kunert, C. Merckling , M. Pantouvaki, Y. Shi, B. Tian, K. Van Gasse, J. Verbist, **R. Wang**, W. Xie, J. Zhang, Y. Zhu, J. Bauwelinck, X. Yin, Z. Hens, J. Van Campenhout, B. Kuyken, R. Baets, G. Morthier, D. Van Thourhout, G. Roelkens, "Novel light source integration approaches for silicon photonics," Laser Photon. Rev. **11**(4), 1700063.

[4] **R. Wang**, A. Malik, I. Šimonytė, A. Vizbaras, K. Vizbaras, G. Roelkens, "Compact GaSb/silicon-on-insulator 2.0x μm widely tunable external cavity lasers, " Opt. Express, **24**(25), 28977-28986 (2016).

[5] **R. Wang**, S. Sprengel, A. Malik, A. Vasiliev, G. Boehm, R. Baets, M.-C. Amann, G. Roelkens, "Heterogeneously integrated III–V-on-silicon 2.3x μm distributed feedback lasers based on a type-II active region," Appl. Phys. Lett., **109**, 221111 (2016).

[6] **R.Wang**, S. Sprengel, G. Boehm, M.Muneeb, R. Baets, M. C. Amann, and G. Roelkens, "2.3 μm range InP-based type-II quantum well Fabry-Perot lasers heterogeneously integrated on a silicon photonic integrated circuit," Opt. Express **24**, 21081- 21089 (2016).

[7] **R. Wang**, M. Muneeb, S. Sprengel, G. Boehm, A. Malik, R. Baets, M.-C. Amann, and G. Roelkens, "III-V-on-silicon 2-μm-wavelength-range wavelength demultiplexers with heterogeneously integrated InP-based type-II photodetectors," Opt. Express **24**(8), 8480–8490 (2016).

[8] **R. Wang**, S. Sprengel, M. Muneeb, G. Boehm, R. Baets, M. C. Amann, and G. Roelkens, "2 μm wavelength range InP-based type-II quantum well

photodiodes heterogeneously integrated on silicon photonic integrated circuits," Opt. Express **23**(20), 26834–26841 (2015).

[9] G. Roelkens, A. Abassi, P. Cardile, U. Dave, A. de Groote, Y. de Koninck, S. Dhoore, X. Fu, A. Gassenq, N. Hattasan, Q. Huang, S. Kumari, S. Keyvaninia, B. Kuyken, L. Li, P. Mechet, M. Muneeb, D. Sanchez, H. Shao, T. Spuesens, A. Subramanian, S. Uvin, M. Tassaert, K. van Gasse, J. Verbist, **R. Wang**, Z. Wang, J. Zhang, J. van Campenhout, J. Bauwelinck, G. Morthier, R. Baets, D. van Thourhout, and X. Yin, "III-V-on-Silicon photonic devices for optical communication and sensing," Photonics **2**(3), 969–1004 (2015).

[10] G. Roelkens, U. Dave, A. Gassenq, N. Hattasan, B. Chen Hu, F. Kuyken, A. Leo, M. Malik, E. Muneeb, D. Ryckeboer, S. Sanchez, R. Uvin, **R. Wang**, Z. Hens, Y. Baets, F. Shimura, B. Gencarelli, R. Vincent, J. Loo, L. Van Campenhout, J.-B. Cerutti, E. Rodriguez, Tournie, M. Xia Chen, G. Nedeljkovic, Mashanovich, N. Li Shen, A. C. Healy, Peacock, R. Xiaoping Liu, Osgood, and W. M. J. Green, "Silicon-based photonic integration beyond the telecommunication wavelength range," IEEE J. Sel. Top. Quantum Electron. 20(4), 394–404 (2014).

Publications in international conferences

[1] **R. Wang,** M. Muneeb, A. Vasiliev, A. Malik, S. Sprengel, G. Boehm, I. Šimonytė, A. Vizbaras, K. Vizbaras, R. Baets, M.-C. Amann, G. Roelkens, "III-V/silicon photonic integrated circuits for spectroscopic sensing in the 2 µm wavelength range," in SPIE Photonics West 2018 (Invited), to be published.

[2] **R. Wang**, S. Sprengel, G. Boehm, R. Baets, M.-C. Amann, G. Roelkens, "Widely tunable 2.3 µm InP-based type-II DFB laser array heterogeneously integrated on silicon for sensing," in 2017 International workshop on opportunities and challenges in mid-infrared laser-based gas sensing, paper MoO10 (2017).

[3] I. Šimonytė, **R. Wang**, K. Vizbaras, G. Roelkens, A. Vizbaras, "GaSb SLDs and gain-chips for sensing applications in the 2-2.5 micron wavelength range," 2017 International workshop on opportunities and challenges in mid-infrared laser-based gas sensing, paper WeO9 (2017).

[4] **R. Wang**, S. Sprengel, G. Boehm, R. Baets, M.-C. Amann, G. Roelkens, "Heterogeneously Integrated InP-based Type-II DFB Laser Array on Silicon," in 2017 European Conference on Integrated Optics (ECIO), Netherlands, paper T2.1 (2017).

[5] **R. Wang**, A. Malik, I. Šimonytė, A. Vizbaras, K. Vizbaras, G. Roelkens, “Widely tunable GaSb-silicon hybrid lasers at 2 µm,” in 43rd Freiburg Infrared Colloquium, paper 47-48 (2017).

[6] **R. Wang**, S. Sprengel, G. Boehm, R. Baets, M.-C. Amann, G. Roelkens, “DFB laser array in the 2.3 µm wavelength range on a silicon photonic integrated circuit,” in 9th THz days, paper M4 (2017).

[7] **R. Wang**, S. Sprengel, M. Muneeb, G. Boehm, A. Malik, R. Baets, M.-C. Amann, G. Roelkens, “Heterogeneous integration of InP-based type-II active devices on silicon for 2.0 µm wavelength range on-chip spectroscopy,” in The 13th International Conference on Mid-Infrared Optoelectronics, paper 35-36 (2016)

[8] **R. Wang**, M. Muneeb, Stephan Sprengel, Gerhard Boehm, R. Baets, Markus-Christian Amann, G. Roelkens, “SWIR InGaAs/GaAsSb type-II quantum well photodetectors and spectrometers integrated on SOI,” in SPIE Photonics West, Silicon Photonics XI (SPIE, 2016), paper 9752-09 (2016).

[9] **R. Wang**, S. Sprengel, M. Muneeb, G. Boehm, R. Baets, M.-C. Amann, G. Roelkens, “Design and fabrication of type-II InP-based lasers and photodetectors integrated on SOI waveguide,” in Proceedings of the 2015 annual symposium of the IEEE Photonics Benelux Chapter, paper (2015)

[10] S. Kumari, Johan Gustavsson, **R. Wang**, E. Haglund, P. Westbergh, D. Sanchez, Eric Haglund, A. Haglund, J. Bengtsson, N. Le Thomas, G. Roelkens, A. Larsson, R. Baets, “Integration of GaAs-based VCSEL array on SiN platform with HCG reflectors for WDM applications,” in SPIE Photonics West, High Contrast Metastructures IV (SPIE,2015), paper 9372-0U (2015).

[11] G. Roelkens, U.D. Dave, A. Gassenq, N. Hattasan, C. Hu, B. Kuyken, F. Leo, A. Malik, M. Muneeb, E.M.P. Ryckeboer, D. Sanchez, S. Uvin, **R. Wang**, Z. Hens, R. Baets, Y. Shimura, F. Gencarelli, B. Vincent, R. Loo, J. Van Campenhout, L. Cerutti, J.B. Rodriguez, E. Tournie, X. Chen, M. Nedeljkovic, G. Mashanovich, L. shen, N. Healy, A. Peacock, X. Liu, R. Osgood, W.M.J. Green, “long-wavelength silicon photonic integrated circuits,” in 11th International Conference on Group IV Photonics (GFP) (invited), paper 23-24 (2014).

[12] **R. Wang**, D. Sanchez, G. Roelkens, “Design of a MEMS tunable mid-infrared VCSEL integrated on the SOI platform,” in Proceedings of the 2013 Annual Symposium of the IEEE Photonics Society Belenux Chapter, paper 159-162 (2013).

[13] **R. Wang**, D. Sanchez, G. Roelkens, "Design of a high contrast grating GaSb-based VCSEL integrated on SOI," in IEEE Photonics Conference 2013 (IPC), paper Me3.3 (2013).

References

[1] I. M. Ross, “The invention of the transistor,” Proc. IEEE **86**(1), 7–27 (1998).

[2] P. Hashemi and T. B. Hook, “CMOS Device Technology Enablers and Challenges for 5nm Node,” in 2017 Symposium on VLSI Technology.

[3] R. A. Soref and J. P. Lorenzo, “All-silicon active and passive guided-wave components for λ=1.3 and 1.6 µm,” IEEE J. Quantum Electron. **22**, 873–879 (1986).

[4] R. A. Soref and B. R. Bennett, “Electrooptical effects in silicon,” IEEE J. Quantum Electron. **23**, 123–129 (1987).

[5] B. L. Weiss, G. T. Reed, S. K. Toh, R. A. Soref, and F. Namavar, “Optical waveguides in SIMOX structures,” IEEE Photonics Technol. Lett. **3**(1), 19–21 (1991).

[6] C. K. Tang, A. K. Kewell, G. T. Reed, A. G. Rickman, F. Namavar, “Development of a library of low-loss silicon-on-insulator optoelectronic devices,” IEE Proc. Optoelectron. **143** ,312-315 (1996).

[7] P. Dumon, W. Bogaerts, V. Wiaux, J. Wouters, S. Beckx, J. Van Campenhout, D. Taillaert, B. Luyssaert, P. Bienstman, D. Van Thourhout, and R. Baets, “Low-loss SOI photonic wires and ring resonators fabricated with deep UV lithography,” IEEE Photon. Technol. Lett. **16**, 1328–1330 (2004).

[8] Y. Vlasov and S. McNab, “Losses in single-mode silicon-on-insulator strip waveguides and bends,” Opt. Express **12**(8), 1622–1631 (2004).

[9] L. Liao, D. Samara-Rubio, M. Morse, A. Liu, D. Hodge, D. Rubin, U. Keil, and T. Franck, “High speed silicon Mach-Zehnder modulator,” Opt. Express **13**(8), 3129–3135 (2005).

[10] Q. Xu, B. Schmidt, S. Pradhan, and M. Lipson, “Micrometre-scale silicon electro-optic modulator,” Nature **435**, 325–327 (2005).

[11] J. Liu, J. Michel, W. Giziewicz, D. Pan, K. Wada, D. D. Cannon, S. Jongthammanurak, D. T. Danielson, L. C. Kimerling, J. Chen, F. O. Ilday, F. X. Kartner, and J. Yasaitis, “High-performance, tensile-strained Ge p-i-n photodetectors on a Si platform,” Appl. Phys. Lett. **87**(10), 103501 (2005).

[12] J. Michel, J. Liu, and L. C. Kimerling, “High-performance Ge-on-Si photodetectors,” Nature Photonics **4**, 527–534 (2010).

[13] D. A. B. Miller, “Device requirements for optical interconnects to silicon chips,” Proc. IEEE **97**, 1166–1185 (2009).

[14] A. W. Fang, H. Park, O. Cohen, R. Jones, M. J. Paniccia, and J. E. Bowers, “Electrically pumped hybrid AlGaInAs-silicon evanescent laser,” Opt. Express **14**, 9203–9210 (2006).

[15] www.intel.com

[16] P. De Heyn, V. Kopp, A. Srinivasan, P. Verheyen, J. Park, M. S. Wlodawski, J. Singer, D. Neugroschl, B. Snyder, S. Balakrishnan, G. Lepage, M. Pantouvaki, P. Absil, J. Van Campenhout, “Ultra-Dense 16x56Gb/s NRZ GeSi EAM-PD Arrays Coupled to Multicore Fiber for Short-Reach 896Gb/s Optical Link ,” in Optical Fiber Communication Conference (OFC 2017), paper Th1B.7.

[17] C. Sun, M. T. Wade, Y. Lee, J. S. Orcutt, L. Alloatti, M. S. Georgas, A. S. Waterman, J. M. Shainline, R. R. Avizienis, S. Lin, B. R. Moss, R. Kumar, F. Pavanello, A. H. Atabaki, H. M. Cook, A. J. Ou, J. C. Leu, Y. Chen, K. Asanovic, R. J. Ram, M. A. Popović, and V. M. Stojanović, “Single-chip microprocessor that communicates directly using light,” Nature **528**, 534–538 (2015).

[18] W. Bogaerts and S. K. Selvaraja, “Compact single-mode silicon hybrid rib/strip waveguide with adiabatic bends,” IEEE Photonics Journal **3**, 422–432 (2011).

[19] A. Subramanian, E. M. P. Ryckeboer, A. Dhakal, F. Peyskens, A. Malik, B. Kuyken, H. Zhao, S. Pathak, A. Ruocco, A. De Groote, P. C. Wuytens, D. Martens, F. Leo, W. Xie, U. D. Dave, M. Muneeb, P. V. Dorpe, J. V. Campenhout, W. Bogaerts, P. Bienstman, N. L. Thomas, D. V. Thourhout, Z. Hens, G. Roelkens, and R. Baets, “Silicon and silicon nitride photonic circuits for spectroscopic sensing on-a-chip,” Photonics Research **5**(3), 47–59 (2015).

[20] N. A. Yebo, D. Taillaert, J. Roels, D. Lahem, M. Debliquy, D. Van Thourhout, and R. Baets, “Silicon-on-insulator (SOI) ring resonator based integrated optical hydrogen sensor,” IEEE Photon. Technol. Lett. **21**(14), 960–962 (2009).

[21] E. Hallynck and P. Bienstman, “Integrated optical pressure sensors in silicon-on-insulator,” IEEE Photon. J. **4**(2), 443–450 (2012).

[22] K. De Vos, I. Bartolozzi, E. Schacht, P. Bienstman, and R. Baets, “Silicon-on-Insulator microring resonator for sensitive and label-free biosensing,” Opt. Express **15**(12), 7610–7615 (2007).

[23] T. Claes, J. Girones, K. De Vos, E. Schacht, R. Baets, and P. Bienstman, “Label-free biosensing with a slot-waveguide-based ring resonator in silicon on insulator,” IEEE Photon. J.1, 197–204 (2009).

[24] C. N. Banwell, Fundamentals of Molecular Spectroscopy, 4th ed. (McGraw-Hill, 1994).

[25] L. S. Rothman, I. E. Gordon, Y. Babikov, A. Barbe, D. Chris Benner, P. F. Bernath, M. Birk, L. Bizzocchi, V. Boudon, L. R. Brown, A. Campargue, K. Chance, E. A. Cohen, L. H. Coudert, V. M. Devi, B. J. Drouin, A. Fayt, J.-M. Flaud, R. R. Gamache, J. J. Harrison, J.-M. Hartmann, C. Hill, J. T. Hodges, D. Jacquemart, A. Jolly, J. Lamouroux, R. J. Le Roy, G. Li, D. A. Long, O. M. Lyulin, C. J. Mackie, S. T. Massie, S. Mikhailenko, H. S. P. Müller, O. V. Naumenko, A. V. Nikitin, J. Orphal, V. Perevalov, A. Perrin, E. R. Polovtseva, C. Richard, M. A. H. Smith, E. Starikova, K. Sung, S. Tashkun, J. Tennyson, G. C. Toon, V. G. Tyuterev, and G. Wagner, "The HITRAN2012 molecular spectroscopic database," J. Quant. Spectrosc. Radiat. Transf. **130**, 4–50 (2013).

[26] Y. Yao, A. J. Hoffman, and C. F. Gmachl, "Mid-infrared quantum cascade lasers," Nat. Photonics **6**(7), 432–439 (2012).

[27] I. Vurgaftman, R. Weih, M. Kamp, J. Meyer, C. Canedy, C. Kim, M. Kim, W. Bewley, C. Merritt, J. Abell, and S. Höfling, "Interband cascade lasers," J. Phys. D **48**(12), 123001 (2015).

[28] S. Stephan, D. Frederic, and A. Markus-Christian, "Novel InP- and GaSb-based light sources for the near to far infrared," Semicond. Sci. Technol. **31**(11), 113005 (2016).

[29] G. Boehm, M. Grau, O. Dier, K. Windhorn, E. Roenneberg, J. Rosskopf, R. Shau, R. Meyer, M. Ortsiefer, and M. C. Amann, "Growth of InAs- containing quantum wells for InP-based VCSELs emitting at 2.3 μm," J. Cryst. Growth **301–302**, 941–944 (2007).

[30] K. Vizbaras, A. Vizbaras, A. Andrejew, C. Grasse, S. Sprengel, and M.-C. Amann, "Room-temperature type-I GaSb-based lasers in the 3.0 - 3.7 μm wavelength range," Proc. SPIE 8277, 82771B, 82771B-7 (2012).

[31] S. Forouhar, R. M. Briggs, C. Frez, K. J. Franz, and A. Ksendzov, "High-power laterally coupled distributed-feedback GaSb-based diode lasers at 2 μm wavelength," Appl. Phys. Lett. **100**(3), 031107 (2012).

[32] S. Sprengel, G. Veerabathran, A. Andrejew, A. Köninger, G. Boehm, C. Grasse, and M. C. Amann, "InP-based type-II heterostructure lasers for wavelengths up to 2.7 μm," in SPIE Photonics West, Novel In-Plane Semiconductor Lasers XIV (SPIE, 2015), paper 9382–29.

[33] G. K. Veerabathrana, S. Sprengel, A. Andrejew, and M.-C. Amann, "Room-temperature vertical-cavity surface-emitting lasers at 4 μm with GaSb-based type-II quantum wells," Appl. Phys. Lett. **110**, 071104 (2017).

[34] J. Faist, F. Capasso, D. L. Sivco, C. Sirtori, A. L. Hutchinson, and A. Y. Cho, “Quantum cascade laser,” Science **264**(5158), 553–556 (1994).

[35] M. S. Vitiello, G. Scalari, B. Williams, and P. De Natale, “Quantum cascade lasers: 20 years of challenges,” Opt. Express **23**(4), 5167–5182 (2015).

[36] Q. Y. Lu, Y. Bai, N. Bandyopadhyay, S. Slivken, and M. Razeghi, “2.4W room temperature continuous wave operation of distributed feedback quantum cascade lasers,” Appl. Phys. Lett. **98**(18), 181106 (2011).

[37] B. G. Lee, H. F. A. Zhang, C. Pflügl, L. Diehl, M. A. Belkin, M. Fischer, A. Wittmann, J. Faist, and F. Capasso, “Broadband distributed-feedback quantum cascade laser array operating from 8.0 to 9.8 μm,” IEEE Photon. Technol. Lett. **21**(13), 914–916 (2009).

[38] A. Hugi, R. Terazzi, Y. Bonetti, A. Wittmann, M. Fischer, M. Beck, J. Faist, and E. Gini, “External cavity quantum cascade laser tunable from 7.6 to 11.4 μm,” Appl. Phys. Lett. **95**(6), 061103 (2009).

[39] R. Q. Yang, “Infrared-laser based on intersubband transitions in quantum-wells,” Superlattices Microstruct. **17**(1), 77–83 (1995).

[40] J. R. Meyer, I. Vurgaftman, R. Q. Yang, and L. R. Ram-Mohan, “Type-II and type-I interband cascade lasers,” Electron. Lett. **32**(1), 45–46 (1996).

[41] I. Vurgaftman, J. R. Meyer, and L. R. Ram-Mohan, “Mid-IR vertical-cavity surface-emitting lasers,” IEEE J. Sel. Top. Quantum Electron. **34**(1), 147–156 (1998).

[42] C.-H. Lin, R. Q. Yang, D. Zhang, S. J. Murry, S. S. Pei, A. A. Allerman, and S. R. Kurtz, “Type-II interband quantum cascade laser at 3.8 μm,” Electron. Lett. **33**(7), 598–599 (1997).

[43] M. Kim, C. L. Canedy, W. W. Bewley, C. S. Kim, J. R. Lindle, J. Abell, I. Vurgaftman, and J. R. Meyer, “Interband cascade laser emitting at $\lambda = 3.75$ μm in continuous wave above room temperature,” Appl. Phys. Lett. **92**(19), 191110 (2008).

[44] I. Vurgaftman, W. W. Bewley, C. L. Canedy, C. S. Kim, M. Kim, C. D. Merritt, J. Abell, J. R. Lindle, and J. R. Meyer, “Rebalancing of internally generated carriers for mid-infrared interband cascade lasers with very low power consumption,” Nature Commun **2**, 585 (2011).

[45] W. W. Bewley, C. L. Canedy, C. S. Kim, M. Kim, C. D. Merritt, J. Abell, I. Vurgaftman, and J. R. Meyer, “Continuous-wave interband cascade lasers operating above room temperature at $\lambda = 4.7$-5.6 μm,” Opt. Express **20**(3), 3235–3240 (2012).

[46] J. Scheuermann, R. Weih, M. V. Edlinger, L. Nähle, M. Fischer, J. Koeth, M. Kamp, and S. Höfling, "Single-mode interband cascade lasers emitting below 2.8 µm," Appl. Phys. Lett. **106**, 161103 (2015).

[47] Z. Tian, L. Li, Y. Hao, R. Q. Yang, T. D. Mishima, M. B. Santos, and M. B. Johnson, " InAs-based interband cascade lasers with emission wavelength at 10.4 µm," Electron. Lett. **48**, 113 (2012).

[48] W. Zeller, L. Naehle, P. Fuchs, F. Gerschuetz, L. Hildebrandt, and J. Koeth, "DFB lasers between 760 nm and 16 µm for sensing applications," Sensors **10**(4), 2492–2510 (2010).

[49] A. Gassenq, F. Gencarelli, J. Van Campenhout, Y. Shimura, R. Loo, G. Narcy, B. Vincent, and G. Roelkens, "GeSn/Ge heterostructure short-wave infrared photodetectors on silicon," Opt. Express **20**(25), 27297–27303 (2012).

[50] A. Rogalski, "Infrared detectors: status and trends," Prog. Quantum Electron. **27**(2-3), 59–210 (2003).

[51] B. Mizaikoff , "Waveguide-enhanced mid-infrared chem/bio sensors," Chem. Soc. Rev. **42**, 8683 (2013).

[52] R. Soref, "Mid-infrared photonics in silicon and germanium," Nat. Photonics **4**(8), 495–497 (2010).

[53] N. Hattasan, A. Gassenq, L. Cerutti, J.-B. Rodriguez, E. Tournie, and G. Roelkens, "Heterogeneous Integration of GaInAsSb p-i-n Photodiodes on a Silicon-on-Insulator Waveguide Circuit," IEEE Photon. Technol. Lett. **23**(23), 1760–1762 (2011).

[54] M. Nedeljkovic, A. Khokhar, Y. Hu, X. Chen, J. Soler Penades, S. Stankovic, D. J. Thomson, F. Y. Gardes, H. M. H. Chong, G. T. Reed, and G. Z. Mashanovich, "Silicon photonic devices and platforms for the mid-infrared," Opt. Mater. Express **3**(9), 1205–1214 (2013).

[55] A. Spott, J. Peters, M. L. Davenport, E. J. Stanton, C. D. Merritt, W. W. Bewley, I. Vurgaftman, C. S. Kim, J. R. Meyer, J. Kirch, L. J. Mawst, D. Botez, and J. E. Bowers, "Quantum cascade laser on silicon," Optica **3**(5), 545–551 (2016).

[56] A. Malik, M. Muneeb, S. Pathak, Y. Shimura, J. Van Campenhout, R. Loo, and G. Roelkens, "Germanium-on-silicon mid-infrared arrayed waveguide grating multiplexers," IEEE Photon. Technol. Lett. **25** (18), 1805–1808 (2013).

[57] A. Densmore, D.-X. Xu, S. Janz, P. Waldron, J. Lapointe, T. Mischki, G. Lopinski, A. Delâge, J. Schmid, and P. Cheben, "Sensitive label-free biomolecular detection using thin silicon waveguides," Adv. Opt. Technol.2008 (2008).

[58] P. T. Lin, S. W. Kwok, H. Y. G. Lin, V. Singh, L. C. Kimerling, G. M. Whitesides, and A. Agarwal, “Mid-infrared spectrometer using opto-nanofluidic slot-waveguide for label-free on-chip chemical sensing,” Nano Lett. **14**(1), 231–238 (2014).

[59] E. J. Zhang, L. Tombez, J. S. Orcutt, S. Kamlapurkar, G. Wysocki, W. M. J. Green, “Silicon photonic on-chip trace-gas spectroscopy of methane,” in Conference on Lasers and Electro-Optics (CLEO:2016), paper SF2H.1.

[60] T. H. Stievater, M. W. Pruessner, D. Park, W. S. Rabinovich, R. A. McGill, D. A. Kozak, R. Furstenberg, S. A. Holmstrom, and J. B. Khurgin, “Trace gas absorption spectroscopy using functionalized microring resonators,” Opt. Lett. **39**, 969–972 (2014).

[61] P. J. Roberts, F. Couny, H. Sabert, B. J. Mangan, D. P. Willliams, L. Farr, M. W.Mason A. Tomlinson, T. A. Birks, J. C. Knight, and P. St.J. Russell, “Ultimate low loss of hollow-core photonic crystal fibres,” Opt. Express **13**, 236–244 (2005).

[62] M. N. Petrovich, F. Poletti, J. P. Wooler, A. M. Heidt, N. K. Baddela, Z. Li, D. R. Gray, R. Slav k, F. Parmigiani, N. V. Wheeler, J. R. Hayes, E. Numkam, L. Grűner-Nielsen, B. Pálsdóttir, R. Phelan, B. Kelly, J. O’Carroll, M. Becker, N. MacSuibhne, J. Zhao, F. C. Gunning, A. D. Ellis, P. Petropoulos, S. U. Alam, and D. J. Richardson, “Demonstration of amplified data transmission at 2 μm in a low-loss wide bandwidth hollow core photonic bandgap fiber,” Opt. Express **21**(23), 28559–28569 (2013).

[63] Z. Li, A. M. Heidt, J. M. O. Daniel, Y. Jung, S. U. Alam, and D. J. Richardson, “Thulium-doped fiber amplifier for optical communications at 2 μm,” Opt. Express **21**(8), 9289–9297 (2013).

[64] J. J. Ackert, D. J. Thomson, L. Shen, A. C. Peacock, P. E. Jessop, G. T. Reed, G. Z. Mashanovich, and A. P. Knights, “High-speed detection at two micrometres with monolithic silicon photodiodes,” Nat. Photonics **9**(6), 393–396 (2015).

[65] M. U. Sadiq, M. R. Gleeson, N. Ye, J. O’Callaghan, P. Morrissey, H. Y. Zhang, K. Thomas, A. Gocalinska, E. Pelucchi, F. C. G. Gunning, B. Roycroft, F. H. Peters, and B. Corbett, “10 Gb/s InP-based Mach-Zehnder modulator for operation at 2 μm wavelengths,” Opt. Express **23**(9), 10905-10913 (2015)

[66] S. Latkowski, A. Hänsel, P. J. van Veldhoven, D. D’Agostino, H. Rabbani-Haghighi, B. Docter, N. Bhattacharya, P. J. A. Thijs, H. P. M. M. Ambrosius, M. K. Smit, K. A. Williams, and E. A. J. M. Bente, “Monolithically integrated widely tunable laser source operating at 2 μm,” Optica **3**, 1412-1417 (2016).

[67] R. Kormann, R. Königstedt, U. Parchatka, J. Lelieveld, and H. Fischer, "QUALITAS: A mid-infrared spectrometer for sensitive trace gas measurements based on quantum cascade lasers in CW operation," Rev. Sci. Instrum. **76**(7), 075102 (2005).

[68] R. Engelbrecht, "A compact NIR fiber-optic diode laser spectrometer for CO and CO2: analysis of observed 2f wavelength modulation spectroscopy line shapes," Spectrochim. Acta A **60**, 3291–3298 (2004).

[69] J. Caron and Y. Durand, "Operating wavelengths optimization for a spaceborne lidar measuring atmospheric CO_2," Appl. Opt. **48**(28), 5413–5422 (2009).

[70] S. Forouhar, R. M. Briggs, C. Frez, K. J. Franz, and A. Ksendzov, "High-power laterally coupled distributed-feedback GaSb-based diode lasers at 2 μm wavelength," Appl. Phys. Lett. **100**(3), 031107 (2012).

[71] J. Hodgkinson and R. P. Tatam, "Optical gas sensing: a review," Meas. Sci. Technol. **24**(1), 012004 (2013).

[72] A. Hangauer, J. Chen, R. Strzoda, M. Ortsiefer, and M.-C. Amann, "Wavelength modulation spectroscopy with a widely tunable InP-based 2.3 microm vertical-cavity surface-emitting laser," Opt. Lett. **33**(14), 1566–1568 (2008).

[73] E. Ryckeboer, R. Bockstaele, M. Vanslembrouck, and R. Baets, "Glucose sensing by waveguide-based absorption spectroscopy on a silicon chip," Biomed. Opt. Express **5**(5), 1636–1648 (2014).

2

III-V-on-silicon platform for the 2 µm wavelength range

2.1 Introduction

Although optically pumped silicon lasers have been demonstrated by utilizing stimulated Raman scatting in silicon waveguides, there is still no efficient electrically pumped laser realized based on pure silicon [1]. III-V compound semiconductors are obtained by combining group III elements (essentially Al, Ga, In) with group V elements (essentially N, P, As, Sb). Semiconductor heterostructures based on III-V materials have been used to realize high-performance laser sources from the deep ultraviolet to terahertz wavelength range [2]. This chapter reports on the development of a heterogeneous III-V-on-silicon platform for the 2 μm wavelength range. This platform is realized by heterogeneously integrating an InP-based type-II epitaxial layer stack on silicon waveguide circuits. The second section of this chapter introduces two wafer bonding approaches (direct and adhesive bonding) and III-V-on-silicon photonic devices based on these two approaches. The third section introduces three types of III-V material systems that can be used to realize high-performance semiconductor diode lasers for the 2-3 μm wavelength range. The fourth section of this chapter presents the design of the InP-based type-II epitaxial layer stack for 2 μm wavelength range III-V-on-silicon photonic circuits. Lastly, this chapter describes the fabrication process flow of such III-V-on-silicon photonic devices and the efforts on process optimizations.

2.2 Heterogeneous III-V-on-silicon platform

2.2.1 Direct and adhesive bonding

In order to combine the best of both worlds, wafer bonding technologies are developed to transfer III-V materials on silicon. Wafer bonding usually refers to a process that brings two mirror-polished wafers into contact to realize a strong bond between them either by interfacial bonds, or by using a ‘glue’ (e.g., polymers or metals). Here we summarize the two wafer bonding technologies most popular for photonic integrated circuits: molecular direct and adhesive bonding [3].

The traditional direct wafer bonding technology requires a high temperature (> 600 ℃) annealing, which is forbidden when bonding III-V material on silicon given the mismatch in the thermal expansion coefficients of these two material systems, as well as the diffusion of elements in the III-V layer stack at these elevated temperatures. To solve this problem, a low temperature bonding technology called “O_2 plasma-assisted wafer bonding” has been developed. Figure 2.1 shows the typical procedure of O_2 plasma-assisted wafer bonding for fabricating III-V-on-silicon photonic devices. Firstly, silicon and III-V material

are rigorously cleaned. Then native oxides on both material surfaces are removed in HF and NH_4OH solutions, respectively, which results in hydrophobic surfaces. The following O_2 plasma step converts the hydrophobic sample surfaces to hydrophilic ones by growing a thin layer of highly reactive native oxide. The Si-O-Si bonds of these oxides are very reactive. After physical mating typically in air at room temperature, the bonded sample is annealed at 300 ℃ with external pressure for an hour or more to form strong covalent bonds. Afterwards, the InP substrate is removed by diluted HCl solution. Then photonic devices are processed on the III-V membrane.

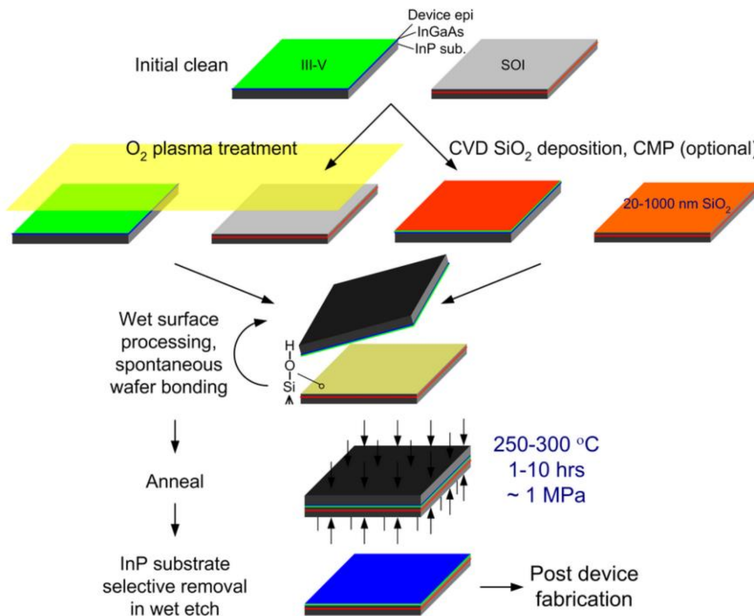

Figure 2.1. *Schematic process flow for O_2 plasma-assisted SiO_2 covalent direct wafer bonding [3].*

Compared with direct bonding, adhesive bonding has relaxed requirements on the surface cleanliness and roughness, thereby enabling much less surface preparation and high bonding yield. There are various polymers that can be used as adhesive, such as SU-8, polyimide, spin-on-glass and DVS-BCB (divinylsiloxane-bis-benzocyclobutene, also referred to as BCB). Among these candidates, DVS-BCB is a well-suited adhesive to integrate III-V photonic devices on silicon since it offers a low dielectric constant, a good thermal stability, a low curing temperature, a high degree of planarization and a high optical clarity. The electrical, optical, mechanical and thermal properties of DVS-BCB are summarized in Table 2.1. Figure 2.2 shows the infrared absorption spectrum of DVS-BCB [4]. This result indicates this polymer can be

used as the bonding agent for III-V-on-silicon photonic devices in 2 μm wavelength range. In the last decade, our group has devoted a lot of effort to develop III-V-to-silicon bonding technology, especially for InP-based material, based on both manual and machine-based bonding using DVS-BCB as the adhesive [5-7]. The detailed process flow of adhesive bonding will be introduced in the section 2.5.4.

Electrical properties	
Dielectric constant	2.5 at 10 GHz
Dissipation factor	0.002 at 10 GHz
Breakdown voltage	5.3 MV/cm
Optical properties	
Refractive index	1.543 at 1.55 μm
Optical loss	<0.1 dB/cm at 1.55 μm
Mechanical properties	
Tensile modulus	2.9 GPa
Intrinsic stress	28 MPa
Tensile strength	89 MPa
Poisson ratio	0.34
Shrinkage upon cure	0.05
Thermal properties	
Glass transition temperature	>350 ℃
Thermal expansion coefficient	42 ppm/K
Thermal conductivity	0.29 W/mK
Other properties	
Planarization	Very good
Moisture uptake	Very low

Table 2.1. *Properties of DVS-BCB [3].*

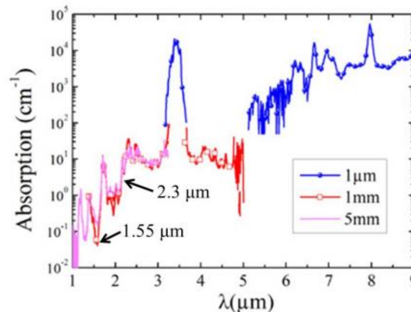

Figure 2.2. *Absorption of DVS-BCB versus wavelength [4].*

Figure 2.3 (a)-2.3(c) show microscope images of 2 inch diameter InP epitaxial wafers adhesively bonded to different substrates [7]. It can be found that a uniform and high-yield III-V membrane can be obtained after substrate removal. Besides this wafer-to-wafer bonding, die-to-wafer DVS-BCB bonding also can be achieved with a high processing yield. Figure 2.3 (d)-2.3(e) show microscope images of four III-V dies with different substrate thickness bonded to a patterned SOI substrate before and after substrate removal, respectively [7]. This nice result indicates different III-V photonic devices based on different III-V epitaxial layer structures can be realized using one adhesive bonding process.

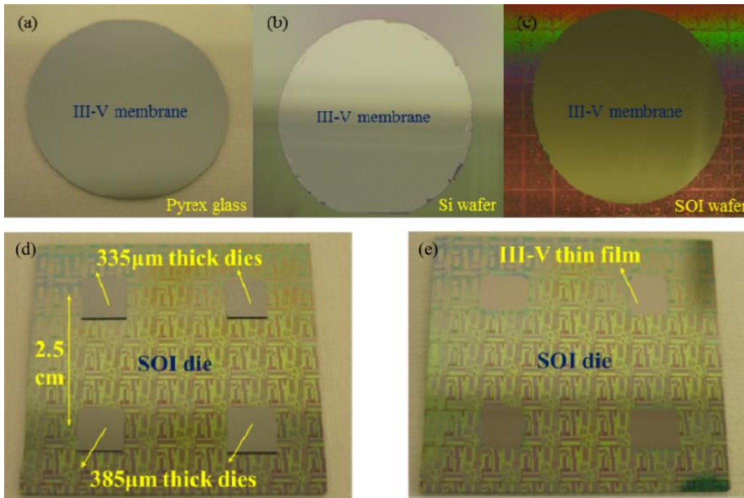

Figure 2.3. *A two inch III-V membrane bonded on a Pyrex glass wafer (a), a silicon wafer (b), and a patterned SOI wafer (c) after substrate removal;(d) four III-V dies bonded to a patterned SOI wafer before substrate removal (d) and after substrate removal (e)[7].*

2.2.2 Optical coupling between the III-V layers and silicon waveguides

When the III-V materials are bonded to silicon waveguide circuits, an efficient optical coupling between the III-V layers and the silicon waveguides become the critical issue for III-V-on-silicon photonic devices. In this section, several coupling methods will be introduced.

In 2006, A. W. Fang *et al.* reported the first electrically pumped III-V-on-silicon laser based on molecular direct bonding technology [8]. In this laser, the optical mode is strongly confined in the silicon waveguide while the evanescent tail of the optical mode overlaps with the III-V active region, as schematically shown in Figure 2.4(a). This evanescent laser ran CW with a threshold current of 65 mA and a maximum on-chip output power of about 14 mW at 15 ℃. Based on the same coupling method, H. Park *et al.* demonstrated a III-V-on-

silicon evanescent waveguide photodetector [9]. The hybrid photodetector has a 400 μm long III-V absorbing region and exhibits an internal quantum efficiency of 90 % over the 1.5 μm wavelength range. Besides molecular bonding, S. Stankovic *et al.* also realized the evanescent III-V-on-silicon laser based on adhesive BCB bonding technology [10]. For the III-V-on-silicon photonic devices based on the evanescent coupling method, a small part of the optical mode overlaps with the III-V active region, resulting in a relatively high threshold current for the lasers and a very long III-V absorbing region for the photodetectors.

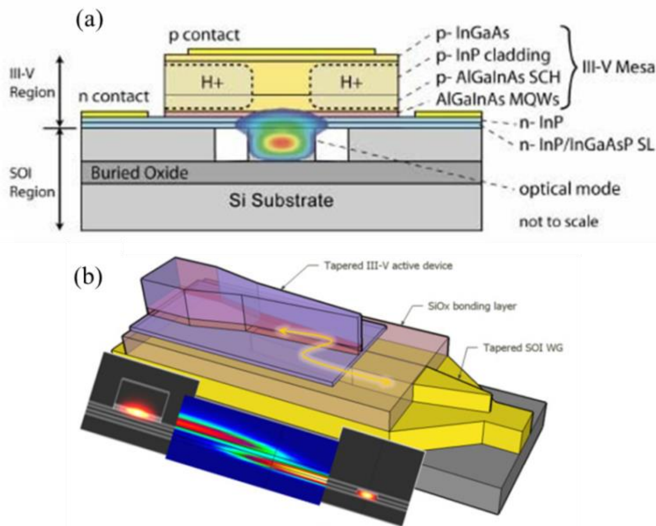

Figure 2.4. *(a) Schematic drawing of the III-V-on-silicon evanescent laser (a) [8], and adiabatically-coupled laser (b) [11].*

The second coupling method is based on adiabatically tapering both the III-V and silicon waveguides. A III-V-on-silicon laser based on this coupling method is shown in Figure 2.4(b) [11]. The device structure can be divided into three parts. In the center of the device, almost the entire optical mode is confined in the III-V waveguide, which provides the optical gain. At both sides, there is a III-V/silicon spot size converter (SSC) to couple the light from the III-V waveguide to the silicon waveguide. The III-V/silicon SSC has two sections. In the first section, the III–V waveguide quickly tapers down, while most of the optical mode is still confined in the III-V waveguide. In the second section, the III–V waveguide slowly tapers down to a very narrow tip, while the underneath silicon waveguide tapers from a narrow tip to a 2-3 μm wide waveguide. The optical mode gradually couples from the III-V waveguide to the silicon waveguide in the second section of the SSC, as shown in the inset of Figure 2.4

(b). In most of III-V-on-silicon photonic devices based on adiabatically coupling, the conversion efficiency of the III-V/silicon SSC is higher than 90%. M. Lamponi and S. Keyvaninia *et al.* reported the first III-V-on-silicon laser based on this adiabatic coupling method [12]. This adiabatically coupled laser exhibits a low threshold current of 30 mA and an output power of more than 4 mW at room temperature. Based on the same structure, a single mode laser with a 8 nm wavelength tuning range, multi-frequency lasers, DFB lasers and mode-lock lasers were also demonstrated [11,13-15].

Besides the two coupling methods as discussed above, the optical coupling between the III-V layers and the silicon waveguides also can be realized by butt-coupling and grating-assisted coupling in III-V-on-silicon photodetectors [16,17].

2.2.3 III-V-on-silicon photonic devices

III-V-on-silicon platforms have been used to fabricate high-performance active opto-electronic devices to enable optical communication applications. Distributed feedback lasers are attractive laser sources for these applications since they have a single longitudinal mode output, high optical output power and relatively narrow linewidth. Very recently, a high-speed directly modulated III-V-on-silicon DFB laser with a 56 Gb/s modulation was demonstrated based on adhesive bonding technology and adiabatic coupling [18]. A threshold current of 32 mA and a waveguide-referred output power of 6 mW were achieved for the 340 μm long (gain section length) high speed DFB laser. Widely tunable silicon photonic laser sources also are realized based on the heterogeneous III-V-on-silicon platform, using silicon micro-ring resonators (MRRs) or sampled gratings as tunable filters [19-21]. For example, a heterogeneously integrated Vernier ring laser with a more than 40 nm wavelength tuning range and linewidth of 338 kHz was demonstrated [19]. Besides laser sources, semiconductor optical amplifiers (SOAs) are another type of photonic devices that cannot be realized based on group IV materials. III-V-on-silicon SOAs have been demonstrated based on different bonding technologies and different coupling methods between the III-V layers and the silicon waveguides [22-24]. P. Kaspar *et al.* reported a III-V-on-silicon SOA using a 1100-μm-long amplifier section and fully packaged with fibers attached to the vertical grating couplers. The device exhibits 28 dB of on-chip gain and a 10 dB of fiber-to-fiber gain. Although high-speed silicon photodetectors and modulators can be realized based on germanium and silicon in the telecommunication wavelength range [25, 26], III-V-on-silicon platforms can also provide a promising solution to fabricate these two silicon photonic components with high performance [27-30]. For example, Y. Tang *et al.* reported traveling-wave electroabsorption modulators (EAM) with a modulation bandwidth of 42 GHz based on the III-V-on-silicon

platform. A dynamic extinction ratio of 9.8 dB with a driving voltage swing of 2 V was demonstrated at a transmission rate of 50 Gb/s.

With a library of functional devices developed on the III-V-on-silicon platform, a fully integrated photonic network-on-chip circuit with wavelength division multiplexing transceivers has been recently demonstrated [31]. Figure 2.5 shows the photo of the transceiver chip with 400 functional components, including passive components and III-V-on-silicon DFB lasers, EAMs, SOAs and photodetectors. The total transmission capacity of the III-V-on-silicon chip is up to 8 × 8 ×40 Gbps for intra- and inter-chip interconnections.

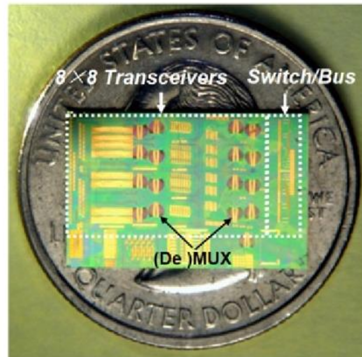

Figure 2.5. *Photo of a 8 × 8 × 40 Gbps III-V-on-silicon transceiver chip [31].*

The heterogeneous III-V-on-silicon platform has been extended beyond the telecommunication wavelength range, into the mid-infrared. Integration of mid-infrared III-V opto-electronic devices on silicon photonic ICs promises to enable fully functional spectroscopic sensing systems on a photonic chip, as discussed in the first chapter of this thesis. Besides, the high-performance and low-cost silicon photonic passive components can be used as the wavelength combiner or the feedback structure for broadly tunable mid-infrared lasers, thereby leading to miniature and portable optical sensors. In recent years, heterogeneously integrated III-V-on-silicon laser sources and photodetectors have been demonstrated at particular mid-infrared wavelengths [17, 32-35]. A.Gassenq *et al.* reported an evanescently-coupled GaInAsSb photodetector on silicon with a responsivity of 1.4 A/W at 2.3 μm wavelength and a dark current of 10 μA under a reverse voltage of 1 V [17]. A. Spott *et al.* demonstrated the first quantum cascade laser (QCL) heterogeneously integrated on a silicon photonic IC [34], based on molecular direct bonding technology and adiabatic coupling. The heterogeneous Fabry-Perot QCL is bonded to a silicon-on-nitride-on-insulator (SONOI) waveguide as schematically shown in Figure 2.6 (a), and lases at 4.8 μm wavelength in pulsed mode. The dependence of output power on

drive current of a 6-μm wide QCL in pulsed mode (250-ns wide pulses at 1- kHz repetition rate) is plotted in Figure 2.6 (b). A threshold current density of 1.6 kA/cm^2 and up to 31 mW of single-sided output power is obtained.

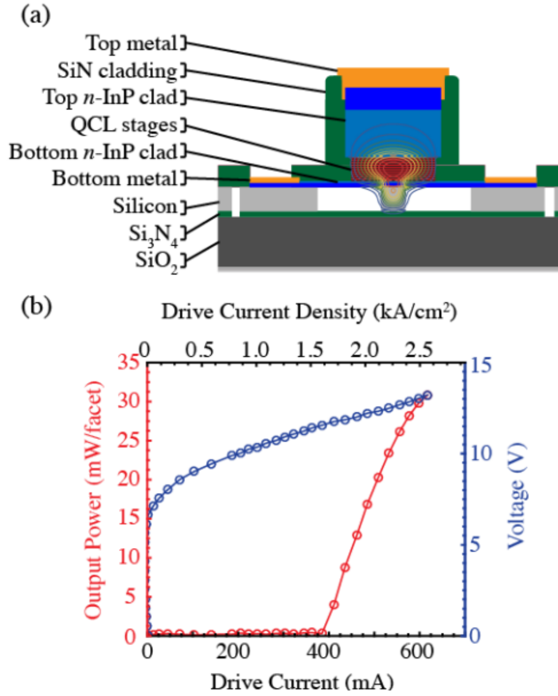

Figure 2.6. *(a) Schematic of the cross-section of a QCL integrated on a SONOI waveguide; (b) the dependence of pulsed single-sided output power and voltage on drive current for the heterogeneously integrated QCL [34].*

2.3 III-V materials for the 2 μm wavelength range

In the telecommunication wavelength range, InP-based type-I (Al)GaInAs or GaInAs(P) quantum wells are commonly used as the gain material for III-V-on-silicon laser sources [8,11]. The development of these gain materials has strongly benefited from the high interest in semiconductor laser diodes for optical communication applications, thereby leading to high quality epitaxy. In the 2 μm wavelength range, InP-based type-I, type-II and GaSb-based type-I heterostructures can be used as the active region of the III-V-on-silicon photonic devices. Because waveguide-coupled photodetectors can use the same epitaxial layer stack as the III-V-on-silicon lasers, here we focus on the III-V materials for the 2 μm range laser diodes. The detailed review on the use of these types of materials for photodetectors will be carried out in the third chapter.

2.3.1 InP-based type-I heterostructure

Based on InP-based type-I (Al)GaInAs materials, the emission wavelength of laser diodes can be selected relatively easily in the 1.3 μm to 2.0 μm range, by varying the composition of the quantum wells. Shifting from short to long emission wavelength, the aluminum-content in the quantum wells is reduced while In-content is increased. This leads to a narrower band gap, but also to higher compressive stain. Recently, heterogeneously integrated III-V-on-silicon Fabry-Perot lasers using strained InGaAs type-I heterostructures, operating at 2 μm wavelength and emitting up to 4.2 mW of single facet CW power at room temperature were demonstrated [36]. CW operation was observed up to 26 ℃ and 35 ℃ for lasers with 1-mm and 2-mm long mesas, respectively. However, longer lasing wavelengths become much more challenging since too high strain degrades the gain material and would impact the heterogeneous integration process. The emission wavelength of highly strained type-I quantum wells on InP substrate is limited to around 2.3 μm [37].

2.3.2 GaSb-based type-I heterostructure

GaSb-based type-I heterostructures offer low threshold and high output power for laser diodes in the 2-3 μm wavelength range. The first GaSb-based lasers with emission wavelength range between 1.9 μm and 2.3 μm were demonstrated in 1985, based on an AlGaAsSb/GaInAsSb/AlGaAsSb double heterostructure [38,39]. These lasers had threshold current densities ranging from 6.9 kA/cm^2 to 20 kA/cm^2 in pulsed operation. Employing strained GaInAsSb type-I quantum wells as the gain material largely improves the device performance. High-performance GaSb-based type-I quantum well laser diodes with CW output power above 1 W and maximum power conversion efficiencies >15% have been demonstrated up to 2.4 μm wavelength [40]. S. Forouhar *et al.* reported a GaSb-based DFB laser emitting more than 40 mW continuous-wave in a single longitudinal mode at 2.05 μm wavelength at 10 ℃ [41].

Similar to their InP-based counterparts, adding more indium to the GaInAsSb quantum well can shift the operation of GaSb-based laser diodes to longer emission wavelength. These quantum wells are embedded in AlGaAsSb barriers, with aluminium content up to 50%. Based on this approach, devices emitting up to 3 μm wavelength and slightly above have been reported [42]. Figure 2.7 (a) shows the CW emission spectra of GaSb-based DFB lasers, covering the entire 1.8–3.0 μm wavelength region [43]. The dependence of threshold current and slope efficiency of the DFB lasers is plotted in Figure 2.7 (b). It can be found that the lasers operating in the 1.9 μm to 2.4 μm wavelength range have the best performance. The threshold currents of the devices almost exponentially increase when the wavelength is getting close to 3 μm. This is because the more

indium is added the more the valence band edge shifts to lower energies, which decreases the band offset to the surrounding barriers consistently until there is virtually no hole confinement left at all [43]. A good solution for GaSb-based laser diodes above 3 μm wavelength is using quinternary material AlGaInAsSb as the barrier. Based on this solution, the longest wavelength demonstrated with GaSb-based type-I quantum well diode lasers is 3.7 μm [44].

However, the heterogeneous integration of GaSb-based active devices on silicon is less mature than that of InP-based devices, which eventually results in a low device yield [45]. In the fifth chapter, we will report compact tunable external cavity lasers by butt coupling a GaSb-based gain chip and a silicon photonic IC, thereby avoiding the heterogeneous integration. For the heterogeneous III-V-on-silicon platform in the 2 μm wavelength range, we still want to use InP-based material since the related heterogeneous integration processes are well established.

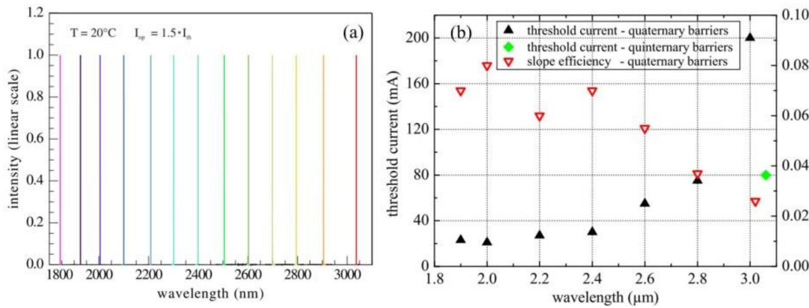

Figure 2.7. (a) Emission spectra of GaSb-based DFB lasers covering the 1.8–3.0 μm wavelength range; (b) threshold current and slope efficiency versus lasing wavelength. All of these results are acquired at room-temperature in CW operation [42].

2.3.3 InP-based type-II heterostructure

The most promising solution to overcome the wavelength limitation of InP-based laser diodes is replacing the type-I quantum well with staggered type-II heterostructures. The type-II quantum well laser diode on InP substrate was firstly demonstrated in 1999. The spontaneous emission wavelength of the type-II InGaAs/GaAsSb quantum well was around 2.1 μm, however, the lasing wavelength of the laser diode shifted to 1.7 μm [46]. In 2012, S. Sprengel *et al.* reported the first InP-based type-II laser diode with emission wavelength above 2.3 μm, electrically pumped up to 2.55 μm [47]. The lasing wavelength was then extended to 2.7 μm in 2014 [48]. To achieve this long wavelength emission, a "W"-shaped quantum well is used.

For the design of the type-II active region, the wavefunction overlap of electrons and holes is crucial, because the spontaneous and stimulated emission is proportional to the square of it. The simplest type-II InGaAs/GaAsSb active region is displayed in Figure 2.8 (a) [49]. The holes are confined in the GaAsSb layer due to their high effective mass, while the electrons are mainly confined in the InGaAs layer. Because the electrons are much lighter, they also strongly penetrate into the hole confining GaAsSb layer, as depicted in the Figure 2.8 (a). As a result, a relatively high wave function overlap is offered. However, the tunneling into the barriers also creates minibands, which leads to a broadening of the optical transition. This type of active region is very interesting for a broadband light source such as a light emitting diode (LED) [50], but it is not well suited as gain material for lasers since such broad spontaneous emission would raise the threshold current density. A promising solution for type-II quantum well laser diodes is the use of a "W"-shaped active region, which is a concept commonly used in GaSb-based interband cascade lasers (ICLs). Figure 2.8(b) shows a "W"-shaped structure consists of a one GaAsSb layer confining holes, surrounded by two InGaAs quantum wells for electrons. In this "W"-shaped structure, the electron wells are strongly coupled, leading to a splitting of the ground state into a symmetric and anti-symmetric state. The lowest hole state is a symmetric heavy hole state Ψ_{HH}. For symmetry reasons, only the symmetric electron state can couple to the heavy hole ground state. Therefore, a narrow emission spectrum is expected for the "W"-shaped quantum well.

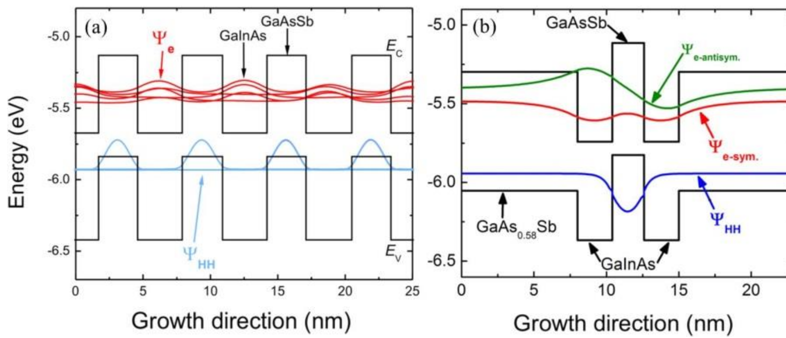

Figure 2.8. *(a) Band structure of a InGaAs/GaAsSb superlattice structure, the wavefunctions of electrons and heavy holes are plotted. Recombination processes mainly take place between electrons and heavy holes, because the ground state of heavy holes is the lowest state due to its low quantization energy. (b) 'W-shaped' InGaAs/GaAsSb active region [49].*

Figure 2.9 shows photoluminescence spectra of a InGaAs/GaAsSb supperlattice and a "W"-shaped active region [50]. It can found that the "W"-shaped structure offers a much narrower emission spectrum.

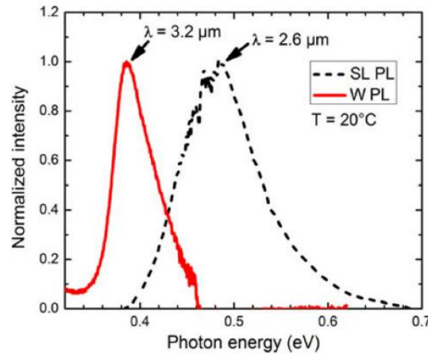

Figure 2.9. *Photoluminescence (PL) spectra of a InGaAs/GaAsSb superlattice (SL) and a "W"-shaped active region [50].*

Based on this "W"-shaped InGaAs/GaAsSb active region, J. Huang *et al.* theoretically predicted that emission wavelengths of InP-based type-II heterostructures can cover the 2-4 µm range [51], but they just demonstrated room-temperature PL emission at ~2.1 µm. S. Sprengel *et al.* from the Walter Schottky Institute (WSI) of the Technical University of Munich (TUM) realized emission up to 3.9 µm, as shown in Figure 2.10 (a) [52]. Using the InGaAs/GaAsSb type-II quantum wells, InP-based resonant-cavity LEDs operating up to a wavelength of 3.5 µm at 20–80 ℃ have been demonstrated [53]. S. Sprengel *et al.* also realized electrically pumped InP-based type-II lasers with emission up to 2.7 µm in pulsed mode, as shown in Figure 2.10 (b) [52]. In addition, in 2015 the first InP-based vertical-cavity surface-emitting lasers (VCSELs) with the "W"-shaped quantum well were demonstrated, with CW operation up to 10 °C at a wavelength of 2.49 µm and a peak output power of 400 µW at −18 °C [54].

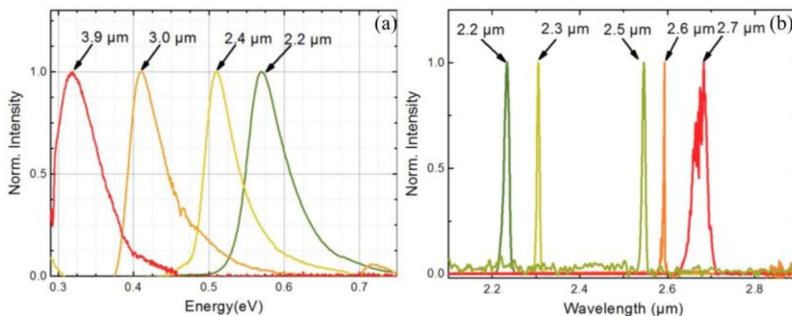

Figure 2.10. *(a) Room-temperature photoluminescence spectra of "W"-shaped InGaAs/GaAsSb quantum wells; (b) emission spectra of InP-based type-II quantum well diode lasers [52].*

2.4 Design of InP-based type-II epitaxial layer stack

Figure 2.11 shows the schematic cross section of the 2 μm range passive and active opto-electronic devices developed during this PhD research. The silicon-on-insulator (SOI) wafer consists of a 400 nm thick silicon device layer and a 2 μm thick buried oxide layer on a ~750 μm thick silicon substrate. The fabricated silicon waveguides are rib waveguides, etched 180 nm deep in the silicon device layer. The InP-based type-II epitaxial layer stack is bonded to a SOI waveguide circuit using an ultra-thin DVS-BCB bonding layer.

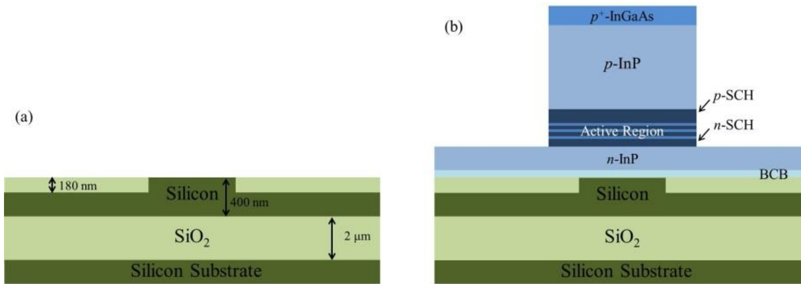

Figure 2.11. *Schematic of the layer stack of passive and active photonic devices for the 2 μm wavelength range: (a) a silicon rib waveguide, (b) a III-V opto-electronic device bonded to a silicon waveguide.*

The III-V epitaxial structure was grown by Prof. Amann's reseach group at TUM, on an *n*-doped InP substrate with a molecular beam epitaxy (MBE) system. Figure 2.12 shows the band structure of the designed InP-based type-II layer structure. The epitaxial layer stack consists of a 200 nm thick *n*-contact layer, an active region sandwiched between a 130 nm thick GaAsSb and a 250 nm thick AlGaAsSb separate confinement heterostrctures (SCH) layer, a 1.5 μm thick *p*-InP cladding layer and a 100 nm thick *p*-contact layer. The thickness of the two SCH layers was optimized for phase matching between the silicon waveguide and III-V waveguide. A highly doped p^+-InGaAs (~$2 \times 10^{20}cm^{-3}$) and n-doped InP (~$1 \times 10^{18}cm^{-3}$) is used as p-contact and n-contact, respectively. The active region consists of six periods of a "W"-shaped quantum well structure, each separated by 9 nm tensile strained $GaAs_{0.58}Sb_{0.42}$ layers. The quantum well structure consists of a 2.9 nm thick $GaAs_{0.33}Sb_{0.67}$ hole-confining layer surrounded by two 2.6 nm thick $In_{0.68}Ga_{0.32}As$ electron-confining layers, as shown in Figure 2.13. A 10 nm AlGaInAs layer and a 20 nm AlAsSb layer is used as hole blocking layer on the n-side and electron blocking layer on the p-side, respectively, to avoid electron and hole leakage from the active region.

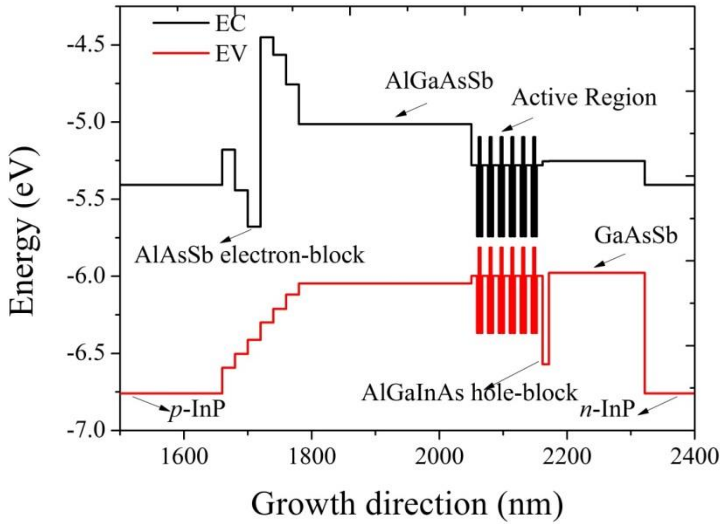

Figure 2.12. *Biased band structure of the InP-based type-II epitaxial layer stack bonded on the silicon waveguide circuit.*

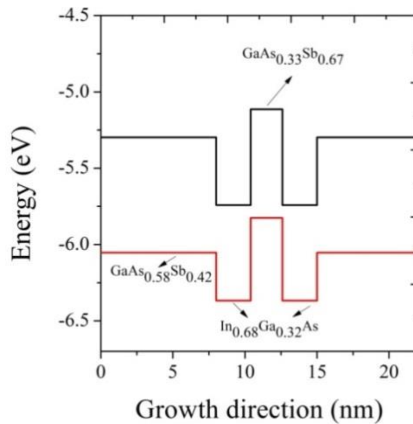

Figure 2.13. *Biased band structure of one "W"-shaped period of the active region.*

The detailed III-V layer stack and material parameters are shown in Table 2.2. Because III-V samples have to be flipped when brought into contact with SOI wafers, the growth sequence of the layer stack is inversed to that shown in Figure 2.11. On top of the wafer, a 100 nm InP and a 100 nm InGaAs are grown as a sacrificial layer for wafer cleaning process before bonding. Below the *p*-contact layer, a 100 nm InP and 250 nm InGaAs are grown, respectively used as etch stop and sacrificial layer during the substrate removal process.

InP-based type-II layer stack for 2.35 μm range III-V-on-silicon photonic devices					
Layer		Material	Doping	Thickness (nm)	Refractive Index
Sacrificial layer		InP		100	3.1105
Sacrificial layer		InGaAs		100	2.9592
Contact Layer		n-InP	1e18	200	3.1105
		n-GaAsSb	1e18	10	3.7646
SCH Layer		GaAsSb		130	3.7774
		n-GaAsSb	1e17	10	3.7762
		AlGaInAs	1e17	10	3.1992
Active region	Barrier	GaAs0.55Sb0.42		9	3.7774
	Well	Ga0.32In0.68As		2.6	3.4760
		GaAs0.33Sb0.67		2.9	3.7774
		Ga0.32In0.68As		2.6	3.4760
		GaAs0.55Sb0.42		9	3.7774
SCH Layer		p-AlGaAsSb	1e16	250	3.4949
		p-AlGaAsSb	5e17	20	3.4934
		p-AlGaAsSb	5e17	20	3.3920
		p-AlGaAsSb	5e17	20	3.2489
		p-AlAsSb	5e17	20	3.0898
		p-GaInAs	5e17	20	3.4747
		p-AlGaInAs	5e17	20	3.3028
		p-AlInAs	5e17	20	2.1619
		p-InP	2e18	20	3.1167
Cladding Layer		p-InP	2e17	500	3.1205
		p-InP	5e17	500	3.1198
		p-InP	2e18	500	3.1167
		p-InP	2e19	20	3.0792
		p-AlInAs	2e19	20	3.1059
Contact Layer		p-GaInAs	2e20	100	2.9592
Sacrificial layer		InP		100	3.1105
Etch Stop Layer		GaInAs		250	2.9592
n-InP substrate			n++		

Table 2.2. *Parameters of the III-V epitaxial layer stack used for 2.35 μm range III-V-on-silicon photonic devices.*

2.5 Fabrication of 2 µm range III-V-on-silicon photonic devices

2.5.1 A general overview of the process flow

The fabrication of SOI waveguides is carried out in imec's CMOS pilot line. Afterwards, the adhesive bonding and III-V device processing are performed in Ghent University's clean room. Before bonding, the SOI and III-V samples are properly cleaned. The III-V epitaxial stack is bonded onto the processed SOI by adhesive bonding using a ultra-thin DVS-BCB bonding layer. Following DVS-BCB curing, the InP substrate is removed by a HCl solution using a InGaAs layer as the etch stop layer. After the bonding and substrate removal process, the InGaAs/InP sacrificial layer pair is removed and then the active opto-electronic devices are processed on the III-V membrane. The first process is to define patterns on a SiN_x hard mask layer. Then the InGaAs contact layer is etched by inductively-coupled plasma (ICP) etching and the *p*-InP cladding layer is etched using a 1:1 $HCl:H_2O$ solution. Afterwards, a SiN_x hard mask layer is deposited again on the sample to protect the InP taper structures in the following wet etching process, and to passivate the thick *p*-InP cladding layer by covering the "V"-shaped sidewall. Then the active region is etched by a H_3PO_4: Citric Acid: $H_2O_2:H_2O$ 1:1:20:70 solution, which has a high etching selectivity of GaAsSb to *n*-InP. The isotropic etching of the active region creates an undercut below the SiN_x mask layer. After the mesa processing, Ni/Ge/Au is deposited as *n*-contact, 5 µm away from the edge of the III-V mesa. Then the *n*-InP is etched by diluted HCl to isolate the different devices. Afterwards, DVS-BCB is spin coated on the sample to passivate the devices. After curing at 250 ℃ for 1.5h, the DVS-BCB layer and SiN_x hard mask layer are etched by reactive ion etching (RIE) to expose the p^+-InGaAs layer. Then Ti/Au is deposited as *p*-contact. In the end, Ti/Au is deposited on the n-contact and *p*-contact as probe pad. Figure 2.14(a)-2.14(q) shows the schematic of the fabrication process flow. A scanning electron microscope (SEM) image of the cross section of fabricated III-V-on-silicon devices is shown in Fig. 2.14(r).

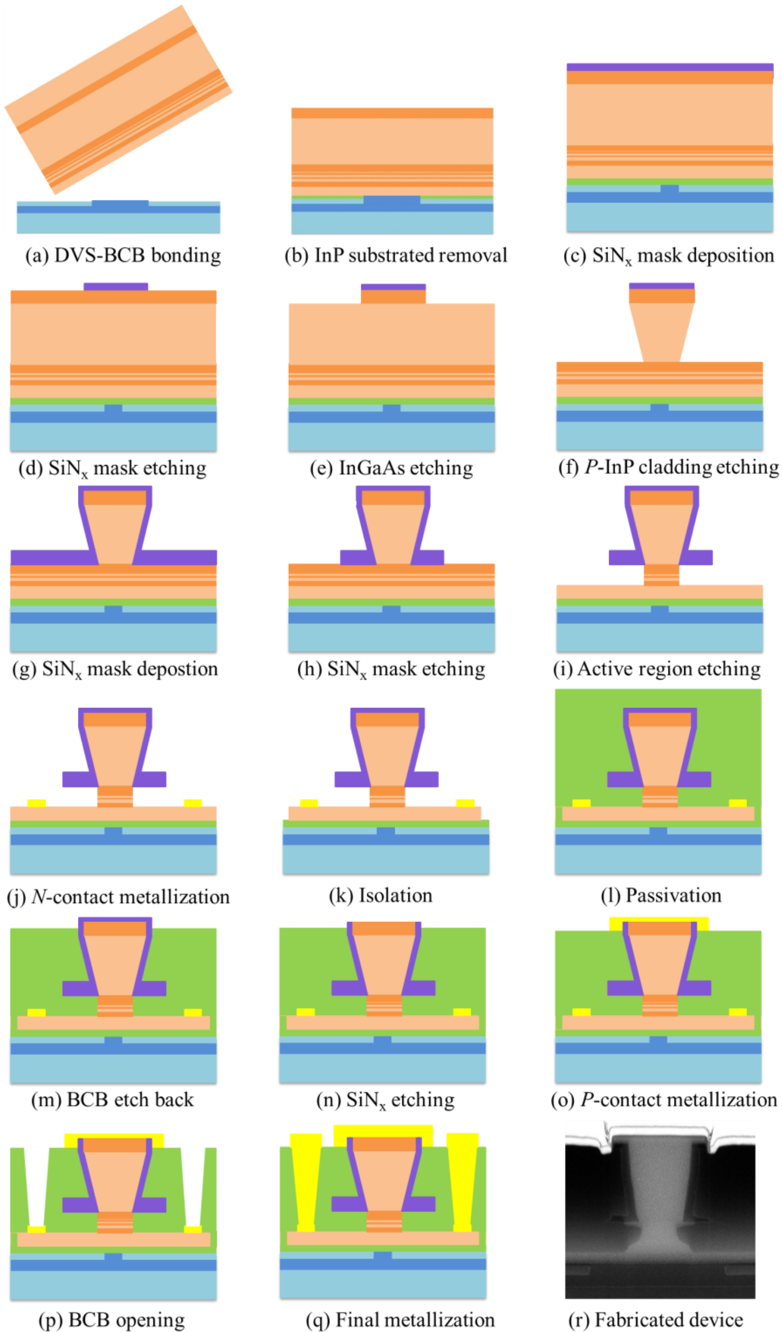

Figure 2.14. *(a)-(q) Fabrication process flow of the 2 μm range III-V-on-silicon devices; (r) SEM image of the device cross section.*

2.5.2 Fabrication of silicon waveguide circuits

The fabrication of SOI waveguide circuits is carried out on 200 mm SOI wafers in imec's CMOS pilot line. It is provided by a multi-project wafer (MPW) run service, which allows cost-effective fabrication [55]. The SOI wafer consists of a 400 nm thick crystalline silicon device layer on a 2 μm buried oxide layer. Before pattern definition, a SiO_2 and a SiN_x layer is deposited using a low-pressure chemical vapor deposition (LPCVD) process as a hard mask. The silicon waveguide patterns are then defined by 193 nm deep UV lithography. Inductively-coupled plasma (ICP) dry etching is used to etch 180 nm deep silicon rib waveguides. Afterwards, a layer of SiO_2 is deposited on the SOI wafer, which is then planarized by a chemical mechanical polishing (CMP) step down to the SiN_x hard mask layer. The SiN_x layer is then removed after the CMP process. The planarized flat surface is required for a high-yield bonding.

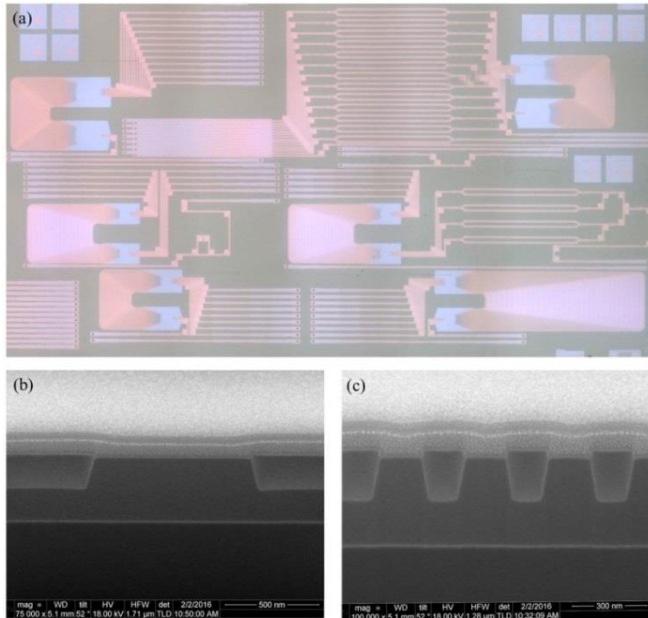

Figure 2.15. *(a) Microscope image of a fabricated silicon waveguide circuit. SEM image of the cross-section of a fabricated SOI waveguide (b) and grating (c).*

Figure 2.15 (a) show the microscope image of a fabricated silicon waveguide circuit. It consists of six arrayed waveguide grating (AWG) spectrometers, a number of reference waveguides, multimode interference (MMI) couplers and Mach-Zehnder interferometers (MZIs). All of these passive photonic devices are built by basic components: SOI waveguides and gratings. A cross-section

image of a fabricated waveguide and grating is shown in Figure 2.15(b) and 2.15(c), respectively. It can be seen that the side wall etching is not ideally vertical. This is should be considered in the design of III-V-on-silicon photonic devices.

2.5.3 Sample preparation for DVS-BCB adhesive bonding

When the fabrication of silicon waveguide circuits is completed, the followed processes are carried out at the clean room of Ghent University. Firstly, the SOI wafer is diced into small dies with dimension around 2.5 cm×2.5 cm. A layer of photoresist is spin-coated on the SOI wafer before dicing to protect the SOI die from particles generated in the mechanical dicing process. After dicing and photoresist removal, the residual SiO_x layer on top of the SOI waveguides after CMP process is removed by HF. Then the SOI die is cleaned by immersing the sample for 15 minutes into a Standard Clean 1 (SC-1) solution, which consists of aqueous ammonia (NH_4OH), hydrogen peroxide (H_2O_2) and deionized (DI) water in volume ratios of 1:1:5, respectively, heated to 70 ℃-80 ℃. Afterwards, the SOI sample should be baked for a few minutes before DVS-BCB spin-coating to remove all moisture.

As the epitaxial growth of InP-based type-II material is not as mature as the growth of III-V materials for the telecommunication wavelength range, many defects can be observed on the surface of the type-II epitaxial wafer, as shown in Figure 2.16. These defects can make the bonding of the III-V on silicon more difficult. The III-V wafer is firstly diced into bars of 8-10 mm long and 4-5 mm wide. Similar to the dicing of SOI, a thin photoresist layer also should be spin-coated on the III-V sample before dicing. Then the top InP and InGaAs sacrificial layer is removed by 1:1 $HCl:H_2O$ and 1:1:18 $H_2SO_4:H_2O_2:H_2O$, respectively. Afterwards, 10 nm of SiO_x is deposited on the III-V die by plasma-enhanced chemical vapor deposition (PECVD).

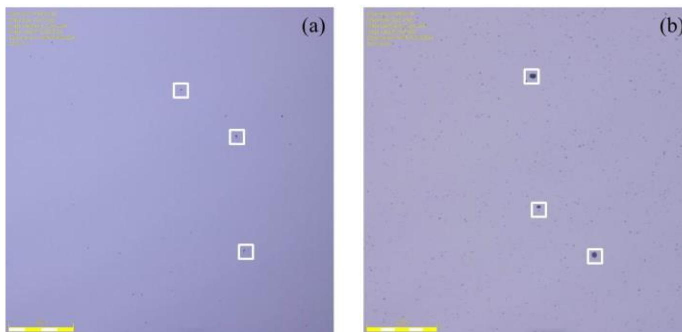

Figure 2.16. *Microscope image of the top surface of the III-V wafer in different positions: center (a) and edge (b). Some defects are markerd.*

2.5.4 Adhesive DVS-BCB bonding and substrate removal

Figure 2.17 shows the process flow of the adhesive DVS-BCB bonding [7]. The process starts with spin-coating of DVS-BCB (CYCLOTENE 3022-35) on the SOI die. Afterward, the SOI substrate is baked at 150 ℃ for 15 minutes to pre-cure the spun DVS-BCB and evaporate all the solvents, and then the SOI substrate is slowly cooled down to room temperature. Then the cleaned III-V dies are brought into contact with the DVS-BCB coated SOI and loaded in a wafer bonding machine (Suss MicroTec's ELAN CB6L). The chamber is pumped-down (target pressure 10^{-3} bar) and heated to 150 ℃ with a ramp of 15 ℃/min. Afterwards, a 300 kPa pressure is applied on the sample. After keeping the pressure on the dies for 10 min at 150 ℃, the temperature is increased up to 250 ℃, with a ramp of 1.5 ℃/min. When the chamber temperature reaches 250 ℃, the dies are kept at this temperature for one hour in a nitrogen atmosphere. After the DVS-BCB is fully cured, the bonded sample is cooled and unloaded from the chamber.

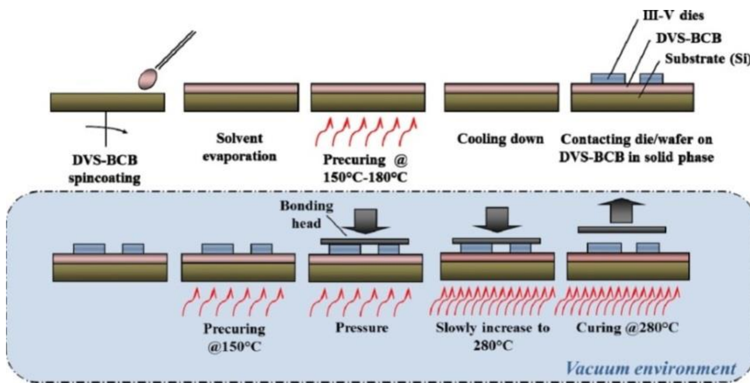

Figure 2.17. Schematic process flow for adhesive bonding using DVS-BCB as the bonding agent [7].

After bonding, the InP substrate is removed by immersing the sample in HCl. The wet etch rate is faster than 10 μm/min. So the 300 μm thick substrate can be completely removed in half an hour. This wet etching process is anisotropic. Therefore, two unetched ridges are formed at two opposite edges of the III-V membrane, as shown in Figure 2.18. These ridges are formed because HCl doesn't etch the expose (01-1) planes of crystalline InP. The two ridges can be up to several tens of micrometers high and thereby prevent the intimate contact between the lithographic mask and III-V membrane in the subsequent lithography. So we use a scalpel to mechanically remove the ridges after substrate removal. Then the III-V-on-silicon photonic devices can be processed on the III-V membrane.

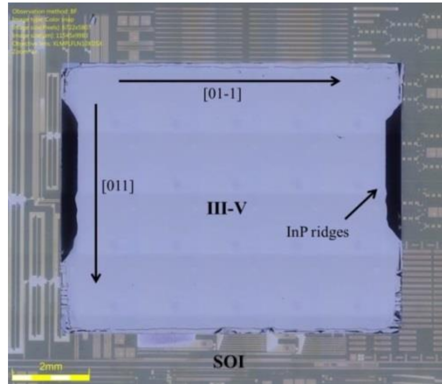

Figure 2.18. Microscope image of a InP-based type-II epitaxial layer stack bonded to a SOI die after substrate removal.

For the III-V-on-silicon photonic devices, the III-V layer should in most cases be brought as close as possible to the silicon waveguide. Adding mesitylene to the DVS-BCB solution can be used to reduce the thickness of the bonding layer. The achievable thickness is determined by amount of mesitylene solvent added. Figure 2.19(a) and 2.19(b) shows the SEM image of the bonding interface of III-V-on-silicon samples using a DVS-BCB: mesitylene dilution of 1:3 and 1:8 (v/v) as the adhesive, respectively, with a spin-coating speed of 3000 rpm. The respective bonding layer thickness is around 120 nm and 50 nm.

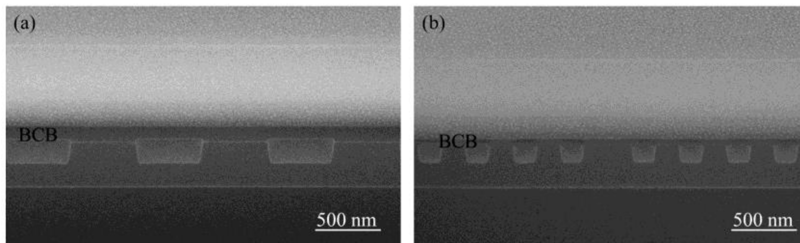

Figure 2.19. Bonding interface between the III-V layer and the silicon device layer with different BCB thickness.

2.5.5 Mesa definition

Before defining III-V mesas on the membrane, the 250 nm thick InGaAs etch stop layer and the 100 nm thick InP sacrificial layer is removed by a H_2SO_4:H_2O_2:H_2O 1:1:18 solution and a 1:1 HCl:H_2O solution, respectively. Then a 200 nm thick SiN_x layer is deposited on the III-V membrane as the hard mask for the following etching processes. After this process, 320 nm UV contact lithography is employed to define III-V mesas of the photonic devices. MIR-701 is used as the photoresist. Because most of III-V-on-silicon photonic devices

shown in this PhD thesis are based on adiabatic coupling between the silicon waveguide and the III-V waveguide, a very narrow III-V taper tip (<0.6 μm, discussed in the third and fourth chapter) is required for an efficient coupling. Therefore, the alignment accuracy of this lithography is quite critical for an efficient optical coupling between the two waveguides. Besides, a clean sample surface and an intimate contact between the mask and sample are required to define the pattern of the very narrow III-V taper tips. After development, the MIR-701 photoresist acts as a soft mask for the etching of the SiN_x in a reactive-ion etching (RIE) tool. Once this dry etching is completed, the remaining photoresist will be removed. Then the 100 nm p^+-InGaAs layer is etched by ICP (using CH_4:H_2 = 30:10 sccm).

The following process is etching of the 1.5 μm thick *p*-InP cladding layer. A wet etching is performed using a 1:1 HCl:H_2O solution. The etch rate is around 110 nm/min. The anisotropic HCl wet etching of InP creates a negative angle etching when the mesa is oriented along the [01-1] direction, which relaxes the lithographic requirements for the taper tip. With a 2.2 μm wide hard mask pattern on this epitaxial stack, the bottom width of the *p*-InP after HCl etching is around 1.15 μm wide, as shown in Figure 2.20. As a result, a 1 μm wide mask pattern can used to create a very narrow III-V tip (<0.6 μm). This process allows relative low-cost device fabrication by using 320 nm UV contact lithography rather than expensive electron beam or deep UV lithography.

Figure 2.21(a) shows a SEM image of the III-V taper after 15 minutes of HCl wet etching. It can be seen that the III-V waveguide closed to the tip is completely etched away and a tip consisting of a InGaAs and SiN_x is hanging over the mesa edge. This etching behavior ensures a very sharp III-V taper tip. However, the suspended strip will fall down and contact with the etch stop layer when the etching time become longer, as shown in Figure 2.21 (b). This result can cause electrical short circuit in the final devices because the InGaAs layer can directly contact with *n*-InP layer after active region etching. Besides, when these structures make contact with silicon waveguides they can introduce extra optical loss. So controlling the etching time is also critical for this process. During this etching, gas bubbles are generated because the reaction between InP and HCl [56]. Some of the bubbles are attached to the sample surface and thereby prevent further etching. Therefore, all of the gas bubbles should be removed from the sample, which can be done by shaking the sample in the HCl solution or occasionally taking the sample out of the solution. During this wet process, the regions close to defects will etch faster than other regions and thereby results in pitting, as shown in Figure 2.21 (d). When the etching reaches the stop layer, the pits will disappear and leave almost flat "marks" for the defects, as shown in Figure 2.21 (e).

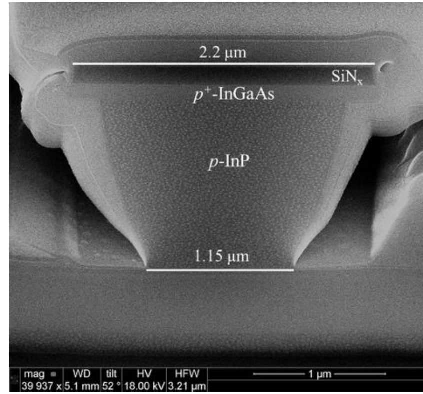

Figure 2.20. *SEM image of the inverted trapezoidal p-InP layer after HCl wet etching.*

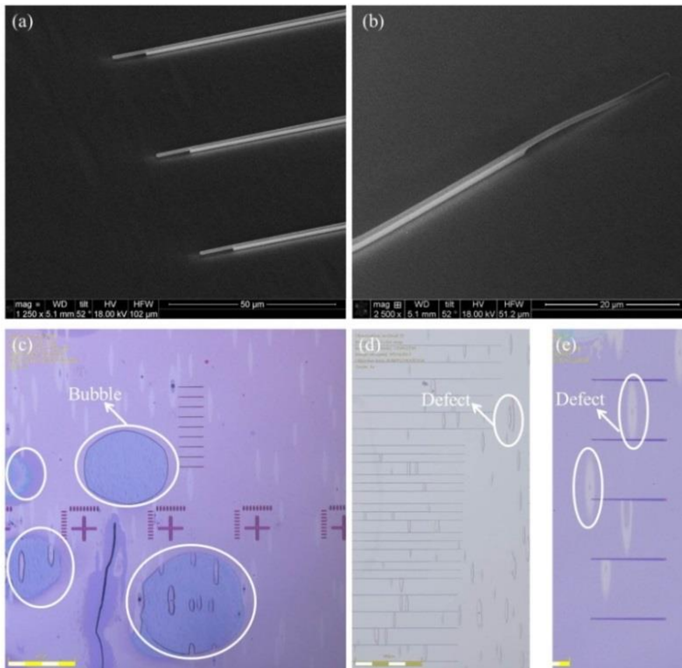

Figure 2.21. *SEM image of (a) tapered III-V waveguides with suspended InGaAs and SiN_x tip, (b) an overetched III-V waveguide structure. (c-e) Microscope image of the sample surface after HCl wet etching.*

2.5.6 Etching of the active region

After wet etching of the *p*-InP cladding layer, a 200 nm thick SiN_x layer is deposited again on the sample. After pattern definition using 320 nm UV contact

lithography, the SiN_x hard mask is etched by RIE. Then a wet etching is carried out to etch the SCH layers and active region, which mainly consist of GaAsSb and AlGaAsSb layers. In the III-V epitaxial layer stack, there is *n*-InP is below the SCH layers and active region. Therefore, a highly selective etching of GaAsSb and AlGaAsSb to InP is required. Previously, there was no report about a recipe for this kind of selective wet etching. Here we developed a recipe, which consists of H_3PO_4: Citric Acid: H_2O_2:H_2O (1:1:20:70, v/v), that provides a selectivity of more than 100. Figure 2.22 shows the etch depth of a 300 nm thick GaAsSb and a 280 nm thick AlGaAsSb layer grown on a InP substrate. The etch rates for both material are around 100 nm/min. However, the etchant almost doesn't attack the InP substrate. So the 1:1:20:70 H_3PO_4: Citric Acid: H_2O_2:H_2O solution is used to etch the SCH layers and active region.

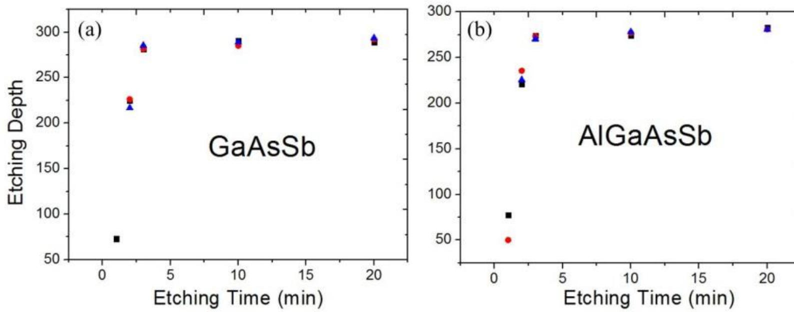

Figure 2.22. *Etch depth of a 300 nm thick GaAsSb layer and a 280 nm thick AlGaAsSb layer grown on a InP substrate. Etching is performed in a H_3PO_4: Citric Acid: H_2O_2:H_2O 1:1:20:70 solution.*

This wet etching is isotropic, so the underetch in the lateral direction is almost equal to the thickness of etched III-V layers. A SEM image of the cross-section of III-V waveguides after this wet etching is shown in Figure 2.23 (a). A 0.5-0.6 μm wide undercut underneath the SiN_x hard mask layer can be seen. Therefore, a wider mask needs to be designed. For example, a 1.5 μm wide mask pattern is designed to fabricate a 0.5 μm wide III-V taper tip. Figure 2.23 (b) shows the microscope image of the III-V taper tip after etching. The suspended tip can be clearly seen in the microscope.

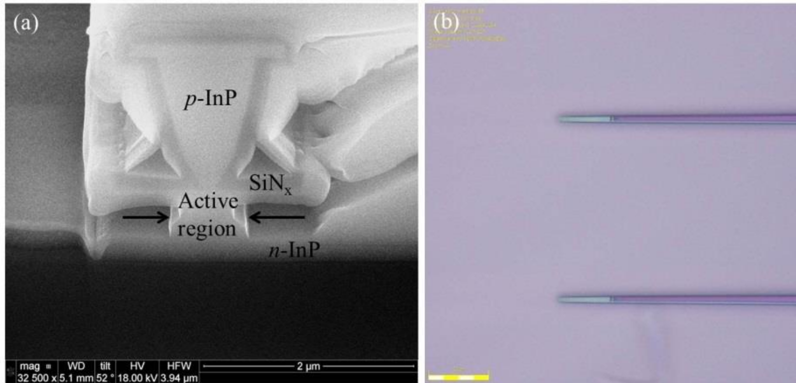

Figure 2.23. (a) SEM image of the cross-section of a III-V waveguide after etching; (b) Microscope image of the III-V taper after active region etching.

2.5.7 N-type contact metallization

In this step, lithography is carried out with a ~ 3 µm thick TI35 resist used as an image reversal photoresist. After photoresist development, the sample is loaded in a RIE tool to clean the residual photoresist for 30 seconds. Then, the sample is dipped in a H_2SO_4:H_2O_2:H_2O 1:1:50 solution for 5-10 seconds to remove the native oxide layer formed on top of the *n*-InP layer. After this process, the sample is immediately loaded in a Leybold Univex thermal evaporation and sputtering system to avoid oxidation of the exposed *n*-InP layer. When the chamber pressure is pumped down to 10^{-5} bar, a 30 nm nickel (Ni) is firstly deposited, followed by a 20 nm thick germanium (Ge) and a 50 nm thick gold (Au) layer. After the metal deposition, the sample is immersed in acetone for around half an hour to lift off the unwanted metal. A microscope image of the sample after this process is shown in Figure 2.24 (a). The metal contact is 5 µm away from the III-V mesa.

In order to measure the specific resistance of the n-contact, a metal/semiconductor structure for transmission line measurement (TLM) is fabricated on the sample [57], as shown in the inset of Figure 2.24 (b). The measured specific contact resistance between the Ni/Ge/Au and n-InP is $6.5\times10^{-5}\Omega.cm^2$. This value is reduced to $4.1\times10^{-7}\Omega.cm^2$ after 400 ℃, 30s annealing. Figure 2.24 (b) shows the current-voltage (I-V) characteristics between two TLM pads before and after annealing. An improved I-V behavior can be observed.

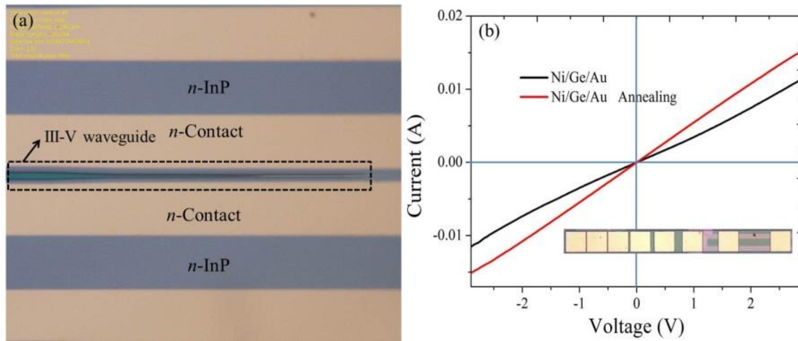

Figure 2.24. *(a) Microscope image of the sample after n-contact metallization; (b) I-V curve of the n-contact before and after annealing.*

2.5.8 Device isolation

After the *n*-contact metallization process, a ~2.5 µm thick AZ5214 photoresist is spin-coated on the sample as a soft mask for the following device isolation process. In this process, the different III-V-on-silicon photonic devices are electrically isolated, i.e. the *n*-InP layer between different devices is etched away. During this wet etching process, the device islands are protected by the covered photoresist while the exposed *n*-InP is completely removed by a 1:1 $HCl:H_2O$ solution. Figure 2.25 shows the microscope image of the sample after 2 minutes of wet etching.

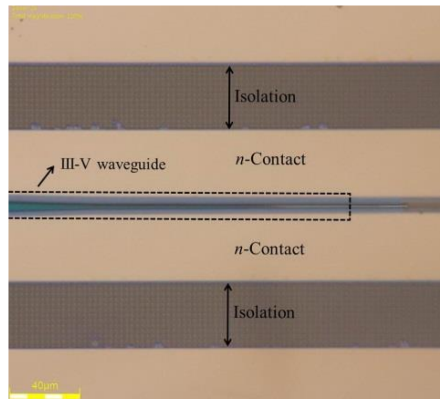

Figure 2.25. *Microscope image of the sample after device isolation.*

2.5.9 Passivation

In order to electrically isolate the *p*-contact on top and the underneath *n*-contact, to reduce the surface recombination velocity of carriers and the dark current of

the III-V-on-silicon photodetectors, a thick layer of DVS-BCB is spin-coated on the sample to passivate the photonic devices after the device isolation process. Here we use a CYCLOTENE 3022-57 DVS-BCB resin, which is the same series of resins as that used in the adhesive DVS-BCB bonding process but can provide much thicker encapsulation under the same spin-coating speed. In our process, the resin is spin-coated at a speed of 3000 rpm, which results in a DVS-BCB layer with thickness of 7.5 μm. Then the sample is baked in an oven at 250 ℃ for 90 minutes. Figure 2.26 shows the microscope image of the sample after this process. This DVS-BCB baking process also slowly anneals the *n*-contact metal, so obvious color and morphology changes can be observed from the microscope.

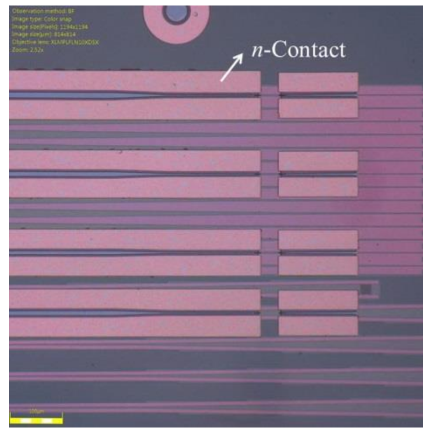

Figure 2.26. *Microscope image of the sample after passivation.*

2.5.10 P-type contact metallization

After passivation, the thick DVS-BCB capsulation layer is etched in a RIE (using SF_6:O_2 = 5:50 sccm) tool until the SiN_x hard mask layer is exposed. Then the ~ 400 nm thick SiN_x layer on top of the p^+-InGaAs is etched in the same tool with another recipe (CF_4:SF_6:H_2=80:3:7 sccm). When the p^+-InGaAs layer is exposed, a 1.8 μm thick AZ5214 photoresist layer is then spin-coated on the sample used as the image reversal photoresist to define the *p*-contact pattern. After photoresist development, the sample is then loaded in the RIE tool to remove the residual photoresist on the area that should be exposed. Afterwards, the sample is dipped in a H_2SO_4:H_2O_2:H_2O 1:1:50 solution for a few seconds to remove the oxidized layer on top of the p^+-InGaAs. Subsequently, the sample is immediately loaded in a Leybold Univex sputtering system. A 40 nm thick Titanium (Ti) layer is firstly sputtered on the sample, followed by thermal evaporation of a 150 nm Au layer. When the contact metallization is finished,

the sample is immersed in acetone for around half an hour to lift off the unwanted Ti/Au layer. A microscope image of the sample after this *p*-contact metallization process is shown in Figure 2.27 (a). The measured specific resistance of the *p*-contact is $2.35\times10^{-4}\Omega.cm^2$. After a thermal annealing (400 ℃, 30s), the I-V behavior of the *p*-contact turns to ohmic and the specific resistance reduce to $5.9\times10^{-5}\Omega.cm^2$. A much improved I-V characteristic of the *p*-contact can be seen in Figure 2.27 (b).

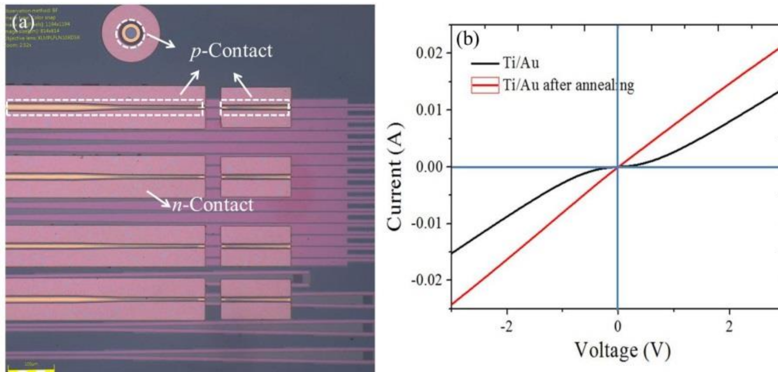

Figure 2.27. *(a) Microscope image of the sample after p-contact metallization; (b) I-V curve of the p-contact before and after annealing.*

2.5.11 Final metallization

After the *p*-contact metallization process, we should open some windows in the DVS-BCB covered *n*-contact for the following final metallization process. In this step, firstly, a layer of 3 μm thick Ti35 photoresist is spin-coated on the sample as a soft mask. After pattern defining and photoresist development, dry etching in a RIE system (using SF_6:O_2 = 5:50 sccm) is used to open the BCB windows. A microscope image after the BCB opening is shown in Figure 2.28. Subsequently, a 3 μm thick Ti35 photoresist layer is spin-coated again on the sample for the final metallization process. Similar to *n*- and *p*-contact metallization processes, the sample is loaded in a RIE tool before metallization, to the clean the potential residual photoresist and thereby reduce the risk of the following photoresist lift-off process. In the metallization process, a 40 nm thick Ni layer is firstly sputtered on the sample followed by a 1 μm thick of gold layer. This very thick gold layer is used to ensure a solid metallic pad for electrical probing. A microscope image of the final III-V-on-silicon photonic chip is shown in Figure 2.29. For the III-V-on-silicon lasers, a common *p*-contact pad is used, which also acts as a heat-spreader for the lasers.

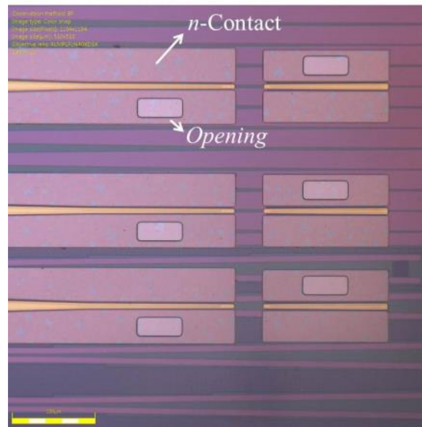

Figure 2.28. *Windows of DVS-BCB covered n-contacts are opened before the final metallization process.*

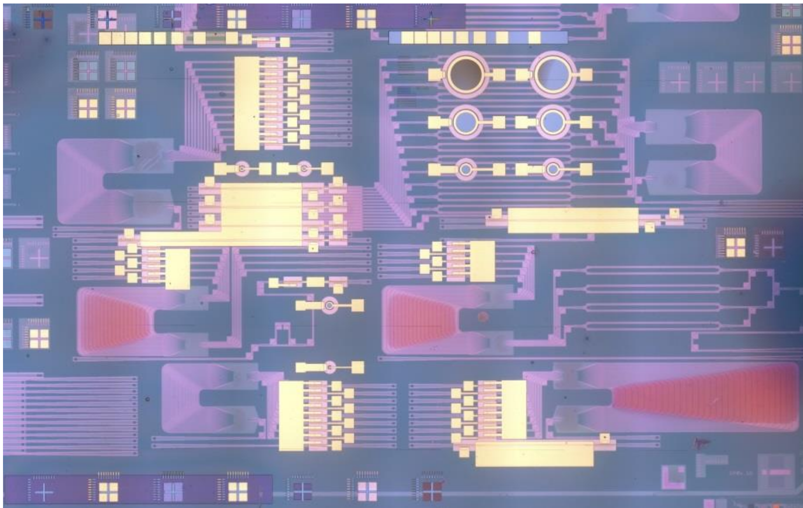

Figure 2.29. *Microscope image of the final III-V-on-silicon photonic IC.*

2.5.12 Wire bonding

For a complete opto-electronic system, the photonic IC should connect with electronic components such as trans-impedance amplifiers (TIA). Therefore, the III-V-on-silicon photonic chip is wire bonded to a printed circuit board (PCB) after the device fabrication process. Before wire bonding, the III-V-on-silicon chip is firstly mounted to a PCB using an electrically conductive epoxy (Epotek

2). During the bonding process, a gold wire is firstly bonded down to the probe pads in the photonic chip. Then the second bond is formed on the PCB. Wedge-wedge bonding is used. In our photonic chips, the probe pads are deposited on top of DVS-BCB layer. But the adhesion between the DVS-BCB layer and the metal layer is not sufficient for the wire bonding process. In order to reduce the risk of damaging a probe pad, a 1 μm thick DVS-BCB is spin-coated on the sample and fully cured. Then a BCB window with a size smaller than the metal pad is opened for wire bonding. A microscope image of a III-V-on-silicon photonic chip wire bonded to a PCB is shown in Figure 2.30.

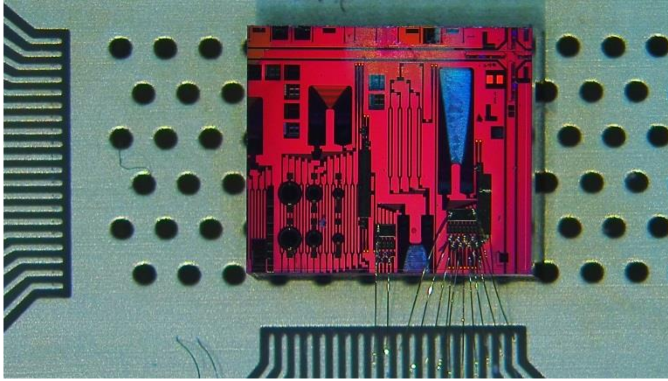

Figure 2.30. *Half of the sample shown in Figure.2.29 is wire bonded to a PCB.*

2.6 Conclusion

In this chapter, we firstly introduced two bonding approaches for heterogeneous integration of III-V materials on silicon. Then two different coupling methods between III-V waveguides and silicon waveguides in the III-V-on-silicon photonic devices are summarized. In our studies, we adopted the adhesive bonding technology and adiabatic coupling method to develop a 2 μm-wavelength-range III-V-on-silicon photonic platform. InP-based type-I, type-II and GaSb-based type-I heterostructures can be used as the active region of 2 μm wavelength range photonic devices. Compared with the GaSb-based material system, the heterogeneous integration processes of InP-based material on silicon are better established, which ensures a higher device yield. Compared with InP-based type-I quantum wells, the lasing wavelength coverage of diode laser based on the InP-based type-II material system is much broader in the 2 μm wavelength range. Therefore, InP-based type-II heterostructures are used to realize our fully integrated III-V-on-silicon photonic system. Towards this goal, we design a InP-based type-II epitaxial layer stack for III-V-on-silicon laser

sources in the 2.3 μm range. In the last section, the process developments for the 2 μm-wavelength-range III-V-on-silicon photonic platform are summarized. The efforts on improving the photonic device performance by optimizing the processes are also presented.

References

[1] H. Rong, “A continuous-wave Raman silicon laser,” Nature **433**, 725–728 (2005).

[2] W. W. Chow and S. W. Koch, Semiconductor-Laser Fundamentals: Physics of the Gain Materials (Springer, 1999).

[3] G. Roelkens, L. Liu, D. Liang, R. Jones, A. Fang, B. Koch, and J. Bowers, “III-V/silicon photonics for on-chip and intera-chip optical interconnects,” Laser Photon. Rev. **4**(6), 751–779 (2010).

[4] A. Gassenq, N. Hattasan, L. Cerutti, J. B. Rodriguez, E. Tournié, G. Roelkens, and G. Roelkens, “Study of evanescently-coupled and grating-assisted GaInAsSb photodiodes integrated on a silicon photonic chip,” Opt. Express **20**(11), 11665–11672 (2012).

[5] G. Roelkens, J. Brouckaert, D. Van Thourhout, R. Baets, R. Nötzel, and M. Smit, “Adhesive bonding of InP/InGaAsP dies to processed Silicon-On-Insulator wafers using DVS-Bis-Benzocyclobutene,” J. Electrochem. Soc. **153**(12), G1015–G1019 (2006).

[6] S. Stankovicić, R. Jones, J. Heck, M. Sysak, D. Van Thourhout, and G. Roelkens, “Die-to-die adhesive bonding procedure for evanescently-coupled photonic devices,” Electrochem. Solid-State Lett. **14**, H326 (2011).

[7] S. Keyvaninia, M. Muneeb, S. Stanković, P. J. Van Veldhoven, D. Van Thourhout, and G. Roelkens, “Ultra-thin DVS-BCB adhesive bonding of III-V wafers, dies and multiple dies to a patterned silicon-on-insulator substrate,” Opt. Mater. Express **3**(1), 35–46 (2013).

[8] A. W. Fang, H. Park, O. Cohen, R. Jones, M. J. Paniccia, and J. E. Bowers “Electrically pumped hybrid AlGaInAs-silicon evanescent laser,” Opt. Express **14**, 9203–9210, (2006).

[9] H. Park, A. W. Fang, R. Jones, O. Cohen, M. J. Paniccia, and J. E. Bowers, “A hybrid AlGaInAs-silicon evanescent waveguide photodetector,” Opt. Express **15**, 6044–6052 (2007).

[10] S. Stanković, R. Jones, M. Sysak, J. Heck, G. Roelkens, and D. Van Thourhout, “1310 nm hybrid III-V/Si Fabry-Perot laser based on adhesive bonding,” IEEE Photon. Technol. Lett. **23**(23), 1781–1783 (2011).

[11] S. Keyvaninia, G. Roelkens, D. Van Thourhout, C. Jany, M. Lamponi, A. Le Liepvre, F. Lelarge, D. Make, G.-H. Duan, D. Bordel, and J.-M. Fedeli, “Demonstration of a heterogeneously integrated III-V/SOI single wavelength tunable laser,” Opt. Express **21**(3), 3784–3792 (2013).

[12] M. Lamponi, S. Keyvaninia, C. Jany, F. Poingt, F. Lelarge, G. de Valicourt, G. Roelkens, D. Van Thourhout, S. Messaoudene, J.-M. Fedeli, and G. H. Duan, “Low-threshold heterogeneously integrated InP/SOI lasers with a double adiabatic taper coupler,” IEEE Photon. Technol. Lett. **24**(1), 76–78 (2012).

[13] S. Keyvaninia, S. Verstuyft, S. Pathak, F. Lelarge, G.-H. Duan, D. Bordel, J.-M. Fedeli, T. De Vries, B. Smalbrugge, E. J. Geluk, J. Bolk, M. Smit, G. Roelkens, and D. Van Thourhout, “III-V-on-silicon multi-frequency lasers,” Opt. Express **21**(11), 13675–13683 (2013).

[14] S. Keyvaninia, S. Verstuyft, L. Van Landschoot, F. Lelarge, G.-H. Duan, S. Messaoudene, J. M. Fedeli, T. De Vries, B. Smalbrugge, E. J. Geluk, J. Bolk, M. Smit, G. Morthier, D. Van Thourhout, and G. Roelkens, “Heterogeneously integrated III-V/silicon distributed feedback lasers,” Opt. Lett. **38**(24), 5434–5437 (2013).

[15] S. Keyvaninia, S. Uvin, M. Tassaert, Z. Wang, X. Fu, S. Latkowski, J. Mariën, L. Thomassen, F. Lelarge, G. Duan, G. Lepage, P. Verheyen, J. Van Campenhout, E. Bente, and G. Roelkens, “III–V-on-silicon anti-colliding pulse-type mode-locked laser,” Opt. Lett. **40**, 3057–3060 (2015).

[16] Joost Brouckaert. Integration of Photodetectors on Silicon Photonic Integrated Circuits (PICs) for Spectroscopic Applications. PhD thesis, Gent University, 2010.

[17] M. Muneeb, A. Vasiliev, A. Ruocco, A. Malik, H. Chen, M. Nedeljkovic, J. S. Penades, L. Cerutti, J. B. Rodriguez, G. Z. Mashanovich, M. K. Smit, E. Tourni, and G. Roelkens, “III-V-on-silicon integrated micro-spectrometer for the 3 µm wavelength range,” Opt. Express **24** (9), 9465-9472 (2016).

[18] A. Abbasi, B. Moeneclaey, J. Verbist, X. Yin, J. Bauwelinck, G. - H. Duan, G. Roelkens, and G. Morthier, “Direct and electro - absorption modulation of a III-V-on-silicon DFB laser at 56 Gbps,” IEEE J. Sel. Top. Quantum Electron. **23**(6), 1501307 (2017).

[19] J. C. Hulme, J. K. Doylend, and J. E. Bowers, “Widely tunable Vernier ring laser on hybrid silicon,” Opt. Express **21**(17), 19718–19722 (2013).

[20] S. Dhoore, L. Li, A. Abbasi, G. Roelkens, and G. Morthier, “Demonstration of a discretely tunable III-V-on-silicon sampled grating DFB laser,” IEEE Photonics Technol. Lett. **28**(21), 2343–2346 (2016).

[21] S. Dhoore, G. Roelkens, G. Morthier, “III-V-on-silicon three-section DBR laser with over 12 nm continuous tuning range,” Opt. Lett. **42**(6), 1121-1124 (2017).

[22] H. Park, A. W. Fang, O. Cohen, R. Jones, M. J. Paniccia, and J. E. Bowers, “An electrically pumped AlGaInAs-Silicon Evanescent Amplifier,” IEEE Photon. Technol. Lett. **19**, 230–232 (2007).

[23] S. Keyvaninia, G. Roelkens, D. Van Thourhout, G. H. Duan, M. Lamponi, F. Lelarge, J.-M. Fedeli, S. Messaoudene, E. J. Geluk, and B. Smalbrugge, “A highly efficient electrically pumped optical amplifier integrated on a SOI waveguide circuit,” in Proceedings of IEEE Group IV Photonics Conference (San Diego, United Sates, 2012), 222–224.

[24] P. Kaspar, G. De Valicourt, R. Brenot, M. A. Mestre, P. Jennevé, A. Accard, D. Make, F. Lelarge, G. Duan, N. Pavarelli, M. Rensing, C. Eason, P. O. Brien, S. Olivier, S. Malhouitre, C. Kopp, C. Jany, and S. Menezo, “Hybrid III–V/ Silicon SOA in Optical Network Based on Advanced Modulation Formats,” IEEE Photon. Technol. Lett. **27**(22), 2382-2386 (2015).

[25] G. T. Reed, G. Mashanovich, F. Y. Gardes, and D. J. Thomson, “Silicon optical modulators,” Nat. Photonics **4**(8), 518–526 (2010).

[26] J. Michel, J. Liu, and L. C. Kimerling, “High-performance Ge-on-Si photodetectors,” Nature Photonics **4**, 527–534 (2010).

[27] G. Roelkens, J. Brouckaert, D. Taillaert, P. Dumon, W. Bogaerts, D. Van Thourhout, R. Baets, R. Nötzel, and M. Smit, “Integration of InP/InGaAsP photodetectors onto silicon-on-insulator waveguide circuits,” Opt. Express **13**, 10102–10108 (2005).

[28] H. Park, Y.-H. Kuo, A. W. Fang, R. Jones, O. Cohen, M. J. Pannicia, and J. E. Bowers, “A hybrid AlGaInAs-silicon evanescent preamplifier and photodetector,” Opt. Express **15**, No. 21, (2007).

[29] Y. Tang, H.-W. Chen, S. Jain, J. D. Peters, U. Westergren, and J. E. Bowers, “50 Gb/s hybrid silicon traveling-wave electroabsorption modulator,” Opt. Express **19**(7), 5811–5816 (2011).

[30] X. Fu, J. Cheng, Q. Huang, Y. Hu, W. Xie, M. Tassaert, J. Verbist, K. Ma, J. Zhang, K. Chen, C. Zhang, Y. Shi, J. Bauwelinck, G. Roelkens, L. Liu, and S. He, “5 × 20 Gb/s heterogeneously integrated III–V on silicon electro-absorption modulator array with arrayed waveguide grating multiplexer,” Opt. Express **23**, 18686–18693 (2015).

[31] C. Zhang, S. Zhang, J. D. Peters, and J. E. Bowers, “8 × 8 × 40 Gbps fully integrated silicon photonic network on chip,” Optica **3**(7), 785–786 (2016).

[32] N. Hattasan, A. Gassenq, L. Cerutti, J. B. Rodriguez, E. Tournié, and G. Roelkens, “Heterogeneous integration of GaInAsSb p-i-n photodiodes on a

silicon-on-insulator waveguide circuit," IEEE Photon. Technol. Lett. **23**(23), 1760–1762 (2011).

[33] A. Spott, M. Davenport, J. Peters, J. Bovington, M. J. R. Heck, E. J. Stanton, I. Vurgaftman, J. Meyer, and J. Bowers, "Heterogeneously integrated 2.0 μm CW hybrid silicon lasers at room temperature," Opt. Lett. **40**(7), 1480–1483 (2015).

[34] A. Spott, J. Peters, M. L. Davenport, E. J. Stanton, C. D. Merritt, W. W. Bewley, I. Vurgaftman, C. S. Kim, J. R. Meyer, J. Kirch, L. J. Mawst, D. Botez, and J. E. Bowers, "Quantum cascade laser on silicon," Optica **3**(5), 545–551 (2016).

[35] A. Spott, J. Peters, M. L. Davenport, E. J. Stanton, C. Zhang, C. D. Merritt, W. W. Bewley, I. Vurgaftman, C. S. Kim, J. R. Meyer, J. Kirch, L. J. Mawst, D. Botez, and J. E. Bowers, "Heterogeneously Integrated Distributed Feedback Quantum Cascade Lasers on Silicon," Photonics **3**(2), 35 (2016).

[36] A. Spott, M. Davenport, J. Peters, J. Bovington, M. J. R. Heck, E. J. Stanton, I. Vurgaftman, J. Meyer, and J. Bowers, "Heterogeneously integrated 2.0 μm CW hybrid silicon lasers at room temperature," Opt. Lett. **40**(7), 1480–1483 (2015).

[37] G. Boehm, M. Grau, O. Dier, K. Windhorn, E. Roenneberg, J. Rosskopf, R. Shau, R. Meyer, M. Ortsiefer, and M. C. Amann, "Growth of InAs- containing quantum wells for InP-based VCSELs emitting at 2.3 μm," J. Cryst. Growth 301–302, 941–944 (2007).

[38] C. Caneau, A. K. Srivastava, A. G. Dentai, J. L. Zyskind, and M. A Pollack, "Room-temperature GaInAsSb/AlGaAsSb DH injection lasers at 2.2 μm,"Electron. Lett. **21**, 815 (1985).

[39] A.É. Bochkarev, L. M. Dolginov, A. E. Drakin, L. V. Druzhinina, P. G. Eliseev and B. N. Sverdlov, "Injection InGaSbAs lasers emitting radiation of wavelengths 1.9–2.3μ at room temperature," Sov. J. Quantum Electron. **15**, 869 (1985).

[40] L. Shterengas, G. Belenky, M. V. Kisin, and D. Donetsky, "High power 2.4 μm heavily strained type-I quantum well GaSb-based diode lasers with more than 1 W of continuous wave output power and a maximum power-conversion efficiency of 17.5%," Appl. Phys. Lett. **90**(1), 011119 (2007).

[41] S. Forouhar, R. M. Briggs, C. Frez, K. J. Franz, and A. Ksendzov, "High-power laterally coupled distributed-feedback GaSb-based diode lasers at 2 μm wavelength," Appl. Phys. Lett. **100**(3), 031107 (2012).

[42] T. Lehnhardt, M. Hümmer, K. Rößner, M. Müller, S. Höfling, and A. Forchel, “Continuous wave single mode operation of GaInAsSb/GaSb quantum well lasers emitting beyond 3µm,” Appl. Phys. Lett. **92**(18), 183508 (2008).

[43] A. Bauer, K. Rner, T. Lehnhardt, M. Kamp, S. Hfling, L. Worschech, and A. Forchel, “Mid-infrared semiconductor heterostructure lasers for gas sensing applications,” Semicond. Sci. Technol. **26**(1), 4032 (2011).

[44] K. Vizbaras, A. Vizbaras, A. Andrejew, C. Grasse, S. Sprengel, and M.-C. Amann, “Room-temperature type-I GaSb-based lasers in the 3.0 - 3.7 µm wavelength range,” Proc. SPIE 8277, 82771B, 82771B-7 (2012).

[45] Nannicha Hattasan. GaSb/Silicon-on-Insulator Heterogeneous Photonic Integrated Circuits for the Short-Wave Infrared. PhD thesis, Gent University, 2014.

[46] M. Peter, R. Kiefer, F. Fuchs, N. Herres, K.-H. Bachem, and J. Wagner, “Light-emitting diodes and laser diodes based on a $Ga_{1-x}In_xAs/GaAs_{1-y}Sb_y$ type II superlattice on InP substrate,” Appl. Phys. Lett. **74**, 1951 (1999).

[47] S. Sprengel, A. Andrejew, K. Vizbaras, T. Gruendl, K. Geiger, G. Boehm, C. Grasse, and M.-C. Amann, “Type-II InP-based lasers emitting at 2.55 µm,” Appl. Phys. Lett. **100**(4), 041109 (2012).

[48] S. Sprengel, G. Veerabathran, A. Andrejew, A. Köninger, G. Boehm, C. Grasse, and M. C. Amann, “InP-based type-II heterostructure lasers for wavelengths up to 2.7 µm,” in SPIE Photonics West, Novel In-Plane Semiconductor Lasers XIV (SPIE, 2015), paper 9382–29.

[49] S. Sprengel, C. Grasse, K. Vizbaras, T. Gruendel, and M.-C. Amann, “Up to 3 µ m light emission on InP substrate using GaInAs/GaAsSb type-II quantum wells,” Appl. Phys. Lett. **99**, 221109 (2011).

[50] S. Sprengel, C. Grasse, P. Wiecha, A. Andrejew, T. Gruendl, G. Boehm, R. Meyer, and M. C. Amann, “InP-Based Type-II Quantum-Well Lasers and LEDs,” IEEE J. Sel. Top. Quantum Electron. **19**(4), 1900909–1900917 (2013).

[51] J. Y. T. Huang, L. J. Mawst, T. F. Kuech, X. Song, S. E. Babcock, C. S. Kim, I. Vurgaftman, J. R. Meyer, and A. L. Holmes, Jr., “Design and characterization of strained InGaAs/GaAsSb type-II 'W' quantum wells on InP substrates for mid-IR emission,” J. Phys. D: Appl. Phys. **42**, 025108 (2009).

[52] S. Stephan, D. Frederic, and M.-C. Amann, “Novel InP- and GaSb-based light sources for the near to far infrared,” Semicond. Sci. Technol. **31**, 113005 (2016).

[53] C. Grasse, P. Wiecha, T. Gruendl, S. Sprengel, R. Meyer, and M.-C. Amann, “InP-based 2.8–3.5 µm resonant-cavity light emitting diodes based on

type-II transitions in GaInAs/GaAsSb heterostructures," Appl. Phys. Lett. **101**(22), 221107 (2012).

[54] S. Sprengel, A. Andrejew, F. Federer, G. K. Veerabathran, G. Boehm, and M.-C. Amann, "Continuous wave vertical cavity surface emitting lasers at 2.5 μm with InP-based type-II quantum wells," Appl. Phys. Lett. **106**(15), 151102 (2015).

[55] http://www.europractice-ic.com.

[56] P. H. L. Notten, "The Etching of InP in HCl Solutions: A Chemical Mechanism," J. Electrochem. Soc. **131**, 2641–2644 (1984).

[57] W.M. Loh, S.E. Swirhun, T.A. Schreyer, "Modeling and measurement of contact resistances," IEEE Trans. Electron Devices **34**, 512(1987).

3

III-V-on-silicon 2-µm-range photodetectors and spectrometers

3.1 Introduction

As we briefly discussed in the first chapter, a fully integrated on-chip spectroscopic sensing system requires a spectrometer or single pixel detector integrated on chip. Each channel of the spectrometer should connect with a photodetector to convert the optical power to electrical current for signal processing and data analysis. In this chapter, we will study heterogeneously integrated III-V-on-silicon photodetectors and spectrometers for the 2 μm-wavelength range. Firstly, I will introduce the state of the art of 2 μm range semiconductor photodetectors. By analyzing the existing photodetectors based on different material systems and structures, we find the direction to take for the integration of 2 μm range photodetectors on silicon. Then, heterogeneously integrated InP-based type-II quantum well photodetectors on silicon with two different coupling approaches are presented. Afterwards, 2 μm range silicon-on-insulator (SOI) arrayed waveguide grating (AWG) spectrometers with different resolutions are shown. Then the performance of the III-V-on-silicon micro-spectrometers by integrating the AWG spectrometers with the III-V photodetectors are presented. In the end, we will present the results of AWG spectrometers integrated with an InP-based type-II light emitting diode (LED).

3.2 III-V photodetectors in the 2 μm wavelength range

Infrared detectors generally fall into two main categories: thermal detectors and photon detectors [1]. Both convert the absorbed photons to an electrical signal, but the conversion mechanisms are different. In thermal detectors, the absorbed infrared radiation increases the temperature of the device, which is converted to an electrical signal by some temperature related physical mechanism, e.g., the pyroelectric effect and thermoelectric effect. In photon detectors, the semiconductor heterostructure converts the absorbed light to electron-hole pairs, resulting in a current in an external circuit. Thermal detectors are usually low cost, but have lower responsivity / detectivity and are slower than semiconductor photon detectors. In order to realize a high-performance lab-on-a-chip spectroscopic system, we choose to integrate semiconductor photodetectors on silicon to convert the optical signal.

Different semiconductor material systems have been developed to realize photodetectors with high performance, such as III-V compounds, II-VI compounds and group IV material. Among these materials, III-V compound semiconductors show excellent laser gain, which enables co-integration of laser sources and photodetectors on a silicon photonic IC using one semiconductor epitaxial layer stack. Therefore, current heterogeneous integration efforts of

active photonic devices on silicon are mostly based on III-V compounds. In the 2 μm wavelength range, III-V photodetectors based on strained InGaAs, InGaAsSb and InP-based type-II quantum wells have shown high detectivity.

Lattice matched InGaAs grown on InP substrate has proven to be a suitable detector material for the 1.0-1.7 μm spectral range. Using $In_{0.53}Ga_{0.47}As$ as the absorber, detectors with cutoff wavelength of around 1.7 μm and a detectivity of 1.5×10^{13} $cmHz^{1/2}W^{-1}$ at room temperature have been realized [2]. In order to extend the detection wavelength to the 2 μm range, highly strained $In_xGa_{1-x}As$ (x>0.53) can be used [3-5]. However, the cutoff wavelength of the detectors based on this material system is limited to around 2.6 μm while the detectivity significantly degrades as the wavelength become longer as shown in Figure 3.1. Besides, the emission wavelength of the strained InGaAs quantum wells is limited to around 2.3 μm [6], which make it difficult to co-integrate InP-based type-I laser sources and photodetectors on silicon photonic ICs beyond 2.3 μm.

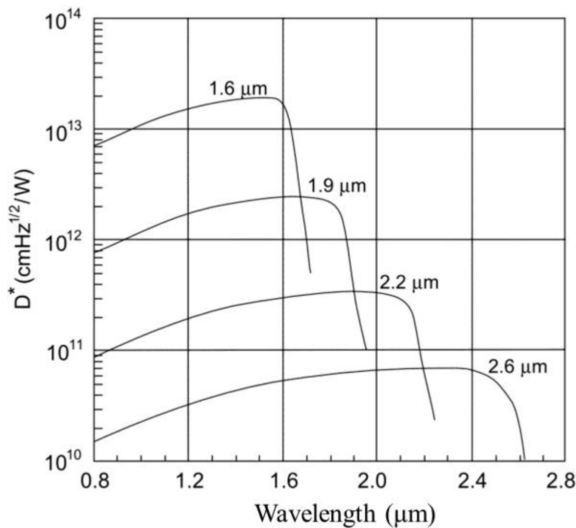

Figure 3.1. *Room temperature detectivity of InP-based InGaAs photodetectors with different cutoff wavelengths [1].*

The quaternary alloy InGaAsSb is a very promising candidate for the development of photodetectors in the 2 μm wavelength range. Its bandgap wavelength can cover 1.7-4.3 μm wavelength when lattice matched to a GaSb substrate [7]. N. Hattasan *et al.* reported the first 2 μm range heterogeneous III-V-on-silicon photodetector by integrating InGaAsSb material on an SOI waveguide [8]. Figure 3.2. (a) and (b) shows the photoresponse measured at different fiber-coupled powers. A peak responsivity of 0.44 A/W at 2.29 μm and a dark current of 1.13 μA at -0.1 V at room temperature are achieved. In the

device, light is coupled from the SOI waveguide to the InGaAsSb absorbing layer using evanescent coupling. With a substantial improvement from A. Gassenq *et al.*, the responsivity of evanescently coupled InGaAsSb photodetectors was improved to 1.4 A/W [9], but the dark current was not reduced in the optimized device. As we discussed in the previous chapter, the heterogeneous integration technology of GaSb is by far less established than InP, which results in a lower device yield. Therefore, we aim for an absorbing III-V material that can combine the advantage of InP processing yield and GaSb-based type-I heterostructures in detection wavelength.

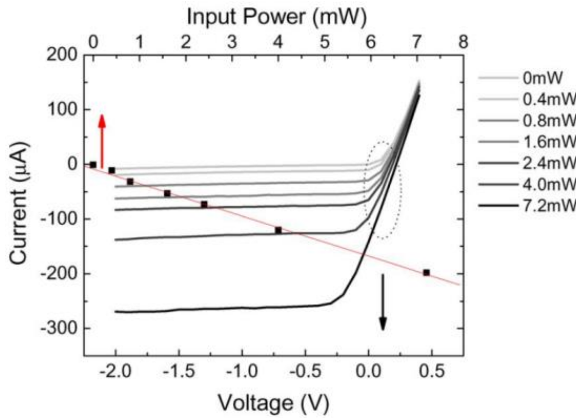

Figure 3.2. *I-V curve of the evanescently coupled InGaAsSb photodetectors under different input power at 2.29 μm. (■)Photocurrent measured at -0.1 V [8].*

InGaAs/GaAsSb type-II quantum well structures can be lattice-matched to an InP substrate, which enables mature fabrication processes. Besides, photoluminescence up to 3.9 μm wavelength and LEDs operating up to 3.3 μm wavelength were reported based on this type-II heterostructure [10, 11]. These results suggest this material system is very suitable for photodetectors in the 2-3 μm wavelength range. R. Sidhu *et al.* initially reported an InP-based type-II photodetector using 150 pairs of $In_{0.53}Ga_{0.47}As$ /$GaAs_{0.51}Sb_{0.49}$ as the absorbing layer, which exhibits a cut-off wavelength of 2.39 μm and a peak room-temperature external quantum efficiency of 43% at 2.23 μm [12]. From modeling, it is found that a response at longer wavelength can be achieved by compressively straining GaAsSb and applying tensile strain in the InGaAs [13]. Based on this method, B. Chen et al. demonstrate a photodetector using 100 pairs of 7-nm $In_{0.34}Ga_{0.66}As$/5-nm $GaAs_{0.25}Sb_{0.75}$ quantum wells strain compensated to InP as the absorber [14, 15]. The device shows a photoresponse up to 3.4 μm, a responsivity of 0.03 A/W at 3 μm and dark current density of 9.6 mA/cm^2 under -0.5 V reverse bias as shown in Figure 3.3. In our work, we

would like to co-integrate laser sources and photodetectors on the silicon using one epitaxial layer stack. However, the spatially indirect transition makes that the gain of type-II quantum wells is lower than that of type-I heterostructures. Therefore, a "W"-shaped InGaAs/GaAsSb active region with optimized gain properties for lasers is used as the absorbing layer in our heterogeneously integrated photodetectors.

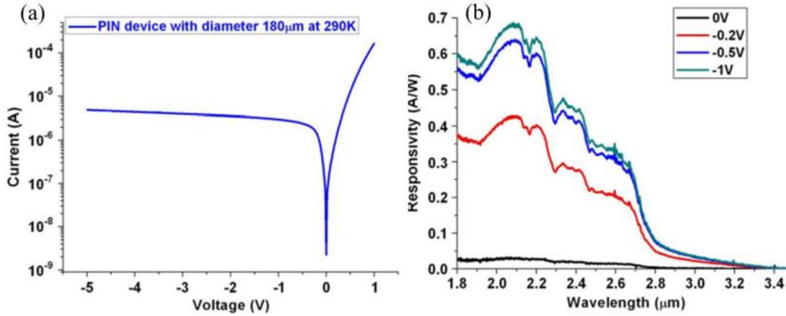

Figure 3.3. *(a) I-V curve of a normal-incidence InP-based type-II photodetector in dark. (b) Responsivity of the device under different reverse voltage [14].*

For a heterogeneously integrated III-V photodetector on SOI waveguide circuit, how to achieve an efficient coupling between the active region and silicon waveguide is one of the key problems in device design. In the following two sections, I will present InP-based type-II photodetectors integrated on silicon with two different coupling methods. The first design is based on adiabatic coupling, in which the light is coupled from the silicon waveguide to the active region by a tapered III-V waveguide with a narrow taper tip. The second one uses a diffraction grating to couple light upwards from the silicon waveguide to the absorbing active region.

3.3 Adiabatically-coupled photodetectors

3.3.1 Device design

Figure 3.4 (a) and 3.4 (b) shows the schematic cross section and top view of the adiabatically-coupled InP-based type-II quantum well photodetector integrated on a SOI waveguide, respectively [16]. The III-V layer stack is bonded to a SOI waveguide circuit using a 100 nm thick DVS-BCB bonding layer. The III-V mesa is a 150 μm long waveguide, tapered from 1 μm width to 3.5 μm (measured at the top of the mesa). The silicon waveguide underneath is a 400 nm thick tapered (from 6 μm to 3 μm width) rib waveguide etched 180 nm deep.

The absorbing active region consists of six periods of a "W"-shaped quantum well structure, each separated by 9 nm tensile strained GaAsSb. Every quantum well contains two 2.6 nm InGaAs layers (with a confined electron energy level) and one 2.9 nm GaAsSb layer (with a confined hole energy level). Detailed information about the epitaxial layer stack can be found in section 2.4.2.

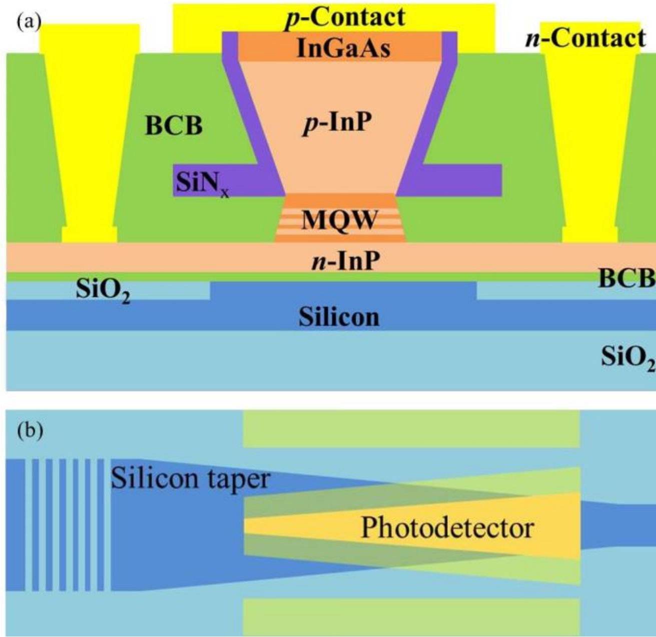

Figure 3.4. *Schematic drawing of the cross section (a) and top view (b) of the adiabatically-coupled type-II quantum well photodetector heterogeneously integrated on a SOI waveguide circuit.*

In order to efficiently couple light from the silicon waveguide to the photodetector, a tapered III-V waveguide with a narrow taper tip is designed for adiabatic coupling between the two waveguides. Commercial software (FIMMWAVE) is used for optical device design. The simulated structure is shown in Figure 3.5. The TE polarized fundamental mode is used (2.35 μm wavelength) in the simulation. As shown in mode profiles – for a 300nm wide taper tip and 2.5 μm III-V taper end width- the light is confined in the 6 μm wide silicon waveguide in the beginning of the III-V/silicon spot size converter (SSC) and completely couples to the III-V waveguide at the end of the SSC.

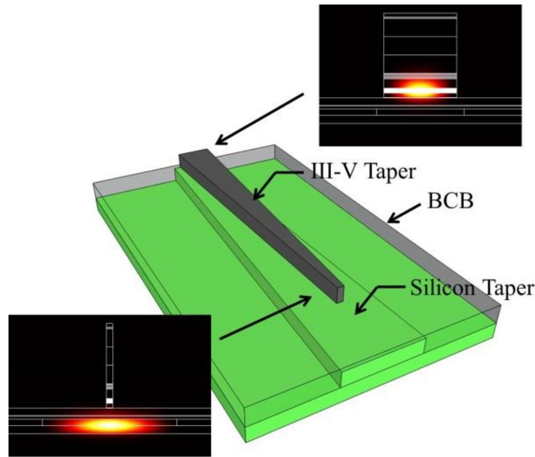

Figure 3.5. *Schematic of the simulated structure with mode profiles of two cross-sections.*

The coupling efficiency of the taper structure is studied for three different taper tip widths: 0.1 μm, 0.3 μm and 0.5 μm, as shown in Figure 3.6. It can be found that a good coupling can be achieved using a 0.5 μm tip width or less.

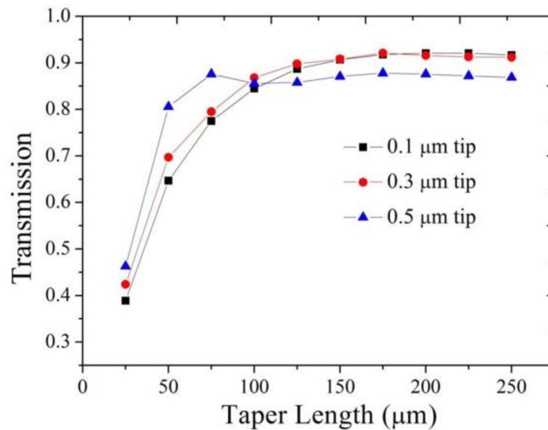

Figure 3.6. *Mode-to-mode coupling efficiency as a function of taper tip width.*

Figure 3.7 (a) shows the optical field intensity distribution in a longitudinal cross section of the designed taper structure. It can be seen that the light gradually couples to the III-V waveguide when the photodetector mesa becomes wider. The typical absorption coefficient of InGaAs/GaAsSb type-II quantum wells in the wavelength range of interest is between 1000 cm^{-1} to 3000 cm^{-1}, as

obtained from theoretical calculations and experimental data [16,17], so 150 μm long devices are designed as a compromise between responsivity and dark current. The intensity distribution for the same structure as in Figure 3.7 (a) when the absorption in the multi-quantum well structure is taken into account is plotted in Figure 3.7 (b). More than 95% of the light at 2.35 μm wavelength is absorbed in the 150 μm long III-V waveguide using an absorption coefficient of 1000 cm^{-1}.

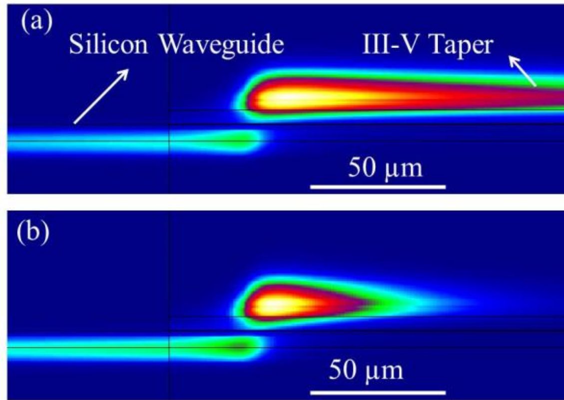

Figure 3.7. *(a) Intensity distribution in a longitudinal cross section of the designed taper structure, without considering the active region absorption; (b) Intensity distribution in the designed taper structure taking the active region absorption into account (1000cm^{-1} quantum well absorption coefficient).*

3.3.2 Device Fabrication

The fabrication of adiabatically-coupled type-II quantum well photodetectors is carried out in the heterogeneous III-V-on-silicon platform, which is described in detail in the second chapter. The III-V epitaxial stack is bonded onto the processed SOI by adhesive bonding using a 100 nm thick DVS-BCB bonding layer. Anisotropic HCl wet etching of InP is used to create a sharp III-V taper tip for efficient optical coupling. Figure 3.8 (a) and 3.8 (b) shows a microscope image of the fabricated device and a scanning electron microscope (SEM) image of the device cross section, respectively. A combination of SiN_x and DVS-BCB is used for the passivation of the photodetector.

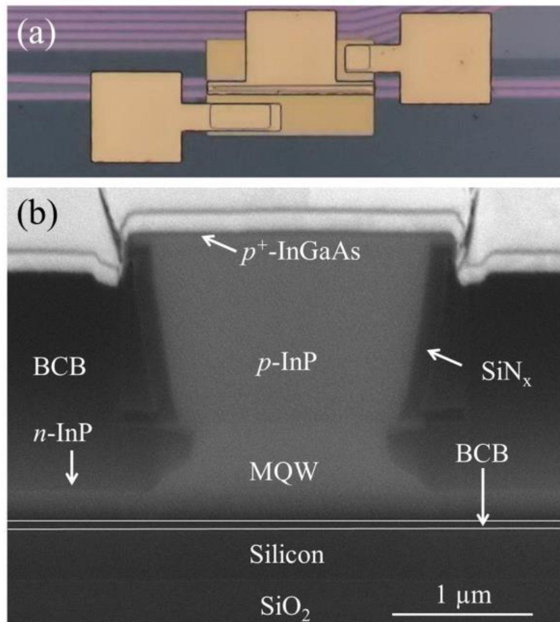

Figure 3.8. *(a) Microscope image of the heterogeneously integrated type-II quantum well photodetector; (b) SEM image of the cross section of the fabricated devices.*

3.3.3 Characterization

The electrical and optical measurements are carried out at room temperature. A Keithley 2400 voltage source is used to apply a bias voltage to the photodetectors during the electrical measurements. In the optical measurements, TE-polarized light from a short-wave infrared (SWIR) tunable laser (IPG Cr:ZnSe solid state laser) is coupled to a standard single mode fiber (SMF-28), which is connected to a 99/1% splitter. The 1% port is connected to an optical spectrum analyzer (Yokogawa AQ6375), which can be used as a power and wavelength reference. 99% of the input power is coupled to a grating coupler to illuminate the silicon waveguide circuit. A 20 μm×20 μm grating coupler with a period of 1 μm is used to couple TE polarized light from fiber to silicon waveguide for measurement. The measured peak coupling efficiency of the grating coupler is around -9.5 dB at 2.35 μm with 150 nm 3 dB bandwidth.

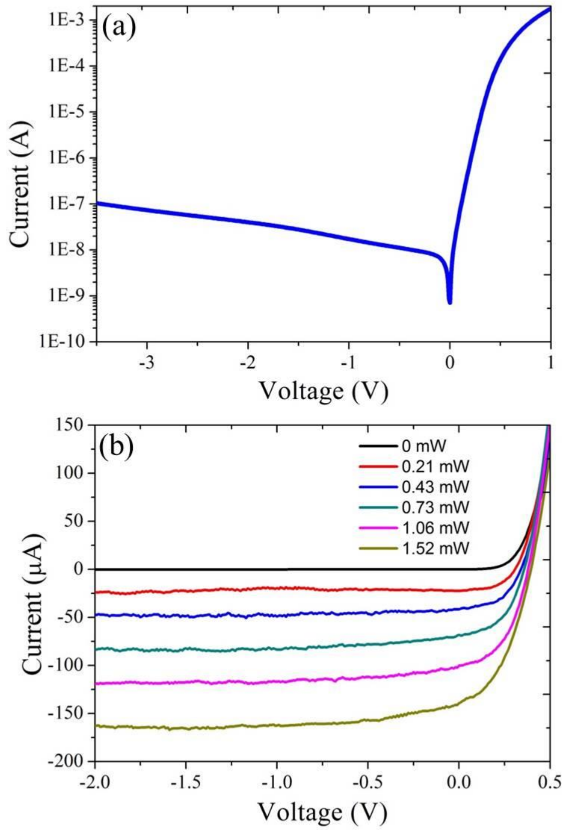

Figure 3.9. *(a) I-V curve of the photodetector without light input; (b) I-V curve of the photodetector for different fiber-coupled input powers at a wavelength of 2.3 μm.*

A typical I-V characteristic of the photodetectors in the dark at room temperature is shown in Figure 3.9(a). The dark current under reverse bias of 0.5 V is 12 nA (0.17 mA/cm^2). As the reverse bias is increased, the dark current increases gradually but it is still lower than 100 nA at a reverse bias of 3.5 V. This is 3 orders of magnitude lower than the heterogeneous GaSb-based photodetectors previously demonstrated [8], enabling a higher sensitivity. This low dark current can be attributed to the better understood and developed InP processing technology, to the timely BCB passivation of the device, and also to the passivation of the thick *p*-InP cladding layer using SiN_x. Figure 3.9(b) shows the I-V curve of the devices for different fiber-coupled input powers at a wavelength of 2.3 μm. In the measurement, the photodetectors show good linearity with a fiber-referred responsivity of 0.1 A/W. Considering a coupling efficiency of -11 dB at 2.3 μm wavelength, the corresponding internal

responsivity of the photodetectors is around 1.2 A/W, leading to a quantum efficiency of 65%. This high responsivity indicates that the light can be efficiently coupled from the silicon waveguide to the photodetector by using the tapered III-V waveguide.

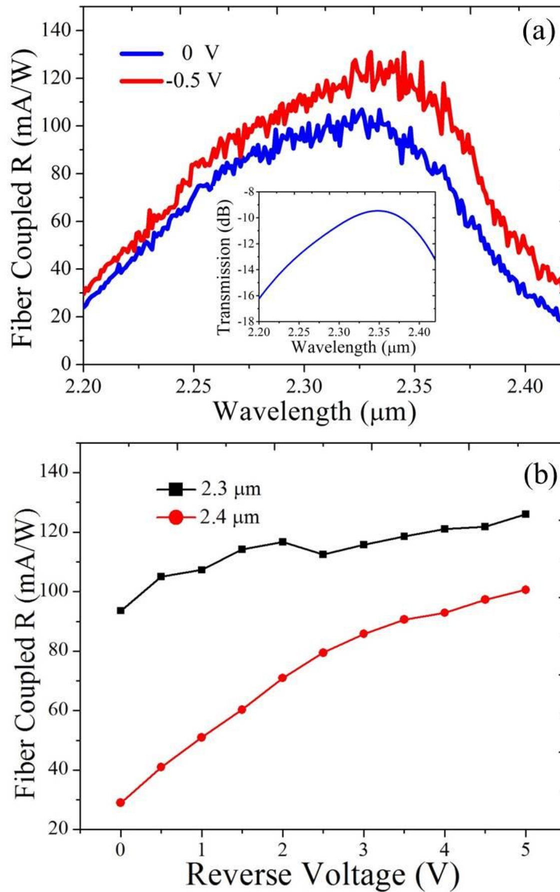

Figure 3.10. *(a) Dependence of the fiber-coupled responsivity (R) on the input laser wavelength under reverse bias of 0 V and 0.5 V, the inset figure shows the grating coupler efficiency; (b) responsivity as a function of the reverse bias at a wavelength of 2.3 μm and 2.4 μm.*

Figure 3.10(a) shows the measured fiber-referred responsivity at 0 V and -0.5 V bias over the 2.2 μm to 2.42 μm wavelength range (the wavelength range of our laser source). The referred grating coupler efficiency with a coupling angle of 15 ° is shown in the inset of Figure 10(a). For the 2.2 to 2.3 μm range the responsivity difference at reverse bias of 0 V and 0.5 V is small. At longer wavelength, the optical response becomes strongly dependent on reverse bias.

Figure 3.10(b) depicts the dependence of responsivity on reverse bias (0 to 5 V) at 2.3 μm and 2.4 μm wavelength. A much stronger bias dependence can be observed at a wavelength of 2.4 μm. This can be attributed to strong electro-absorption at wavelengths close to the band gap wavelength of the active region. The photodetectors have a waveguide-referred efficiency higher than 0.5 A/W over the 2.2-2.42 μm wavelength range. The measured peak fiber-referred responsivity is 0.12 A/W at 2.32 μm, corresponding to a waveguide-referred efficiency of 1.2 A/W.

3.4 Grating-assisted photodetectors

3.4.1 Design and fabrication

As a very sharp taper tip is required and only a small misalignment in the lithography of the III-V waveguide can be tolerated in the adiabatically-coupled photodetector, a photodetector structure with better III-V processing tolerance is also presented here. Figure 3.11(a) shows the schematic of a grating-assisted InP-based type-II photodetector. In this design, light is coupled from a SOI waveguide into the III-V active region bonded on top by using a grating to diffract the light out of the SOI waveguide. The top p-contact layer (Ti/Au) has a high reflectivity at the device operating wavelength thereby enhancing the photoresponse. The size of the diffraction grating used in this work is 20 μm×20 μm, and has a period of 1 μm and duty cycle of 50%. The size of the photodetector mesa is 25 μm×25 μm. A SEM image of the photodetector cross section is shown in Figure 3.11(b). The fabrication process of this device is the same as that of the adiabatically-coupled photodetector. A 100 nm DVS-BCB layer is used for adhesive bonding.

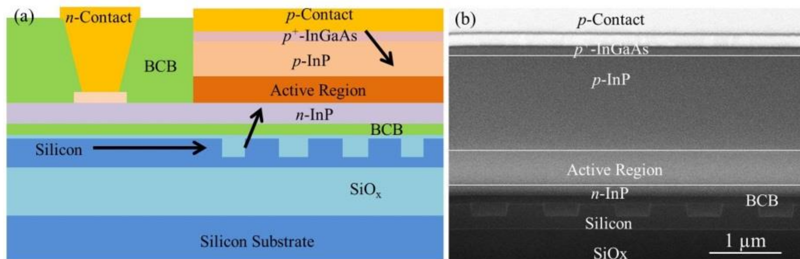

Figure 3.11. *(a) Schematic cross-section of the grating-assisted photodetector; (b) SEM image of the device cross-section.*

3.4.2 Characterization

A typical I-V characteristic of the grating-assisted photodetectors without light input at room temperature is shown in Figure 3.12(a). The dark current is half of that in adiabatically-coupled photodetectors, around −5 nA at −0.5 V, which is attributed to the smaller perimeter of the grating-assisted devices compared to that of the adiabatically coupled devices. As the reverse voltage increase to 3 V, the dark current is still below 35 nA. Figure 3.12(b) shows the I-V characteristic of the photodetector under different waveguide-coupled input power levels at 2.35 µm wavelength. The heterogeneously integrated photodetectors behave linearly under 0 V bias as the input power increases until the maximum available output power of our light source (~630 µW). The waveguide-referred responsivity is around 0.1 A/W. This value is much lower than that of the adiabatically-coupled devices. For the adiabatically-coupled photodetector, light is efficiently coupled from the silicon waveguide to the active region (simulated to be above 90%) and fully absorbed along the III-V waveguide. In the grating-assisted photodetector, the responsivity is determined by the up-coupling efficiency of the grating coupler (simulated to be 40 %) and the active region thickness. The active region in this epitaxial layer stack is a very thin multiple quantum wells layer stack (~100 nm), thereby leading to a low responsivity. The responsivity of the grating-assisted photodetector can be improved by increasing the thickness of the absorbing active region and introducing a mirror below the diffraction grating, to enhance the directionality of the grating coupler [18].

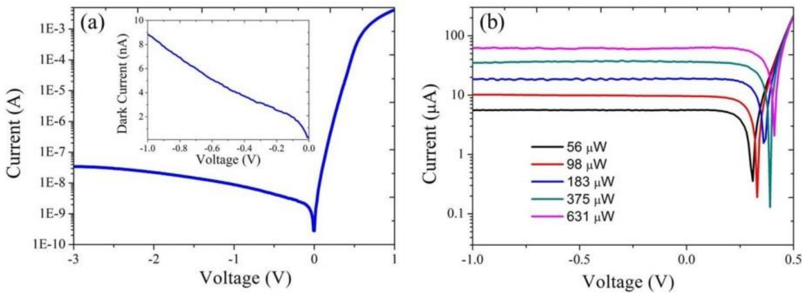

Figure 3.12. *(a) I-V characteristic of the photodetector in the dark, the inset picture shows the device dark current as a function of reverse bias; (b) I-V curve of the device under different waveguide-coupled input power levels.*

3.5 2.3 µm AWG spectrometers

Arrayed waveguide gratings (AWGs) are widely used (de)multiplexers in wavelength division multiplexing (WDM) systems. They can also be applied for spectroscopic sensing [19]. High performance AWGs have been demonstrated in

several low-index-contrast material systems, such as silica [20]. However, the footprint of these AWGs is usually very large. As a high-index-contrast material system, the silicon-on-insulator (SOI) platform can be used to fabricate waveguides with a tight bending radius, and consequently ultracompact AWGs [21]. In recent years, AWG demultiplexers based on the silicon photonics platform have been demonstrated in wavelength ranges beyond the classical telecommunication window [22, 23]. E. Ryckeboer et al. reported a low resolution (4.8 nm) and high resolution (1.6 nm) AWG spectrometer based on strip SOI waveguides having a crosstalk of -12 dB and -16 dB and an insertion loss of 2.1 dB and 4 dB, respectively [23]. As crosstalk significantly influences spectroscopic sensing performance it should be as low as possible. In our work, we have realized low insertion loss and low cross-talk AWGs.

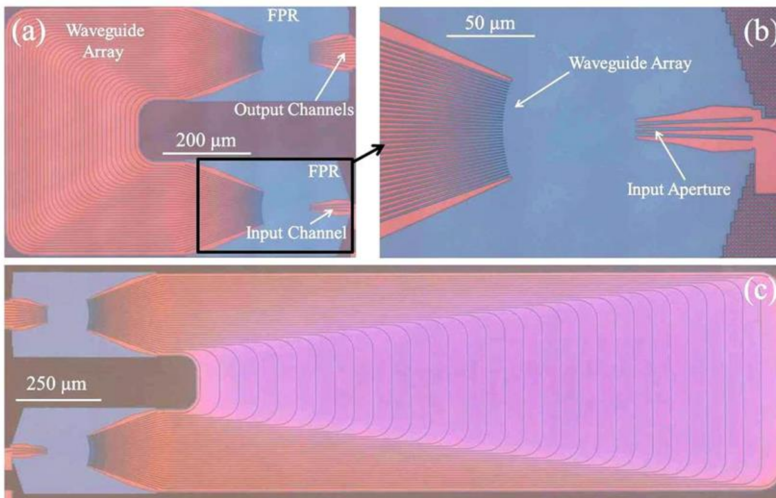

Figure 3.13. *Microscope image of (a) the low-resolution AWG; (b) magnification of the input section of the low-resolution AWG; (c) the high-resolution AWG.*

The AWGs are fabricated on a 200 mm SOI wafer with a 400 nm thick silicon device layer on a 2 μm buried oxide layer. Inductively-coupled plasma (ICP) dry etching is used to etch 180 nm deep silicon rib waveguides. Figure 3.13 shows the microscope images of a fabricated low resolution and high resolution AWG [24]. The AWGs consist of two free propagation regions (FPRs) and 32 arrayed waveguides (known as delay lines) with constant length increment located between the two FPRs. When the light enters the input aperture through a 3 μm wide waveguide as shown in Figure 3.13(b), it diverges and couples into the waveguide array (2 μm wide waveguides with a pitch of 2.2 μm) at the end of the FPR. After passing through the waveguide array, different wavelengths will

be refocused on a certain 3 μm wide output waveguide in the output aperture. The path length difference between the delay lines is 30.8 μm / 108.3 μm for the low-resolution and high-resolution device respectively. The footprint of the low-resolution and high-resolution AWG is 0.45 mm^2 and 1.1 mm^2, respectively. Detailed information about the principle of AWG design can be found in [20]. Four different AWGs designed for the 2.3-2.4 μm wavelength range are presented in this work. All of the AWGs are designed for TE polarized light. The detailed AWG design parameters are summarized in Table 3.1.

	AWG1	AWG2	AWG3	AWG4
Center wavelength (nm)	2375	2375	2375	2375
FSR (nm)	50	14.1	18.8	59.2
Channel spacing (nm)	5	1.41	3.76	4.23
No. of arrayed waveguides	32	32	20	48
FPR length (μm)	108	108	98.15	235.46
Single mode WG width (nm)	826	826	826	826
Expanded WG width (μm)	1.5	1.5	1.5	1.5
Taper length (μm)	90	90	90	90
Bend radius (μm)	50	50	50	50
Aperture width (μm)	3	3	3	3
Space between WGs (nm)	200	200	200	200
Device size: L×W (mm × mm)	0.78 × 0.57	1.98 × 0.57	1.06 × 0.57	0.94 × 0.68

Table 3.1 *Design and layout parameters summary for AWGs*

The passive device performance is characterized by measuring the transmission spectrum of each channel. TE polarized light tuned with a step of 0.1nm from a tunable Cr^{2+}:ZnSe solid state laser is coupled to the input channel of the AWG through the grating coupler. An optical spectrum analyzer (OSA, Yokogawa AQ6375) is used to collect light from different output grating couplers. The insertion loss and crosstalk of the AWGs is acquired by normalizing the transmission spectra of the AWGs to a reference waveguide. Figure 3.14(a) and 3.14(b) show the spectral responses of all the 8 channels in the low-resolution and high-resolution AWG, which correspond to the devices shown in Figure 3.13(a) and 3.13(c), respectively. From the measurement, it can be found that the insertion loss is around 2.5 dB and the crosstalk level is -30 dB for the low-resolution AWG (AWG-1) as shown in Figure 3.14 (a). The high-resolution AWG (AWG-2) has an insertion loss of about 2.8 dB and crosstalk level of -25 dB. The low-resolution and high-resolution AWG has a channel spacing of 5 nm and 1.4 nm, respectively. Figure 3.14(c) shows a 5 channel

AWG (AWG-3) that has an insertion loss of about 2.5 dB and crosstalk level of -26 dB and Figure 3.14(d) shows a 12 channel AWG (AWG-4) that has an insertion loss of about 3 dB and a crosstalk level of -28 dB. AWG-3 and AWG-4 have a channel spacing of 3.8 nm and 4 nm, respectively. All four AWGs show a good channel uniformity. The performance of these 2-μm-wavelength-range AWGs is comparable with state-of-the-art SOI AWGs at classical telecommunication wavelengths [25].

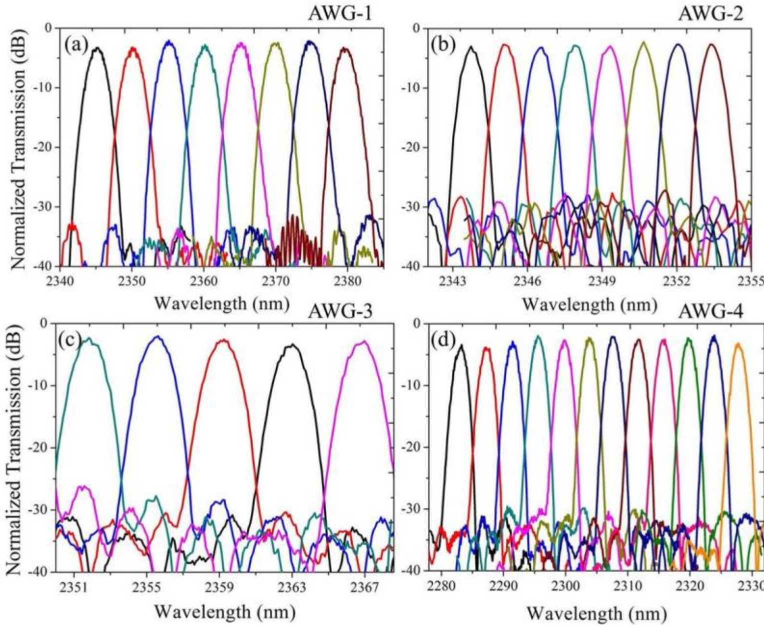

Figure 3.14. *The measured spectral responses of all the channels in four different AWGs.*

3.6 AWGs integrated with photodetectors

In this section, I will address integration of photodetector arrays with the AWG spectrometers. For telecommunication applications, the integration of an AWG demultiplexer with a photodetector array allows realizing a WDM receiver [26]. For spectroscopic applications, it is the first step towards a fully integrated spectroscopic sensing system [27].

3.6.1 AWGs integrated with adiabatically-coupled photodetectors

By improving the III-V wet etching processing to fabricate sharper III-V tips, we integrated AWG spectrometers with adiabatically-coupled photodetectors with higher efficiency than the one shown in Figure 3.8. Figure 3.15(a) shows a

typical current-voltage (I-V) curve of the improved adiabatically-coupled photodetectors without light input. The measured average dark current is around 10 nA at a bias voltage of -0.5 V. The optical response of the photodetectors at 2.35 μm wavelength under different optical input powers in the silicon waveguide is shown in Figure 3.15(b). The waveguide-referred responsivity is around 1.6 A/W, which corresponds to a quantum efficiency of 85%. The linearity of the photodetector is analyzed in Figure 3.15(c). At 0 V bias the photodetector linear operation is obtained for optical input powers below 200 μW. For linear operation at higher optical input power, a reverse bias is required to extract all photogenerated carriers. Under a reverse bias voltage of 1 V, linear operation is obtained up to an optical input power of around 630 μW, which is the maximum power that can be obtained from our light source.

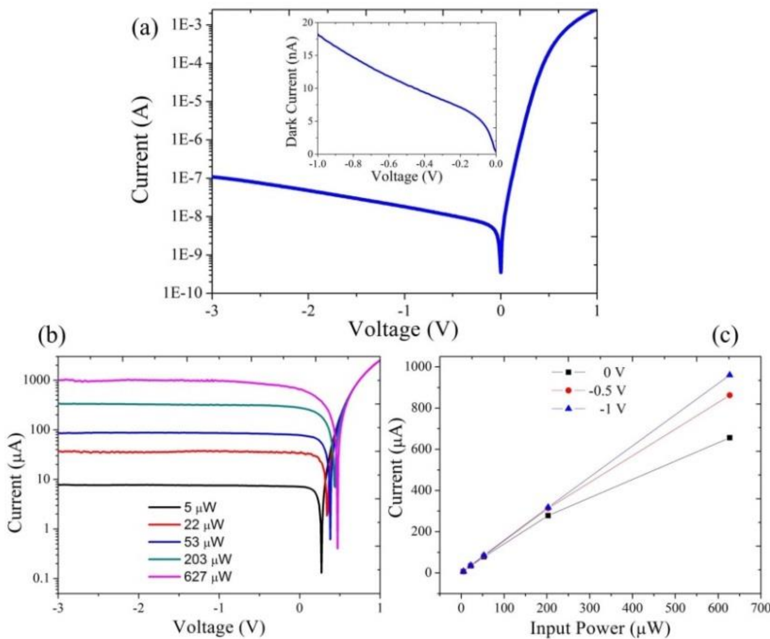

Figure 3.15. *(a) I-V curve of the adiabatically-coupled photodetectors without light input, the inset figure shows the dark current of the devices; (b) photoresponse of the devices under different input power levels; (c) linearity analysis of the adiabatically-coupled III-V-on-silicon photodetectors.*

Figure 3.16(a) shows a microscope image of the low-resolution AWG (AWG-1, shown in Figure 3.13(a)) integrated with adiabatically-coupled photodetectors. All of the eight channels are integrated with photodetectors, the pitch of which is 60 μm. A reference photodetector is fabricated for photodetector characterization and insertion loss measurement of the AWG spectrometers after

III-V processing. In device measurements, TE-polarized light from the tunable laser source is coupled to a standard single mode fiber (SMF-28) and then split by a 1/99 splitter. The 1% port is connected to the OSA as a wavelength and power reference. The light in 99% path is coupled to the AWG spectrometer and read out through the heterogeneously integrated photodetectors. The photodetectors are probed individually and the photocurrent is acquired by a Keithley SourceMeter. Figure 3.16(b) and 3.16(c) display the photoreponse of two AWGs (AWG-1 and AWG-3) integrated with adiabtically-coupled photodetectors. The bias voltage is fixed at -0.5 V. By normalizing the responsivity with the reference photodetector, an insertion loss of 3 dB and a crosstalk level of -27 dB are obtained for AWG-1. With integrated photodetectors, the AWG-3 has an insertion loss of 3.5 dB and crosstalk level of -29 dB as shown in Fig. 3.16(c), illustrating the fact that the post-processing doesn't affect the spectrometer performance substantially. A red-shift in the recorded spectra after photodetector integration can be observed, which is due to the DVS-BCB cladding applied during the photodetector array processing, resulting in a change of the effective refractive index of the silicon waveguides of ~0.01 which induces a 6.5 nanometer red shift of the AWG transmission spectrum, which matches our measurement results (5 nm-7 nm).

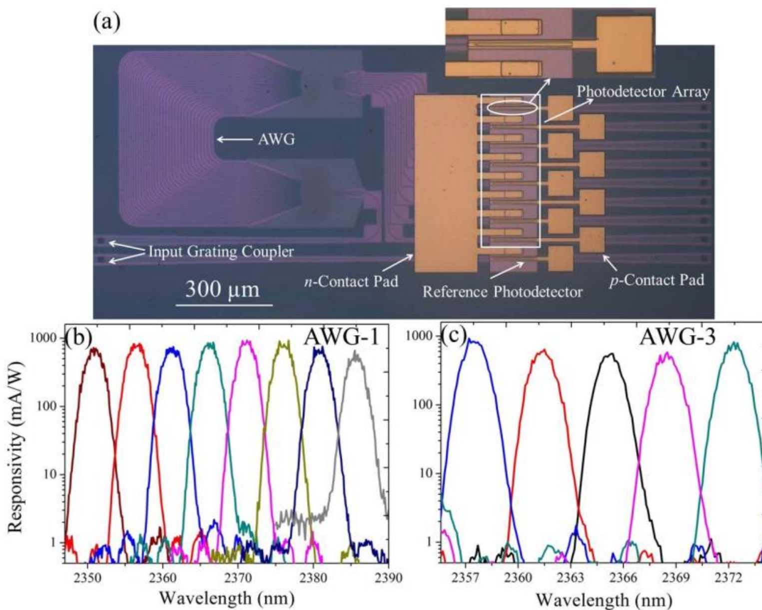

Figure 3.16. *(a) Microscope image of an AWG integrated with adiabatically-coupled photodetectors; (b) and (c) response of two AWG spectrometers with integrated photodetectors.*

3.6.2 AWGs integrated with grating-assisted photodetectors

Figure 3.17(a) shows a microscope picture of the 8-channel high resolution AWG (AWG-2, shown in Figure 3.13(c)) integrated with grating-assisted photodetectors. The performance of the grating-assisted photodetectors used here is the same as the one shown in Figure 3.12. All of the photodetectors share a common n-contact, and an individual p-contact. The pitch of the photodetectors is 60 μm, the same as the adiabatically-coupled devices. Figure 3.17 (b) and 3.17(c) shows the measured waveguide-referred responsivity as a function of wavelength for all of the channels in AWG-2 and AWG-4, respectively. Insertion loss can be obtained by normalizing the responsivity with the reference photodetector. The high-resolution AWG-2 exhibits an insertion loss of 3 dB and crosstalk levels of -24 dB after III-V heterogeneous integration. For the 12 channel AWG-4 device, an insertion loss of 3 dB and a crosstalk level of -23 dB is obtained.

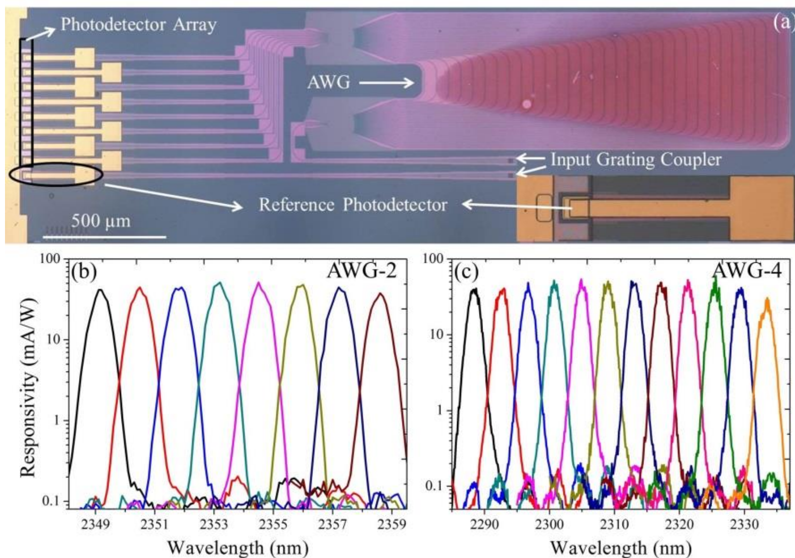

Figure 3.17. *(a) Microscope image of the hig- resolution AWG integrated with grating-assisted photodetectors; (b) and (c) measurement results of AWG-2 and AWG-4 integrated with grating-assisted photodetectors.*

3.7 AWG integrated with SLED

As we discussed in the first chapter, broadband light sources, photodetectors and spectrometers should be integrated on the same chip for a fully integrated liquid spectroscopic sensor. In the design of this work, the epitaxial structure of the InP-based type-II quantum well photodetectors also can be used to realize the

integration of light sources on the SOI waveguide platform. Figure 3.18(a) shows a microscope image of an AWG (AWG-1) and reference waveguide integrated with an InP-based type-II LED. A broadband emission between 2.2 μm and 2.45 μm with peak position at 2.35 μm is coupled to the reference silicon waveguide as seen in Figure 3.18 (b). An optical power ~10 μw is coupled to the silicon waveguide when 500 mW electrical power is injected into the LED. For the LED integrated with AWG, the broadband emission is filtered by the AWG and coupled to different channels with a channel spacing of 5 nm and free spectral range of 50 nm as shown in Figure 3.18(c). From the emission spectrum coupled out from the reference waveguide and AWG, an insertion of 3 dB is deduced. The crosstalk of the AWG after LED integration is estimated to be -22 dB. These results indicate the integration of the LED with AWG spectrometer does not degrade the insertion loss and crosstalk of the device.

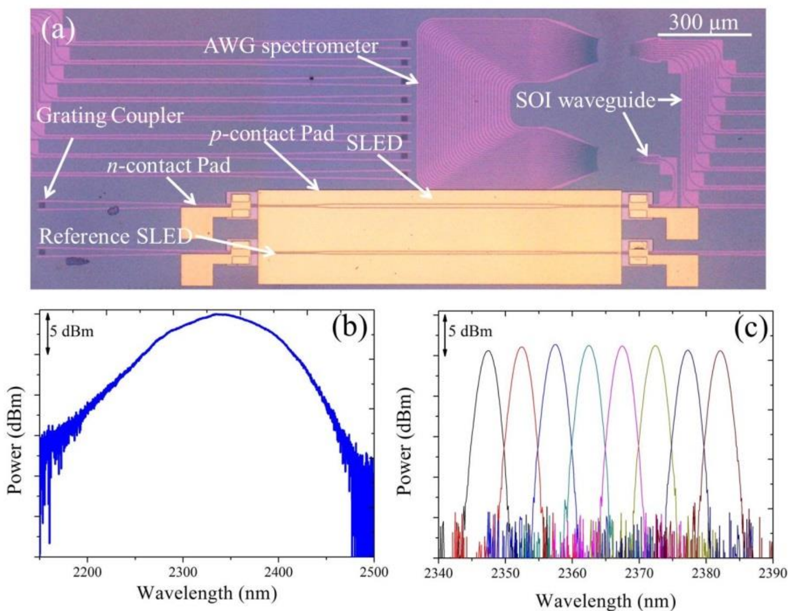

Figure 3.18. *(a) Microscope image of an AWG integrated with an InP-based type-II LED; (b) fiber-coupled emission spectrum of the heterogeneously integrated LED; (c) filtered spectrum of the light coupled from LED to the different channels of the AWG.*

3.8 Conclusion

In this chapter, we report 2 μm range III-V-on-silicon photodetectors and spectrometers based on the heterogeneous integration of InP-based type-II heterostructures on silicon photonic ICs. Firstly, we discussed the state-of-the-

art of 2 μm III-V photodetectors based on three different material systems. Because InP-based type-II heterostructures allow broad wavelength coverage and leverage well-developed processes, we choose this material system to realize heterogeneous III-V-on-silicon photodetectors. Then we demonstrate heterogeneously integrated InP-based type-II quantum well photodetectors based on two coupling approaches between silicon waveguide and III-V active region. The first batch of adiabatic-taper-based photodetectors show a responsivity of 1.2 A/W at 2.32 μm wavelength and dark current of 12 nA at −0.5 V, while photodetectors using grating-assisted coupling have a responsivity of 0.1 A/W and dark current of 5 nA at −0.5 V. The first structure has much higher optical responsivity while the grating-assisted photodetector has better fabrication tolerance. Afterwards, we show AWGs operating in the 2.3-2.4 μm wavelength range with different resolution and channel numbers. Low insertion loss of 2.5-3 dB and low crosstalk of -30 to -25 dB are obtained for all of these passive AWGs. Then, the AWG spectrometers heterogeneously integrated with photodetectors are presented. The integration of the photodetector array does not degrade the insertion loss and crosstalk of the AWGs. A InP-based type-II LED is also heterogeneously integrated with the AWG by using the same epitaxial layer stack as the photodetectors. It enables the realization of a fully integrated 2-μm-wavelength-range spectroscopic sensing system on silicon photonics.

References

[1] A. Rogalski, “Infrared detectors: status and trends,” Progress in Quantum Electronics, **27**, 59-210 (2003).

[2] L.J. Kozlowski, K. Vural, J.M. Arias, W.E. Tennant, R.E. DeWames, “Performance of HgCdTe, InGaAs and quantum well GaAs/AlGaAs staring infrared focal plane arrays,” Proc. SPIE, **3182**, 2–13 (1997).

[3] G. H. Olsen, A. M. Joshi, S. M. Mason, K. M. Woodruff, E. Mykietyn, V. S. Ban, M. J. Lange, J. Hladky, G. C. Erickson, G. A. Gasparian, “Room-temperature InGaAs detector arrays for 2.5 μm,” Proc. SPIE, **1157**, 276–282 (1989).

[4] J. C. Dries, M. R. Gokhale, K. J. Thomson, and S. R. Forrest, “Strain compensated $In_{1-x}Ga_xAs$(x<0.47) quantum well photodiodes for extended wavelength operation,” Appl. Phys. Lett., **73**, 2263-2265 (1998).

[5] Y. Arslan, F. Oguz, C. Besikci, “640 × 512 extended short wavelength infrared $In_{0.83}Ga_{0.17}As$ focal plane array,” IEEE J. Quantum Electron., **50**, 957–964 (2014).

[6] G. Boehm, M. Grau, O. Dier, K. Windhorn, E. Roenneberg, J. Rosskopf, R. Shau, R. Meyer, M. Ortsiefer, and M. C. Amann, “Growth of InAs- containing quantum wells for InP-based VCSELs emitting at 2.3 μm,” J. Cryst. Growth, **301-302**, 941–944 (2007).

[7] I. Vurgaftman, J. R. Meyer, and L. R. Ram-Mohan, “Band parameters for III–V compound semiconductors and their alloys,” J. Appl. Phys., **89**(11), 5815–5875 (2001).

[8] N. Hattasan, A. Gassenq, L. Cerutti, J. B. Rodriguez, E. Tourni é, and G. Roelkens, “Heterogeneous integration of GaInAsSb p-i-n photodiodes on a silicon-on-insulator waveguide circuit,” IEEE Photon. Technol. Lett. **23**(23), 1760–1762 (2011).

[9] A. Gassenq, N. Hattasan, L. Cerutti, J. B. Rodriguez, E. Tourni é, G. Roelkens, and G. Roelkens, “Study of evanescently-coupled and grating-assisted GaInAsSb photodiodes integrated on a silicon photonic chip,” Opt. Express **20**(11), 11665–11672 (2012).

[10] S. Sprengel, C. Grasse, P. Wiecha, A. Andrejew, T. Gruendl, G. Boehm, R. Meyer, and M.-C. Amann, “InP-Based Type-II Quantum-Well Lasers and LEDs,” IEEE J. Sel. Top. Quantum Electron. **19**(4), 1900909 (2013).

[11] C. Grasse, P. Wiecha, T. Gruendl, S. Sprengel, R. Meyer, and M.-C. Amann, “InP-based 2.8–3.5 μm resonant-cavity light emitting diodes based on

type-II transitions in GaInAs/GaAsSb heterostructures," Appl. Phys. Lett., **101**(22), 221107 (2012).

[12] R. Sidhu, N. Duan, J. C. Campbell, A. L. Holmes, "A Long-Wavelength Photodiode on InP Using Lattice-Matched GaInAs–GaAsSb Type-II Quantum Wells, " IEEE Photon. Technol. Lett., **17**(12), 2715-2717 (2005).

[13] B. Chen, W.Y. Jiang, A. L. Holmes Jr, "Design of Strain Compensated InGaAs/GaAsSb Type-II Quantum Well Structures for Mid-infrared Photodiodes," Optical and Quantum Electronics, **44**(3), 103-109 (2012).

[14] B. Chen, W. Y. Jiang, J. Yuan, A. L. Holmes, Jr, and B. M. Onat, "Demonstration of a Room-Temperature InP-Based Photodetector Operating Beyond 3 μm," IEEE Photon. Technol. Lett., **23**(4), 218-220 (2011).

[15] B. Chen, W. Y. Jiang, J. Yuan, A. L. Holmes, Jr, and B. M. Onat, "SWIR/MWIR InP-Based p-i-n Photodiodes with InGaAs/GaAsSb Type-II Quantum Wells," IEEE. Quantum Electron., **47**(9), 1244-1250 (2011).

[16] R. Wang, S. Sprengel, M. Muneeb, G. Boehm, R. Baets, M. C. Amann, and G. Roelkens, "2 μm wavelength range InP-based type-II quantum well photodiodes heterogeneously integrated on silicon photonic integrated circuits," Opt. Express **23**(20), 26834–26841 (2015).

[17] B. Chen and A.L. Holmes Jr, "Optical gain modeling of InP based InGaAs (N)/GaAsSb type-II quantum wells laser for mid-infrared emission," Opt. Quantum Electron. **45** (2), 127-134 (2013).

[18] C. B. Li, R. W. Mao, Y. H. Zuo, L. Zhao, W. H. Shi, L. P. Luo, B. W. Cheng, J. Z. Yu, and Q. M. Wang, "1.55 μm Ge islands resonant-cavity-enhanced detector with high-reflectivity bottom mirror," Appl. Phys. Lett. **85**(14), 2697–2699 (2004).

[19] A. Subramanian, E. M. P. Ryckeboer, A. Dhakal, F. Peyskens, A. Malik, B. Kuyken, H. Zhao, S. Pathak, A. Ruocco, A. De Groote, P. C. Wuytens, D. Martens, F. Leo, *et al.*, "Silicon and silicon nitride photonic circuits for spectroscopic sensing on-a-chip," Photonics Research **5**(3), 47–59 (2015).

[20] M. Smit and C. Van Dam, "PHASAR-based WDM-devices: Principles, design and applications," IEEE J. Sel. Top. Quantum Electron. **2**(2), 236–250 (1996).

[21] W. Bogaerts, S. K. Selvaraja, P. Dumon, J. Brouckaert, K. De Vos, D. Van Thourhout, and R. Baets, "Silicon-on-insulator spectral filters fabricated with CMOS technology," IEEE J. Sel. Top. Quantum Electron. **16**(1), 33–44 (2010).

[22] M. Muneeb, X. Chen, P. Verheyen, G. Lepage, S. Pathak, E. Ryckeboer, A. Malik, B. Kuyken, M. Nedeljkovic, J. Van Campenhout, G. Z. Mashanovich,

and G. Roelkens, “Demonstration of Silicon-on-insulator mid-infrared spectrometers operating at 3.8 µm,” Opt. Express **21**(10), 11659–11669 (2013).

[23] E. Ryckeboer, A. Gassenq, M. Muneeb, N. Hattasan, S. Pathak, L. Cerutti, J. B. Rodriguez, E. Tournié, W. Bogaerts, R. Baets, and G. Roelkens, “Silicon-on-insulator spectrometers with integrated GaInAsSb photodiodes for wide-band spectroscopy from 1510 to 2300 nm,” Opt. Express **21**(5), 6101–6108 (2013).

[24] R. Wang, M. Muneeb, S. Sprengel, G. Boehm, A. Malik, R. Baets, M.-C. Amann, and G. Roelkens, “III-V-on-silicon 2-µm-wavelength-range wavelength demultiplexers with heterogeneously integrated InP-based type-II photodetectors,” Opt. Express **24**(8), 8480–8490 (2016).

[25] K. Okamoto, “Wavelength-Division-Multiplexing Devices in Thin SOI: Advances and Prospects,” IEEE J. Sel. Top. Quantum Electron. **20**, 248 (2014).

[26] H. Nishi, T. Tsuchizawa, R. Kou, H. Shinojima, T. Yamada, H. Kimura, Y. Ishikawa, K. Wada, and K. Yamada, “Monolithic integration of a silica AWG and Ge photodiodes on Si photonic platform for one-chip WDM receiver,” Opt. Express **20**(8), 9312–9321 (2012).

[27] R. Yu, R. Proietti, J. Kurumida, A. Karalar, B. Guan, and S. J. B. Yoo, “Rapid high-precision in situ wavelength calibration for tunable lasers using an athermal AWG and a PD array,” IEEE Photon. Technol. Lett. **24**(1), 70–72 (2012).

4

III-V-on-silicon 2.3 μm range laser sources

4.1 Introduction

In the previous chapter, we presented 2.3 μm range III-V-on-silicon photodetectors and arrayed waveguide grating (AWG) spectrometers. This chapter will report 2.3 μm range III-V-on-silicon laser sources. The epitaxial layer stack used for the heterogeneously integrated photodetectors and lasers is the same. The second section of this chapter gives a short introduction on InP-based type-II quantum well lasers, mainly focusing on the device performance. The third section presents the design of optical coupling between the III-V waveguide and silicon waveguide in the lasers. Then different III-V-on-silicon laser sources are reported in the next three sections, including Fabry-Perot lasers, distributed feedback (DFB) lasers and laser arrays. A preliminary tunable diode laser absorption spectroscopy (TDLAS) measurement of CO using the III-V-on-silicon DFB laser is also presented.

4.2 Type-II quantum well laser diodes on InP

The concept of "W"-shaped InGaAs/GaAsSb type-II quantum wells has been introduced in the second chapter. Based on this active region design, S. Sprengel *et al.* from Technical University of Munich (TUM) demonstrated InP-based edge emitting laser diodes with emission up to 2.7 μm [1-3]. These edge emitters are ridge waveguide based Fabry-Perot lasers, which were processed on InP substrates after epitaxial growth in a molecular beam epitaxy (MBE) system. Fabry-Perot cavities are formed by two cleaved III-V facets. During laser characterization, the samples were mounted episide-up on copper heat sinks. Figure 4.1(a) shows the continuous wave (CW) power-current-voltage (L-I-V) characteristics of the first demonstrated (in 2012) InP-based type-II laser with emission wavelength above 2.3 μm. This λ=2.3 μm laser diode is based on a 1 mm long and 10 μm wide ridge waveguide. The highest CW operation temperature is around 0 ℃. In Figure 4.1(b), the pulsed threshold current is plotted as a function of temperature for a laser with emission wavelength of 2.31 μm and 2.55 μm. It can be seen that the λ=2.55 μm laser can lase up to 42 ℃ heatsink temperature. The characteristic temperature gradually decreases from 51K to 16K and 69K to 21K for the 2.31 μm laser and 2.55 μm laser, respectively. This result indicates carrier loss increases with temperature [1]. By optimizing the epitaxial layer stack design and epitaxial growth, S. Sprengel *et al.* have much improved the laser performance since. In 2014, they reported 2.5 μm InP-based type-II lasers with CW operation above 30 ℃ and pulsed operation up to 80 ℃ [4], as shown in Figure 4.2 (a). In 2015, the first InP-based vertical cavity surface emitting lasers (VCSELs) with type-II quantum wells

were demonstrated [5], lasing at ~2.5 μm. The VCSEL emits a peak optical power of 0.4 mW at -18 ℃, and can lase up to 10 ℃ in CW. A typical emission spectrum of the VCSEL is shown in Figure 4.2 (b). A side mode suppression ratio (SMSR) of 30 dB is obtained.

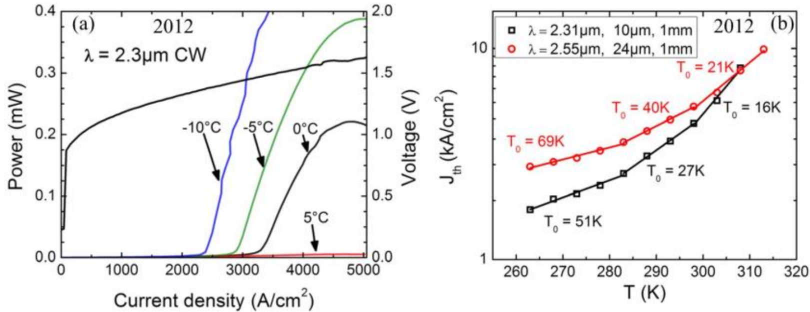

Figure 4.1. *Lasing performance of the first demonstrated 2.3 μm InP-based type-II quantum well laser diode [1]. (a) CW L-I-V curve; (b) Pulsed threshold current as a function of temperature.*

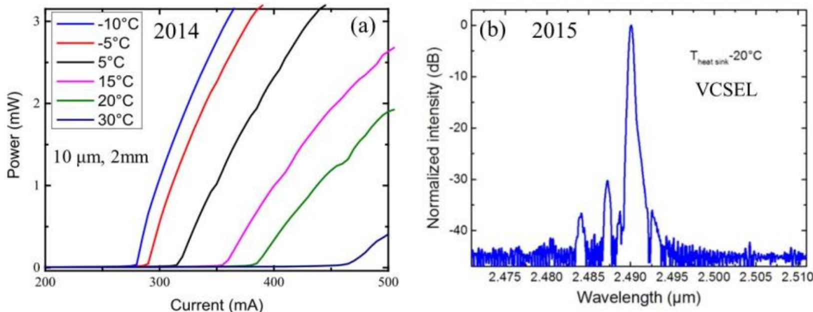

Figure 4.2. *Performance of improved type-II quantum well laser diodes on InP. (a) CW L-I-V curve of a λ=2.5 μm edge emitting laser [4]; (b) emission spectrum of a λ=2.49 μm InP-based type-II VCSEL, driven at 15 mA and -20 ℃ [5].*

Besides TUM, C. H. Pan *et al*. from National Chiao Tung University also demonstrated InP-based type-II lasers in 2012. The laser was lasing at 2.56 μm by optical pumping [6]. A threshold current density of ~40 kW/cm^2 was obtained. In 2015, the same research group also reported an electrically pumped 2.35 μm type-II quantum laser on InP substrate with a low threshold current density at infinite cavity length of 83 A/cm^2 per quantum well under pulsed operation at room temperature [7].

4.3 Optical coupling design

III-V-on-silicon laser sources usually consist of a III-V-on-silicon semiconductor amplifier (SOA) and a wavelength-selective optical feedback structure implemented in the silicon. In these devices, the light generated in the III-V waveguide couples to the silicon waveguide, and after filtering by the silicon waveguide structures, it is coupled back to the III-V waveguide where it is amplified. So an efficient coupling between the III-V waveguide and silicon waveguide is critical for III-V-on-silicon laser sources. In this section, I will present the adiabatic coupling structure used in our 2.3 μm III-V-on-silicon lasers. The heterogeneously integrated SOA on a silicon-on-insulator (SOI) waveguide is schematically shown in Figure 4.3 (a) and (b). The III-V epitaxial structure is adhesively bonded to the SOI waveguide circuit using an ultra-thin DVS-BCB layer as bonding agent. The device consists of a III-V gain section, III-V/silicon spot size converters and single mode SOI waveguides. In the center of the device the light is confined in the III-V waveguide as shown in Figure 4.3(c), which provides maximum gain. Light is coupled from the III-V waveguide to the silicon waveguide by using a III-V/silicon spot size converter (SSC). At the III-V taper tip position, the light is completely coupled into the silicon waveguide as shown in Figure 4.3(d). All of the III-V-on-silicon laser devices shown in this chapter are based on this SOA structure, but have different silicon waveguide feedback structures.

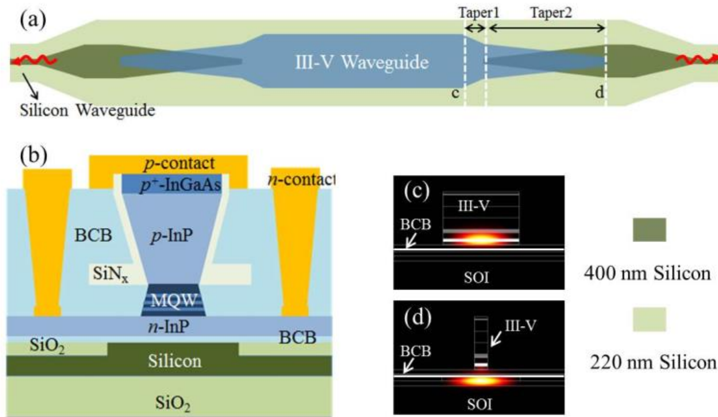

Figure 4.3. *(a) Schematic drawing of the top view of the InP-based type-II SOA heterogeneously integrated on a SOI waveguide circuit, showing the III-V mesa and SOI waveguide structure. The electrical contacts were omitted for clarity; (b) detailed cross-section of the III-V/silicon waveguide; (c) and (d) TE- polarized mode intensity distribution in different parts of the device, the position of which is marked in (a).*

The mode intensity profiles and optical coupling efficiency of the III-V/silicon SSC are calculated using a full-vectorial mode solver FIMMWAVE to optimize the device design [8]. The silicon rib waveguide is 400 nm high with an etch depth of 180 nm as described in the second chapter. A 5 μm wide III-V mesa is chosen to obtain low waveguide loss and high optical confinement in the active region of the gain section. The calculated confinement factor of the TE polarized fundamental mode (at 2.35 μm wavelength) in the six quantum wells is 10.2%. An efficient optical coupling between the III-V waveguide and silicon waveguide is realized by tapering both waveguides. The III-V/silicon SSC has two tapered sections as shown in Figure 4.3(a). In the first taper section, the III-V waveguide is linearly tapered from 5 μm to 1.2 μm over a length of 50 μm. The second section is an adiabatic inverted taper coupler, where the III-V waveguide is slowly tapered to a very narrow tip while the silicon waveguide underneath is tapered from 200 nm to 3 μm. Figure 4.4(a) shows the coupling efficiency of the III-V/silicon spot size converter as a function of the III-V taper tip width. We can find that high coupling efficiency can be achieved when a 0.5 μm wide taper tip is used. Although 90 μm long tapers with 0.5 μm wide tip provide a coupling efficiency higher than 90% as shown in Figure 4.4(b), 180 μm long tapers are used in all our devices shown in this chapter to get a more robust coupling. The fundamental mode evolution in a longitudinal cross section of the 180 μm long III-V-on-silicon adiabatic taper with a 0.5 μm wide taper tip is shown in the inset picture of Figure 4.5. The III-V/silicon spot size converters are electrical pumped during device operation to avoid optical loss as the III-V taper contains the same active region as in the gain section.

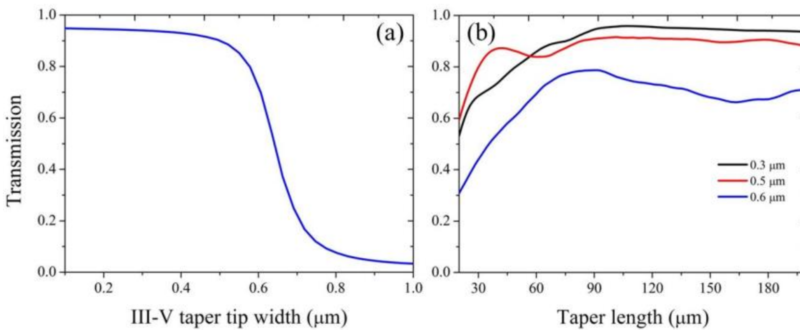

Figure 4.4. *(a) Simulated coupling efficiency of a 180 μm long adiabatic taper as a function of the taper tip width. (b) Coupling efficiency of the adiabatic tapers with different tip widths as a function of the taper length.*

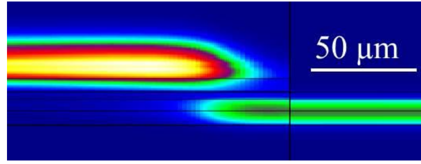

Figure 4.5. *Fundamental mode intensity evolution in a 180 µm long adiabatic taper with 0.5 µm wide III-V taper tip.*

Figure 4.6 shows the electroluminescence (EL) spectrum from a heterogeneously integrated InP-based type-II SOA on a SOI waveguide (150 mA bias). It can be seen that a broadband emission between 2.2 µm and 2.45 µm with peak position at 2.35 µm is coupled to the silicon waveguide.

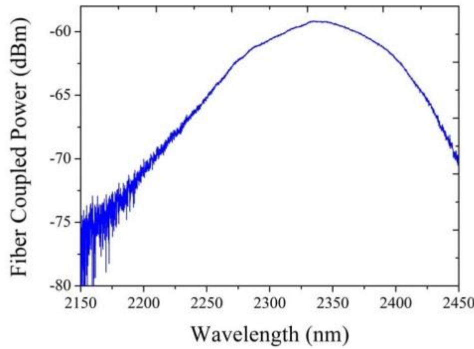

Figure 4.6. *Fiber coupled emission spectrum from a heterogeneously integrated InP-based type-II SOA at 150 mA bias current.*

4.4 III-V-on-silicon 2.3 µm Fabry-Perot laser

The Fabry-Perot cavity is one of the simplest laser structures, consisting of a gain medium sandwiched between two broadband mirrors. The laser mirrors can be easily obtained by cleaving two facets in the grown III-V wafer. Therefore, the first laser device made of new gain materials is usually based on a Fabry-Perot cavity structure. Fabry-Perot lasers offer a broadband optical output with multiple longitudinal modes, which has been explored in the recently developed multimode absorption spectroscopy technology and multiheterodyne spectroscopy technology [9-11]. In this section, 2.3 µm range III-V-on-silicon Fabry-Perot lasers will be presented.

4.4.1 Design and fabrication

The schematic of a heterogeneously integrated InP-based type-II Fabry-Perot laser is shown in Figure 4.7 [12]. The device consists of a III-V-on-silicon SOA

and two distributed Bragg reflectors (DBR) implemented in an SOI waveguide. The feedback is realized using a high-reflectivity silicon DBR (DBR1, 20 periods, 435 nm period, duty cycle 50%, 180 nm etch depth) and a lower reflectivity silicon DBR (DBR2, 4 periods, 435 nm period, duty cycle 50%, 180 nm etch depth) used as output port. Simulation results indicate the DBR1 and DBR2 can provide ~90% and 32% reflectivity at 2.35 μm wavelength, respectively, as shown in Figure 4.8. Due to the high refractive index contrast the bandwidth of the reflector is very large.

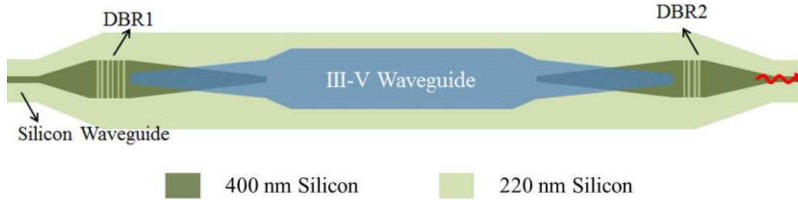

Figure 4.7. *Schematic drawing of the top view of the InP-based type-II Fabry-Perot laser heterogeneously integrated on a SOI waveguide circuit.*

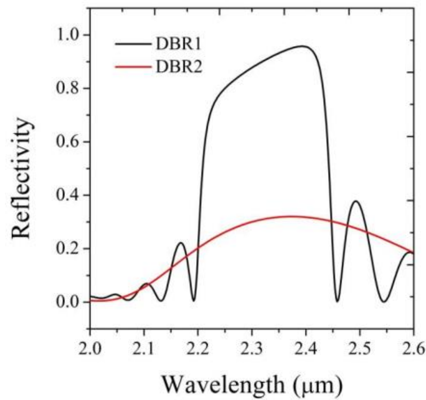

Figure 4.8. *Simulated reflectivity of the two DBRs.*

In the III-V-on-silicon Fabry-Perot lasers, the InP-based epitaxial layer stack is adhesively bonded to the SOI waveguide circuit using a 100 nm thick DVS-BCB layer (1:3 DVS-BCB:mesitylene). Detailed information about the epitaxial layer stack and III-V process have been presented in the second chapter. Figures 4.9(a) and 4.9(b) show the top view microscope image and scanning electron microscope (SEM) cross-section image of the heterogeneously integrated lasers on silicon waveguides, respectively. The laser devices have a 1000 μm×5 μm gain section. A common p-contact pad is used serving as a heat-spreader for the integrated lasers.

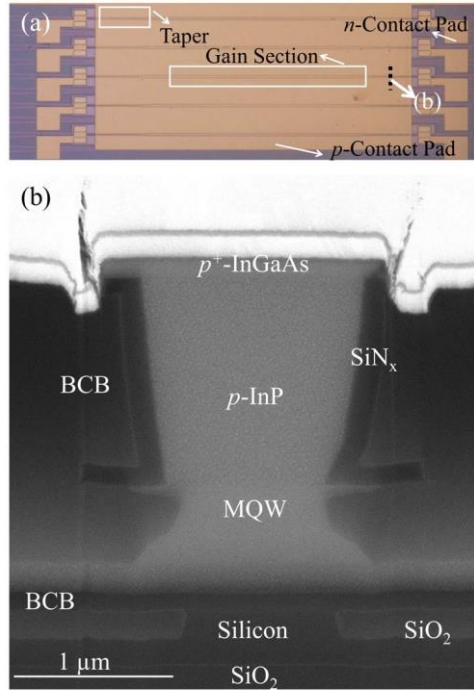

Figure 4.9. *(a) Microscope image of the heterogeneously integrated lasers; (b) SEM image of the cross-section of the device.*

4.4.2 Characterization

The devices are characterized using DC and pulsed current sources. The light in the silicon waveguide is coupled out by a grating coupler and collected by a standard single mode fiber (SMF-28), which is connected to an optical spectrum analyzer (OSA, Yokogawa AQ6375). The laser power coupled into the silicon waveguide is calibrated by measuring the coupling efficiency of reference grating coupler structures. At 2.35 μm wavelength, the coupling efficiency is around −10 dB, and the 3 dB bandwidth is 150 nm. The samples are mounted on a temperature controller which allows the device operating temperature to be varied from 0 ℃ to 80 ℃. Figure 4.10 shows the L-I-V curve of the heterogeneously integrated laser with a DBR period of 435 nm under CW operation at 5 ℃. A maximum optical output power of 1.3 mW coupled into the silicon waveguide is obtained. The laser has a threshold current of 135 mA, corresponding to a threshold current density of 2.7 kA/cm^2. The series resistance of the laser is 8.5 Ω. It can be reduced by optimizing the metallization processes and reducing the gap between the III-V waveguide and n-InP (currently 5 μm). The slope efficiency near threshold current is 0.035 W/A at 5 ℃.

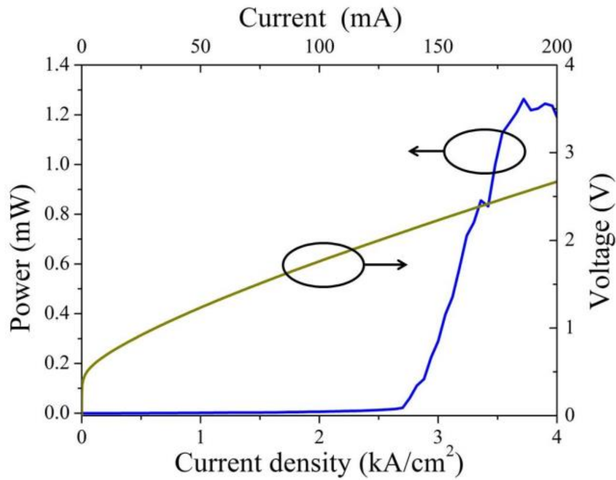

Figure 4.10. *I-V curve of the laser and CW output power as a function of drive current at 5 ℃.*

Figure 4.11 shows the emission spectra of two heterogeneously integrated lasers with different DBR period (420 nm and 435 nm), driven at an injection current of 160 mA at 5 ℃ in CW operation. The spectra are measured with a Yokogawa AQ6375 OSA with a resolution bandwidth of 0.1 nm. The longitudinal modes of the Fabry-Perot laser cavity can clearly be observed. As shown in Figure 4.11 (a), the lasing wavelength can be tuned by adjusting the grating period. The dominant lasing wavelength shifts from 2332.5 nm to 2351.3 nm when the DBR period increases from 420 nm to 435 nm. A close up of the lasing Fabry-Perot modes is shown in Figure 4.11(b). The free spectral range of the longitudinal modes is 0.52 nm, which correspond to an average group index of 3.8 for an overall 1400 μm long Fabry-Perot cavity (with DBRs located 20 μm away from the III-V taper tip). A modulation of the intensity of the longitudinal modes can be observed, which is attributed to a parasitic reflection of the grating coupler structure used to couple light to single mode fiber. The side mode suppression ratio (SMSR) is around 17 dB for the Fabry-Perot lasers. Under CW operation, the maximum operating temperature of the InP-based type-II lasers integrated on SOI is around 9 ℃.

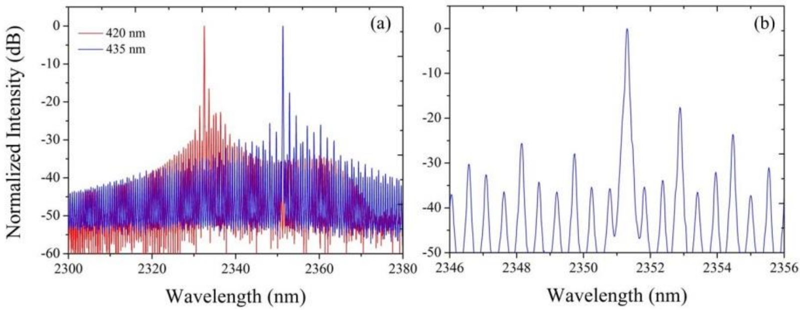

Figure 4.11. *(a) Two typical emission spectra from the heterogeneously integrated Fabry-Perot lasers with different DBR period (420 nm and 435 nm), characterized under CW operation at 5 ℃ and 160 mA injected current; (b) zoom of the emission spectrum from the Fabry-Perot laser with DBR period of 435 nm.*

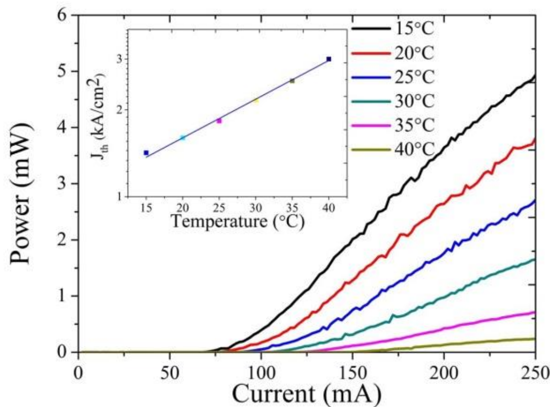

Figure 4.12. *Peak laser output power as a function of pulsed driving current at temperatures from 15 ℃ to 40 ℃, for a pulse length of 0.5 μs and a repetition rate of 20 kHz. The inset picture shows the dependence of the pulsed threshold current density on temperature.*

Figure 4.12 shows the laser output power coupled to the silicon waveguide as a function of the injected pulsed current (pulse duration 0.5 μs, period of 50 μs) at a stage temperature ranging from 15 ℃ to 40 ℃. As can be seen from the figure, the laser has a threshold current of 72 mA and a maximum (peak) output power of 4.7 mW at 15 ℃. The inset in Figure 4.12 plots the corresponding dependence of the threshold current density on temperature. The characteristic temperature T_0 is fitted to be 33K, which is in the typical range of 20K-50K for the recently demonstrated type-II lasers on InP substrate [1].

4.4.3 Towards a widely tunable single mode laser

In order to achieve single mode lasing with higher SMSR, the broadband DBR used in the Fabry-Perot laser structure should be replaced by a narrow band reflector, or integrating an additional wavelength selective element in the cavity, such as high quality factor micro-ring resonators (MRRs). Figure 4.13 shows the schematic of a tunable single mode III-V-on-silicon laser by integrating two cascaded MRRs in the Fabry-Perot cavity. Single mode lasing can be obtained by selecting one of multiple lasing modes of the Fabry-Perot cavity while filtering the other modes by the two MRRs. Besides, the lasing wavelength of this device can be tuned by thermally tuning the overlapping resonant peak of the two MRRs. The principle of this silicon waveguide filter consisting of two MRRs will be discussed in the fifth chapter in detail. As a proof of concept, Figure 4.14 shows a typical lasing spectrum of such a device, driven at 150 mA. A SMSR of more than 40 dB is achieved. In this device, micro-heaters on the MRRs have not been fabricated. So the output power is limited since the resonant peaks of the two MRRs are not perfectly aligned. To tune the lasing wavelength, micro-heaters will be integrated on the two MRRs in following research.

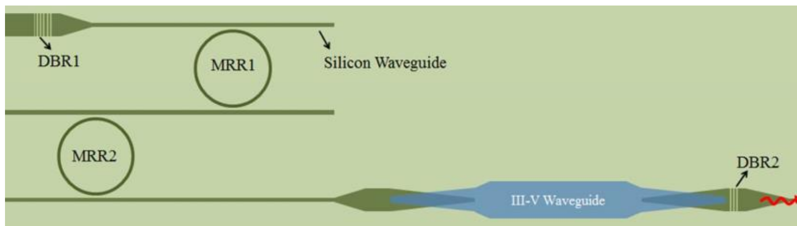

Figure 4.13. *Schematic of a tunable single mode III-V-on-silicon laser by integrating two cascaded MRRs in the Fabry-Perot cavity.*

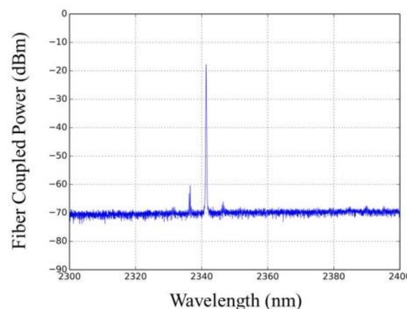

Figure 4.14. *Fiber-coupled emission spectrum from the tunable single mode III-V-on-silicon laser with 150 mA drive current.*

4.5 III-V-on-silicon 2.3 μm DFB laser

4.5.1 Distributed feedback laser for the 2 μm range

Although III-V-on-silicon lasers with integrated silicon waveguide filters in a Fabry-Perot cavity can offer high SMSR, these lasers also suffer from strong mode hopping during wavelength tuning. DFB lasers are attractive for spectroscopic sensing since they produce single mode output powers in the mW range and their device structure allows a few nanometers of (thermal) mode-hop-free wavelength tuning while still keeping high SMSR during the tuning. In DFB lasers, the optical feedback is obtained by the periodic variation of the effective index of the active waveguide. The periodic index variation is realized by introducing a Bragg grating. This optical feedback is very wavelength selective since the maximum reflectivity of the grating occurs around the Bragg wavelength, which determines the lasing wavelength. So the DFB laser emission wavelength is given by

$$\lambda_0 = \frac{2n_{eff} \cdot \Lambda}{m} \tag{4.1}$$

where λ_0 is the light wavelength in vacuum, n_{eff} is the effective refractive index of the optical mode in the active waveguide, Λ is the pitch of the Bragg grating and m is the diffraction order. The variations of heat-sink temperature and drive current of DFB lasers results in changes of the effective index of the active waveguides. Therefore, continuous mode-hop-free tuning can be achieved in DFB lasers by adjusting the drive current and heat-sink temperature.

For DFB lasers operating in the telecommunication wavelength range, InP- and GaAs-based heterostructures are often used as the gain medium. In these DFB lasers, buried DFB gratings are commonly used [13], then regrowth of III-V material is required after the DFB grating fabrication. For the 2 μm wavelength range, all of previously demonstrated DFB lasers are based on GaSb-based material systems or highly strained InP-based type-I material systems. However, regrowth of epitaxial layers on fabricated gratings is not well established for GaSb-based material systems. A commonly used approach is to use laterally-coupled metal gratings defined next to the III-V active waveguide as shown in Figure 4.15 [14,15]. This type of 2 μm range GaSb-based DFB lasers have been commercially produced by Nanoplus for gas sensing markets [16]. To date, the output power of 2 μm range DFB lasers using lateral coupled metal gratings has been limited to <10 mW. The option of fabricating laterally coupled DFB grating in the top cladding layer of the device also does not require a regrowth process. Based on this approach, a 2-mm-long DFB laser on GaSb

with maximum output power of 40 mW in single mode near 2.05 μm wavelength was demonstrated by Jet Propulsion Laboratory in 2012 [14]. In very recent years, GaSb-based DFB lasers with buried gratings have been developed thanks to better regrowth technology [17,18]. For example, based on this structure, a GaSb-based DFB laser operating at 2.2 μm was reported in 2014 [17]. A maximum output power closed to 30 mW is achieved at 15 ℃. Besides GaSb-based devices, InP-based type-I DFB lasers also have been demonstrated for the wavelength range near 2 μm[19,20]. Based on the mature technology of regrowth of epitaxial material on corrugated surfaces, InP-based DFB lasers with buried grating have shown good performance.

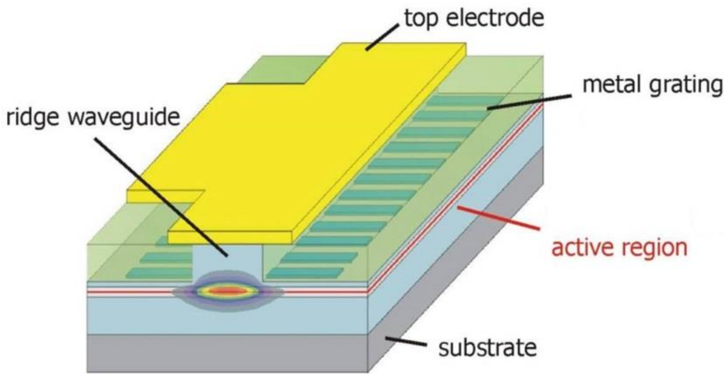

Figure 4.15. *A commonly used DFB laser structure for the 2 μm wavelength range, employing a laterally coupled metal grating as the feedback structure [15].*

4.5.2 Design and fabrication

The heterogeneously integrated InP-based type-II DFB laser is schematically shown in Figure 4.16 [21]. First-order DFB gratings with an etch depth of 180 nm in a 400 nm silicon device layer are defined beneath the III-V-on-silicon SOA. The tail of the optical mode interacts with this grating, which sets the emission wavelength of the laser. A quarter-wave shifted grating structure is implemented to break modal degeneracy and ensure single mode lasing. In this section, the DFB laser with a silicon grating pitch of 348 nm will be presented. The grating has a duty cycle of 50%. The light is coupled from the III-V active region to the silicon waveguide using III-V/silicon SSCs as shown in section 4.2.

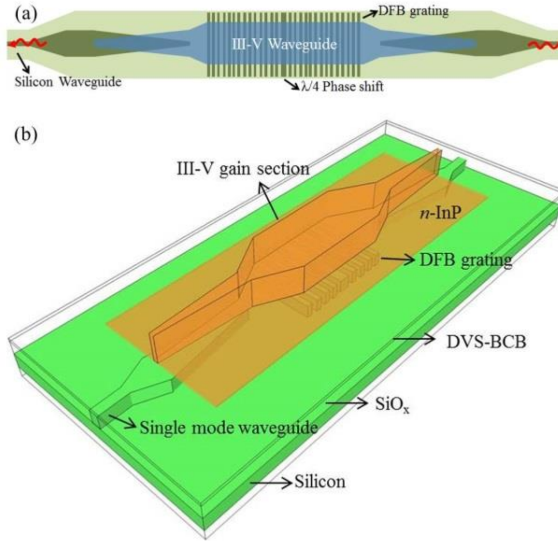

Figure 4.16. *(a) Top view and (b) three-dimensional schematic of a heterogeneously integrated InP-based type-II DFB laser on a silicon waveguide.*

For DFB lasers, the threshold current and output power depends on the coupling coefficient κ of the grating [22], which represents the optical reflection of the grating per unit length and is expressed in cm^{-1}. For a rectangular DFB grating with duty cycle Λ_d/Λ, the coupling coefficient can be written as:

$$\kappa = \frac{2(n_{eff}^{h} - n_{eff}^{l})}{\lambda_0} \cdot \sin(n \cdot \pi \frac{\Lambda_d}{\Lambda}) \tag{4.2}$$

where n_{eff}^{h} and n_{eff}^{l} is the effective refractive index of the optical mode in the unetched region (with higher effective refractive index) and etched region, n is the diffraction order. It is easy to understand that the maximum κ is achieved when the duty cycle Λ_d/Λ is 50% for a first order DFB grating. Using commercial software (FIMMWAVE) [8], n_{eff}^{h} and n_{eff}^{l} can be calculated based on the material parameters shown in Table 2.2. Figure 4.18 shows the calculated coupling coefficient of the first-order DFB grating (with duty cycle 50%) as a function of the DVS-BCB thickness and grating etch depth. With a 50 nm thick bonding interface, the coupling coefficient of the DFB grating is around 78 cm^{-1}, which reduces to 35 cm^{-1} as the thickness of DVS-BCB thickness increases to 100 nm.

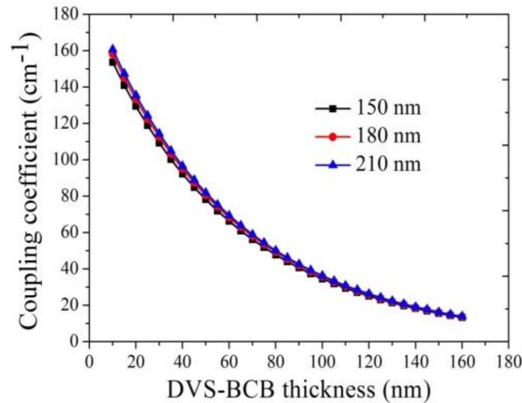

Figure 4.17. *Calculated coupling coefficient of the DFB grating as a function of the DVS-BCB thickness for three different etch depths (150, 180, 210 nm) in the 400 nm silicon device layer.*

The III-V epitaxial layer stack is adhesively bonded onto the processed silicon photonic IC using a 60 nm thick DVS-BCB layer (1:6 DVS-BCB: mesitylene). The general DFB laser process flow is identical to our previously demonstrated photodetectors, enabling the co-integration of both types of devices on the same silicon photonic IC for a fully integrated spectroscopic sensor. A SEM image of the longitudinal cross-section of the fabricated laser is shown in Figure 4.18, showing the quarter wave shifted silicon DFB grating, the DVS-BCB bonding layer and the III-V p-i-n layer stack.

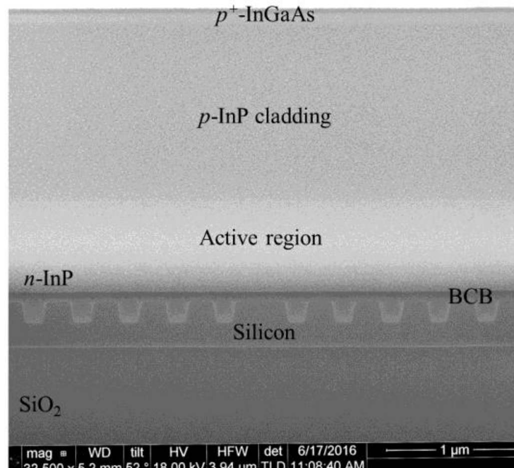

Figure 4.18. *SEM image of the longitudinal cross section of the III–V-on-silicon DFB laser.*

4.5.3 Measurements

The fabricated DFB lasers are characterized by collecting the light coupled to the silicon waveguides through integrated fiber-to-chip grating couplers. The measurement method is identical to that used to characterize Fabry-Perot lasers as presented in section 4.4.2. Figure 4.19 shows the light-current-voltage (L-I-V) curve of the DFB laser with a 348 nm period first-order grating. The series resistance of the laser is around 8 Ω. In order to characterize the L-I properties of the laser, the device is measured in CW regime at a temperature of 5˚C, 10˚C and 15˚C. At 5˚C, the III-V-on-silicon laser has a threshold current of 90 mA, which corresponds to a current density of 1.8 kA/cm^2. The threshold current density is much lower than the first demonstrated "W"-shaped InGaAs/GaAsSb quantum well lasers grown on InP substrate (~3.2 kA/cm^2 at 0 ˚C) [1]. The maximum on-chip output power is around 1.3 mW. The maximum CW operating temperature of the two lasers is around 17˚C. The threshold current and operating temperature can be improved by reducing the thermal resistance of the devices, e.g., by further reducing the DVS-BCB thickness and connecting the top *p*-contact to the silicon substrate. Reducing the series resistance by optimizing the metallization processes also can further improve the device performance.

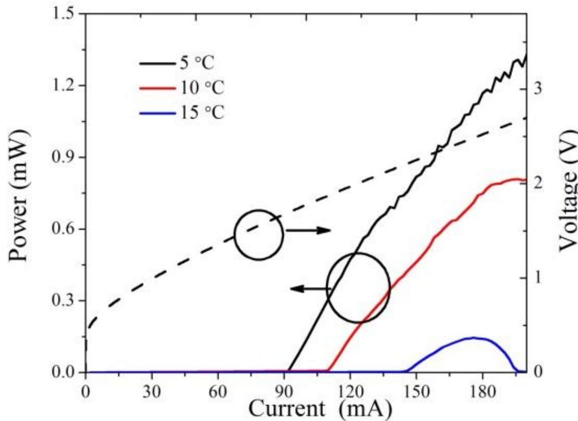

Figure 4.19. *CW L-I-V curve of the DFB laser with a 5 μm×1000 μm gain section and with a grating period of 348 nm.*

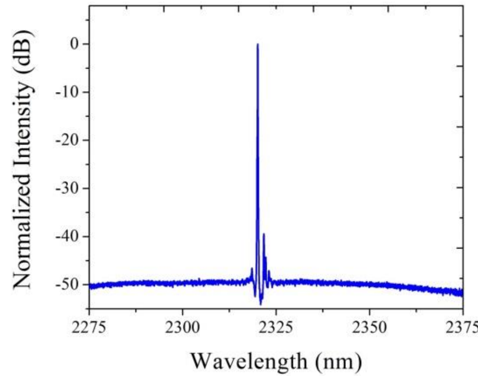

Figure 4.20. *Normalized emission spectrum of the DFB laser with a grating period of 348 nm, measured at 10 ℃ with 190 mA bias current.*

The laser emission spectrum is acquired using a Yokogawa AQ6375 OSA with a resolution bandwidth of 0.1 nm. Figure 20 shows the high resolution output spectrum of the laser with a grating period of 348 nm, biased at 190 mA at a temperature of 10 ˚C. The lasing wavelength is at 2320 nm. Single mode lasing with a SMSR around 40 dB is obtained, which can be improved to > 43 dB at 5 ˚C. A stop band $\Delta\lambda_{sb}$ of 3.2 nm wide is deduced from the emission spectrum. According to the coupled-mode theory of DFB lasers [22], the stop band width can be calculated based on the normalized coupling coefficient κL by the following expression:

$$\Delta\lambda_{sb} = \frac{\lambda_0^2}{\pi n_{eff} L}\sqrt{(\kappa L)^2 + \pi^2} \tag{4.3}$$

For the 1000 μm long laser structure, the normalized coupling coefficient κL is calculated to be 5.5, which is close to the simulated value shown in Figure 4.17.

Figure 4.21(a) shows the evolution of the laser emission spectra as a function of the heat-sink temperature at a fixed injected current of 190 mA. The dependence of the lasing wavelength on temperature is plotted in the insets. The measured temperature-tuning rate is ~0.15 nm/˚C. This tuning rate is determined by the change in effective index of the DFB lasers. The lasers emission spectra for different bias currents at a heat-sink temperature of 10 ˚C are shown in Figure 4.21(b). The corresponding laser wavelength versus bias current for heat-sink temperatures of 5˚C, 10˚C and 15˚C are shown in the inset. The current-tuning rate is about 0.01 nm/mA for the laser. Single-mode lasing behavior is observed over the whole bias current range as the heat-sink temperature varies from 5˚C to 15˚C. This indicates that no substantial spatial hole burning occurs in the DFB laser at high bias currents. At a heat-sink temperature of 10˚C, a

SMSR better than 35 dB over an injection current range of 120 mA-210 mA is obtained.

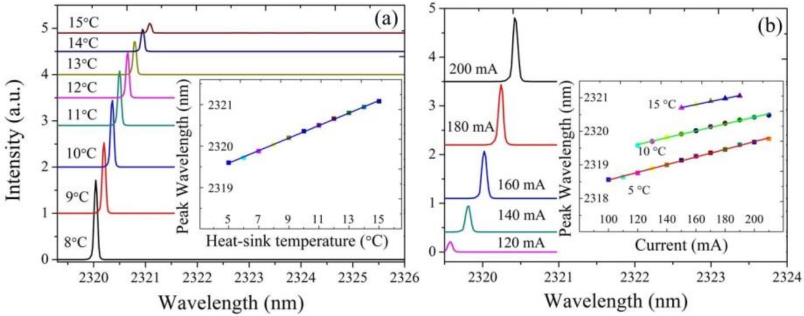

__Figure 4.21.__ (a) Evolution of the lasing spectra as a function of the heat-sink temperature for a laser with grating period of 348 nm. The device is biased at 190 mA. The inset pictures show the dependence of the lasing wavelength on temperature. (b) Emission wavelength as a function of bias current for the laser operated at a heat-sink temperature of 10 ˚C. The inset pictures show the laser wavelength as a function of injected current at a temperature of 5 ˚C, 10 ˚C and 15 ˚C.

4.5.4 Tunable diode laser absorption spectroscopy

As the first step on the path to TDLAS on a silicon photonic integrated circuit, the direct absorption spectroscopy of CO in a gas cell is carried out using our III-V-on-silicon DFB lasers as the light source. The gas cell contains pure CO at a pressure of 740 Torr [23], with a length of 10 cm and is AR-coated for 2.34 µm wavelength. In the sensing setup, the gas cell is positioned between the DFB laser with grating period of 348 nm and the detector. The light is coupled from the DFB laser to a single mode fiber through the on-chip grating coupler, and then coupled into and out of the gas cell through a collimator. The laser heat-sink temperature is fixed at 13 ˚C during the measurement. As the injection current increases, the DFB laser emission shifts to longer wavelength. When the lasing wavelength reaches the CO absorption wavelength, a strong dip can be observed in the L-I curve. Using the current-wavelength relationship extracted from measured data at 13 ˚C, the TDLAS spectrum of CO is shown in Figure 4.21. The current sweep step is 0.5 mA, which corresponds to a wavelength step of around 5 pm. It can be found that the peak absorption and fitted full width at half maximum (FWHM) of the experimental TDLAS spectrum matches very well to the reference HITRAN values [24]. These results showcase the potential of this laser source for on-chip spectroscopic gas sensing.

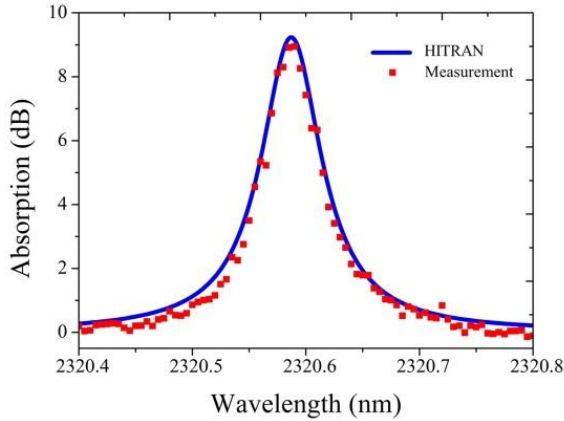

Figure 4.22. *TDLAS spectrum of CO and the corresponding HITRAN spectrum.*

4.6 Broad wavelength coverage 2.3 μm range III-V-on-silicon DFB laser array

In the previous section, we presented a 2.32 μm heterogeneous III-V-on-silicon DFB laser source based on an InP-based type-II heterostructure [21]. This laser has been proven to be suitable for carbon monoxide gas detection using direct absorption spectroscopy, but the tuning range (by changing the drive current) of a single device is limited to 2 nm. The development of a widely tunable silicon photonics laser source in the 2-3 μm range enables to simultaneously detect several gases or broad absorption features of bio-molecules on a compact chip [25,26]. Mid-infrared DFB laser arrays have been realized on a III-V substrate at wavelengths beyond 4 μm based on quantum cascade structures [27,28]. These arrays attract great interest for gas sensing applications [29]. However, 2-4 μm range DFB laser arrays and further integrating the arrays on a photonic IC still need to be demonstrated. In this section we report a broad wavelength coverage DFB laser array in the 2.3 μm wavelength range.

4.6.1 Design and Fabrication

The III-V-on-silicon DFB lasers in the laser array have the same structure as shown in Figure 4.16. Different lasing wavelengths are realized in the 2.3 μm range by varying the DFB grating pitch. A common *p*-contact pad is used, which also acts as a heat-spreader for the laser array as schematically shown in Figure 4.23 [30]. The used DVS-BCB bonding layer is 50 nm thick (1:8 DVS-BCB: mesitylene), which is thinner than that used to bond the DFB laser shown in the last section. The DVS-BCB thickness difference can be seen by comparing the

SEM image of the device cross section shown in Figure 4.18 and Figure 4.23 (b). From the data shown in Figure 4.14, this thinner bonding layer leads to a higher coupling coefficient (80 cm^{-1}) for the DFB grating.

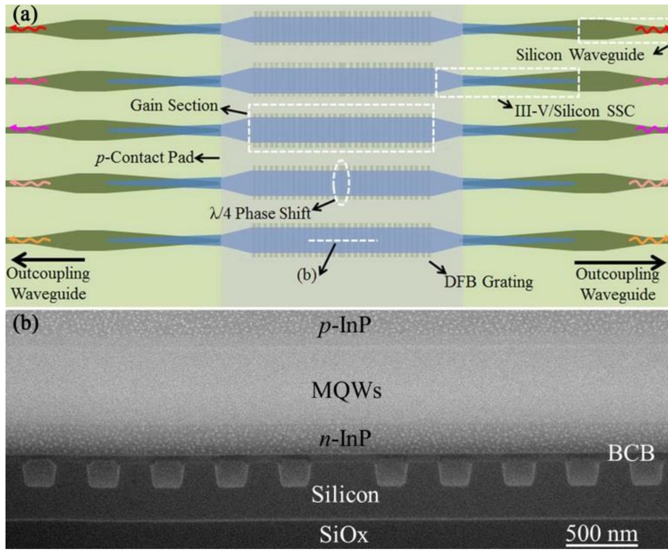

Figure 4.23. *(a) Schematic of the III-V-on-silicon DFB laser array; (b) SEM image of the longitudinal cross-section of the gain section.*

4.6.2 Measurement results

The I-V and CW on-chip L-I characteristics of a III-V-on-silicon DFB laser with a grating pitch of 353 nm are shown in Figure 4.24(a) at different heat-sink temperatures. The threshold current is 60 mA at 5 ˚C and increases to 110 mA at room temperature. For a device with a 3.8 μm wide and 1000 μm long gain section, these threshold current values correspond to a current density of 1.6 kA/cm^2 and 2.9 kA/cm^2, respectively. Figure 4.24(b) shows the fiber-coupled emission spectra as a function of the bias current. The stop band width deduced from the spectrum is around 3.8 nm, so a normalized coupling coefficient κL of 7.5 is calculated using equation 4.3. As seen in Figure 4.24(a) and 4.24(b), the band edge mode starts lasing as the bias current increases to 185 mA at 5 ˚C. In the current region II (185 mA-270mA) marked in 4.24(b), the DFB laser shows dual-mode operation. This is the result of spatial-hole burning in the DFB laser due to the high normalized coupling coefficient κL. In the current range I (60mA-185mA) and III (270mA-350mA), the DFB laser exhibits stable single mode operation. A tuning range of 1.5 nm and 1.2 nm is achieved in these two current ranges, respectively. The maximum single mode (SMSR>20 dB) on-chip

output power is 0.5 mW and 2.7 mW for the defect mode and band edge mode, respectively.

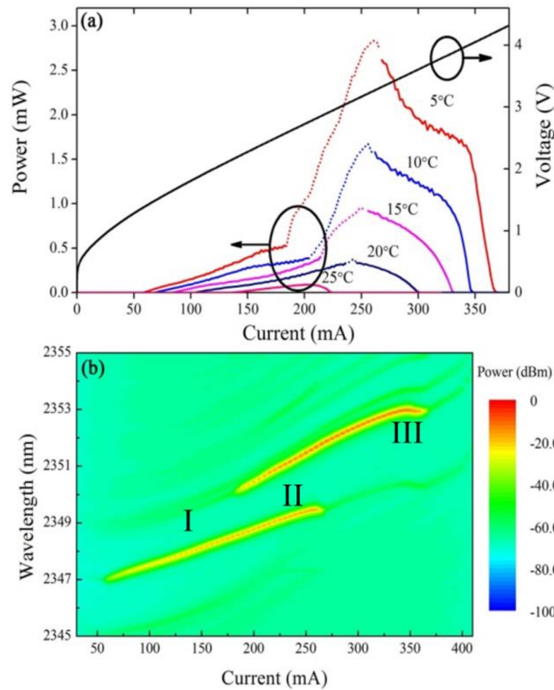

__Figure 4.24.__ (a) CW L-I-V characteristics of a heterogeneously integrated DFB laser with a grating pitch of 353 nm at different heat-sink temperatures. The solid portions of the L-I curve indicate a single-mode emission with a SMSR of at least 20 dB, while the dashed portions correspond to dual-mode operation. (b) Spectral map of the laser device as a function of the bias current at a heat-sink temperature of 5˚C.

Figure 4.25 shows the normalized emission spectra and maximum single mode output power (indicated by the stars) of six DFB lasers with silicon grating pitch ranging from 343 nm (Laser1) to 368 nm (Laser6). The lasers are 1000 µm long. A side mode suppression ratio (SMSR) of 30 dB is achieved for all the lasers. During measurements, all devices are driven in a CW mode at a heat-sink temperature of 5 ˚C, with 150 mA drive current for Laser1-Laser5 and 220 mA for Laser6. As the silicon grating pitch increases from 343 nm to 368 nm, the laser wavelength shifts from 2280 nm to 2430 nm. 1 nm change in the DFB grating pitch results in ~6 nm shift in the lasing wavelength. The 150 nm lasing wavelength span overlaps with the absorption window of several important gases, including CH_4, CO, NH_3, C_2H_2 and HF. The maximum on-chip output power in single mode increases from 1 mW at 2280 nm to 3.1 mW at

2375 nm and reduces to 0.2 mW at 2430 nm. This trend matches the amplified spontaneous emission spectrum of the devices.

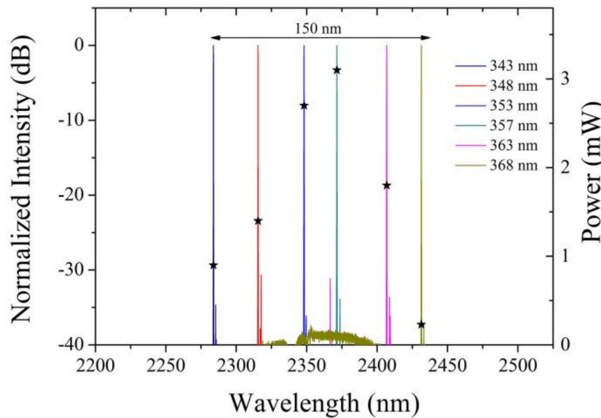

Figure 4.25. *Emission spectra and single mode peak output power of six DFB lasers with different silicon grating pitch in an array. The width of Laser1-Laser5 and Laser6 is 3.8 μm and 3.2 μm, respectively.*

An effective way to get rid of the mode hopping between the defect mode and band edge mode in the DFB laser is to have a device with a lower κL. Here, we present the results of III-V-on-silicon lasers with a 5 μm wide and 700 μm long gain section, corresponding to κL=5.6. The CW L-I-V characteristics of a DFB laser with grating pitch of 353 nm are shown in Figure 4.26(a). The threshold current is 62 mA (corresponding to a current density of 1.77 kA/cm^2) with a maximum on-chip output power of 1.8 mW at 190 mA at 5˚C. In CW mode, the laser can operate close to room temperature. Figure 4.26(b) shows the spectral map as a function of bias current at 5˚C. A tuning range of more than 3 nm is achieved with a current-tuning coefficient of around 0.19 nm/mA. Single mode lasing without mode hopping is observed in the whole CW operational current range (62 mA-245 mA). With this shorter cavity length, a DFB laser array is also fabricated on the same silicon chip as the 1000 μm long one. Figure 4.27 shows the emission spectra of four DFB lasers biased at 150 mA at 5˚C. All of these lasers have a 5 μm wide and 700 μm long gain section. The lasing wavelength shifts from 2290 nm to 2375 nm as the silicon grating pitch increases from 343 nm to 357 nm. The devices with grating pitch of 363 and 368 nm do not lase in CW mode at 5˚C. This narrower wavelength span is attributed to the lower κL of the 700 μm long DFB lasers, which results in higher mirror loss. A SMSR above 43 dB is achieved for all devices.

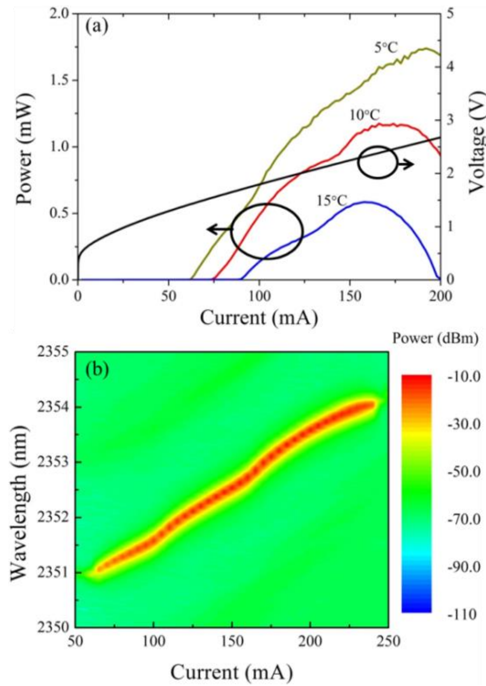

Figure 4.26. *(a) CW L-I-V plot of a heterogeneous InP-based type-II DFB laser with a 5 μm wide and 700 μm long gain section and grating pitch of 353 nm; (b) The inset shows the evolution of the laser emission spectrum with increasing bias current at 5˚C.*

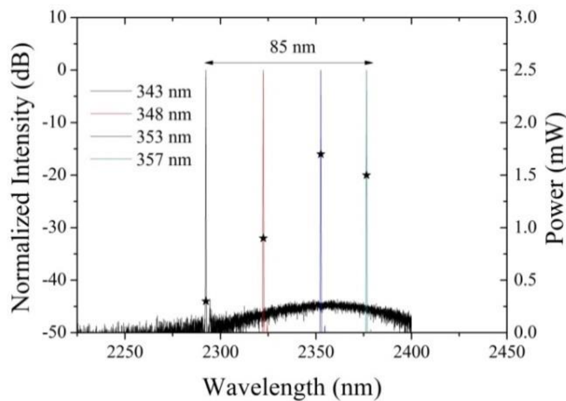

Figure 4.27. *Normalized lasing spectra of four 700 μm long DFB lasers with a grating pitch ranging from 343 nm to 357 nm.*

The tuning range of an individual DFB laser by varying the bias current is limited to about 3 nm as shown in the inset of Figure 4.26(b). So the silicon

grating pitch should be fabricated with 0.5 nm increments to get a continuously tunable DFB laser array, which is quite challenging for current silicon photonics pilot lines. Another method to control the lasing wavelength is to adjust the modal index of the device. As the modal index is dependent on the width of III-V waveguide, which can be controlled using standard III-V contact lithography, a laser array with fine emission wavelength spacing (<3 nm) can be achieved by varying the gain section width. Figure 4.28(a) and 4.28(b) show the normalized lasing spectra as a function of the bias current for a four- wavelength DFB laser array with a 700 μm long gain section and a silicon grating pitch of 353 nm and 357 nm, respectively. The III-V gain section width varies from 3.8 μm to 6 μm while the width of the silicon DFB grating underneath is fixed at 8 μm. All of the lasers are driven in CW mode at 5 ˚C. The wavelength spacing (~2.5 nm) of the lasers in each array is sufficiently small such that both arrays can continuously tune over a 10 nm wavelength range by varying the bias current. Laser arrays with much broader continuous-tuning range can be achieved by fabricating DFB gratings with a pitch step of 2 nm and varying the gain section width of five lasers with same grating pitch. In this way, in principle more than 100nm continuous wavelength coverage is possible. The corresponding laser output power as a function of the emission wavelength is shown in Figure 4.28(c) and 4.28(d). Our results also suggest a method of accurately controlling the lasing wavelength of III-V-on-silicon DFB lasers by changing the III-V waveguide widths, which can be applied as well for the realization of dense wavelength-division-multiplexed laser arrays on silicon for optical communication applications.

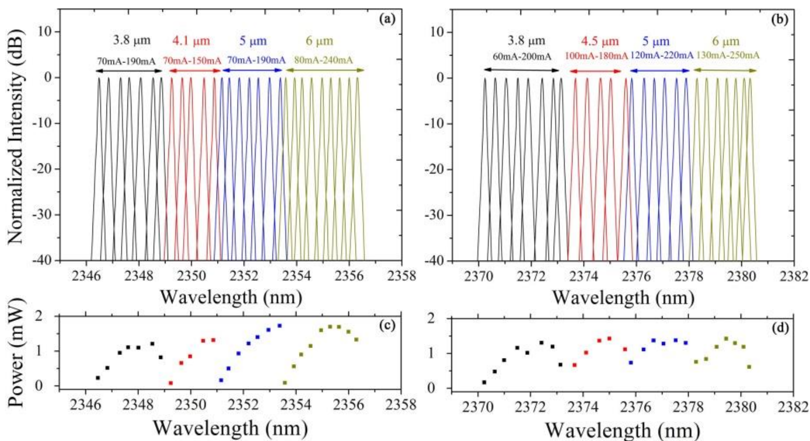

Figure 4.28. *Evolution of the lasing spectra as a function of the bias current (20 mA step) for four DFB lasers with different gain section widths and the same silicon grating pitch of 353 nm (a) and 357 nm (b). (c) and (d): the dependence of optical output power on lasing wavelength.*

4.6.3 Pulsed characterization and thermal resistance

Figure 4.29(a) shows the peak output power of the laser with grating pitch of 353 nm and 1000 μm×5 μm gain section as a function of drive current (pulse duration 0.5 μs, period of 50 μs) at a heat-sink temperature from 5 ˚C to 25 ˚C. At 5 ℃, the laser has threshold current of 40 mA and a peak output power of 6.8 mW. The maximum operation temperature in pulsed operation is 50 ˚C. The threshold current at various heat-sink temperatures is shown in Figure 4.29(b).

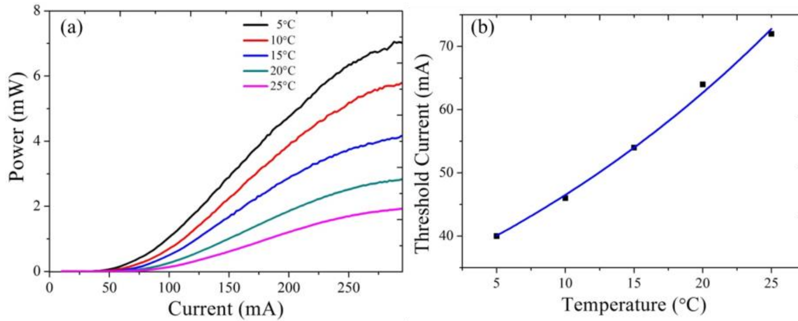

Figure 4.29. *(a) Peak laser output power as a function of pulsed drive current at temperatures from 5 ˚C to 25 ˚C; (b) Dependence of the pulsed threshold current on temperature.*

The temperature dependence of the threshold current can be described as follows:

$$I_{th}(T) = I_o e^{T/T_o}. \tag{4.4}$$

where $I_{th}(T)$ is the threshold current at an active region temperature of T, T_0 is the characteristic temperature. A characteristic temperature of 34 K is fitted from Figure 4.29(b). From Equation 4.4, the temperature rise of the active region in continuous wave (CW) regime can be calculated as:

$$\Delta T = T_0 ln\left[I_{th}(cw)/I_{th}(pulsed)\right] \tag{4.5}$$

Then, the thermal resistance R_{th} can be calculated using the known dissipated power in the device in CW operation [31]:

$$R_{th} = \Delta T / \Delta P \tag{4.6}$$

Based on the measured L-I-V data, a thermal resistance of 87 K/W is calculated. This high thermal resistance is attributed to the relatively high thermal impedance of the laser caused by the presence of the buried oxide layer with low thermal conductivity. The lasing threshold and maximum operating temperature could be further improved by reducing the thermal resistance of the device. Reducing the buried oxide thickness or connecting the top heat spreader to the

silicon substrate also can be used to reduce the thermal resistance. Besides, the carrier injection efficiency of the InP-based type-II epitaxial structure should be further enhanced to improve the maximum operating temperature.

4.7 Conclusion

This chapter starts with introducing the device performance of recently developed type-II quantum well diode lasers on InP substrate. In order to heterogeneously integrate these InP-based type-II lasers on silicon photonic ICs, an adiabatic III-V/silicon spot size converter is designed to achieve efficient optical coupling between the III-V waveguide and silicon waveguide. Based on the InP-based type-II quantum well structure and using adiabatic coupling, 2.3 μm range III-V-on-silicon Fabry-Perot lasers, DFB lasers and laser arrays are realized. The Fabry-Perot lasers consist of a III-V-on-silicon SOA and two silicon Bragg grating reflectors to form the laser cavity. In CW operation, we obtain a threshold current density of 2.7 kA/cm^2 and an output power of 1.3 mW at 5 °C for 2.35 μm Fabry-Perot lasers. In the DFB lasers, the III-V-on-silicon SOA is adhesively bonded to first-order silicon DFB gratings. These 2.3 μm range III-V-on-silicon distributed feedback (DFB) lasers can operate up to 25 ℃ in CW regime and show an output power of 3 mW in a single mode. By varying the silicon grating pitch, a DFB laser array with broad wavelength coverage from 2.28 μm to 2.43 μm is achieved. Four-channel DFB laser arrays with a continuous tuning range of 10 nm and side mode suppression ratio of 40 dB over the whole range are also demonstrated. A direct absorption measurement of CO indicates that our DFB lasers are suitable for gas sensing.

References

[1] S. Sprengel, A. Andrejew, K. Vizbaras, T. Gruendl, K. Geiger, G. Boehm, C. Grasse, and M.-C. Amann, "Type-II InP-based lasers emitting at 2.55 µm," Appl. Phys. Lett. **100**(4), 041109 (2012).

[2] S. Sprengel, G. Veerabathran, A. Andrejew, A. Köninger, G. Boehm, C. Grasse, and M. C. Amann, "InP-based type-II heterostructure lasers for wavelengths up to 2.7 µm," in SPIE Photonics West, Novel In-Plane Semiconductor Lasers XIV (SPIE, 2015), paper 9382–29.

[3] S. Stephan, D. Frederic, and M.-C. Amann, "Novel InP- and GaSb-based light sources for the near to far infrared," Semicond. Sci. Technol. **31**, 113005 (2016).

[4] S. Sprengel, G. Veerabathran, A. Köninger, F. Federer, G. Boehm, and M.-C. Amann, "InP-based type-II heterostructure lasers for 2.5 µm working CW at room temperature and above," in IEEE International Semiconductor Laser Conference (2014), paper MC.05.

[5] S. Sprengel, A. Andrejew, F. Federer, G. K. Veerabathran, G. Boehm, and M.-C. Amann, "Continuous wave vertical cavity surface emitting lasers at 2.5 µm with InP-based type-II quantum wells," Appl. Phys. Lett. **106**(15), 151102 (2015).

[6] C. H. Pan, C. H. Chang, and C. P. Lee, "Room Temperature Optically Pumped 2.56- µm Lasers With "W" Type InGaAs/GaAsSb Quantum Wells on InP Substrates," IEEE Photon. Tech. Lett. **24**(13), 1145-1147(2012).

[7] C.-H. Chang, Z. –L. Li, H.-T. Lu, C. -H. Pan, C. –P. Lee, G. Lin, S.-D. Lin, "Low-threshold short-wavelength infrared InGaAs/GaAsSb 'W'-type quantum well laser on InP substrate," IEEE Photon. Tech. Lett. **27**(3), 225 – 228 (2015).

[8] https://www.photond.com.

[9] J. H. Northern, A. W. J. Thompson, M. L. Hamilton, and P. Ewart, "Multi-species detection using multi-mode absorption spectroscopy (MUMAS)," Appl. Phys. B **111**(4), 627–635 (2013).

[10] M. L. Hamilton, G. A. D. Ritchie, Y. Arita, and P. Ewart, "Multi-mode absorption spectroscopy, MUMAS, using wavelength modulation and cavity enhancement techniques," Appl. Phys. B **100**(3), 665–673 (2010).

[11] A. Hangauer, J. Westberg, E. Zhang, and G. Wysocki, "Wavelength modulated multiheterodyne spectroscopy using Fabry-Pérot quantum cascade lasers," Opt. Express **24**(22), 25298-25307 (2016).

[12] R. Wang, S. Sprengel, G. Boehm, M. Muneeb, R. Baets, M. C. Amann, and G. Roelkens, “2.3 μm range InP-based type-II quantum well Fabry-Perot lasers heterogeneously integrated on a silicon photonic integrated circuit,” Opt. Express **24**(18), 21081–21089 (2016).

[13] J. L. Zilko, L. J. P. Ketelsen, Y. Twu, D. P. Wilt, S. G. Napoltz, J. P. Blaha, K. E. Strege, V. G. Riggs, D. L. Van Haren, S. Y. Leung, P. M. Nitzche, J. A. Long, C. B. Roxlo, G. Przyblek, J. Lopata, M. W. Focht, and J. Koszi, “Growth and characterization of high yield, reliable, high-power, high-speed, InP/InGaAs capped mesa buried heterostructure distributed feedback (CMBH-DFB) lasers,” IEEE J. Quantum Electron. **25**(10), 2091–2095 (1989).

[14] T. Bleuel, M. Müller, and A. Forchel, “2-μm GaInSb-AlGaAsSb distributed-feedback lasers,” IEEE. Photon. Technol. Lett. **13**, 553–555 (2001).

[15] http://nanoplus.com.

[16] S. Forouhar, R. M. Briggs, C. Frez, K. J. Franz, and A. Ksendzov, “High-power laterally coupled distributed-feedback GaSb-based diode lasers at 2 μm wavelength,” Appl. Phys. Lett. **100**(3), 031107 (2012).

[17] Q. Gaimard, L. Cerutti, R. Teissier, and A. Vicet, “Distributed feedback GaSb based laser diodes with buried grating,” Appl. Phys. Lett. **104**(16), 161111 (2014).

[18] Q. Gaimard, M. Triki, T. Nguyen-Ba, L. Cerutti, G. Boissier, R. Teissier, A. Baranov, Y. Rouillard, and A. Vicet, “Distributed feedback GaSb based laser diodes with buried grating: a new field of single-frequency sources from 2 to 3 μm for gas sensing applications,” Opt. Express **23**(15), 19118–19128 (2015).

[19] M. Mitsuhara, M. Ogasawara, M. Oishi, H. Sugiura, and K. Kasaya, “2.05- μ m wavelength InGaAs-InGaAs distributed-feedback multiquantum-well lasers with 10-mW output power,” IEEE Photon. Tech. Lett. **11**(1), 33-35 (1999).

[20] F. Xu, S. Luo, F. Gao, H.-M. Ji, Z.-R. Lv, X.-G. Yang, and T. Yang, “2004-nm Ridge-Waveguide Distributed Feedback Lasers With InGaAs Multi-Quantum Wells,” IEEE Photon. Tech. Lett. **28**(20), 2257-2260 (2016).

[21] R. Wang, S. Sprengel, A. Malik, A. Vasiliev, G. Boehm, R. Baets, M.-C. Amann, G. Roelkens, “Heterogeneously integrated III–V-on-silicon 2.3x μm distributed feedback lasers based on a type-II active region,” Applied Physics Letters, **109**, 221111 (2016).

[22] G. Morthier and P. Vankwikelberge, Handbook of Distributed Feedback Laser Diodes (Arctech House, Norwood, MA, 1997).

[23] http://www.wavelengthreferences.com/

[24] L. S. Rothman, I. E. Gordon, Y. Babikov, A. Barbe, D. Chris Benner, P. F. Bernath, M. Birk, L. Bizzocchi, V. Boudon, L. R. Brown, A. Campargue, K. Chance, E. A. Cohen, L. H. Coudert, V. M. Devi, B. J. Drouin, A. Fayt, J.-M. Flaud, R. R. Gamache, J. J. Harrison, J.-M. Hartmann, C. Hill, J. T. Hodges, D. Jacquemart, A. Jolly, J. Lamouroux, R. J. Le Roy, G. Li, D. A. Long, O. M. Lyulin, C. J. Mackie, S. T. Massie, S. Mikhailenko, H. S. P. Müller, O. V. Naumenko, A. V. Nikitin, J. Orphal, V. Perevalov, A. Perrin, E. R. Polovtseva, C. Richard, M. A. H. Smith, E. Starikova, K. Sung, S. Tashkun, J. Tennyson, G. C. Toon, V. G. Tyuterev, and G. Wagner, "The HITRAN2012 molecular spectroscopic database," J. Quant. Spectrosc. Radiat. Transf. **130**, 4–50 (2013).

[25] B. L. Upschulte, D. M. Sonnenfroh, and M. G. Allen, "Measurements of CO, CO_2, OH, and H_2O in room-temperature and combustion gases by use of a broadly current-tuned multisection InGaAsP diode laser," Appl. Opt. **38**, 1506-1512 (1999).

[26] D. Weidmann, A. A. Kosterev, F. K. Tittel, N. Ryan, and D. McDonald, "Application of a widely electrically tunable diode laser to chemical gas sensing with quartz-enhanced photoacoustic spectroscopy," Opt. Lett. **29**, 1837-1839 (2004).

[27] B. G. Lee, M. Belkin, C. Pflugl, L. Diehl, H. A. Zhang, R. M. Audet, J. MacArthur, D. Bour, S. Corzine, G. Hofler, and F. Capasso, "Distributed feedback quantum cascade laser arrays," IEEE J. Quantum Electron. **45**, 554–565 (2009).

[28] P. Rauter and F. Capasso, Laser Photonics Rev. "Multi-wavelength quantum cascade laser arrays," **9**, 452-477 (2015).

[29] L. Bizet, R. Vallon, B. Parvitte, M. Brun, G. Maisons, M. Carras, V. Zeninari, "Multi-gas sensing with quantum cascade laser array in the mid-infrared region," Appl. Phys. B **123**, 145 (2017).

[30] R. Wang, S. Sprengel, G. Boehm, R. Baets, M.-C. Amann, and G. Roelkens, "Broad wavelength coverage 2.3 μm III-V-on-silicon DFB laser array," Optica, **4**, 972 (2017).

[31] K. Doi, T. Shindo, J. Lee, T. Amemiya, N. Nishiyama, and S. Arai, "Thermal analysis of lateral current injection membrane distributed feedback laser," IEEE J. Quantum Electron. **50**, 321–326 (2014).

5

Widely tunable GaSb/silicon hybrid external cavity laser

5.1 Introduction

Compact semiconductor lasers with wide tunability around 2 μm wavelength enable high-performance trace gas sensors for CO_2 and other atmospheric trace gases. In the previous chapter, we demonstrated 2.3 μm wavelength range heterogeneously integrated III-V-on-silicon DFB laser arrays based on a InP-based type-II active region. In the 2 μm wavelength range, GaSb-based laser sources have better performance than currently available InP-based lasers. However, the heterogeneous integration processes of GaSb-based active devices on silicon are less mature than that of InP-based devices, which eventually results in lower device yield and performance, as we discussed in the second chapter. In this chapter, we report compact external cavity lasers using a GaSb-based gain chip and silicon photonic integrated circuit (IC) for wavelength selective feedback. The light coupling between the GaSb-based chip and silicon photonic IC is realized using butt-coupling, thereby avoiding the heterogeneous integration. In the devices, a silicon spot size converter (SSC) is designed to achieve an efficient butt-coupling. Widely and quasi-continuously tunable silicon photonic filters are realized using two micro-ring resonators (MRRs) and a phase section. The CMOS compatible fabrication of the silicon photonic IC ensures a high-volume, low-cost and reliable manufacturing of the GaSb/silicon hybrid laser. Besides, the external feedback cavity is ultra-compact since silicon-on-insulator (SOI) is a high-index-contrast material system.

5.2 External cavity laser

After decades of development, semiconductor lasers have become an important part of modern technology. The rapid growth of applications of tunable semiconductor lasers requires that the tuning range becomes increasingly wider and size becomes smaller. The integration of a semiconductor gain chip with an external cavity is an attractive solution to realize widely tunable single mode lasers. External cavity lasers can provide much wider tuning and narrower linewidth compared with vertical cavity surface emitting lasers (VCSELs) and distributed feedback (DFB) lasers [1].

In the classical external cavity laser, light from a semiconductor gain chip is coupled to an external cavity that incorporates a diffraction grating as a frequency-selective element, which can provide wavelength-selective feedback to the gain chip. Typically, there are two kinds configurations used, which are named Littrow and Littman configuration as shown in Figure 5.1.

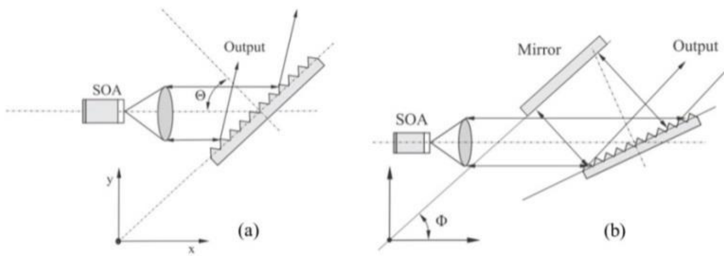

Figure 5.1. *Two principal designs of semiconductor external cavity lasers with bulk diffraction gratings: (a) Littrow configuration and (b) Littman configuration [1].*

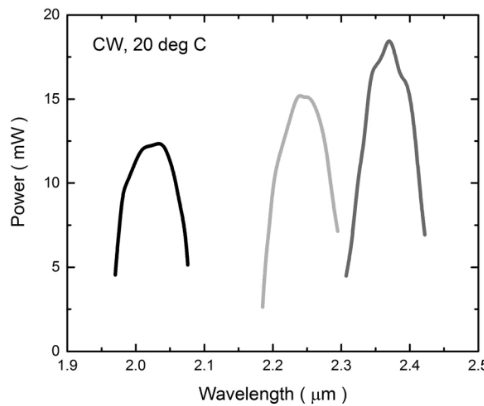

Figure 5.2. *Tuning curve of three GaSb-based external cavity lasers based on the Littrow configuration [3].*

The lasing wavelength of both designs is given by the grating equation:

$$n\lambda = d(\sin\phi + \sin\varphi) \qquad (5.1)$$

where n is the diffraction order, λ is the diffracted wavelength, d is the grating constant (the distance between grooves), ϕ is the incident angle (measured with respect to the grating normal), and φ is the diffracted angle. In the Littrow configuration, the diffraction grating is oriented so that the first-order diffraction is retro-reflected back into the gain chip, i.e., $\phi = \varphi = \theta$. Then, the equation 5.1 reduces to the following:

$$n\lambda = 2dsin\theta \qquad (5.2)$$

When the laser cavity is designed such that only one longitudinal mode is reflected back to the gain chip, the external cavity laser produces a single wavelength emission. Wavelength tuning can be achieved by rotating the diffraction grating.

In the Littman configuration, the diffraction grating is fixed, and the first-order beam is reflected back to the gain chip by an additional mirror as shown in Figure 5.1(b). This configuration can provide a fixed direction of the output beam, and also offers a narrower linewidth since the wavelength selectivity is stronger. However, its output power is lower than the in the Littrow configuration because the zero-order reflection of the beam reflected by the tuning mirror is lost.

The first 2 μm range semiconductor laser based on these external cavity configurations was demonstrated in 2004, using a GaSb-based gain chip [2]. The 2.1 μm laser exhibited a total tuning range of 43 nm with an optical output power of up to 14.7 mW. Recently, K. Vizbaras *et al.* reported 2 μm range external cavity lasers with tuning range around 120 nm based on Littrow configuration [3]. Using three different GaSb-based gain chip, maximum output powers of 13.6 mW at 2.05 μm, 16.7 and 18.6 mW for 2.25 and 2.38 μm were achieved, respectively, as shown in Figure 5.2 .

As a bulky optics system and mechanical controllers are required, the external cavity laser based on Littrow and Littman configurations are often heavyweight and expensive. Figure 5.3 shows an example of a commercial external cavity laser [4]. The dimension of the device is around 19cm×16cm×0.8cm, while it weighs a few kilograms. For some applications, e.g. portable spectroscopic sensing systems, more compact, lightweight and cost-effective widely tunable semiconductor lasers are required.

Figure 5.3. *A picture of an external cavity laser from Thorlabs [4].*

Photonic integrated circuits can be used to provide external feedback to a III-V gain chip in order to realize compact widely tunable lasers. Different

integrated photonics platforms have been developed to realize this for the telecommunication wavelength range, including polymer [5], silica [6], silicon nitride [7], and silicon [8,9]. Among these platforms, silicon photonics attracts a lot of interest since it can offer highly compact waveguide structures. Besides, it takes advantage of mature CMOS processes, allowing the fabrication of compact photonic circuits at low cost. Also, the circuits can efficiently be tuned by integrated micro-heaters. In the next section, I will introduce the design of a widely tunable GaSb/silicon hybrid external cavity laser using a silicon photonic IC as the feedback circuit.

5.3 Design of GaSb/silicon hybrid external cavity laser

5.3.1 A general overview of the device design

The hybrid laser consists of a GaSb-based superluminescent diode (SLD) used as the gain chip and a silicon photonic IC used as the external feedback circuit, as schematically shown in Figure 5.4 [10]. The light coupling between the gain chip and silicon photonic IC is realized by a silicon SSC. A Fabry-Perot laser cavity is formed between the HR-coated gain chip facet and a silicon waveguide DBR. The silicon photonics external cavity contains a Vernier filter consisting of two thermally tuned MRRs and a phase section to allow for quasi-continuous wavelength tuning. A Ti/Au micro-heater is integrated on the Vernier filter and phase section to thermally tune the lasing wavelength.

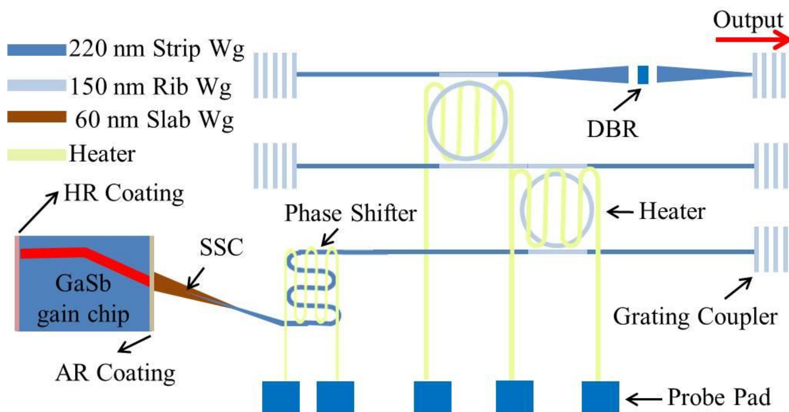

Figure 5.4. *Schematic of a tunable GaSb/silicon external cavity laser using a silicon photonic IC as the feedback circuit.*

The silicon photonic IC consists of 0.7 μm wide strip waveguides and 0.9 μm wide rib waveguides (70 nm shallow etched). The MRRs and bus waveguides are based on rib waveguides which have lower propagation loss and allow realizing MRRs with higher Q-factor, while the phase section is implemented as a spiral-shaped strip waveguide to allow a small footprint. A 10 μm long silicon waveguide tapered from 0.9 μm to 0.7 μm is used as a SSC to convert the optical mode between the strip waveguide and rib waveguide. The simulated reflection and loss in the strip/rib waveguide SSC is lower than −50dB and 0.2 dB, respectively. 17 μm × 20 μm grating couplers with a period of 0.9 μm and duty cycle of 0.5 are connected with silicon waveguides for device characterization.

5.3.2 GaSb-based gain chip

A GaSb-based SLD is used as the gain chip in our external cavity laser, since its wide spectral width can cover a wide tuning range [3]. The SLD is manufactured by Brolis Semiconductors. The GaSb-based epitaxial structure is grown on a 3-inch Te-doped GaSb substrate by a molecular beam epitaxy system. Compressively strained $Ga_{0.7}In_{0.3}As_{0.03}Sb_{0.97}$ quantum-wells separated by $Al_{0.1}Ga_{0.9}As_{0.01}Sb_{0.99}$ barriers are used as the active region for the gain chip operating around 2.05 μm wavelength. After the epitaxial growth, the wafers are processed into single-angled-waveguide gain chips. For single-spatial mode operation, a ridge of 5 μm width and 2 μm height is chosen and defined using inductively-coupled plasma (ICP) etching and reactive-ion etching (RIE). After ridge definition, a top Ti/Pt/Au layer is deposited using e-beam evaporation as ohmic contacts. Then a 4 μm thick electroplated Au heatsink was applied for improved heat removal. Afterwards, the wafers were thinned down to 120 μm, and the back side Ti/Pt/Au contact was evaporated. The processed III-V wafer is cleaved into 2 mm long bars and AR/HR coatings are applied. A single layer of Ta_2O_5 is used as the AR coating, resulting in <0.1% reflectivity. For the HR side, a multiple quarter-wavelength stack of Si/SiO_2 is used to achieve a reflectivity above 95%. The devices are In bonded to a C-mount. To reduce the facet reflection and the spectral ripple of the SLD, the gain chips used in this work had a facet with a tilt-angle of 5.2 degrees.

5.3.3 Chip-to-chip coupling

The optical mode field diameter at the facet is 4.72 μm × 1 μm (width × height) for the GaSb-based gain chip used in this work. The III-V waveguide angle at the facet is 5.2 degrees, which corresponds to an emission angle of 19.5 degrees in air. The butt coupling between the GaSb gain chip and silicon photonic IC is realized by a silicon SSC, schematically shown in Figure 5.5.

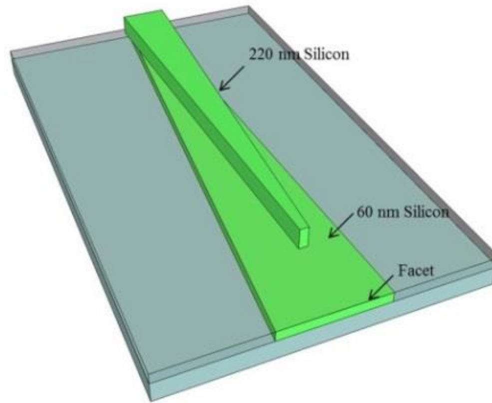

Figure 5.5. *Schematic of the silicon spot size converter.*

At the silicon SSC facet, a 6 μm × 0.06 μm silicon slab waveguide tilted 12 degrees is used to achieve good coupling between the silicon SSC and III-V waveguide. A top view microscope image of the silicon SSC is shown in Figure 5.6(a). Figure 5.6(b) shows the TE-polarized fundamental mode intensity distribution at the facet of the silicon SSC. Simulations indicate a butt-coupling loss of 1 dB at the GaSb/silicon slab waveguide interface. In order to efficiently convert the mode from the slab waveguide to that of the single mode strip waveguide (0.7 μm × 0.22 μm), a 200 μm long silicon taper structure is used in the SSC. Figure 5.6(c) shows the simulated mode conversion loss in the slab/strip waveguide SSC as a function of the taper tip width. Considering the fabrication capabilities of the CMOS line, a 180 nm wide taper tip is used. The calculated reflection in this slab/strip waveguide SSC is lower than -30 dB. A SEM image of the silicon taper tip is shown in the inset of Figure 5.6(c).

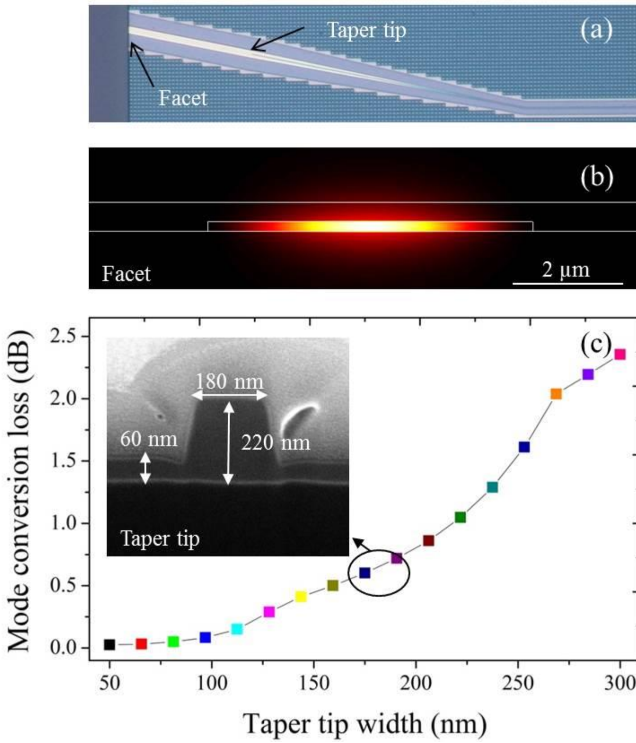

Figure 5.6. *(a) Microscope image of the silicon SSC; (b) TE-polarized fundamental mode intensity distribution at the facet of the SSC at a wavelength of 2 µm; (c) simulated mode conversion loss for SSCs with different taper tip width, a SEM image of the 180 nm wide taper tip is shown in the inset.*

5.3.4 Distributed grating reflector

As the terminal GaSb-facet in the laser cavity is HR coated, a silicon waveguide DBR is implemented in the end of silicon photonic IC to form a Fabry-Perot cavity. The design of the DBR reflectivity is a tradeoff between output power and threshold current. In our device, the DBR consists of two 250 nm wide slits spaced 500 nm, etched through the 220 nm silicon device layer. Simulations show that the DBRs have a reflectivity of more than 65% in the 2 µm wavelength range (TE-polarization) as shown in Figure 5.7(a). A scanning electron microscope (SEM) image of the fabricated DBR is shown in Figure 5.7(b).

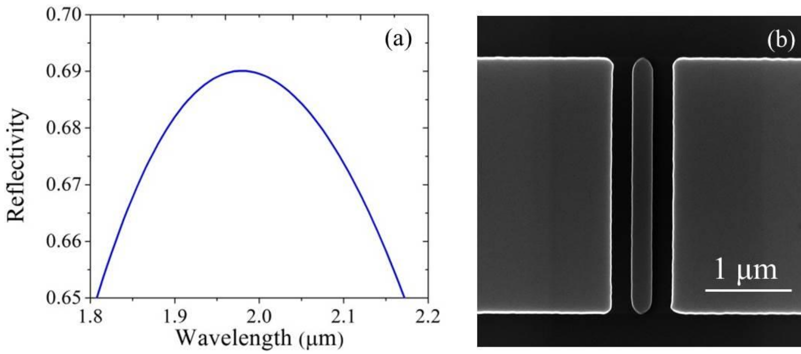

Figure 5.7. *(a) Simulated reflectivity of the DBR outcoupling mirror; (b) SEM image of the fabricated DBR.*

5.3.5 Vernier filter

Silicon MRRs are used here as filters to select the lasing wavelength out of the Fabry-Perot cavity modes. Therefore, the free spectral range (FSR) of the filter should be larger than the bandwidth of the amplified spontaneous emission (ASE) spectrum of the gain chip to achieve stable single mode lasing. The FSR of the MRR is determined as follow:

$$FSR = \frac{\lambda^2}{n_g L_{ring}} \tag{5.3}$$

where L_{ring} is the circumference of the MRR, λ is the wavelength and n_g is the group index of the silicon waveguide. The radius of the microring should be smaller than 3.5 μm if a single resonator is used to achieve an FSR larger than 50 nm. In that case, the ring resonator quality factor would be compromised by the severe leakage loss in the ring resonator structure. In this work, a cascade of two silicon MRRs, acting as a Vernier filter, is used to achieve single mode lasing and wide tuning. Figure 5.8(a) shows the calculated transmission spectra of two MRRs with FSR of 6 nm and 6.5 nm at 2.03 μm wavelength, assuming a coupling coefficient κ=0.3 and no waveguide loss.

As the FSR of both the MRRs is slightly different, the individual transmission peaks are slightly shifted with respect to each other. The transmission spectrum of the Vernier filter is shown in Figure 5.8(b), which is the product of transmission spectra of the two MRRs. The transmittance reaches a maximum where the resonant peaks of the individual ring resonators overlap, which determines the lasing wavelength of the external cavity laser. By thermally adjusting the position of the overlapping transmission peaks the lasing

wavelength can be tuned. The tuning range is limited by the FSR of the Vernier filter, which is given by:

$$\Delta\lambda = \left| \frac{FSR1 \cdot FSR2}{FSR1 - FSR2} \right| \tag{5.4}$$

where FSR1 and FSR2 are the FSRs of the two MRRs. In this work, the Vernier filter consists of two MRRs with designed FSR of 6 nm (Ring1, corresponding to a ring radius of 31.5 μm) and 6.5 nm (Ring2, corresponding to a ring radius of 29 μm).

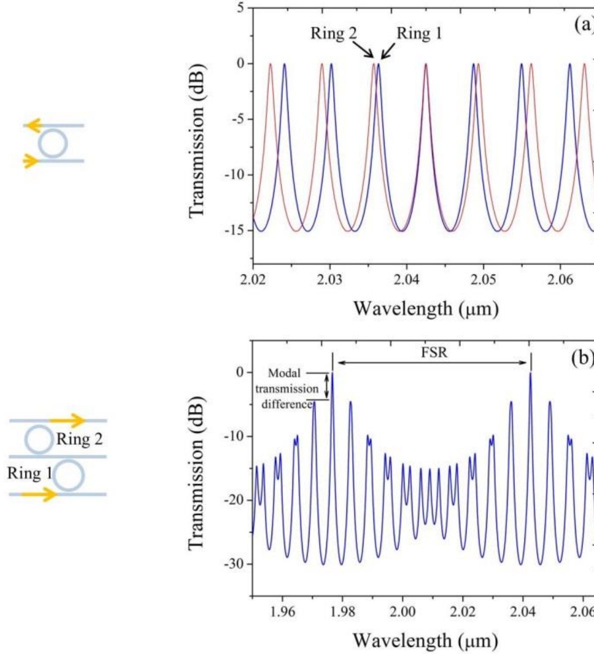

Figure 5.8. *(a) Simulated transmission spectra of two different MRRs with coupling coefficient κ=0.3; (b) transmission spectrum of the Vernier filter.*

The modal transmission difference between the dominant lasing mode and the nearest side-mode [marked in Fig. 5.8(b)] can significantly affect the SMSR and stability of the laser. The calculated dependence of the transmission difference on the coupling coefficient of the MRRs is shown in Figure 5.9. It can be found that the transmission difference monotonically decreases as the coupling coefficient increases. The coupling coefficient can be controlled by adjusting the coupling gap between the MRRs and bus waveguides. In our work, three pairs of MRRs with coupling gap of 200nm, 350 nm and 500 nm are used in the laser feedback circuit, which have a simulated coupling coefficient κ of around 0.3, 0.13 and 0.06 at a wavelength of 2 μm, respectively.

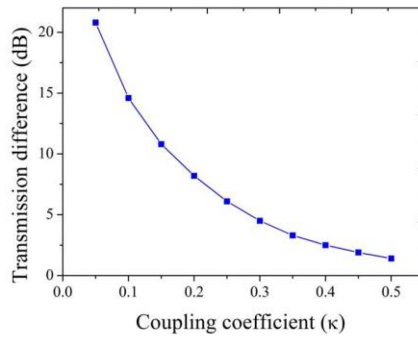

Figure 5.9. *Modal transmission difference between the dominant lasing mode and the nearest side-mode as a function of the coupling coefficient of the MRRs.*

5.4 Fabrication

The silicon photonic ICs are fabricated in a CMOS pilot line on 200 mm silicon-on-insulator (SOI) wafers with a 220 nm thick silicon device layer and a 2 μm thick buried oxide layer. Silicon waveguide structures are defined by 193 nm deep UV lithography and etched by ICP dry etching. 220 nm, 150nm and 70nm deep dry etching are carried out to fabricate the strip, slab and rib silicon waveguide, respectively. This silicon photonics platform is used rather than the platform with 400 nm thick silicon layer shown in the previous two chapters as the 150 nm deep etching in the 220 nm silicon layer can produce efficient spot size converters to couple light from the III-V gain chip to silicon photonic ICs. On top of the silicon photonic IC, a 1.2 μm thick SiO_2 layer is deposited as the top cladding. A microscope image of the fabricated silicon photonics feedback structure for the GaSb/silicon hybrid laser is shown in Figure 5.10.

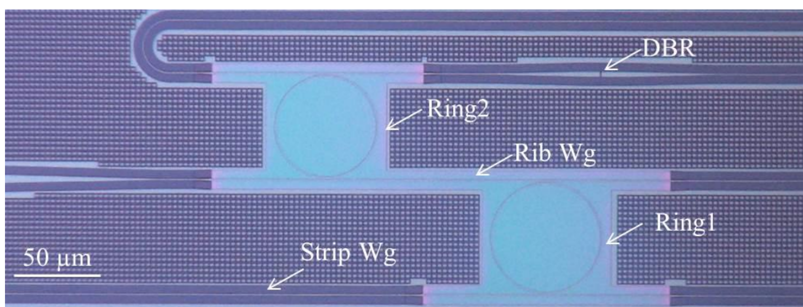

Figure 5.10. *Microscope image of the fabricated silicon waveguide circuit.*

In the silicon photonic IC, metal heaters are used to control the resonant peaks of MRRs and tune the lasing wavelength of the hybrid laser. After the fabrication of the passive photonic ICs at IMEC, the metal heaters were processed on the SOI sample at the clean room of Ghent University. The heaters contain two levels of metal wires for the heater resistor and contacting layer. The first metal layer is a high resistivity layer, which consists of 100 nm of titanium and 10 nm of gold. While in the second layer, 500 nm thick gold is used to realize contacting wires and pads. The second metal layer overlaps with the first layer except in the metal spiral on the MRRs. Therefore, the input electrical power is mainly dissipated in the metal on top of the MRRs, which results in a temperature increase and in a shift of the resonant peak of the MRRs. Figure 5.11 shows a microscope image of the fabricated heaters.

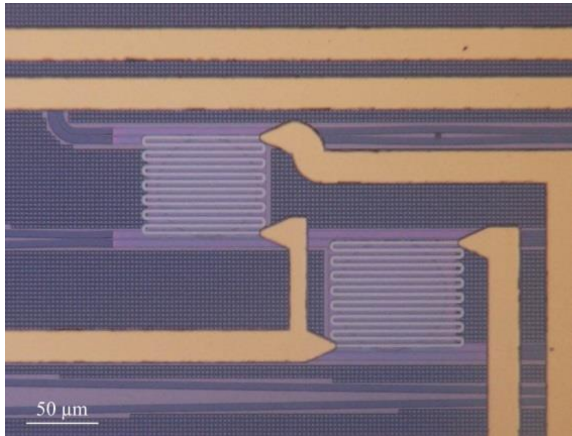

Figure 5.11. *Microscope image of the metal heater on the silicon MRRs.*

5.5 Characterization of the Vernier filter

In the silicon photonic IC, waveguide spirals with different length are fabricated for waveguide propagation-loss measurement. The measured loss of the strip waveguide and rib waveguide is around 1.8 dB/cm and 0.6 dB/cm for TE-polarized light at 2 μm wavelength, respectively.

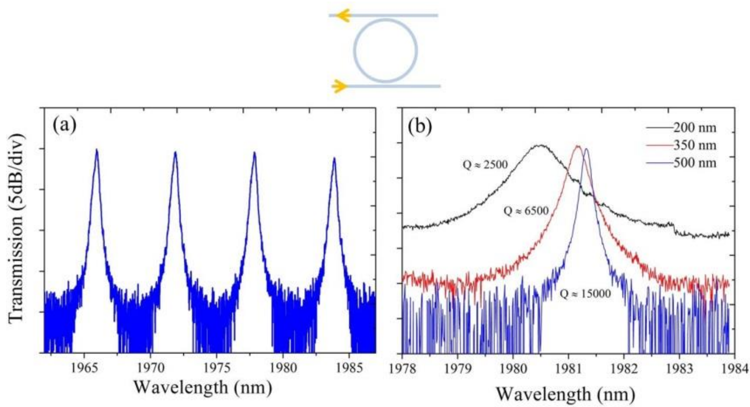

Figure 5.12. *(a) Transmission spectrum of a SOI MRR with coupling gap of 350 nm, measured from the drop port; (b) Comparison of the quality factor of three MRRs with different coupling gaps.*

Since the Vernier filter plays a key role in the silicon circuit, a detailed characterization of the silicon MRRs is carried out. Figure 5.12(a) shows the transmission spectrum of a MRR with coupling gap of 350 nm at the drop port. The FSR of the resonators is measured to be 6.2 nm at 2 μm wavelength, which closely matches the expected FSR of a MRR with radius of 29 μm and a theoretical group index of 3.5. An extinction ratio of more than 17 dB is achieved. In order to study the effect of the quality factor of the MRR on the performance of the external cavity laser, MRRs with three different coupling gaps are fabricated in our photonic IC. It can be found that the quality factor increases from 2500 to 15000 as the coupling gap increases from 200 nm to 500 nm.

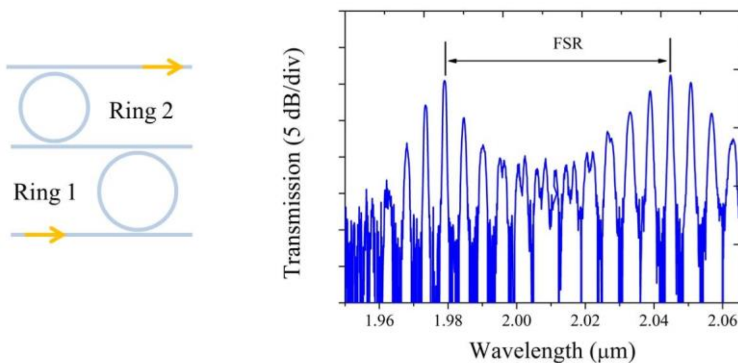

Figure 5.13. *Measured transmission spectrum of the Vernier filter consisting of MRRs with coupling coefficient κ = 0.3.*

Figure 5.13 shows the measured transmission spectrum of the Vernier filter with coupling coefficient κ=0.3. A FSR of around 66 nm is obtained, which matches the theoretical data very well as shown in Figure 5.8(b). The modal transmission difference shown in Figure 5.13 is lower than the simulated value shown in 5.8(b) since the transmission spectra of the two MRRs are not perfectly aligned through thermal tuning.

5.6 Measurement setup

The external cavity laser characterization is carried out by mounting the GaSb-based gain chip-on-carrier and the silicon photonic chip on XYZ precision alignment stages, as shown in Figure 5.14 (a). Light coupling between the gain chip and the silicon photonic IC is realized by butt coupling. The light is coupled out from the silicon waveguide through a grating coupler and collected by a standard single mode fiber (SMF-28), which is connected to an optical spectrum analyzer (OSA, Yokogawa AQ6375) measuring at a resolution of 0.05nm. The optical alignment between the two chips is performed by maximizing the light output power from the grating coupler. A top-view microscope image of the butt-coupling between the GaSb-based gain chip and silicon photonic IC is shown in Figure 5.14(b). The laser output power coupled to the silicon waveguide is calculated by measuring the coupling efficiency of a reference grating coupler. The coupling efficiency at 2 μm is −10 dB, and the 3 dB bandwidth is 80 nm. During all the measurements, the GaSb gain chip operates un-cooled.

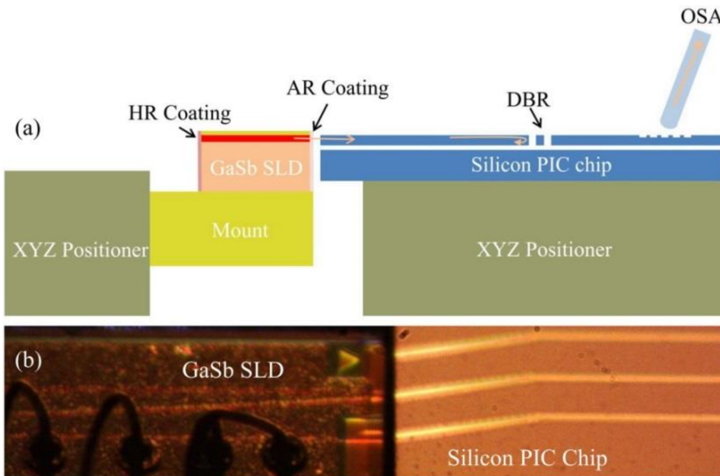

Figure 5.14. *(a) Schematic of the experimental setup; (b) top view of the butt-coupling between the GaSb-based gain chip and silicon photonic IC.*

Figure 5.15 shows the spectrum of amplified spontaneous emission coupled from the GaSb-gain chip to a silicon waveguide through the silicon spot size converter. The GaSb-based SLD is driven with injection current of 100 mA during measurement. The light is coupled out through the integrated grating coupler and collected by a fiber. It can be found that the spectrum is smooth without any sign of lasing modes, suggesting that the parasitic reflections are small.

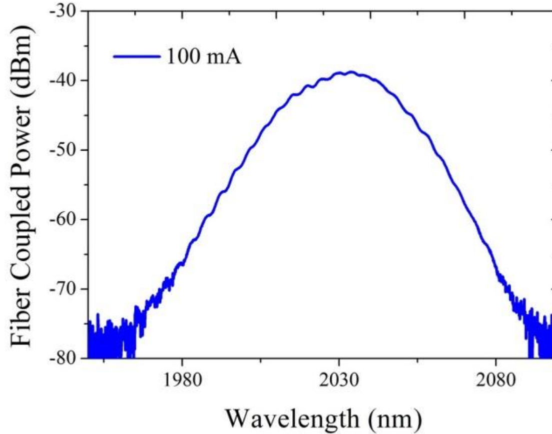

Figure 5.15. *Measured amplified spontaneous emission coupled to a silicon waveguide when the gain chip is driven with 100 mA injection current.*

5.7 Laser performance

5.7.1 L-I-V properties

Figure 5.16 shows the light-current-voltage (L-I-V) curve of the three external cavity lasers with different coupling gaps (200 nm, 350 nm and 500 nm) between the two MRRs and bus waveguide. The waveguide referenced L-I curves are measured at a lasing wavelength of 2060 nm. The threshold current density and maximum output power is 0.8 kA/cm^2 and 7.5 mW respectively for the device with a 200 nm coupling gap in the MRRs. When the coupling gap is increased to 500 nm, the threshold current density increases to 1 kA/cm^2 and the maximum output power reduces to 3.8 mW, which is attributed to the lower transmission of the ring resonator as the coupling gap increases (i.e. the ring resonator becomes undercoupled). The kinks in the L-I curve are the result of mode hopping in the laser cavity. From the three L-I curves presented here, it can be found that the laser with the weakest coupled MRRs shows the most stable operation, while the laser with smallest coupling gap shows strong mode

hopping behavior. The corresponding electro-optic conversion efficiency is ~2.3% for the 7.5 mW maximal output power, which is lower than the value of the external cavity laser using a bulky optics system (~3.4%) as shown in [15]. The laser wall-plug efficiency can be improved by further reducing the butt coupling loss at the GaSb/silicon interface, propagation loss of the silicon waveguides and the drop efficiency of the ring resonators.

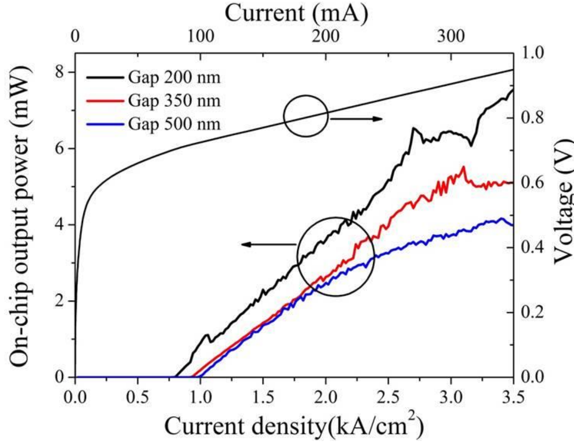

Figure 5.16. *Light-current-voltage curves of the GaSb/silicon external cavity lasers. Three devices with different coupling gap are shown.*

A typical emission spectrum from the laser with 500 nm coupling gap is shown in Figure 5.17. Single mode lasing with a SMSR higher than 60 dB is obtained.

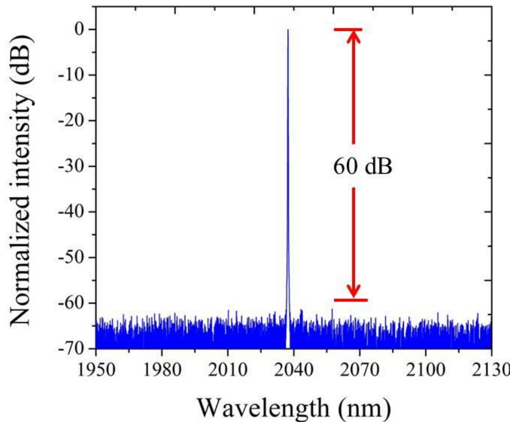

Figure 5.17. *A typical output spectrum from the laser with coupling gap of 500 nm, measured at an injection current of 300 mA.*

5.7.2 Tuning by one MRR

Wavelength tuning is realized by adjusting the power dissipated in the micro-heaters on top of the ring resonators and phase section. Figures 5.18(a)-5.18(c) shows the superimposed (normalized) laser emission spectra of the three tunable lasers, by tuning only one ring resonator. As discussed above, changing the temperature of one ring resonator shifts its transmission spectrum and thus the overlapping wavelength jumps from one transmission peak of the unheated ring resonator to the next. The spacing of these peaks is found to be 6.5 nm, which corresponds to the FSR of the unheated ring. It can be found that the SMSR of the three lasers increases as the coupling gap increases as shown in Figure 5.18(a)-5.18(c). This is because the Vernier filter with weaker coupled MRRs has higher modal transmission difference. The current injected in the gain chip is kept at 300 mA during the measurements.

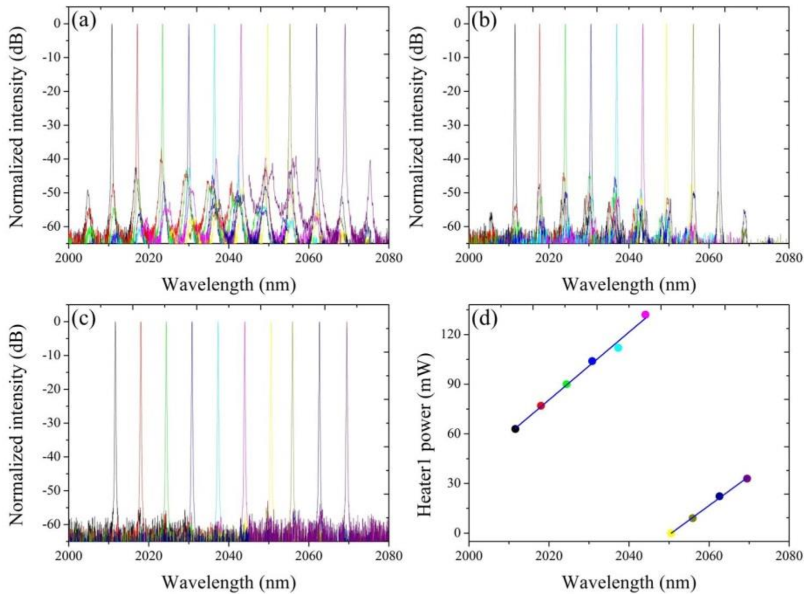

Figure 5.18. Superimposed spectra of three lasers with coupling gap of 200 nm (a), 350 nm (b) and 500 nm (c), tuned by varying the heater power of Ring1; (d) wavelength tuning as a function of Heater1 power, for the case of MRRs with a coupling gap of 500 nm.

The dependence of the lasing wavelength on the power dissipated in Heater1 is shown in Figure 5.18(d), for the case of MRRs with a coupling gap of 500 nm. A tuning range of 58 nm is obtained with a heater power consumption of 132 mW. This power efficiency can be improved by optimizing the heater

design. In this work, heaters consisting of metal spirals covering the whole MRRs are used. More efficient heaters can be made by overlapping the metal wires with the silicon waveguide, or by providing a better thermal isolation of the ring resonators. The dependence of the output power and SMSR on the lasing wavelength for an injection current of 300 mA is shown in Figure 5.19(a) and 5.19(b), respectively. It can be seen that the laser with smaller coupling gap has higher output power, due to the reduced internal losses of the external cavity. The power dip at 2040 nm observed for the device with coupling gap of 200 nm and 350 nm is currently not well understood. The lasers with a coupling gap of 200 nm, 350 nm and 500 nm have a SMSR better than 36 dB, 43 dB and 52 dB over the full tuning range, respectively. The best SMSR is higher than 60 dB.

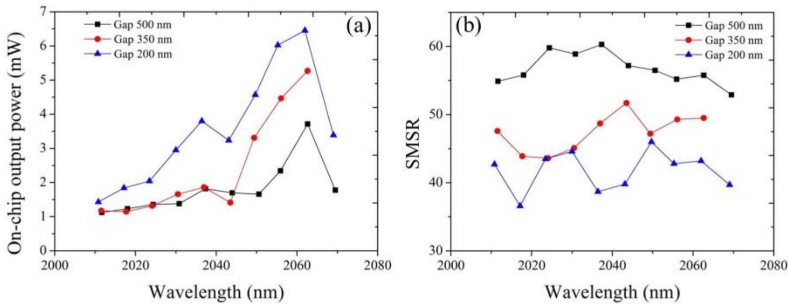

Figure 5.19. Dependence of on-chip output power (a) and SMSR (b) on the lasing wavelength for the lasers with different coupling gap.

5.7.3 Tuning by two MRRs

When only one of the MRRs is tuned, the wavelength resolution of tuning is limited by the FSR of the MRRs. To achieve fine tuning, both of the MRRs should be simultaneously tuned. Figures 5.20(a) and 5.20(b) show the superimposed spectra with 0.7 nm (a) and 0.2 nm (b) resolution tuning over 25 nm and 2 nm, respectively. Power efficient tuning to a specific wavelength can be realized using the following two steps. Firstly, the lasing wavelength is tuned to the position close to the targeted wavelength by heating only one MRR as shown in Figure 5.18. Then, the resonant peaks of the two MRRs are moved together by increasing the dissipated power in the micro-heaters on both ring resonators. An example of this method is shown in Figure 5.20(b) and 5.20(c), covering the 2031-2033 nm wavelength range. By dissipating 105 mW power in Heater1, the lasing wavelength is adjusted to 2031 nm as shown in Figure 5.19(d). Then by increasing the power dissipated in both heaters, the lasing wavelength is tuned with a fine wavelength step.

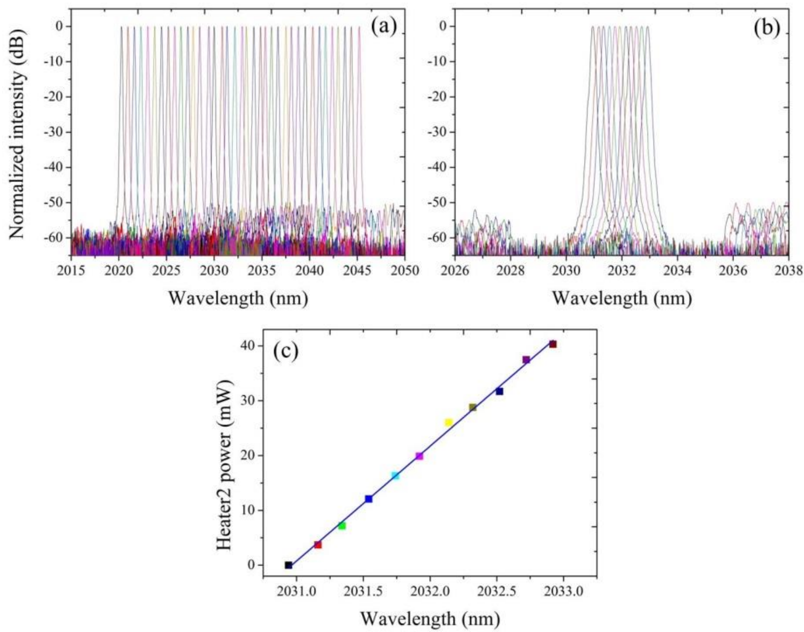

Figure 5.20. *Superimposed spectra of the laser with 500 nm coupling gap showing 0.7 nm (a) and 0.2 nm (b) resolution tuning over 25 nm and 2 nm, respectively; (c) dependence of the lasing wavelength on the power of Heater2 for the 0.2 nm resolution tuning shown in (b).*

5.7.4 Tuning by phase section

The wavelength resolution of tuning by two heaters is limited by the FSR of the longitudinal modes of the Fabry-Perot cavity. To achieve a continuous and more precise wavelength tuning (<0.1 nm), a heated 350 μm long silicon spiral waveguide structure is used in the laser cavity to control the position of the longitudinal modes in the laser cavity. Figure 5.21 shows a contour map of the fiber-coupled laser spectra as a function of the dissipated power in the heater of the phase shifter of the device with 500 nm coupling gap. A continuous tuning with span around 0.1 nm is achieved with a power consumption of 60 mW. In this operation, the optical length of the laser cavity continuously increases as the heater power increases, which results in a red shift of the longitudinal modes. In this fine tuning, the laser with weakly coupled MRRs show more stable tuning than the devices with strongly coupled MRRs.

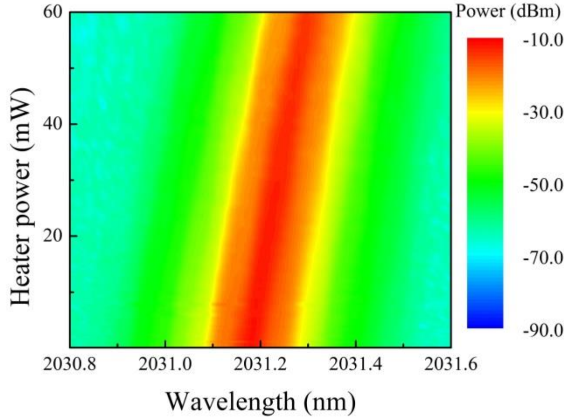

Figure 5.21. *Contour map of the fiber-coupled laser spectra as a function of the dissipated power in the heater of the phase shifter of the laser with 500 nm coupling gap.*

5.8 Conclusion

In this chapter, we report 2 μm wavelength range widely tunable GaSb-based external cavity lasers using a silicon photonics feedback circuit. In the feedback circuit, the lasing wavelength is selected and thermally tuned by utilizing the Vernier effect of two cascaded silicon MRRs. A phase shifter structure is used in the silicon photonic IC to achieve continuous tuning. A 58 nm tuning range is achieved in the 2.01-2.07 μm range. We experimentally present the effects of the coupling coefficient of the MRRs on the performance of the tunable laser. With strongly coupled MRRs, the laser has higher output power and lower threshold current, while the SMSR and tuning stability is lower than for a laser with weakly coupled MRRs. The uncooled laser has a maximum output power of 7.5 mW and threshold current density of 0.8 kA/cm^2 when the coupling gap of the MRRs is 200 nm. A SMSR higher than 52 dB over the full tuning range and in the optimum operation point above 60 dB are obtained for the laser with weakly coupled MRRs. This result enables the implementation of compact, high performance tunable laser sources for the 2 μm wavelength range.

References

[1] B. Mroziewicz, “External cavity wavelength tunable semiconductor lasers – a review,” Opto-Electron. Rev. **16**(4), 347–366 (2008).

[2] U. H. Jacobs, K. Scholle, E. Hermann, G. Huber, M. Rattunde, and J.Wagner, Appl. Phys. Lett. **85**, 5825 (2004).

[3] K. Vizbaras, E. Dvinelis, I. Šimonytė, A. Trinkūnas, M. Greibus, R. Songaila, T. Žukauskas, M. Kaušylas, and A. Vizbaras, “High power continuous-wave GaSb-based superluminescent diodes as gain chips for widely tunable laser spectroscopy in the 1.95–2.45 μm wavelength range,” Appl. Phys. Lett. **107**(1), 011103 (2015).

[4] www.thorlabs.com

[5] B.-S. Choi, S. H. Oh, K. S. Kim, K.-H. Yoon, H. S. Kim, M.-R. Park, J. S. Jeong, O.-K. Kwon, J.-K. Seo, H.-K. Lee, and Y. C. Chung, “10-Gb/s direct modulation of polymer-based tunable external cavity lasers,” Opt. Express **20**(18), 20368–20375 (2012).

[6] T. Takeguchi, M. Takahashi, K. Suzuki, S. Watanabe, and H. Yamazaki, “Wavelength tunable laser with silica-waveguide ring resonators,” IEICE Trans. Electron, E92-C, 198–204 (2009).

[7] Y. Fan, R. M. Oldenbeuving, C. G. Roeloffzen, M. Hoekman, D. Geskus, R. G. Heideman, and K.-J. Boller, “290 Hz Intrinsic Linewidth from an Integrated Optical Chip-based Widely Tunable InP-Si_3N_4 Hybrid Laser,” in CLEO-Laser Applications to Photonic Applications 2017, paper JTh5C.9 (2017).

[8] T. Chu, N. Fujioka, and M. Ishizaka, “Compact, lower-power-consumption wavelength tunable laser fabricated with silicon photonic-wire waveguide micro-ring resonators,” Opt. Express **17**(16), 14063–14068 (2009).

[9] T. Kita, R. Tang, and H. Yamada, “Narrow spectral linewidth silicon photonic wavelength tunable laser diode for digital coherent communication system,” IEEE J. Sel. Top. Quantum Electron. **22**(6), 1500612 (2016).

[10] R. Wang, Aditya Malik, I. Šimonytė, A. Vizbaras, K.ristijonas Vizbaras, and G. Roelkens “Compact GaSb/silicon-on-insulator 2.0x μm widely tunable external cavity lasers,” Opt. Express **24**(25), 28977-28986 (2016).

6

Conclusions and perspectives

6.1 Conclusions

Almost sixty years ago, silicon electronic integrated circuits (ICs) were invented for computing applications. In the last fifteen years, silicon photonic ICs have been rapidly developed for telecommunication applications. These low-cost ICs have the potential to bring transformative changes in the field of sensing as well. In the recent past, there have been considerable research efforts aiming to exploit the integration capability of IC technology, both electronics and photonics, to realize fully integrated sensors. For silicon photonic ICs, the mid-infrared spectral range (2 μm-30 μm) is more interesting for spectroscopic sensing applications than the telecommunication wavelengths (1.31 μm and 1.55 μm). As a spectral region overlapping with the (extended) telecommunication wavelength window and molecular fingerprinting region, the 2 μm wavelength range is of interest for optical communication and spectroscopic sensing of many important gases and biological molecules.

For an on-chip spectroscopic sensing system, a light source, a probe component and a spectrometer or single pixel detector should be integrated on the chip. The silicon photonics platform can offer low-loss and ultra-compact waveguide structures used as the probe component, and high-performance spectrometers. However, it cannot provide efficient light sources and photodetectors in the 2 μm wavelength range, which are typically implemented in III-V material. Combining III-V opto-electronic devices with silicon waveguide circuits can provide a compact platform for miniaturized spectroscopic sensors. In this wavelength range, InP-based type-II and GaSb-based type-I heterostructures can be used as the active region of lasers and photodetectors. Among these two material systems, for now, the former inherits a mature heterogeneous integration technology, while the latter has better optical performance but less-established heterogeneous integration processes. Therefore, we chose to integrate InP-based type-II epitaxial layer stacks on silicon waveguide circuits to realize a heterogeneous III-V-on-silicon platform, and combine a GaSb gain chip with a silicon photonics IC by butt-coupling to realize widely tunable GaSb/silicon lasers sources for spectroscopic sensing.

In the III-V-on-silicon platform, the InP-based type-II epitaxial layer stack is adhesively bonded on silicon waveguides using DVS-BCB (divinylsiloxane-bis-benzocyclobutene), a polymer, as the bonding agent. The epitaxial layer stack is designed for III-V-on-silicon lasers, but it also allows co-integrating photodetectors based on the same material. The silicon-on-insulator (SOI) waveguides are fabricated in 200 mm CMOS pilot lines and have a propagation loss around 0.5 dB/cm. A wet etching process flow is developed to create the III-V device mesa and very sharp III-V tip in the spotsize converter. We also

devote efforts to optimize the metallization, passivation and dry etching processes.

2 μm range III-V-on-silicon photodetectors based on two different structures are reported in this thesis. Adiabatically-coupled photodetectors have a high responsivity of 1.6 A/W at 2.35 μm wavelength and a dark current of 10 nA under a bias voltage of −0.5 V at room temperature. Grating-assisted photodetectors show a responsivity of 0.1 A/W and dark current of 5 nA. These photodetectors are heterogeneously integrated with several high-performance SOI arrayed waveguide spectrometers (AWGs), which have a low insertion loss (2.5-3 dB) and low crosstalk (−30 to −25 dB) in the 2.3 μm wavelength range. The performance of the AWG spectrometers does not degrade after photodetector array integration. A broadband III-V-on-silicon 2.3 μm range LED is also integrated with AWG spectrometers. This integration of LEDs and photodetector arrays with spectrometers enables the realization of a fully integrated 2- μm-wavelength-range spectroscopic system in silicon photonics.

We also demonstrated III-V-on-silicon Fabry-Perot lasers, distributed feedback (DFB) lasers, and DFB laser arrays for the 2.3 μm wavelength range, based on the same III-V epitaxial layer stack that was used for the III-V-on-silicon photodetectors. A high efficiency III-V/silicon spot size converter is designed to realize light coupling between the III-V waveguide and silicon waveguide. The Fabry-Perot laser cavity consists of a III-V-on-silicon semiconductor optical amplifier (SOA) sandwiched between two SOI waveguide distributed Bragg gratings (DBRs), while SOAs are adhesively bonded on the first-order silicon DFB gratings in the DFB lasers. In CW operation, the DFB lasers have a threshold current density of 1.6 kA/cm^2 and maximum light output power of 3 mW at 5 ℃, and operate up to 25 ℃. By varying the silicon grating pitch, a DFB array with broad wavelength coverage from 2.28 μm to 2.43 μm is realized. Besides, a continuous current-tuning range of more than 10 nm can be achieved by fabricating four DFB lasers with different waveguide widths.

Besides on-chip spectroscopic sensing applications, the silicon photonic ICs also can be used to miniaturize 2 μm range optical components. In the fifth chapter, we show a GaSb/silicon external cavity laser using a silicon photonic IC as the feedback element, which features negligible size compared to the use of an external diffraction grating. In the GaSb/silicon hybrid laser, a Fabry-Perot laser cavity is formed between the HR-coated facet of the gain chip and the silicon waveguide DBR. The silicon photonic IC contains a Vernier filter consisting of two thermally tuned micro-ring resonators (MRRs) and a phase section to allow for quasi-continuous wavelength tuning. In this way, a compact external cavity laser with a 58 nm tuning range and side mode suppression ration (SMSR) better than 52 dB over the whole range is realized.

6.2 Perspectives

In this PhD thesis, I have presented a heterogeneous III-V-on-silicon platform and III-V/silicon hybrid external cavity lasers for spectroscopic sensing in the 2 μm wavelength range. In future work we can further improve the device performance and realize miniaturized and portable III-V/silicon gas sensors and bio-sensors.

In section 4.4.3, we have shown a laser structure with two integrated silicon MRRs in a III-V-on-silicon Fabry-Perot laser cavity. A single mode emission with SMSR >40 dB is achieved. To tune the lasing wavelength, in the future, micro-heaters should be deposited on the MRRs. Based on the same silicon structure used to tune the 2.0x GaSb/silicon external cavity laser, we can realize a more integrated widely tunable III-V-on-silicon laser at 2.35 μm. This kind of laser is very interesting for multi-species trace gas spectroscopy and bio-molecule detection. Besides, integrating an AWG filter in the Fabry-Perot laser cavity can be used to realize a multi-wavelength laser for these applications.

In the fourth chapter, we demonstrated broad wavelength coverage 2.3 μm DFB laser arrays. For a number of spectroscopic sensing applications envisioned for the DFB laser arrays, it is important to combine the light from individual lasers to a common path. Silicon photonic ICs can provide plenty of high-performance waveguide-based beam combiners (such as AWGs), thereby enabling a more compact sensing system than using discrete diffraction gratings for wavelength combination.

In recent years, dual-comb spectroscopy has attracted a lot of interest as a promising spectroscopic tool that enables superior resolution, high-sensitivity broadband spectroscopy compared with traditional Fourier transform infrared spectroscopy (FTIR) [1]. The currently available comb generators are mostly based on bulky and high-cost mode-locked fiber lasers and solid state lasers Low-loss silicon waveguide circuits promise to enable compact ultra-dense III-V-on-silicon comb lasers. While Z. Wang *et al.* have demonstrated a heterogeneously integrated III-V-on-silicon mode-locked laser that passively mode-locks at a record-low repetition rate of 1 GHz at 1.6 μm [2], III-V-on-silicon mode lock lasers with a comb line spacing < 10 GHz in the 2 μm wavelength range are more interesting for spectroscopic sensing. Besides, integrated highly nonlinear, dispersion-engineered silicon waveguides can be used for further comb broadening in the 2 μm wavelength range.

In the fifth chapter, a GaSb/silicon hybrid external cavity laser with 58 nm wavelength tuning range is demonstrated. Using the same GaSb-based gain chip, K. Vizbaras *et al.* realized an external cavity laser with tuning range >120 nm based using an external diffraction grating [3]. This result indicates it is possible to get a GaSb/silicon hybrid laser with much broader wavelength tuning range

than 58 nm. To achieve this goal, the free spectral range (FSR) of the Vernier filter should be increased, which can be realized by reducing the radius of the two MRRs. In addition, the butt-coupling loss and waveguide propagation loss should be further reduced to ensure a broader wavelength tuning.

Two typical configurations for fully integrated III-V/silicon spectroscopic sensors are shown in Figure 1.10. We have demonstrated all optical components required for these kinds of sensors, including laser sources, photodetectors, spectrometers and low loss silicon waveguides. In the next step, we need to test the performance of these III-V/silicon optical sensors in actual gas sensing and bio-sensing experiments. Before such tests, electrical drivers should be integrated with these sensors to read out the optical signal.

References

[1] I. Coddington, N. Newbury, and W. Swann, “Dual-comb spectroscopy,” Optica **3**(4), 414–426 (2016).

[2] Z. Wang, K. V. Gasse, V. Moskalenko, S. Latkowski, E. Bente, B. Kuyken and G. Roelkens, “A III-V-on-Si ultra-dense comb laser,” Light: Science & Applications **6**, e16260 (2017).

[3] K. Vizbaras, E. Dvinelis, I. Šimonytė, A. Trinkūnas, M. Greibus, R. Songaila, T. Žukauskas, M. Kaušylas, and A. Vizbaras, “High power continuous-wave GaSb-based superluminescent diodes as gain chips for widely tunable laser spectroscopy in the 1.95–2.45 μm wavelength range,” Appl. Phys. Lett. **107**(1), 011103 (2015).